

SISSA

Scuola
Internazionale
Superiore di
Studi Avanzati

Physics Area - PhD course in
Astrophysics & Cosmology

ISTEDDAS:
a new direct N-Body code on GPUs
to study merging compact-object binaries
in star clusters

Candidate:
Mattia Mencagli

Advisor:
Mario Spera

Academic Year 2022-23



Acknowledgements

I want to express my gratitude to my supervisor, Mario Spera, whose guidance, and expertise were crucial in completing ISTEDDAS and, therefore, this thesis.

A special thanks go to Alessandro Alberto Trani and Cecilia Sgalletta, whose collaboration enhanced my understanding of TSUNAMI and SEVN respectively.

Additionally, I am grateful to Ugo di Carlo for his work in reviewing and correcting this thesis.

Finally, I thank the NVIDIA developers, Mauro Bisson, Josh Romero, and Massimiliano Fatica for getting in touch, and for their dedicated efforts in optimizing the ISTEDDAS' GPU kernels and contributing to my overall knowledge of GPU programming.

Contents

Abstract	1
1 Gravitational waves from merging compact objects in star clusters	3
1.1 Gravitational waves	3
1.2 Merging compact objects	4
1.3 Formation channels	5
1.4 Isolated binary channel	6
1.4.1 Mass transfer	7
1.4.2 Common envelope (CE)	8
1.4.3 Chemically homogeneous evolution (CHE)	10
1.5 Dynamical channel	10
1.5.1 Two-body encounters, dynamical friction, and core-collapse	11
1.5.2 Binary – single-body encounter	12
1.5.3 Hardening	12
1.5.4 Exchange	13
1.5.5 BHs in the pair-instability mass gap	15
1.5.6 Direct three-body binary formation	17
1.5.7 Dynamical ejection	17
1.5.8 Formation of intermediate-mass black holes by runaway collisions	18
1.5.9 Hierarchical BBH formation and IMBHs	19
1.5.10 Von Zeipel-Kozai-Lidov resonance	20
1.6 GWs detectors	21
1.7 N-body simulations	23
2 The direct N-body code ISTEDDAS on GPU	25
2.1 The Hermite integrator	25
2.1.1 Polynomial interpolation for the sixth-order integrator	27
2.2 The block time steps method	28
2.3 The Ahmad-Cohen neighbours scheme	28
2.4 Optimizations and parallelization	32
2.4.1 Forces evaluation algorithm	33
2.4.2 Forces reduction and gather	34
2.4.3 Ahmad-Cohen tree building optimization	36

3	The few body code TSUNAMI	41
3.1	The algorithmic regularization chain	41
3.1.1	The time regularization	42
3.1.2	Chain coordinates	42
3.1.3	The modified midpoint method	43
3.1.4	The Bulirsch-Stoer algorithm	44
3.2	Coupling ISTEDDAS and TSUNAMI	45
3.2.1	Decision Making	46
3.2.2	Time synchronization with the block time-step method	49
3.2.3	Parallelization	50
4	The population-synthesis code SEVN	51
4.1	SEVN description	51
4.1.1	Single stars evolution	52
4.1.2	Compact remnant formation	58
4.1.3	Binary stars evolution	61
4.1.4	The evolution algorithm	71
4.2	Coupling ISTEDDAS and SEVN	75
4.2.1	Single star evolution	75
4.2.2	Binary star evolution	79
4.2.3	Energy conserving scheme	82
5	Numerical tests	85
5.1	ISTEDDAS tests	85
5.2	TSUNAMI tests	92
	Conclusions	97
	A GWs analytical derivation	99
	B Keplerian coordinates	103
	Bibliography	106

Abstract

On February 11th, 2016, the LIGO and Virgo scientific collaborations announced the first direct detection of gravitational waves (GWs), a signal caught by the LIGO interferometers on September 14th, 2015, and produced by the coalescence of two stellar-mass black holes. The discovery represented the beginning of an entirely new way to investigate the Universe. The latest gravitational-wave catalog by LIGO, Virgo, and KAGRA brings the total number of gravitational-wave events to 90, and the count is expected to significantly increase in the next years when additional ground-based and space-born interferometers will be operational. From the theoretical point of view, we have only fuzzy ideas on where the detected events came from, and the answers to most of the five Ws and How for the astrophysics of compact binary coalescences are still unknown.

However, two main formation channels have been proposed so far for the formation of merging compact objects (neutron stars - NSs, and black holes BHs). In the isolated binary channel, two progenitor stars are bound since their formation, evolve, and then turn into (merging) compact objects at the end of their life, without experiencing any kind of external perturbation. This scenario is driven by single and binary stellar evolution processes, and it is sometimes referred to as the “field” scenario because it assumes that binaries are born in low-density environments, i.e., that they evolve in isolation. In contrast, in the dynamical channel, two compact objects get very close to each other after one (or more) gravitational interactions with other stars or compact objects. This evolutionary scenario is quite common in dense stellar environments (e.g., star clusters), and it is driven mainly by stellar dynamics. In reality, the two formation pathways might have a strong interplay. In star clusters, the orbital parameters of binaries might be perturbed by many passing-by objects.

One of the main issues is that most stars form in dense stellar environments, and numerical simulations of merging compact-object binaries in such crowded stellar systems are very challenging. However, to investigate the origins and the properties of merging compact objects we need a powerful N-body code, which can handle, at the same time, the large spatial and time-evolutionary scales of star clusters ($\sim\text{pc}$ and $\sim\text{Gyr}$), and the small scales typical of tight binaries ($\sim\text{AU}$ and $\sim\text{days}$). Therefore, in this thesis, I discuss the innovative algorithms behind ISTEDDAS, a new direct N-body code I developed in C++ from scratch that natively supports CUDA to run on Graphics Processing Unit (GPU) supercomputers. I coupled ISTEDDAS with the few-body code TSUNAMI, which numerically integrates the orbits of tight systems (e.g., binaries or three-body encounters) with very high accuracy, and also with the population-synthesis code SEVN, which

includes up-to-date prescriptions for the evolution of both single and binary stars.

In this Thesis, I will explain the complex machinery behind ISTEEDDAS. In particular, the first chapter is a wide overview of the astrophysical problems that are uniquely addressed by ISTEEDDAS. The second, third, and fourth chapters are overviews of ISTEEDDAS, TSUNAMI, and SEVN, respectively. In those chapters I will go through the implementation details of the codes, I will explain how they are interfaced with each other, and I will show some results that validate the first version of the ISTEEDDAS code.

Chapter 1

Gravitational waves from merging compact objects in star clusters

In this chapter, I will give an overview of the astrophysical aspects involved in my research. In particular, I will delve into the details of the astrophysical processes involved in the emission of gravitational waves (GWs), which were detected by the interferometers of the LIGO-VIRGO collaboration (LVC). These processes are thought to be crucial for the formation of merging compact-object binaries, such as black holes (BHs) or neutron stars (NSs) binaries, and promising astrophysical environments where such mergers can happen are star clusters (SCs). To understand the complex interplay of all the ingredients necessary to obtain a GW event we utilize a very powerful tool: N-body simulations. Thus, in this chapter, I am going to describe GWs, the laser interferometers LIGO and VIRGO, the merger process of compact objects, star clusters, and, finally, N-body simulations.

1.1 Gravitational waves

As predicted by Einstein’s general relativity (GR), GWs are disturbances or ripples in the curvature of spacetime, generated by accelerated masses. They are transverse (oscillating perpendicular to the direction of propagation), travel at the speed of light, and possess two polarizations. GWs physically manifest themselves as time-dependent strains or perturbations in spacetime ($\delta L/L$), where L is the distance between two reference points in space and δL is the induced displacement over the baseline L . Therefore, δL is the quantity to be measured to detect the passage of a GW and, to measure it, we use the laser interferometers LIGO and Virgo, see Section 1.6. GR predicts that the induced strain is perpendicular to the axis of GW propagation and is quadrupolar, that is, a wave traveling along the z-axis stretches (then compresses) the path along the x-axis while shrinking (then stretching) the y-axis (for one polarization; in the orthogonal polarization, the elongation/compression occurs along axes rotated 45° relative to the x-axis and y-axis). See Appendix.A for a deeper explanation on GWs’ analytical derivation and quadrupolar emission.

Fundamentally different and complementary to other astrophysical “messengers”

such as photons, neutrinos, or cosmic rays, GWs provide unique information about the most energetic astrophysical processes in the Universe by carrying information about the dynamics of massive objects such as black holes and neutron stars moving at relativistic speeds [26]. Single-object events were taken into consideration but even the most energetic event, a supernova, because of its roughly spherical symmetry, has a negligible quadrupolar emission. Therefore, the scientific community attributes the detected GWs to the merging of compact objects, that indeed can produce a quadrupolar wave. In the next section (Section 1.2) I will go through an in-depth discussion about merging compact objects.

1.2 Merging compact objects

Merging compact-object binaries are binary systems composed of two compact objects that are so close to each other that they merge via GW emission. The members of such binaries can be white dwarfs (WDs), NSs, BHs, and their combinations, e.g., BH-NS binary systems. These systems have been investigated for decades by many authors, who predicted their existence through theoretical studies that go from the formation and evolution of the stellar progenitors to accurate numerical relativity simulations of the final merger phase [58, 59, 125, 160, 215, 230, 245, 294, 321].

From the observational point of view, proving the existence of merging compact-object binaries has always been challenging. While such systems are potentially loud GW sources, catching their GW signal is not straightforward. The passage of a GW produces a relative change in the distance between two points which is

$$\frac{\delta L}{L} = \frac{4m_1 m_2 G^2}{r l_0 c^4}, \quad (1.1)$$

where r is the distance from the GW source, l_0 is the orbital separation of the binary, L is the reference distance, m_1 and m_2 are the masses of the GW source, G is the gravitational constant, and c is the speed of light [78]. The factor $G^2 c^{-4}$ is minuscule ($\sim 5 \times 10^{-55} \text{ m}^2 \text{ kg}^{-2}$), thus, when a GW reaches the Earth, it causes an extremely small perturbation, which is very hard to detect. Even without direct evidence of GWs, the loss of orbital energy of a compact binary via GWs was verified through radio observations of the binary pulsar PSR B1913+16 [129]. The observed orbital decay of the Hulse–Taylor binary is remarkably consistent with a GW-induced shrinking. This system, which is expected to merge in ~ 300 Myr, provided not only an additional confirmation of Einstein’s theory of general relativity, but it also suggested that there might be not just one, but a population of binary NSs that can merge in relatively short times via GW emission. For the first direct evidence of merging compact-object binaries and their GW’s fingerprint, we had to wait until 14 September 2015, when the two ground-based interferometers of the Laser Interferometer Gravitational-wave Observatory (LIGO) were able to *measure* the effect of a passing GW. The signal, named GW150914, was attributed to the coalescence of two stellar-mass BHs with masses $m_1 = 36_{-4}^{+5} M_\odot$ and $m_2 = 29_{-4}^{+4} M_\odot$ [6, 7]. The event carried many scientific implications with itself and it laid the foundations of a new way to investigate the

Universe by allowing us to access data never collected before. An important, solid conclusion was that GW150914 marked a new starting point for the astrophysical community. It gave an unprecedented boost to the development of new theoretical models to study the formation and evolution of compact-object binaries and their progenitor stars, with a new goal: providing an astrophysical interpretation to GW sources.

1.3 Formation channels

From the theoretical point of view, two main formation channels have been proposed, so far, for the formation of merging compact objects. In the **isolated binary channel**, two progenitor stars are bound since their formation; they evolve, and then turn into (merging) compact objects at the end of their life, without experiencing any kind of external perturbation [33, 37, 65, 66, 72, 107, 131, 132, 184, 194, 226, 238, 274, 296, 308, 309, 322]. This scenario is driven by single and binary stellar evolution processes, and it is sometimes referred to as the “field” scenario, because it assumes that binaries are born in low-density environments, i.e., that they evolve in isolation. In contrast, in the **dynamical channel**, two compact objects become bound to each other after one (or more) gravitational interactions with other stars or compact objects. This evolutionary scenario is quite common in dense stellar environments (e.g., star clusters), and it is driven mainly by stellar dynamics [21, 27, 73, 121, 124, 133, 145, 165, 185, 199, 209, 222, 251, 260, 264, 290, 322, 325, 326]. In reality, the two formation pathways might have a strong interplay. In star clusters, the orbital parameters of binaries might be perturbed by many passing-by objects. Dynamical interactions might be strong enough to eject the stellar binary from the cluster and trigger the merger event in the field. Such an apparently isolated merger would not have occurred if the progenitor stars had evolved in isolation. Such **hybrid scenarios** blur the line between the dynamical and the isolated binary channel, and they have already been investigated by various authors [23, 71, 155, 292].

Our theoretical knowledge of the formation scenarios is hampered by the uncertainties and degeneracies of the astrophysical models. Single-star evolutionary tracks, the strength of stellar winds (especially for massive stars at low metallicity), core-collapse and pair-instability supernova (PISN), the orbital parameters of binary stars at birth, binary mass transfer, compact-object birth kicks, stellar mergers, tidal interactions, common envelope (CE), and GW recoil, are only part of the uncertain ingredients of the unknown recipe of merging binaries. In contrast, stellar dynamics is simple and elegant, but developing accurate and fast algorithms for the long-term evolution of tight binaries is challenging. Furthermore, studying the evolution of small-scale systems (2 bodies within $\sim 10^{-6}$ pc) in large star clusters ($\gtrsim 10^5$ objects within a few pc) is computationally intensive [4, 50, 51, 134, 149, 196, 201, 205, 252, 303].

Therefore, disentangling different shades of flavors by tasting the final result and going back to the responsible ingredients is very challenging. The consequence is that the GW catalog is growing faster than our theoretical understanding of merging compact-object binaries. At the time of writing, we have already achieved a historic break-

through: we have just started talking about a population of BHs. Indeed, the latest Gravitational Wave Transient Catalog (GWTC) reports $\sim 90^1$ events, see Fig.1.1 for the complete catalogue by LVK.

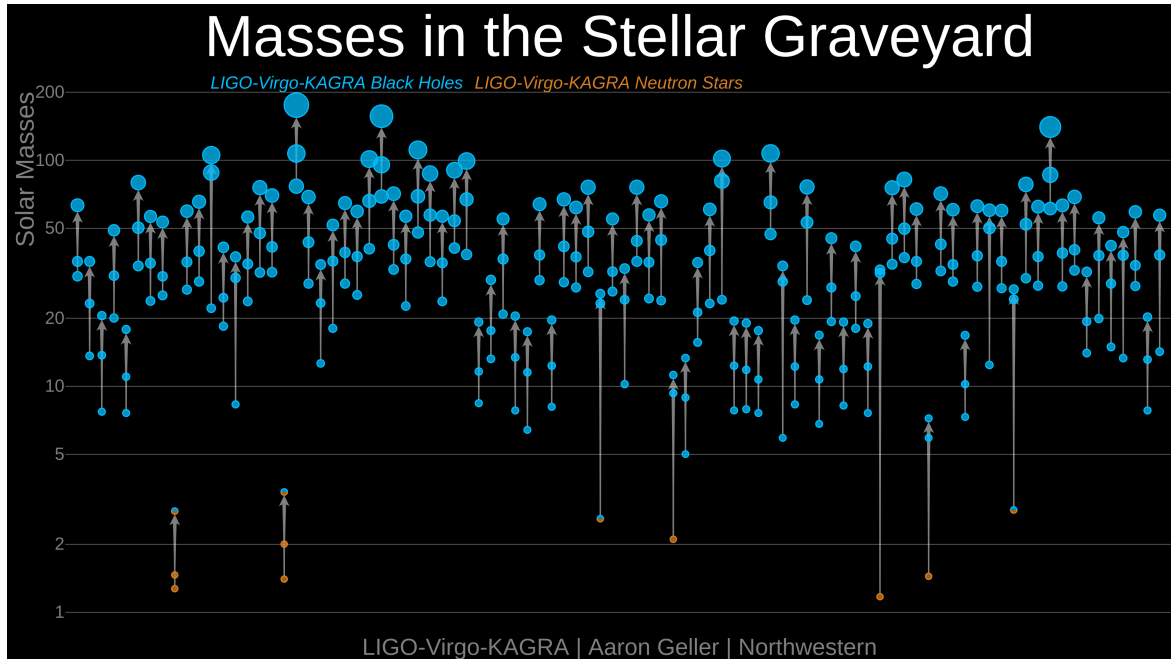


Figure 1.1: Compact object masses. Each point represents a different compact object and the vertical scale indicates the mass in solar masses (M_{\odot}). Blue points represent black holes and orange circles represent neutron stars. Half-blue / half-orange mixed circles are compact objects whose classification is uncertain. Each merger involves three compact objects: two merging objects and the merger product. The arrows indicate which compact object merged and the remnant they produced. (Credits: LIGO-Virgo-KAGRA Collaborations/Frank Elavsky, Aaron Geller/Northwestern.)

1.4 Isolated binary channel

In a simplistic view, one might assume that the formation of a binary black hole (BBH) is an inevitable outcome when two massive stars are part of a binary system and that the mass of each black hole would mirror the mass of its progenitor star as if they evolve as single stars. However, this holds true only when the binary system maintains sufficient separation (referred to as a detached binary) throughout its entire evolutionary trajectory. If the binary is compact, various processes come into

¹LVK-independent analyses have even found a few additional GW candidates (e.g., [219, 223, 318]), mostly black holes binary (BBH) mergers, and the count is expected to significantly increase in the next years, at even faster rates than ever because new ground-based interferometers will be operational and the existing ones will increase their sensitivity [282, 283].

play during its evolution, potentially altering its ultimate destiny. Binary population-synthesis codes are semi-analytical tools commonly employed to investigate the impact of binary evolution on BBH formation in isolated binaries (e.g., [29, 34, 81–83, 106–108, 110, 131, 153, 190, 193, 202, 231, 237, 270, 274, 278]). These codes integrate a description of stellar evolution with models for supernova explosions and a framework for binary evolution processes. In this section, I outline key binary-evolution processes and provide a brief examination of their representation in widely utilized population-synthesis codes.

1.4.1 Mass transfer

When two stars begin an exchange of material, it means they undergo a mass transfer event, which can be triggered by either stellar winds or Roche-lobe filling episodes. When a massive star loses mass by stellar winds, depending on the amount of mass that is lost and on the relative velocity of the wind with respect to the companion star, its companion could capture some of the ejected material. According to the Bondi & Hoyle formalism [42], the mean mass accretion rate from stellar winds is modeled as [131]:

$$\dot{m}_2 = \frac{1}{\sqrt{1-e^2}} \left(\frac{Gm_2}{v_W^2} \right)^2 \frac{\alpha_W}{2a^2} \frac{1}{[1+(v_{orb}/v_W)^2]^{3/2}} |\dot{m}_1|. \quad (1.2)$$

Here, e represents binary eccentricity, G is the gravitational constant, m_1 and m_2 are the masses of the donor and accreting star, respectively, v_W is the wind velocity, $\alpha_W \sim 3/2$ is an efficiency constant, a is the binary’s semi-major axis, $v_{orb} = \sqrt{G(m_1+m_2)}/a$ is the binary’s orbital velocity (with m_1 denoting the donor’s mass), and \dot{m}_1 signifies the donor’s mass loss rate. Given that $|\dot{m}_1|$ is typically quite low ($|\dot{m}_1| < 10^{-3} M_\odot \text{yr}^{-1}$) and v_W is generally high ($> 1000 \text{km/s}$ for a line-driven wind) compared to orbital velocity, this form of mass transfer tends to be inefficient. However, wind-fed systems, especially those observed in high-mass X-ray binaries [296, 298], including those with a Wolf-Rayet star companion [85], are not uncommon.

In contrast, mass transfer through Roche lobe overflow is typically more efficient than wind accretion. The Roche lobe, a teardrop-shaped equipotential surface surrounding a star in a binary system, becomes pivotal in this process. The Roche lobes of both binary members connect at a single point, known as the Lagrangian L1 point. A commonly used formula for the Roche lobe is [77]:

$$R_{L,1} = a \frac{0.49q^{2/3}}{0.6q^{2/3} + \ln(1+q^{1/3})}. \quad (1.3)$$

Here, a represents the binary’s semi-major axis, and $q = m_1/m_2$. This formula characterizes the Roche lobe of a star with mass m_1 , and swapping the subscripts provides the corresponding Roche lobe of a star with mass m_2 ($R_{L,2}$). If a star’s radius is larger (smaller) than its Roche lobe, it overfills (underfills) the lobe, leading to the flow of some of its mass toward the companion star, which can subsequently accrete a portion of it. This mass transfer alters not only the binary stars’ masses and the final mass of their compact remnants but also the binary’s orbital characteristics. In cases

of non-conservative mass transfer, the most realistic scenario, angular momentum loss occurs, impacting the semi-major axis. Recent work by [43] highlights that highly non-conservative mass transfer (mass accretion efficiency $f_{MT} \leq 0.5$) poses challenges when reconciling with LVC data under the assumption that all LVC-observed binary black holes originate from isolated binary evolution. An essential consideration in Roche lobe overflow is whether the process is stable or unstable and the timescale involved. A common approach, as outlined by [76, 131, 237, 287], assumes a simple relation between stellar radius and mass, with the variation in the donor’s radius during Roche lobe overflow given by:

$$\frac{dR_1}{dt} = \frac{\partial R_1}{\partial t} + \zeta \frac{R_1}{m} \frac{dm_1}{dt}. \quad (1.4)$$

In this equation, the term $\partial R_1/\partial t$ accounts for nuclear burning, and the ζ term measures the adiabatic or thermal response of the donor star to mass loss. Note that dm_1/dt , representing donor mass loss, is always negative. Similarly, the change in the donor’s Roche lobe size $R_{L,1}$ can be approximated as:

$$\frac{dR_{L,1}}{dt} = \frac{\partial R_{L,1}}{\partial t} + \zeta_L \frac{R_{L,1}}{m} \frac{dm_1}{dt}. \quad (1.5)$$

Here, $\partial R_{L,1}/\partial t$ accounts for tides and gravitational wave radiation, while ζ_L describes the Roche lobe’s response to mass loss—whether it contracts or expands. If $\zeta_L > \zeta$, the Roche lobe contracts faster than the star’s radius, rendering mass transfer unstable. Stability persists until the radius undergoes significant changes due to nuclear burning. Mass transfer instability can occur either on a dynamical timescale (if ζ describes the adiabatic response of the donor and $\zeta_L > \zeta$) or on a thermal timescale (if ζ describes the thermal response of the donor and $\zeta_L > \zeta$). If the mass transfer is dynamically unstable or both stars overfill their Roche lobe, the binary is expected to merge if the donor lacks a steep density gradient between the core and the envelope or to enter a common envelope (CE) phase if the donor exhibits a clear core-envelope distinction.

1.4.2 Common envelope (CE)

When two stars undergo a common envelope (CE) phase, their envelopes cease to co-rotate with their cores. The cores (or the compact object and the companion star’s core, in the case of a single degenerate binary) find themselves immersed in a non-co-rotating envelope, initiating a spiraling motion due to gas drag exerted by the envelope. The energy lost by the cores during this drag contributes to heating the envelope, causing it to become more loosely bound. If this process results in the ejection of the envelope, the binary endures. However, the post-CE binary consists of two exposed stellar cores (or a compact object and an exposed stellar core), and the orbital separation between the cores (or between the compact object and the stellar core) is significantly smaller than the initial separation before the CE phase, due to the spiral-in effect. This reduction in orbital separation is crucial for the fate of a binary black hole (BBH). If the surviving binary evolves into a BBH, the BBH will possess a short semi-major axis ($a \lesssim 100R_\odot$), considerably shorter than the sum of

the maximum radii of the progenitor stars. This compact configuration increases the likelihood of BBH merger through gravitational wave emission within a Hubble time.

In contrast, if the envelope is not expelled, the two cores (or the compact object and the core) continue spiraling inward until they eventually merge. The premature merger of a binary during a CE phase prevents it from evolving into a BBH. The commonly adopted α formalism [309] is used to describe a common envelope, proposing that the energy required to unbind the envelope is exclusively derived from the loss of orbital energy during the cores' spiral-in. The fraction of orbital energy used to unbind the envelope is expressed as:

$$\Delta E = \alpha (E_{b,f} - E_{b,i}) = \alpha \frac{Gm_{c1}m_{c2}}{2} \left(\frac{1}{a_f} - \frac{1}{a_i} \right). \quad (1.6)$$

Here, $E_{b,i}$ ($E_{b,i}$) represents the orbital binding energy of the two cores before (after) the CE phase, a_i (a_f) is the semi-major axis before (after) the CE phase, m_{c1} and m_{c2} are the masses of the two cores, and α is a dimensionless parameter indicating the fraction of removed orbital energy transferred to the envelope. If the primary is already a compact object, m_{c2} denotes the mass of the compact object. The binding energy of the envelope is given by:

$$E_{env} = \frac{G}{\lambda} \left[\frac{m_{env,1}m_1}{R_1} + \frac{m_{env,2}m_2}{R_2} \right]. \quad (1.7)$$

Here, m_1 and m_2 are the masses of the primary and secondary members of the binary, $m_{env,1}$ and $m_{env,2}$ are the masses of the envelope of the primary and secondary members, R_1 and R_2 are the radii of the primary and secondary members, and λ is a parameter reflecting the concentration of the envelope (smaller λ implies a more concentrated envelope).

Setting $\Delta E = E_{env}$ allows us to determine the final semi-major axis a_f for which the envelope is ejected. Larger (smaller) values of α correspond to larger (smaller) final orbital separations. If the resulting a_f is less than the sum of the radii of the two cores (or the sum of the Roche lobe radii of the cores), the binary merges during the CE phase; otherwise, the binary survives. However, it's acknowledged that the α formalism [309] provides a simplistic representation of CE physics, which is inherently more intricate. A comprehensive treatment of CE should consider factors beyond the orbital energy of the cores and the binding energy of the envelope, including the thermal energy of the envelope (the combined radiation energy and kinetic energy of gas particles) [118], recombination energy (as the expanding envelope cools, plasma recombines, and binding energy is released) [154], tidal heating (cooling) from stellar spin down (up) [139], nuclear fusion energy [140], envelope enthalpy [138], and accretion energy that may drive outflows and jets [64, 171, 176, 177, 266, 267]. Additionally, the envelope concentration parameter λ is expected to vary widely among stars and during different evolutionary stages of the same star. Some authors [169, 316] have directly estimated E_{env} from their stellar models, enhancing this formalism. However, the α parameter remains an intrinsic part of the model. Consequently, it is imperative to employ analytic models and numerical simulations to adequately model CE physics.

Although significant efforts have been directed toward this in recent years, the challenge remains formidable. Some recent studies explore the initiation of CE when unstable mass transfer prevents envelope co-rotation with the core, resulting in the companion’s plunge into the envelope [172–175, 299].

Various hydrodynamical simulations focus on the fast spiral-in phase following the plunge-in [221, 227, 247, 248], during which the two cores spiral in on a dynamical timescale (approximately 100 days). At the conclusion of this dynamic spiral-in, only a small fraction of the envelope (approximately 25% according to [221]) appears to be ejected in most simulations. When the two cores are in close proximity, separated by a small gas mass, the spiral-in decelerates, and the system evolves on the Kelvin-Helmholtz timescale of the envelope (approximately 10^{3-5} years). However, simulating the system for a Kelvin-Helmholtz timescale poses challenges for current three-dimensional simulations [162].

1.4.3 Chemically homogeneous evolution (CHE)

Massive stars with rapid rotation may undergo chemically homogeneous evolution (CHE), wherein the absence of a chemical composition gradient results from rotation-induced mixing. This tendency is particularly pronounced in metal-poor stars, as stellar winds are less effective in eliminating angular momentum. In tightly bound binaries, the spins of the stellar components may even increase during their lifetimes due to tidal synchronization. Stars undergoing CHE typically exhibit significantly smaller radii compared to stars that develop a chemical composition gradient, as noted by [66]. Consequently, even binaries with close proximity (a few tens of solar radii) can circumvent the common envelope (CE) phase.

1.5 Dynamical channel

The influence of collisional dynamics becomes prominent in binary evolution when they exist in a dense environment, typically with a stellar density exceeding $\sim 10^3$ stars pc^{-3} , as observed in star clusters (SC). It is widely believed among astrophysicists that the majority of massive stars, which serve as progenitors for black holes (BH), originate within star clusters [159, 235, 307, 311, 312].

Star clusters manifest in various forms. **Globular clusters** (GC) [114], for instance, represent aged stellar systems (approximately ~ 12 Gyr), typically characterized by considerable mass ($M_{SC} \geq 10^4 M_\odot$) and high density (central density $\rho_c \geq 10^4 M_\odot \text{pc}^{-3}$). These clusters undergo dynamic processes such as the gravothermal catastrophe and constitute a relatively minor portion of the baryonic mass in the local Universe (less than $\lesssim 1\%$ [119]). The majority of studies examining the dynamical formation of binary black holes (BBH) concentrate on globular clusters [22, 25, 35, 44, 73, 74, 92, 151, 187, 250, 251, 254, 257–259, 264, 277, 326].

Young dense star clusters (YDSC), characterized by youthfulness (approximately $\lesssim 100$ Myr) and relatively high density ($\rho_c \geq 10^3 M_\odot \text{pc}^{-3}$), are believed to be the primary birthplaces of massive stars [159, 235]. After dispersion through gas

evaporation or disruption caused by the tidal field of their host galaxy, their stellar constituents become part of the galactic field. Consequently, it is plausible that a substantial proportion of field BBHs originated in young star clusters, actively participating in the cluster's dynamics. Some young star clusters might endure gas evaporation and tidal disruption, evolving into older open clusters, akin to Messier 67. Studies exploring BBHs in young and open clusters include references such as [27, 69–71, 97, 145, 155, 156, 185, 325, 326].

Nuclear star clusters (NSC), positioned in the nuclei of galaxies, are a common feature in galaxies [40, 90, 113, 216]. Typically more massive and denser than globular clusters, NSCs may coexist with supermassive black holes (SMBHs). Stellar-mass black holes formed in a galaxy's innermost regions could potentially be captured in the accretion disc of the central SMBH, triggering their eventual merger [30, 198, 275]. These distinctive characteristics render nuclear star clusters unique among star clusters.

1.5.1 Two-body encounters, dynamical friction, and core-collapse

The main driver of the dynamics of star clusters is gravity force. Gravitational two-body encounters between stars lead to local fluctuations in the potential of the star cluster and drive major changes in the internal structure of the star cluster over a two-body relaxation timescale [272, 273]:

$$t_{relax} = 0.34 \frac{\sigma^3}{G^2 \langle m \rangle \rho \ln \Lambda}, \quad (1.8)$$

where σ is the local velocity dispersion of the star cluster, $\langle m \rangle$ is the average stellar mass in the star cluster, ρ is the local mass density, G is the gravity force and $\ln \Lambda \sim 10$ is the Coulomb logarithm. The two-body relaxation timescale is the time needed for a typical star in the stellar system to completely lose memory of its initial velocity due to two-body encounters. In star clusters, t_{relax} is much shorter than the Hubble time ($t_{relax} \sim 10 - 100$ Myr in young star clusters [235]), while in galaxies and large-scale structures, it is much longer than the lifetime of the Universe. Hence, close encounters are common in dense star clusters.

Dynamical friction is another consequence of gravity force: a massive body of mass M orbiting in a sea of lighter particles feels a drag force that slows down its motion over a timescale [53]:

$$t_{DF}(M) = \frac{3}{4\sqrt{2\pi}G^2 \ln \Lambda} \frac{\sigma^3}{M\rho(r)}. \quad (1.9)$$

It is apparent that two-body relaxation and dynamical friction are driven by the same force and are related by

$$t_{DF}(M) \sim \frac{\langle m \rangle}{M} t_{relax}, \quad (1.10)$$

i.e., dynamical friction happens over a much shorter timescale than two-body relaxation and leads to mass segregation (or mass stratification) in a star cluster. This process speeds up the collapse of the core of a star cluster and can trigger the so-called Spitzer's instability [271]. Two-body relaxation, dynamical friction, and their effects play a crucial role in shaping the demography of BBHs in star clusters.

1.5.2 Binary – single-body encounter

The internal energy within a binary system is expressed as:

$$E_{int} = \frac{1}{2}\mu v^2 - \frac{Gm_1m_2}{r}, \quad (1.11)$$

where $\mu = m_1m_2/(m_1 + m_2)$ denotes the reduced mass of the binary with components of mass m_1 and m_2 , v represents the relative velocity between the binary components, and r stands for the distance separating the two members. According to Kepler’s laws, $E_{int} = -E_b = -Gm_1m_2/(2a)$, where E_b signifies the binding energy of the binary system, and a is the semi-major axis.

The exchange of internal energy within a binary is achievable only through close encounters with other stars, wherein the binary’s orbital parameters are perturbed by the intruder. This scenario occurs when a single star approaches the binary at a proximity of a few times its orbital separation, characterizing it as a three-body encounter. For such encounters to transpire frequently, the binary must reside in a dense environment, as the rate of three-body encounters scales with the local density of stars. Notably, three-body encounters play a pivotal role in influencing the dynamics of black hole binaries, contributing to phenomena like hardening, exchanges, and ejections.

1.5.3 Hardening

If a binary of black holes (BBH) experiences multiple three-body encounters over its lifetime, its semi-major axis will shrink as a consequence of these encounters. This phenomenon is known as dynamical hardening.

We classify binaries with binding energy greater (lesser) than the average kinetic energy of a star in the star cluster as hard (soft) binaries. According to Heggie’s law [121], hard binaries tend to undergo hardening, i.e., they become increasingly bound through binary–single encounters. In these interactions, a portion of the internal energy of a hard binary can be transferred to the kinetic energy of the intruder and the center-of-mass of the binary. This energy transfer results in a reduction of the binary’s internal energy and, consequently, a decrease in its semi-major axis.

Given that black holes (BHs) are among the most massive objects in star clusters, most BBHs are expected to be hard binaries. Consequently, BBHs are likely to undergo dynamical hardening through three-body encounters. This hardening process may be potent enough to contract a BBH to a state where gravitational wave (GW) emission becomes efficient. Initially, loose BBHs may transform into GW sources due to dynamical hardening. The hardening rate for hard binaries with a semi-major axis a can be estimated as [121]

$$\frac{d}{dt} \left(\frac{1}{a} \right) = 2\pi\xi \frac{G\rho}{\sigma}, \quad (1.12)$$

where $\xi \sim 0.1 - 10$ is a dimensionless hardening parameter (estimated through numerical experiments, [123, 240]), ρ is the local mass density of stars, σ is the local velocity dispersion, and G is the gravitational constant.

Dynamical hardening predominantly drives the contraction of a binary until it reaches a sufficiently small semi-major axis for efficient GW emission. This critical semi-major axis can be determined using the following equation [228]:

$$\frac{da}{dt} = -\frac{64 G^3 m_1 m_2 (m_1 + m_2)}{5 c^5 (1 - e^2)^{7/2}} a^{-3}. \quad (1.13)$$

By combining Eqs. 1.12, 1.13, it is possible to derive a simple analytical estimate of the evolution of the semi-major axis of a BBH affected by three-body encounters and GW emission:

$$\frac{da}{dt} = -2\pi\xi \frac{G\rho}{\sigma} a^2 - \frac{64 G^3 m_1 m_2 (m_1 + m_2)}{5 c^5 (1 - e^2)^{7/2}} a^{-3}. \quad (1.14)$$

This equation assumes that the binary star is hard, the total mass of the binary star significantly exceeds the average mass of a star in the star cluster (minimizing exchanges), and most three-body encounters have a small impact parameter. The first term on the right-hand side of Eq. 1.14 accounts for the impact of three-body hardening on the semi-major axis, scaling as $da/dt \propto -a^2$. This dependence reflects the increased effectiveness of hardening as the binary size grows, attributable to the geometric cross section for three-body interactions scaling as a^2 . The second term represents energy loss due to GW emission, scaling as $da/dt \propto -a^{-3}$, indicating efficient GW emission only when the two BHs are in close proximity.

1.5.4 Exchange

Dynamical exchanges denote three-body encounters wherein the intruder replaces one member of the binary. These exchanges have the potential to give rise to new binary black hole (BBH) systems: for instance, if a binary comprising a black hole (BH) and a low-mass star undergoes an exchange with a single BH, it results in the formation of a new BBH. This distinction is fundamental between BHs in the field and those in star clusters. A BH formed as a solitary entity in the field has minimal prospects of joining a binary system, whereas a solitary BH in the core of a star cluster has favorable odds of becoming part of a binary through exchanges.

Exchanges are expected to contribute more to the formation than the destruction of BBHs. The probability of an intruder replacing a binary member is approximately zero if the intruder is less massive than both binary members, but it abruptly rises to around one if the intruder surpasses the mass of one of the binary members [124]. Given that BHs are among the most massive entities in a star cluster post-formation, they efficiently acquire companions through dynamical exchanges. Consequently, exchanges play a crucial role in dynamically forming BH binaries. Direct N-body simulations [325] demonstrate that over 90% of BBHs in young star clusters form through dynamical exchanges. Additionally, BBHs formed via exchanges exhibit distinctive features compared to field BBHs [325]:

BBHs formed through exchanges are, on average, more massive than isolated BBHs because more massive intruders have higher chances of acquiring companions. Exchanges lead to the formation of highly eccentric BBHs; subsequent circularization

induced by gravitational wave (GW) emission, upon entering the effective GW emission regime, reduces eccentricity significantly. BBHs born through an exchange are likely to exhibit misaligned spins, as exchanges and other dynamical interactions tend to result in isotropically distributed spin directions concerning the binary orbital plane, erasing any memory of previous alignments. Other simulations [323] compare a set of field binaries with a set of globular cluster binaries, both run using the same population-synthesis code. A notable difference observed in their globular cluster simulations is the scarcity of merging BHs with a mass below 10 solar masses (M_{\odot}). This is attributed to the tendency of exchanges to disrupt binaries composed of light BHs.

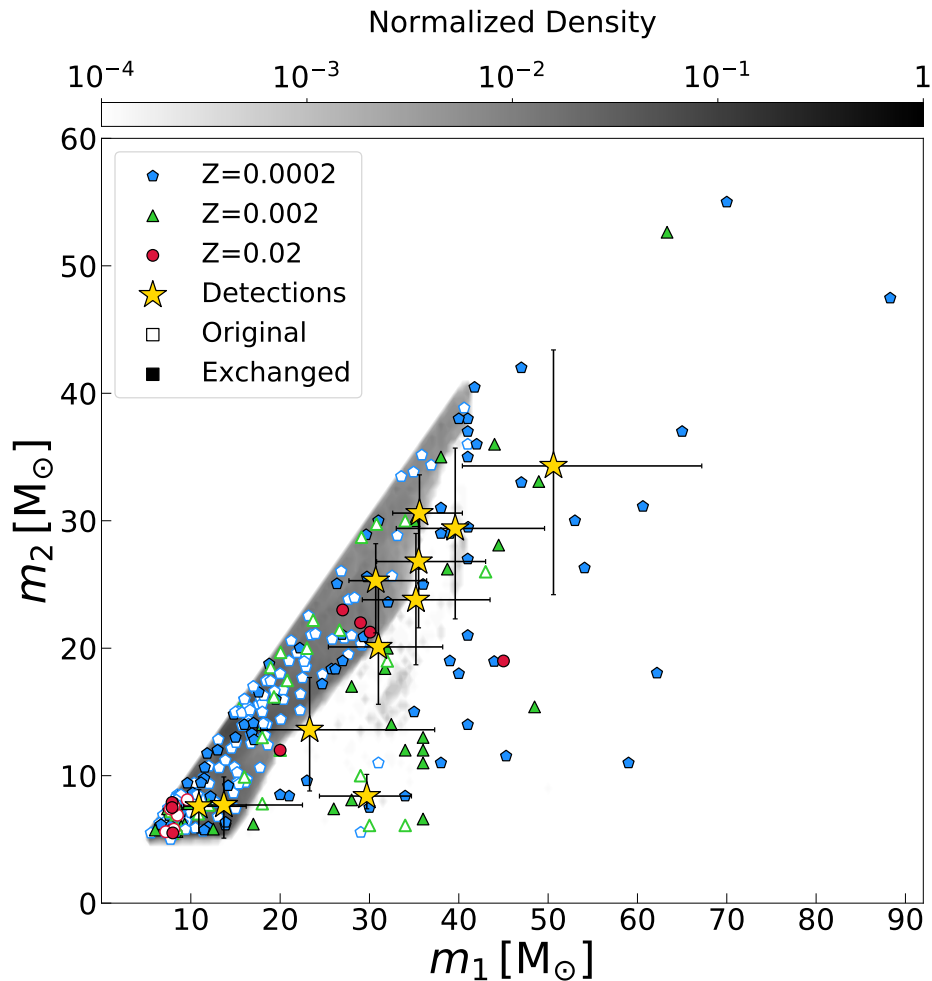


Figure 1.2: Mass of the secondary BH versus mass of the primary BH in a set of BBH mergers in isolation and in young star clusters. Yellow stars represent O1 and O2 BBHs plus GW190412. Blue, green, and red symbols depict simulated BBHs in young star clusters with metallicities of $Z = 0.0002$, 0.002 , and 0.02 . Filled symbols denote dynamical exchanges, while open symbols represent original binaries. Gray contours indicate BBHs resulting from isolated binary evolution. Simulations from [71]. Courtesy of Ugo N. Di Carlo.

Figure 1.2 compares the masses of simulated BBH mergers in isolated binaries and

young star clusters. While the maximum total mass of BBH mergers in isolated binaries is approximately $80M_{\odot}$, BBH mergers in young star clusters exhibit total masses up to around $130M_{\odot}$ [186]. This discrepancy is primarily due to two factors [186]:

Single stellar evolution at low metallicity can lead to the formation of single BHs with a mass up to approximately $70M_{\odot}$. In the field, such massive BHs remain solitary, whereas, in a star cluster, they can acquire companions through dynamical exchanges and merge through dynamical hardening and GW emission. In star clusters, stellar collisions are relatively common and can result in the production of more massive BHs, including those within the pair-instability mass gap [69–71, 152, 246]. Spin misalignments serve as another potential discriminant between field binaries and star cluster binaries [87, 88]. An isolated binary system where both primary and secondary components undergo direct collapse is expected to yield a BBH with nearly aligned spins. In contrast, dynamically formed BH binaries are anticipated to possess misaligned or even nearly isotropic spins due to the complete reset of any initial spin alignment by three-body encounters.

Currently, constraints on BHs spins from gravitational wave (GW) detections are limited. In a few events, such as GW151226 [8], GW170729 [9], and particularly GW190412 [15], the measured value of the effective spin parameter (χ_{eff}) is significantly nonzero, indicating at least partial alignment. However, the majority of events in GWTC-2 have χ_{eff} consistent with zero, which may be attributed to either low spins, misaligned spins, or a combination of both. On the other hand, a recent population study by the LVC [12] suggests that approximately 12% to 44% of BBH systems exhibit spins tilted by more than 90° with respect to their orbital angular momentum, supporting a negative effective spin parameter.

Notably, GW190412 displays a non-zero precessing spin (χ_p) to the 90% credible level [13], and GW190521 [14], the most massive BBH event to date, exhibits mild evidence for a non-zero precessing spin. This lends support to the idea of a dynamical formation for these events [13, 14, 93, 100, 256]."

1.5.5 BHs in the pair-instability mass gap

Encounters between binary systems and single massive stars within young star clusters instigate collisions among these massive stellar entities. The presence of dynamical friction speeds up this process, leading to an accumulation of massive stars in the cluster core in less than a million years. These stellar collisions have the potential to give rise to exceedingly massive stars (exceeding $150M_{\odot}$), as well as blue straggler stars [189] and exceptionally massive black holes.

Fig.1.3 showcases the dynamic formation of a BBH with a primary mass $m_1 = 88M_{\odot}$ and a secondary mass $m_2 = 47.5M_{\odot}$ [71]. The masses of these BBH components closely resemble those of GW190521 [14, 16]. Notably, the primary black hole (BH) in this scenario possesses a mass within the pair-instability mass gap. Its formation is facilitated by the merger between a giant star with a well-developed helium core and a main sequence companion, resulting in a massive core helium-burning (cHeB) star with an oversized hydrogen envelope relative to the helium core [69–71, 152, 246]. Due

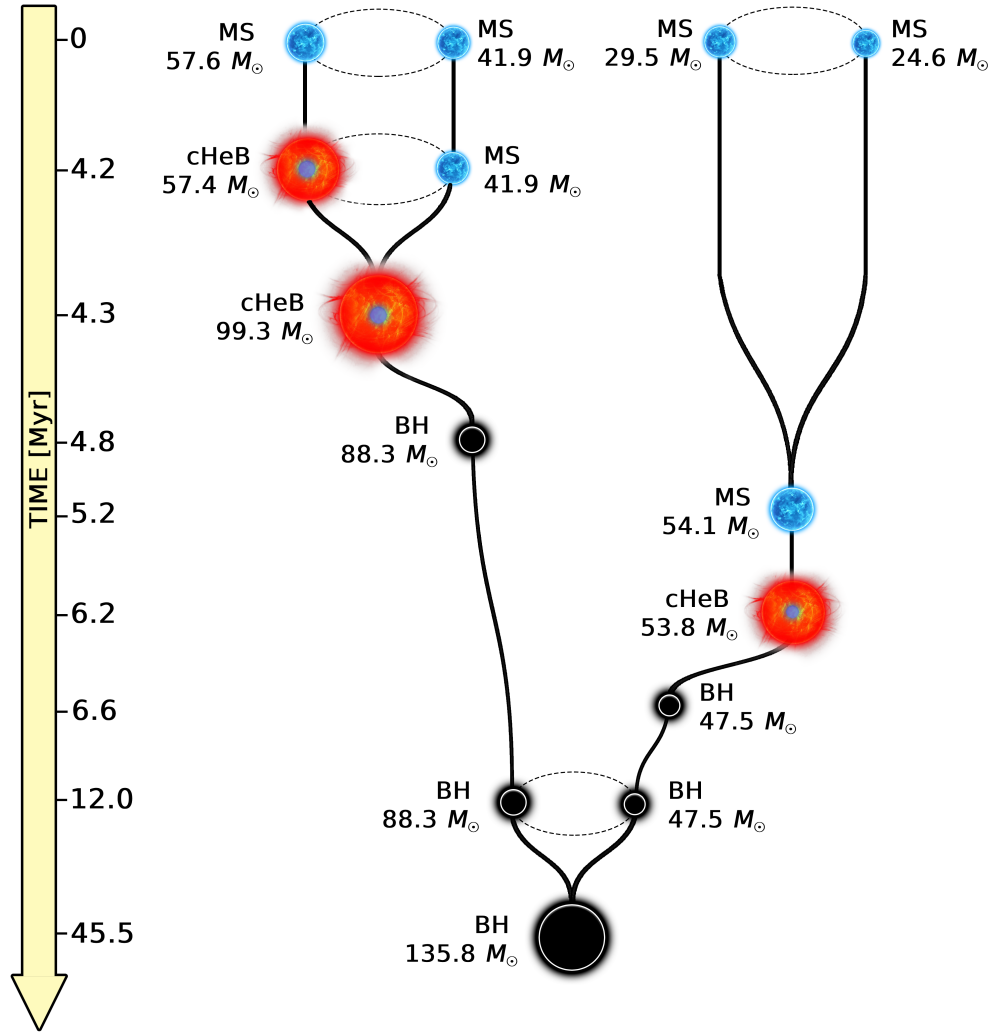


Figure 1.3: Illustration depicting the dynamical assembly of a binary black hole (BBH) resembling GW190521, derived from simulations conducted by [71]. Courtesy of Ugo N. Di Carlo.

to the rapid timescale for helium, carbon, oxygen, neon, and silicon burning compared to hydrogen burning, the star undergoes collapse to form a BH before the helium core surpasses the pair-instability threshold, resulting in a BH with a mass of approximately $88M_{\odot}$. Subsequently, this BH obtains a companion through dynamical exchanges and merges within a Hubble time.

This proposed scenario offers a plausible explanation for the formation of systems resembling GW190521, not only due to the close match in BBH masses but also because a BH originating from the direct collapse of a highly massive star may exhibit a substantial spin (dependent on the final spin of the massive progenitor). Additionally, this dynamical formation process results in BBHs with spins oriented isotropically. The primary uncertainties in this model pertain to factors such as mass loss during stellar collisions [98] and potential envelope loss during the final collapse [89].

1.5.6 Direct three-body binary formation

In the densest stellar assemblies, such as globular clusters and nuclear star clusters, the substantial stellar velocities often result in dynamical encounters capable of disrupting a significant fraction of the original binary stars (those binaries existing at the cluster’s formation). The critical relative velocity v_c required to unbind a binary is determined by [265]:

$$v_c = \sqrt{\frac{Gm_1m_2(m_1 + m_2 + m_3)}{m_3(m_1 + m_2)a}}, \quad (1.15)$$

where m_1 , m_2 , and m_3 represent the masses of the two binary members and the intruder, respectively, while a denotes the binary semi-major axis.

In these extreme environments, the prevailing mechanism for binary black hole (BBH) formation involves direct encounters among three single bodies [212, 259] during core collapse. This results in the creation of highly compact BBHs, resilient to further disruption by intruders. The timescale for BBH formation through three single-body encounters is given by [21, 163]:

$$t_{3b} = 0.1 \text{ Myr} \left(\frac{n}{10^6 \text{ pc}^{-3}} \right)^{-2} \left(\frac{\sigma}{30 \text{ km/s}} \right)^9 \left(\frac{m_{BH}}{30M_\odot} \right)^{-5}, \quad (1.16)$$

where n represents the local stellar density, σ is the local velocity dispersion of the star cluster, and m_{BH} is the typical black hole (BH) mass in the star cluster. BBHs formed through three single-body encounters share characteristics with those arising from dynamical exchanges: they tend to be more massive than isolated binaries, possess high initial eccentricities, and exhibit isotropically oriented spins [18]. Direct three-body encounters are likely the predominant channel for BBH formation in globular clusters and nuclear star clusters [212], while binary–single-star exchanges are presumed to be the prevailing formation mechanism for BBHs in young star clusters [69, 325]. Dynamical exchanges influence both pre-existing BHs and their stellar progenitors in young star clusters.

1.5.7 Dynamical ejection

In the course of three-body encounters, a portion of the internal energy of a robust binary undergoes a transfer into the kinetic energy of both the intruders and the center-of-mass of the binary. Consequently, both the binary and the intruder experience a recoil, typically characterized by velocities on the order of a few km/s, although they can extend to several hundred km/s.

Given that the escape velocity from a globular cluster is approximately ~ 30 km/s, and even lower for young star clusters or open clusters, both the recoiling binary and the intruder stand the chance of being expelled from their parent star cluster. Once ejected, these entities transition into field objects, disengaging from the dynamics of the star cluster. This not only halts the hardening process for the expelled binary black hole (BBH) but also precludes the ejected intruder, if another compact object, from participating in new binary formations through dynamical exchanges.

A general expression for the recoil velocity of the binary center of mass, applicable when $(m_1 + m_2) \gg \langle m \rangle$ (where $\langle m \rangle$ denotes the average mass of a star in a star cluster), is given by:

$$v_{rec} \sim \frac{\langle m \rangle}{m_1 + m_2} \sqrt{\frac{2\xi}{m_1 + m_2 + \langle m \rangle} E_b}, \quad (1.17)$$

where $E_b = Gm_1m_2/(2a)$ is the binary binding energy. This equation allows the derivation of the minimum binding energy required for the ejection of a binary star through a binary–single-body encounter, denoted as $E_{b,min}$ [209]:

$$E_{b,min} \approx \frac{(m_1 + m_2)^3}{2\xi \langle m \rangle^2} v_{esc}^2, \quad (1.18)$$

In many cases, binary neutron stars (BNSs), BBHs, and black hole–neutron star (BH–NS) systems within young star clusters are expelled prior to merging [69, 244]. The dynamical ejections of BNS and BH–NS binaries have been proposed as potential explanations for host-less short gamma-ray bursts, constituting around $\sim 25\%$ of all short gamma-ray bursts [91].

The expulsion of compact objects and compact-object binaries from their parent star cluster may arise from at least three distinct mechanisms:

- Dynamical ejections, as described above;
- Supernova (SN) kicks [96, 127];
- Gravitational wave (GW) recoil [47, 112, 168].

GW recoil, a relativistic kick occurring during the merger of a BBH, is the outcome of asymmetric linear momentum loss due to gravitational wave emission, particularly when the binary exhibits asymmetric component masses and/or misaligned spins. This phenomenon results in kick velocities reaching up to thousands of km/s, typically falling within the range of hundreds of km/s.

The ejection mechanisms, whether through dynamics, SN kicks, or GW recoil, play a significant role in impeding the merger of second-generation black holes (those born from the merger of two BHs rather than the collapse of a star [105]). In globular clusters, open clusters, and young star clusters, a BH has a high likelihood of being ejected by three-body encounters before merging [209], and a very high probability of ejection by GW recoil after merging [188, 254]. The exception lies in nuclear star clusters, where merging BHs can more easily avoid ejection by GW recoil due to higher escape velocities reaching hundreds of km/s [18, 21, 94, 188].

1.5.8 Formation of intermediate-mass black holes by runaway collisions

Intermediate-mass black holes (IMBHs), characterized by masses in the range $100M_\odot \lesssim m_{BH} \lesssim 104M_\odot$, could potentially originate from the direct collapse of metal-poor, exceptionally massive stars [268]. Various avenues have been proposed for IMBH formation, with many implicating the dynamic processes within star clusters. The concept

of massive black hole (BH) formation through runaway collisions was initially introduced around half a century ago [60, 262], subsequently refined by numerous researchers [69, 70, 95, 111, 117, 185, 189, 191, 232–234, 249].

In dense star clusters, the phenomenon of dynamical friction [53] results in the deceleration of massive stars due to the drag exerted by lighter bodies, occurring over a timescale $t_{DF}(M) \sim (\langle m \rangle / M) t_{relax}$ (Eq.1.9).

Given that the two-body relaxation timescale in a young star cluster can be as brief as $t_{relax} \sim 10 - 100 M_{\odot}$ [235], for a star with a mass $M \geq 40 M_{\odot}$, we estimate $t_{DF} \leq 2.5$ Myr, signifying the highly effective nature of dynamical friction in dense massive young star clusters. Due to dynamical friction, massive stars tend to segregate towards the core of the cluster before they evolve into black holes.

When the most massive stars in a dense young star cluster migrate to the core via dynamical friction in a timespan shorter than their lifetime, and before core-collapse supernovae remove a significant portion of their mass, the density of massive stars in the cluster core becomes exceptionally high. This heightened density significantly increases the likelihood of collisions between massive stars. Indeed, direct N-body simulations illustrate that collisions between massive stars progress in a runaway fashion, culminating in the formation of a very massive ($\gg 100 M_{\odot}$) star [234].

Determining the final mass of the collision product involves addressing two crucial questions: how much mass is lost during the collisions? and how much mass does the resulting very massive star lose through stellar winds?

Hydrodynamical simulations focusing on colliding stars [98, 99] indicate that massive stars can lose approximately $\approx 25\%$ of their mass during collisions. Even in an optimistic scenario where no mass is lost during and immediately after the collision, when the collision product relaxes to a new equilibrium, the resulting very massive star is expected to be strongly radiation-pressure dominated and likely to lose a significant fraction of its mass through stellar winds. Recent investigations, accounting for the Eddington factor’s impact on mass loss [185, 268], reveal that IMBHs are unlikely to form from runaway collisions at solar metallicity. However, at lower metallicity ($Z \lesssim 0.1 Z_{\odot}$), approximately 10 – 30% of runaway collision products in young dense star clusters may evolve into IMBHs through direct collapse, successfully avoiding disruption by pair-instability supernovae.

While the majority of runaway collision products might not transform into IMBHs, they often manifest as relatively massive black holes ($\sim 20 - 90 M_{\odot}$ [185]). If these massive black holes remain within their parent star cluster, they prove highly efficient in acquiring companions through dynamical exchanges. The stable binaries formed by runaway collision products predominantly take the form of binary black holes (BBHs), presenting potential sources of gravitational waves (GWs) within the LIGO–Virgo detection range [185].

1.5.9 Hierarchical BBH formation and IMBHs

The scenario of runaway collisions is exclusive to the initial phases of star cluster evolution, occurring when massive stars are still in their main sequence phase (with a

lifetime of approximately 6 million years for a star of about 30 solar masses). However, an alternative could be that intermediate-mass black holes (IMBHs) can form even in aged clusters, such as globular clusters, through the repeated merging of smaller black holes [19, 94, 111, 188, 209].

In a stellar binary black hole (BBH) system within a star cluster, the binary is typically in a hardened state, gradually contracting due to dynamical interactions until it enters the regime where gravitational wave (GW) emission becomes significant. At this point, the BBH merges, resulting in a single, more massive black hole. With its increased mass, the new black hole has favorable conditions for engaging in a new binary through dynamical exchange. Subsequently, the new binary undergoes further hardening via three-body encounters, and this cycle may repeat multiple times until the primary black hole evolves into an IMBH.

This scenario offers a notable advantage as it is independent of stellar evolution, ensuring confidence in the growth of the black hole through mergers as long as it remains within the cluster. However, there are several challenges to address. Firstly, the BBH may face ejection due to dynamical recoil resulting from three-body encounters, with stronger recoils as the orbital separation decreases (see Eq. 1.18). To avoid ejection by dynamical recoil, the BBH needs to be sufficiently massive (around $\gtrsim 50M_{\odot}$ for a dense globular cluster [61]). If the BBH is ejected, the sequence is disrupted, and no IMBH is formed. Secondly, the merger of two black holes induces a relativistic kick, potentially reaching speeds of hundreds of km/s [168], leading to the possible expulsion of the black hole from the parent star cluster [128]. Once again, the sequence breaks and no IMBH is produced. Finally, even if the black hole binary avoids ejection, this scenario is relatively inefficient, requiring several Gyrs to form an IMBH with a mass of approximately $\sim 500M_{\odot}$ if the seed black hole is around $\sim 50M_{\odot}$ [209].

Monte Carlo simulations [111] indicate that both the runaway collision scenario and the repeated-merger scenario can coexist in star clusters. Runaway collision-induced IMBHs form efficiently within the first few million years of a star cluster's lifespan, while IMBHs resulting from repeated mergers begin formation much later (after $\gtrsim 5$ Gyrs) with a less efficient growth rate.

1.5.10 Von Zeipel-Kozai-Lidov resonance

In contrast to the previously discussed dynamical mechanisms, the von Zeipel-Kozai-Lidov (ZKL) resonance [137, 150, 164, 214, 263, 301] can manifest both in isolated environments and within star clusters. The ZKL resonance arises in stable hierarchical triple systems, characterized by an inner binary and an outer body orbiting the inner binary, where the orbital plane of the outer body is inclined with respect to the orbital plane of the inner binary. Periodic perturbations exerted by the outer body induce oscillations in the eccentricity of the inner binary and the inclination between the orbital planes, without affecting the binary's semi-major axis. Notably, ZKL resonance, despite lacking an energy exchange between the inner and outer binaries, can enhance the merger probability of binary black holes (BBHs) [24, 116, 126, 145, 290]. This enhancement arises from the dependence of the gravitational wave (GW) emission

timescale for mergers on the eccentricity (denoted as e) of the binary, given by $t_{GW} \propto (1 - e^2)^{7/2}$ (refer to Eq.1.13 [228]).

Despite the initial perception of hierarchical triples as exotic systems, they are not uncommon. Approximately $\sim 10\%$ of low-mass stars exist within triple systems [241, 284, 285], a fraction that rises gradually for more massive stars [75], reaching up to $\sim 50\%$ for B-type stars [211, 261, 286]. Within star clusters, stable hierarchical triple systems can dynamically form through four-body or multiple-body encounters.

ZKL resonances find intriguing applications in nuclear star clusters. In scenarios where a stellar black hole (BH) binary is gravitationally bound to the supermassive BH (SMBH) at the galaxy’s center, a peculiar triple system emerges, with the stellar BH binary constituting the inner binary and the SMBH serving as the outer body [20]. Even in this configuration, the merging binary black hole (BBH) maintains favorable conditions for retaining a non-zero eccentricity until emitting gravitational waves (GWs) within the LIGO–Virgo frequency range.

1.6 GWs detectors

Gravitational wave (GW) detectors operate by measuring the changes in light travel time between separated reference points, or “test masses”, induced by passing GWs. These test masses are arranged to approximate a local inertial frame, experiencing near-perfect free fall, and are positioned over extensive baselines. The variations in light travel times between pairs of test masses are monitored and detected by the instrument, translating any alterations in spacetime curvature caused by passing GWs into modulations in these travel times.

Current ground-based observatories explore the high-frequency segment of the GW spectrum, spanning from around 10 Hz to approximately 10 kHz, predominantly influenced by compact sources of stellar mass, such as coalescing binary black holes and neutron star systems. Employing enhanced Michelson interferometry with suspended mirrors, all ground-based detectors directly measure a GW’s phase and amplitude. Detecting GWs in the audio-band frequency range necessitates stringent isolation of the mirrors from local forces and disturbances. The Advanced LIGO detectors in the U.S. feature 4 km arm lengths, while Advanced Virgo in Europe and KAGRA in Japan have 3 km arms. Astrophysical sources typically induce strains ($\delta L/L$) on the order of 10^{-21} or less, requiring displacement sensitivities (δL) of less than $\sim 10^{-18}$ m for effective GW detection, an exceedingly small displacement comparable to the proton’s radius of approximately $8.5 \cdot 10^{-16}$ m. Figure 1.4 illustrates the configuration of the current generation of ground-based detectors.

LIGO–Virgo observations, spanning just a few years, have already provided insights into some of the Universe’s most energetic and cataclysmic phenomena. Discoveries from events like GW150914 and subsequent black hole and neutron star mergers highlight the presence of black holes forming orbitally bound binary systems that evolve through GW emission, merging within a Hubble time. These observations have also unveiled the existence of black holes with masses ranging from tens to hundreds of solar masses.

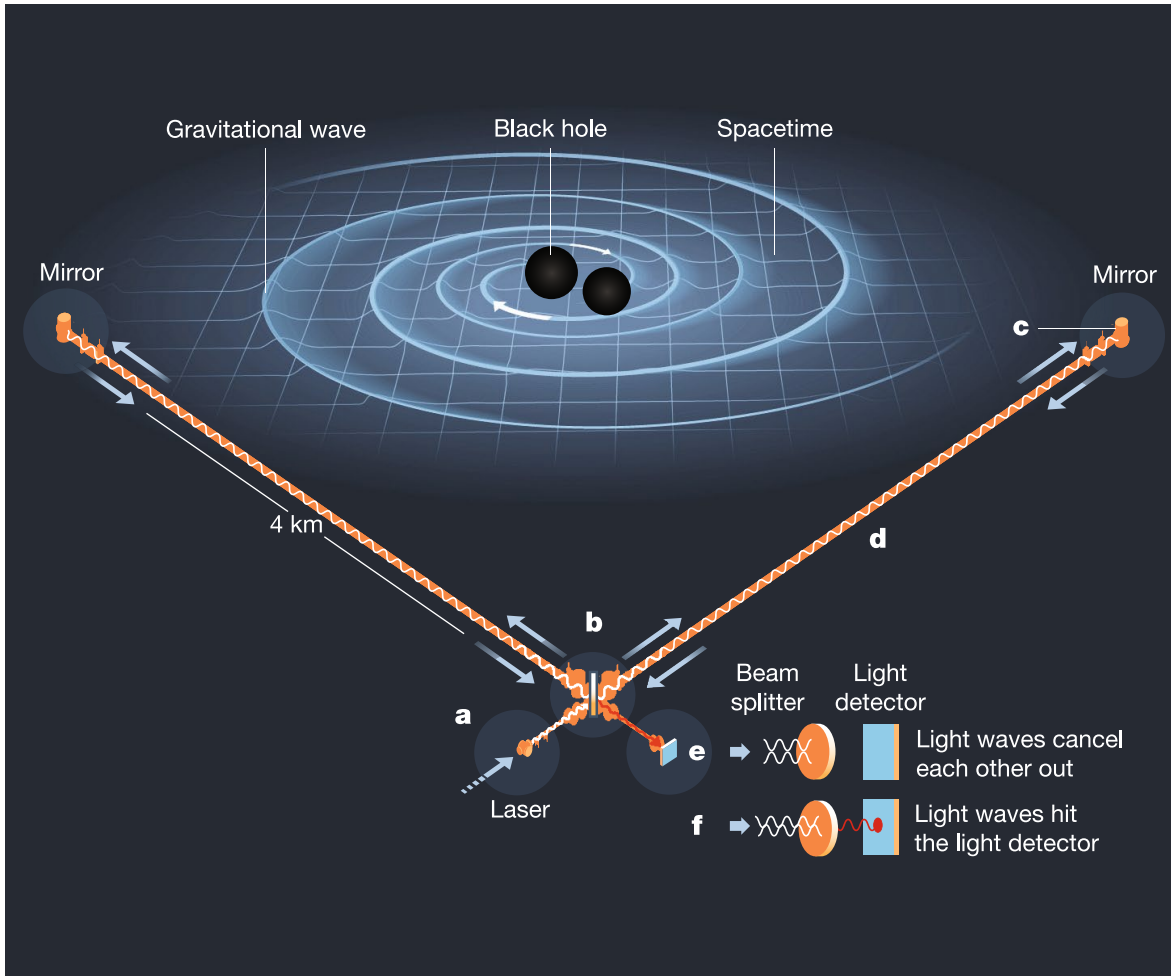


Figure 1.4: Operation of a L-shaped laser interferometer, such as LIGO and Virgo. **a)** Laser light is sent into the instrument to measure changes in the length of the two arms. **b)** A ‘beam splitter’ splits the light and sends out two identical beams along the arms. **c)** The light waves bounce off the mirror and return. **d)** A gravitational wave affects the interferometer’s arms differently: one extends and the other contracts as they pass from the peaks and troughs of the gravitational waves. **e)** Normally, the light returns unchanged to the beam splitter from both arms, and the light waves cancel each other out. **f)** If a gravitational wave passes through the interferometer, the two beams do not cancel out and their combination reaches the detector. (Image credit: ©Johan Jarnestad/The Royal Swedish Academy of Sciences [210])

The latest gravitational-wave catalog encompasses a total of 90 events (see Fig. 1.1), with expectations of a substantial increase in the count in the coming years as additional ground-based (e.g., the Einstein Telescope) and space-borne (e.g., the Laser Interferometer Space Antenna, LISA) interferometers become operational.

1.7 N-body simulations

Studying the formation and evolution of merging compact objects in dense star clusters is challenging because it involves the complex interplay between different spatial and time scales [235]. For a typical GC, with a half-mass radius of ~ 1 pc, the two-body relaxation time (t_{relax}) is of the order of Gyrs and the crossing time is of the order of Myrs [38, 52, 84, 304]. At the same time, the orbital period of tight binaries can be as short as \sim days [121, 122]. Furthermore, it is also crucial to consider time-scales related to binary stellar evolution, such as the typical timescale for stable mass transfer (SMT) $O(10^3)$ yr, or the common envelope (CE) time scale, that is $O(10^3 - 10^5)$ yr [186]. N-body simulations that aim at investigating merging compact objects in GCs need to cover, at least, t_{relax} (\sim Gyrs) of evolution and to resolve all the mentioned time-scales simultaneously. Therefore, such simulations are challenging because they require the use of small time steps, significantly smaller compared to the total integration time. This means that such simulations are slow, and they accumulate significant numerical error, in the form of both truncation and round-off errors.

The dynamical evolution of stars is governed by the gravitational N-body problem, which can be solved numerically using a direct or non-direct approach. In the first one, all the forces are computed between star pairs, with a computational complexity of $O(N^2)$, where N is the total number of stars. In the second approach, either an approximated mathematical expression is used instead of the Newton's gravitational force, or only the force from close stars is computed directly, softening the $O(N^2)$ computational complexity. Non-direct approaches are faster but less accurate than the direct approach. Besides stellar dynamics, both direct and non-direct N-body codes generally include fitting formulas or look-up tables to treat stellar evolution of single and binary stars.

Given the high computational complexity, special-purpose hardware components, such as GRAPE, were developed to speed up direct N-body simulation of massive star clusters [179, 181, 182]. Today, graphics processing units (GPUs) have replaced the GRAPE system as main computing accelerators for N-body simulations. Various codes with only Central Processing Unit (CPU) support exist (e.g. MYRIAD, STARLAB/KIRA [149, 236]) but they can take advantage of external libraries to speed-up the force calculation process through GPUs (e.g. SAPPORO [32, 98]). The hybrid CPU-GPU approach represents the state-of-the-art for N-body codes and simulations [1, 2, 31, 36, 51, 134, 197, 203, 252, 253, 303, 305]. Finally, stellar evolution of single and binary stars is implemented, in most cases, through population-synthesis codes that use, in general, polynomial fitting formulas [63, 107, 110, 130, 131, 190, 287, 302].

Chapter 2

The direct N-body code ISTEDDAS on GPU

In this chapter, I will give an overview of the strategies adopted in our code to numerically solve the N-body problem using GPUs. ISTEDDAS (the word for “stars” in Sardinian language) is a direct N-body code that implements the Hermite 6th order time integrator combined with the block time steps method, and the Ahmad-Cohen neighbours scheme. ISTEDDAS is written by combining utilities of C and C++ and it uses CUDA, MPI, and OpenMP to exploit GPU workstations as well as GPU clusters [201]. The main features of ISTEDDAS are described in the following sections.

2.1 The Hermite integrator

The Hermite time integrators (4th, 6th and 8th order) represent the state-of-the-art for direct N-body simulations [2, 5]. The 4th order scheme is, by far, the most used algorithm in this context [1, 36, 197, 236, 303, 305], but the 6th order can be more accurate and almost as fast as the 4th order when implemented on GPUs [218]. The Hermite integrators are based on the Taylor series of positions, velocities, and accelerations and their most important feature is that they need to evaluate the distances between particles just once per time step. For instance, this is a huge advantage compared to a classic 4th order Runge-Kutta method, which needs to evaluate accelerations 4 times per integration step.

To evolve a stellar system from time t_0 to time t_1 ($\Delta t = t_1 - t_0$, 1 integration step), the Hermite 6th order integrator takes advantage of a predictor-evaluation-corrector scheme. The prediction step performs a Taylor expansion on stars’ positions (\mathbf{r})¹,

¹Throughout the manuscript, I use bold letters to refer to three-dimensional vectors.

velocities (\mathbf{v}) and accelerations (\mathbf{a}), using time derivatives up to $\ddot{\mathbf{a}}$:

$$\mathbf{r}_p = \mathbf{r}_0 + \mathbf{v}_0 \Delta t + \mathbf{a}_0 \frac{\Delta t^2}{2} + \dot{\mathbf{a}}_0 \frac{\Delta t^3}{6} + \ddot{\mathbf{a}}_0 \frac{\Delta t^4}{24} + \ddot{\ddot{\mathbf{a}}}_0 \frac{\Delta t^5}{120}, \quad (2.1)$$

$$\mathbf{v}_p = \mathbf{v}_0 + \mathbf{a}_0 \Delta t + \dot{\mathbf{a}}_0 \frac{\Delta t^2}{2} + \ddot{\mathbf{a}}_0 \frac{\Delta t^3}{6} + \ddot{\ddot{\mathbf{a}}}_0 \frac{\Delta t^4}{24}, \quad (2.2)$$

$$\mathbf{a}_p = \mathbf{a}_0 + \dot{\mathbf{a}}_0 \Delta t + \ddot{\mathbf{a}}_0 \frac{\Delta t^2}{2} + \ddot{\ddot{\mathbf{a}}}_0 \frac{\Delta t^3}{6}, \quad (2.3)$$

where the quantities labeled with p are the predicted ones and the quantities labeled with 0 come from the corrector performed in the previous step, or from initial conditions.

During the evaluation step, the code computes the total force on the star i from all the other stars in the system, using the classical Newtonian formula and the predicted values \mathbf{p} , \mathbf{v} , and \mathbf{a} :

$$\mathbf{a}_{i,1} = \sum_{j \neq i}^N \frac{m_j}{|\mathbf{r}_{ij,p}|^3} \mathbf{r}_{ij,p}, \quad (2.4)$$

$$\dot{\mathbf{a}}_{i,1} = \sum_{j \neq i}^N \frac{m_j}{|\mathbf{r}_{ij,p}|^3} \left(\mathbf{v}_{ij,p} - 3 \frac{\mathbf{r}_{ij,p} \cdot \mathbf{v}_{ij,p}}{|\mathbf{r}_{ij,p}|^2} \mathbf{r}_{ij,p} \right), \quad (2.5)$$

$$\begin{aligned} \ddot{\mathbf{a}}_{i,1} = \sum_{j \neq i}^N \frac{m_j}{|\mathbf{r}_{ij,p}|^3} & \left[\mathbf{a}_{ij,p} - 6 \frac{\mathbf{r}_{ij,p} \cdot \mathbf{v}_{ij,p}}{|\mathbf{r}_{ij,p}|^2} \mathbf{v}_{ij,p} + \right. \\ & \left. + \frac{3}{|\mathbf{r}_{ij,p}|^2} \left(5 \frac{(\mathbf{r}_{ij,p} \cdot \mathbf{v}_{ij,p})^2}{|\mathbf{r}_{ij,p}|^2} - \mathbf{r}_{ij,p} \cdot \mathbf{a}_{ij,p} - |\mathbf{v}_{ij,p}|^2 \right) \mathbf{r}_{ij,p} \right], \end{aligned} \quad (2.6)$$

where the quantities with subscript “ ij, p ” are the relative predicted values between the stars i and j (e.g. $\mathbf{r}_{ij,p} = \mathbf{r}_{j,p} - \mathbf{r}_{i,p}$), and the gravitational constant it is assumed as $G = 1$. Finally, in the corrector step, the predicted quantities are corrected to obtain a more accurate solution using the newly evaluated accelerations. Positions and velocities are corrected as:

$$\mathbf{v}_c = \mathbf{v}_0 + (\mathbf{a}_1 + \mathbf{a}_0) \frac{\Delta t}{2} - (\dot{\mathbf{a}}_1 - \dot{\mathbf{a}}_0) \frac{\Delta t^2}{10} + (\ddot{\mathbf{a}}_1 + \ddot{\mathbf{a}}_0) \frac{\Delta t^3}{120}, \quad (2.7)$$

$$\mathbf{r}_c = \mathbf{r}_0 + (\mathbf{v}_c + \mathbf{v}_0) \frac{\Delta t}{2} - (\mathbf{a}_1 - \mathbf{a}_0) \frac{\Delta t^2}{10} + (\dot{\mathbf{a}}_1 + \dot{\mathbf{a}}_0) \frac{\Delta t^3}{120}. \quad (2.8)$$

During the correction phase, a new time step for each star is computed using the new accelerations, as in [218]:

$$\Delta t = \eta_h \sqrt[6]{\frac{|\mathbf{a}_1| |\ddot{\mathbf{a}}_1| + |\dot{\mathbf{a}}_1|^2}{|\mathbf{a}_1^{(5)}| |\ddot{\mathbf{a}}_1| + |\mathbf{a}_1^{(4)}|^2}}, \quad (2.9)$$

where η_h is an accuracy parameter that set to 0.4 [36, 51]. $\ddot{\mathbf{a}}_1$, $\mathbf{a}_1^{(4)}$, and $\mathbf{a}_1^{(5)}$ are the third, fourth, and fifth derivatives of the acceleration. Furthermore, $\ddot{\mathbf{a}}_1$ is saved for the next iteration since it is needed in the predictor for the Taylor expansion.

2.1.1 Polynomial interpolation for the sixth-order integrator

For each star, the third, fourth, and fifth derivatives of the acceleration at the next step ($\ddot{\mathbf{a}}_1$, $\mathbf{a}_1^{(4)}$, and $\mathbf{a}_1^{(5)}$) are estimated analytically during the corrector step using \mathbf{a}_0 , \mathbf{a}_1 , $\dot{\mathbf{a}}_0$, $\dot{\mathbf{a}}_1$, $\ddot{\mathbf{a}}_0$ and $\ddot{\mathbf{a}}_1$ [218]. It is convenient to define the following summations and differences between them as:

$$\mathbf{A}^+ = \mathbf{a}_1 + \mathbf{a}_0, \quad (2.10)$$

$$\mathbf{A}^- = \mathbf{a}_1 - \mathbf{a}_0, \quad (2.11)$$

$$\mathbf{J}^+ = h(\dot{\mathbf{a}}_1 + \dot{\mathbf{a}}_0), \quad (2.12)$$

$$\mathbf{J}^- = h(\dot{\mathbf{a}}_1 - \dot{\mathbf{a}}_0), \quad (2.13)$$

$$\mathbf{S}^+ = h^2(\ddot{\mathbf{a}}_1 + \ddot{\mathbf{a}}_0), \quad (2.14)$$

$$\mathbf{S}^- = h^2(\ddot{\mathbf{a}}_1 - \ddot{\mathbf{a}}_0), \quad (2.15)$$

where $h = \Delta t/2 = (t_1 - t_0)/2$. The coefficients of the polynomial interpolation at the midpoint $t = h$ are:

$$\mathbf{a}_{1/2} = \frac{1}{16} (8\mathbf{A}^+ - 5\mathbf{J}^- + \mathbf{S}^+), \quad (2.16)$$

$$h\dot{\mathbf{a}}_{1/2} = \frac{1}{16} (15\mathbf{A}^- - 7\mathbf{J}^+ + \mathbf{S}^-), \quad (2.17)$$

$$\frac{h^2}{2}\ddot{\mathbf{a}}_{1/2} = \frac{1}{8} (3\mathbf{J}^- - \mathbf{S}^+), \quad (2.18)$$

$$\frac{h^3}{6}\ddot{\mathbf{a}}_{1/2} = \frac{1}{8} (-5\mathbf{A}^- + 5\mathbf{J}^+ - \mathbf{S}^-), \quad (2.19)$$

$$\frac{h^4}{24}\mathbf{a}_{1/2}^{(4)} = \frac{1}{16} (-\mathbf{J}^- + \mathbf{S}^+), \quad (2.20)$$

$$\frac{h^5}{120}\mathbf{a}_{1/2}^{(5)} = \frac{1}{16} (3\mathbf{A}^- - 3\mathbf{J}^+ + \mathbf{S}^-). \quad (2.21)$$

Thus $\ddot{\mathbf{a}}_1$, $\mathbf{a}_1^{(4)}$, and $\mathbf{a}_1^{(5)}$ are obtained by expanding their midpoint counterparts to t_1 :

$$\ddot{\mathbf{a}}_1 = \ddot{\mathbf{a}}_{1/2} + h\mathbf{a}_{1/2}^{(4)} + \frac{h^2}{2}\mathbf{a}_{1/2}^{(5)}, \quad (2.22)$$

$$\mathbf{a}_1^{(4)} = \mathbf{a}_{1/2}^{(4)} + h\mathbf{a}_{1/2}^{(5)}, \quad (2.23)$$

$$\mathbf{a}_1^{(5)} = \mathbf{a}_{1/2}^{(5)}. \quad (2.24)$$

Finally, by integrating, we obtain the sixth-order corrector:

$$\mathbf{v}_1 = \mathbf{v}_0 + h \left(\mathbf{A}^+ - \frac{2}{5}\mathbf{J}^- + \frac{1}{15}\mathbf{S}^+ \right), \quad (2.25)$$

$$\mathbf{r}_1 = \mathbf{r}_0 + h\mathbf{v}_1 + h^2 \left(-\frac{2}{5}\mathbf{A}^- + \frac{1}{15}\mathbf{J}^+ \right), \quad (2.26)$$

here \mathbf{v}_1 and \mathbf{r}_1 correspond exactly to \mathbf{v}_c and \mathbf{r}_c in Eqs.2.7,2.8.

2.2 The block time steps method

Stars in an N-body system can have very different accelerations. This corresponds to have a large variety of evolutionary dynamical time scales. In this context, it is convenient to assign to all stars their individual time step, which becomes a function of the physical parameters that describe the kinematic state of stars. To avoid time-synchronization issues between the stars, and to simplify the parallelization process, the time step of the i -th star is discretized to powers of two: $\Delta t_i^{discretized} = 2^{-n}$, where n is an integer. In the code, by default, the maximum and minimum time steps are $\Delta t_{max} = 2^{-3}$ and $\Delta t_{min} = 2^{-35}$ respectively. For each star, we use Eq.2.9 to calculate the ideal time step Δt_i^{real} , but we always approximate n to the largest integer value, so the effective time step is $\Delta t_i^{discretized} \leq \Delta t_i^{real}$. Thus, particles are sub-divided into several groups (blocks) that share the same time step [3] and the groups are indexed according to n . The latter strategy is very effective to select, for each step, the stars that need to be integrated, since we need to update positions and velocities only for m stars per time step, where $m \leq N$. Specifically, stars with smaller time steps will be updated more often than stars with larger time steps, and for the latter, the kinematic state will be estimated using the predictor step only. This implies that the computational complexity is reduced from $O(N^2)$ to $O(mN)$. This is a significant gain in terms of performance, with a negligible cost in terms of the precision of the integrator.

Fig.2.1 shows a cartoon that explains the block time steps method. Stars in lower blocks have a smaller time step compared to stars in higher blocks, and the time steps are all integer multiples of the minimum one so that it is straightforward to synchronize the blocks with each other. In Fig.2.1, red arrows show that the stars in block 0 are always updated (time step dt), while the stars in block 1 are updated every two steps ($2dt$) and the stars in block 2 every four steps ($4dt$). Each star can jump from its block to another one, accordingly to its time step variation. The jump is possible only when the current block of the star is synchronized with the block where the star aims to jump. In Fig.2.1, these jumps are shown as green lines. It is worth noting that jumps toward lower blocks are always permitted (by construction, a block is always synchronized with its lower blocks); in contrast, stars can jump toward higher blocks only at synchronous times (forbidden transitions are shown as yellow arrows that end up on red crosses).

2.3 The Ahmad-Cohen neighbours scheme

Star clusters may contain a large number of stars (up to $\sim 10^6$ for massive GCs), and this makes direct N-body simulations very challenging because of the high computational complexity of $O(N^2)$. In order to deal with such numerical challenges, a neighbour procedure that requires fewer total force calculations can be introduced. A very common strategy for direct N-body simulations is to adopt the Ahmad-Cohen (AC) neighbour scheme [17, 178]. In this method, the force on a star is split into two contributions that evolve over different time scales. The first contribution depends only on near stars and the other one is owed to distant stars. It is apparent that the latter

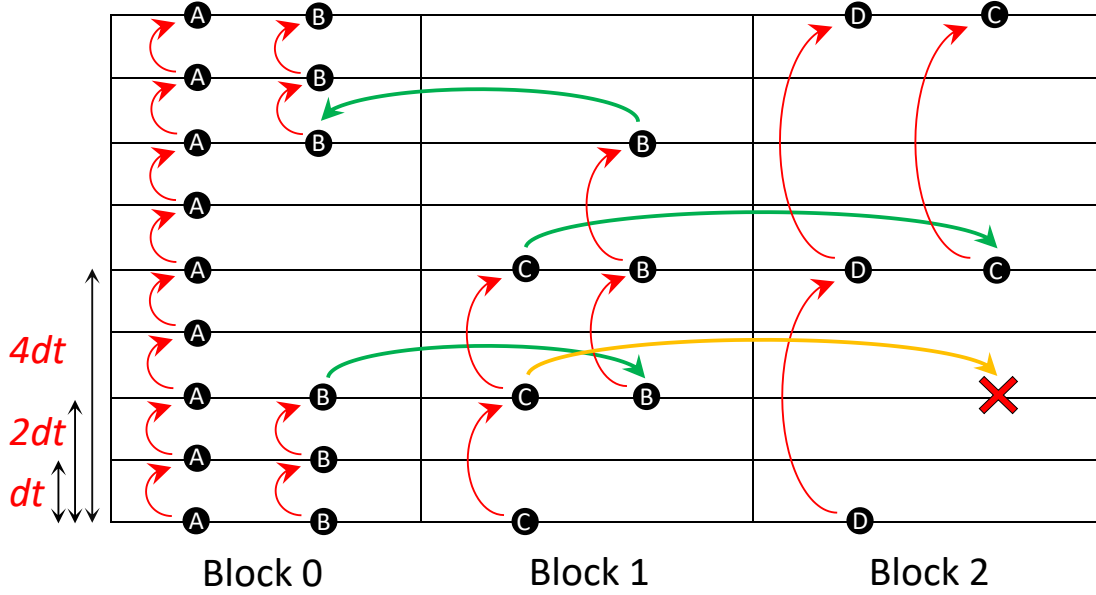


Figure 2.1: A cartoon of the block time steps method with four particles (indicated as “A”, “B”, “C” and “D”) as an example. Horizontally, three example blocks are placed, with three time steps: dt , $2dt$, $4dt$. The vertical axis represents the discretized time. The red arrows represent a particle doing its time step. The green arrows represent a particle changing time step, and therefore block. The yellow arrows represent a particle that is trying to change time step, but it fails because the arriving block is not synchronized with the its actual block. At the bottom of the cartoon, particles “A” and “B” are in block 0, “C” is in block 1 and “D” is in block 2. Particles “A” and “D” do not change block, “A” keeps doing time steps dt (fast evolution) while “D” $4dt$ (slow evolution). “B” changes block after two steps, then it switch back to the previous block. “C” tries to change time step when blocks 1 and 2 were not synchronized, failing; later it was able to successfully change it when the two block were synchronized.

force evolves over much slower time scales than the one from close stars, therefore it does not have to be recalculated with the same frequency. This implies fewer operations per step and a significant performance gain. The combination with the block time steps method described above is straightforward: each star will be in two separate blocks, corresponding to two (discretized) time steps Δt_{close} and Δt_{far} , calculated for close and distant stars, respectively. For each star, we only compute the forces from its neighbours, proceeding with a time step Δt_{close} (neighbour steps), and the forces from distant particles are approximated using a Taylor expansion; in contrast, every k steps (with $k\Delta t_{close} = \Delta t_{far}$), we compute the force from both close and distant particles self-consistently. ISTEEDAS implements the AC neighbours scheme entirely on the GPU. This is a significant advantage in terms of performance since, for each step, there is no need to communicate the neighbours between the CPU and the GPU, reducing communication latencies.

To identify neighbours, we use the external C++ library [ANN](#) (to see why we have chosen this library see the subsection [2.4.3](#)) that builds a three-dimensional k -d tree structure using an approximate nearest neighbor searching algorithm. Actually, there is the possibility to use a fixed number or a variable number of neighbours.

Let us first discuss the case with a variable number of neighbours. To calculate the ideal number of neighbours, we evaluate the total number of operations performed with and without neighbours within a time step Δt_f :

$$\begin{aligned} \text{with neighbours:} \quad N_{operations} &= n_n \frac{\Delta t_f}{\Delta t_c} + (N - n_n), \\ \text{without neighbours:} \quad N_{operations} &= \frac{\Delta t_f}{\Delta t_c} N, \end{aligned}$$

dividing the above contribution we obtain the cost function:

$$Cost(n_n) = \frac{n_n}{N} + \frac{\Delta t_c}{\Delta t_f} \left(1 - \frac{n_n}{N}\right), \quad (2.27)$$

where n_n is the number of neighbours. The ideal number of neighbours is retrieved from the above equation in the minimum of the cost function. To compute both Δt_c and Δt_f we use the Hermite 4th order time step criterion [[178](#)]:

$$\Delta t = \eta_\ell \sqrt{\frac{|\mathbf{a}_1| |\ddot{\mathbf{a}}_1| + |\dot{\mathbf{a}}_1|^2}{|\dot{\mathbf{a}}_1| |\ddot{\mathbf{a}}_1| + |\ddot{\mathbf{a}}_1|^2}}, \quad (2.28)$$

where η_ℓ is a free parameter that we take as 0.05 for Δt_c and 0.1 for Δt_f . In Eq. [2.28](#), the time step depends on n_n through the accelerations. The cost function is computed for different values of n_n until the maximum value, that is [[180](#)]:

$$n_{n,max} = \frac{1}{4} \left(\frac{N}{4}\right)^{\frac{3}{4}}. \quad (2.29)$$

The ideal value for n_n is the one that minimizes the cost function. For each star, we save the radius of its neighbour sphere, r_{neigh} , which corresponds to the distance of the star's n_n -th neighbour. To stabilize the number of neighbors per star, that is to avoid too frequent neighbors' changes, we have introduced a threshold value, so if the minimum cost is bigger than 0.6 no neighbours are selected ($r_{neigh} = 0$). The three-dimensional k -d tree structure and the number of neighbours are updated every time all stars are synchronized (every Δt_{max}), therefore every time the code computes N^2 forces. However, r_{neigh} can change before one global synchronization and the next one. After the update of the tree structure, we calculate the local star density considering, for each star, the distance to its 6th nearest neighbor, and we use it to estimate the system's radial density profile, $\rho(r)$. Every Δt_f , we update r_{neigh} so the number of neighbours per star does not change significantly, that is:

$$r_{neigh,new} = r_{neigh,old} \left(\frac{\rho(r_{*,old})}{\rho(r_{*,new})}\right)^{\frac{1}{3}}, \quad (2.30)$$

where $r_{*,old}$ and $r_{*,new}$ are the position of the star in the system at the previous and current time-step respectively.

Let us now consider the case with a fixed number of neighbours. The more natural choice is to take as a fixed number of neighbours a multiple of 32 ($n_n \propto 32$). In this way, the force calculation on GPU during the neighbour step is more efficient since 32 is the number of threads in a single GPU warp. In this case, we do not use r_{neigh} , therefore, to always have the right neighbours, we compute the three-dimensional k -d tree structure every time that at least one star is doing a distant step. This last case, for ISTEEDAS, is much more stable than the configuration with a variable number of neighbours: the numerical errors are accumulated much slower with respect to the case with variable neighbours due to the decreased number of operations made, and the block distribution is more stable overall. Moreover, since it does much less work on the CPU, we get a reduction of the latencies between the CPU and GPU speeding up the simulation. Furthermore, using a fixed number of neighbors, there is no need to calculate and adjust the neighbor distance (see Eq. 2.30), which relies crucially on the assumption of spherical symmetry of the N-body system. This means that, with fixed neighbors, we can evolve even systems that are far from spherical symmetry (e.g., fractal clusters).

Moving forward, some complications arise when using this scheme combined with the Hermite integrator. With the AC method, during the neighbour integration steps (Δt_n), no issues are encountered, since the neighbours are constant. Though during a distant step (i.e. every Δt_f), the neighbours might have changed, thus the Hermite corrector is not self-consistent anymore because in Eqs. 2.7, 2.8 we are summing and subtracting accelerations and derivatives computed with potentially different neighbours, in fact, the Hermite 6th order corrector writes as:

$$\mathbf{v}_c = \mathbf{v}_{0,old} + (\mathbf{a}_{1,new} + \mathbf{a}_{0,old}) \frac{\Delta t}{2} - (\dot{\mathbf{a}}_{1,new} - \dot{\mathbf{a}}_{0,old}) \frac{\Delta t^2}{10} + (\ddot{\mathbf{a}}_{1,new} + \ddot{\mathbf{a}}_{0,old}) \frac{\Delta t^3}{120}, \quad (2.31)$$

$$\mathbf{r}_c = \mathbf{r}_{0,old} + (\mathbf{v}_c + \mathbf{v}_{0,old}) \frac{\Delta t}{2} - (\mathbf{a}_{1,new} - \mathbf{a}_{0,old}) \frac{\Delta t^2}{10} + (\dot{\mathbf{a}}_{1,new} + \dot{\mathbf{a}}_{0,old}) \frac{\Delta t^3}{120}, \quad (2.32)$$

where the variables labeled with *old* and *new* are computed using the neighbours of the previous and the actual step respectively. Therefore, we apply the following steps, as in [178] for the Hermite 4th order integrator, to solve the problem:

- Compute the acceleration and its derivatives due to neighbors based on the list of neighbours calculated in the previous step ($\mathbf{a}_{close,old}$).
- Apply the corrector calculated for the acceleration due to neighbors
- Compute the acceleration and its derivatives due to neighbors and distant stars based on the new list of neighbours calculated in this step ($\mathbf{a}_{close,new}$ and $\mathbf{a}_{far,new}$)
- Compute the acceleration and its derivatives due to distant particles based on the old neighbor list as $\mathbf{a}_{far,old} = \mathbf{a}_{far,new} + \mathbf{a}_{close,new} - \mathbf{a}_{close,old}$.
- Apply the corrector for the acceleration due to distant particles using $\mathbf{a}_{far,old}$ and its derivatives.

It is worth noting that \mathbf{a} , $\dot{\mathbf{a}}$ and $\ddot{\mathbf{a}}$ are computed with the new neighbours list, during the evaluation step, while $\ddot{\mathbf{a}}$ (far and close) is estimated during the corrector step using the old neighbours list. Since in the Hermite 6th order scheme $\ddot{\mathbf{a}}$ is needed in the predictor step and to calculate the correct individual time steps for stars, it is important to compute it self-consistently. To achieve this, we keep track of the incoming and outgoing neighbors with respect to r_{neigh} , and we retrieve $\ddot{\mathbf{a}}_{new}$ by subtracting and summing on $\ddot{\mathbf{a}}_{old}$ the contribution from outgoing and incoming neighbours:

$$\ddot{\mathbf{a}}_{new} = \ddot{\mathbf{a}}_{old} - \ddot{\mathbf{a}}_{outgoing} + \ddot{\mathbf{a}}_{incoming}. \quad (2.33)$$

We compute the outgoing and the incoming contributions using the explicit Newtonian formula for $\ddot{\mathbf{a}}$:

$$\begin{aligned} \ddot{\mathbf{a}}_{i,1} = \sum_{k=1}^S \frac{m_k}{|\mathbf{r}_{ik,p}|^3} & \left\{ \dot{\mathbf{a}}_{ik,p} - 9 \frac{\mathbf{r}_{ik,p} \cdot \mathbf{v}_{ik,p}}{|\mathbf{r}_{ik,p}|^2} \mathbf{a}_{ik,p} + \right. \\ & + \frac{9}{|\mathbf{r}_{ik,p}|^2} \left[5 \frac{(\mathbf{r}_{ik,p} \cdot \mathbf{v}_{ik,p})^2}{|\mathbf{r}_{ik,p}|^2} - \mathbf{r}_{ik,p} \cdot \mathbf{a}_{ik,p} - |\mathbf{v}_{ik,p}|^2 \right] \mathbf{v}_{ik,p} + \\ & + \frac{1}{|\mathbf{r}_{ik,p}|^2} \left[24 \frac{(\mathbf{r}_{ik,p} \cdot \mathbf{v}_{ik,p})(\mathbf{r}_{ik,p} \cdot \mathbf{a}_{ik,p} + |\mathbf{v}_{ik,p}|^2)}{|\mathbf{r}_{ik,p}|^2} - 21 \frac{\mathbf{r}_{ik,p} \cdot \mathbf{v}_{ik,p}}{|\mathbf{r}_{ik,p}|^2} \left(5 \frac{(\mathbf{r}_{ik,p} \cdot \mathbf{v}_{ik,p})^2}{|\mathbf{r}_{ik,p}|^2} + \right. \right. \\ & \left. \left. - \mathbf{r}_{ik,p} \cdot \mathbf{a}_{ik,p} - |\mathbf{v}_{ik,p}|^2 \right) - 3(\mathbf{r}_{ik,p} \cdot \dot{\mathbf{a}}_{ik,p} + 3\mathbf{a}_{ik,p} \cdot \mathbf{v}_{ik,p}) \right] \mathbf{r}_{ik,p} \left. \right\}, \end{aligned} \quad (2.34)$$

where, as in Eqs.(2.4,2.5,2.6), the quantities with subscript “ ik,p ” are the relative predicted values between stars i and k (e.g. $\mathbf{r}_{ik,p} = \mathbf{r}_{k,p} - \mathbf{r}_{i,p}$), S is the total number of incoming or outgoing neighbours, and we have assumed the gravitational constant $G = 1$.

Finally, to estimate Δt_{close} and Δt_{far} we use Eq.2.9 only if the neighbours do not change; otherwise, we use the low order, Hermite 4th order, criterion as in Eq.2.28. This is necessary because $\mathbf{a}^{(4)}$ and $\mathbf{a}^{(5)}$ would be inconsistent if the neighbor list changes. Furthermore, $\mathbf{a}^{(4)}$ and $\mathbf{a}^{(5)}$ are not needed in the predictor step, and correcting them with the corresponding Newtonian formulas, as we do for $\ddot{\mathbf{a}}$, would have a significant computational cost without increasing the order of the integrator.

2.4 Optimizations and parallelization

ISTEDDAS runs almost completely on GPU accelerators. Therefore we were able to minimize the amount of data communication between the CPU and the GPU.

ISTEDDAS can run on single or multiple GPUs, and on single or multiple MPI nodes, in this way, the code can exploit GPU workstations as well as GPU clusters. One problem that is important to address is related to the evaluation kernel. The calculation of the newtonian gravitational force involves the computation of the inverse

square root:

$$\mathbf{F}_{ij} = \frac{m_i m_j G}{|\mathbf{r}_{i,j}|^3} \mathbf{r}_{i,j} = \left(\frac{1}{\sqrt{(x_j - x_i)^2 + (y_j - y_i)^2 + (z_j - z_i)^2}} \right)^3 m_i m_j G \mathbf{r}_{i,j}, \quad (2.35)$$

that is famous to be a computationally heavy operation, in fact, in the early 1990s the fast inverse square root was invented to overcome this problem. The algorithm is, as one can guess by the name, a faster implementation of the inverse square root that approximates the exact value of $1/\sqrt{x}$. We cannot use such an algorithm since we need as much accuracy as we can. Thankfully, nowadays the algorithms to compute the inverse square root are quite fast, therefore we use the CUDA function `rsqrt()`, which is a native reciprocal square root instruction. However, to speed up the code as much as possible, we try to optimize every operation. For example, whenever we can, we use the fused multiply-addition (`fma()`), which is a floating-point operation ($a \cdot b + c$) performed in one step with a single rounding error. It can be used to compute the square module of a vector \mathbf{v} :

$$|\mathbf{v}|^2 = v_x \cdot v_x + v_y \cdot v_y + v_z \cdot v_z = \text{fma}(v_x, v_x, \text{fma}(v_y, v_y, \text{fma}(v_z, v_z, 0))) , \quad (2.36)$$

where v_x, v_y, v_z are the 3D components of the vector \mathbf{v} . In this simple example, we pass from 5 floating-point operations (3 multiplications and 2 summations) to just 3 floating-point operations. It can also be used to compute the Taylor expansions of any quantity q , for example, for a third-order expansion:

$$\begin{aligned} q_1 &\simeq q_0 + \dot{q}_0 dt + \ddot{q}_0 \frac{dt^2}{2} + \dddot{q}_0 \frac{dt^3}{6} = \\ &= \text{fma} \left(dt, \text{fma} \left(\frac{dt}{2}, \text{fma} \left(\frac{dt}{3}, \ddot{q}_0, \ddot{q}_0 \right), \dot{q}_0 \right), q_0 \right). \end{aligned} \quad (2.37)$$

In this simple example, we pass from 6 floating-point operations (3 multiplications and 3 summations) to just 3 floating-point operations.

2.4.1 Forces evaluation algorithm

Computing $\mathbf{a}_{i,1}$, $\dot{\mathbf{a}}_{i,1}$, $\ddot{\mathbf{a}}_{i,1}$, and $\dddot{\mathbf{a}}_{i,1}$ can be extremely computationally expensive due to the huge amount of multiplications, divisions, summations, and inverse square roots (see Eqs. 2.4, 2.5, 2.6, 2.34). However, a lot of these calculations are repeated, therefore, for each couple (i, j) of stars, we define the following quantities to avoid these repetitions:

$$S_0 = \mathbf{r}_{ij,p} \cdot \mathbf{r}_{ij,p}, \quad (2.38)$$

$$S_1 = \mathbf{r}_{ij,p} \cdot \mathbf{v}_{ij,p}, \quad (2.39)$$

$$S_2 = \mathbf{r}_{ij,p} \cdot \mathbf{a}_{ij,p} + \mathbf{v}_{ij,p} \cdot \mathbf{v}_{ij,p}, \quad (2.40)$$

$$S_3 = \mathbf{r}_{ij,p} \cdot \dot{\mathbf{a}}_{ij,p} + 3\mathbf{v}_{ij,p} \cdot \mathbf{a}_{ij,p}, \quad (2.41)$$

$$Q_1 = -3r_{inv}^2 S_1, \quad (2.42)$$

$$Q_2 = -r_{inv}^2 (5S_1 Q_1 + 3S_2), \quad (2.43)$$

$$Q_3 = -r_{inv}^2 (8S_2 Q_1 + 7S_1 Q_2 + 3S_3), \quad (2.44)$$

where, again, the quantities with subscript “ ij,p ” are the relative predicted values between stars i and j (e.g. $\mathbf{r}_{ij,p} = \mathbf{r}_{j,p} - \mathbf{r}_{i,p}$), and $r_{inv} = 1/\sqrt{S_0}$. Using the above quantities we can rewrite the equations for the acceleration and its derivatives as:

$$\mathbf{a}_{i,1} = \sum_{j \neq i}^N m_j r_{inv}^3 \mathbf{r}_{ij,p}, \quad (2.45)$$

$$\dot{\mathbf{a}}_{i,1} = \sum_{j \neq i}^N m_j r_{inv}^3 (Q_1 \mathbf{r}_{ij,p} + \mathbf{v}_{ij,p}), \quad (2.46)$$

$$\ddot{\mathbf{a}}_{i,1} = \sum_{j \neq i}^N m_j r_{inv}^3 (Q_2 \mathbf{r}_{ij,p} + 2Q_1 \mathbf{v}_{ij,p} + \mathbf{a}_{ij,p}), \quad (2.47)$$

$$\ddot{\ddot{\mathbf{a}}}_{i,1} = \sum_{j \neq i}^N m_j r_{inv}^3 (Q_3 \mathbf{r}_{ij,p} + 3Q_2 \mathbf{v}_{ij,p} + 3Q_1 \mathbf{a}_{ij,p} + \dot{\mathbf{a}}_{ij,p}). \quad (2.48)$$

By computing this equation we avoid a lot of extra calculations, even the inverse square root is done just once. On top of this, we also use the tricks explained above (e.g. the `fma()` function).

2.4.2 Forces reduction and gather

When simulating star clusters with more than 10^4 - 10^5 stars, it is very useful to use multiple GPUs to speed up the calculation of the forces. The predictor and corrector kernels are computed equally on each GPU since they scale with the number of stars (N), and therefore are light kernels from the computational point of view. Thus they do not need any kind of communication between GPUs, however, we do transfer the results of GPU 0 to all the other GPUs every time that all the stars are synchronized. In this way we avoid the arise of discrepancies in the quantities among the GPUs.

Anyway, the force evaluation is a computationally heavy kernel, it scales at maximum as N^2 (distant step for N stars) and at minimum as $N \cdot n_n$ (neighbours step for N stars). Thus the evaluation process is split among the available GPUs to decrease the computational load on each GPU, this is done for both the far and the close accelerations. This split of the forces evaluation inevitably introduces extra communication between GPUs and CPUs at each step. The two cases, distant and neighbours steps, are handled separately with two different GPU kernels, and also different communication strategies. For the distant step, every GPU computes the interactions between all the i stars (N) with only a fraction of the j stars (N/n_{gpu}), in this way they will perform $\sim N^2/n_{gpu}$ operations, that is a perfectly balanced use of the devices. In more detail, every star has its own one-dimensional block with 128 threads (4 warps), so each thread will compute and accumulate the forces from $(N/n_{gpu})/128$ j stars. Since we have divided the j stars, at the end a reduction will be necessary to build the total forces between stars. Instead, for the neighbours step, since n_n is much smaller than N or N/n_{gpu} would not make sense to divide the neighbours among the GPUs (n_n/n_{gpu}), because each i star would have to interact with a very small amount of j star on each

device, that is not optimal, especially if that number is smaller than 32. Thus, every GPU computes the interactions between a fraction of the i stars (N/n_{gpu}) with all their neighbours, or j stars, (n_n), in this way they will perform $\sim N \cdot n_n/n_{gpu}$ operations. In more detail, every block is, again, one-dimensional and has 128 threads, but this time it will handle 4 i stars (one for each warp). So, each thread of the warp will compute and accumulate the forces from $n_n/32$ j stars, and this is the reason why we choose $n_n \propto 32$ for the value of the number of neighbours. Since this time we have divided the i stars, at the end a gather will be necessary to communicate the total forces between stars to all the GPUs.

For the reduction we apply the following strategy: first of all, there is the single GPU reduction, which is done at warp level, to be as efficient as possible, using the CUDA function `__shfl_down_sync()`, see Fig.2.2². Then, since in the evaluation

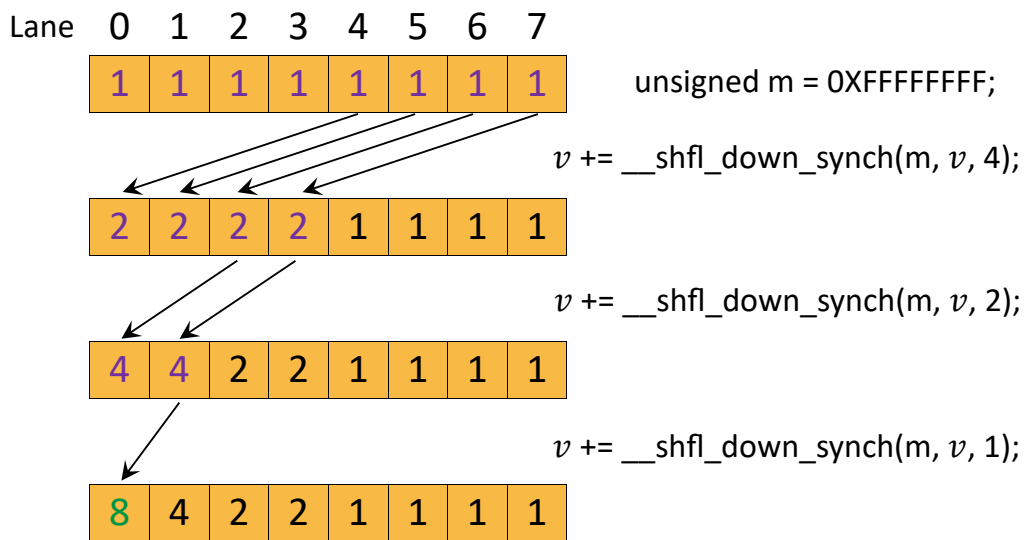


Figure 2.2: The cartoon shows an example of using warp-level primitives. It uses `__shfl_down_sync()` to perform a tree-reduction to compute the sum of the v variable held by each thread in a warp. At the end of the loop, v of the first thread in the warp contains the desired sum (8 in this example). $m = 0xFFFFFFFF$ is the standard mask used to perform this operation, and it is an hexadecimal integer constant where the prefix `0X` means the next number is written in the hexadecimal, and `FFFFFFFF` is $2^{32} - 1$ in decimal notation, or 32 consecutive “1” in binary notation. A warp comprises 32 lanes, with each thread occupying one lane, so it needs 5 uses of the function to be reduced. The data exchange is performed between registers, and it is more efficient than going through shared memory, which requires a load, a store, and an extra register to hold the address.

kernel each block handles an i star, we reduce all the values of the first threads of each warp of each block. After these passages, every GPU has the reduced forces on

²See the link <https://developer.nvidia.com/blog/using-cuda-warp-level-primitives/> for extra details about warp level reductions.

each i star from N/n_{gpu} stars. To obtain the total force from all the N stars of the simulation there are two final steps: the computed forces are copied to the CPUs that perform an intra-node reduction between the GPUs within each node and in the end an MPI reduction (`MPI_Allreduce()`) is performed between the nodes to finally have the complete far and close forces for each star. For the gather we use a similar strategy as above: first of all, there is the single GPU reduction, which is done at warp level exactly as before. Since every warp handles the interaction of each star with its neighbours, this is the only reduction required. In fact, after this step, we already pass to the intra-node gather between the GPUs within each node, and in the end, we perform an MPI gather (`MPI_Allgatherv()`) between the nodes to finally have the complete neighbours forces for each star on all the GPUs.

2.4.3 Ahmad-Cohen tree building optimization

In order to identify neighbours, we needed a nearest-neighbour searching tree library, therefore we test 5 different codes to decide which one best match our needs ISTEDDAS:

- ANN³ (Approximate Nearest Neighbor searching): a library written in C++, running on CPU, which supports data structures and algorithms for both exact and approximate nearest neighbor searching in arbitrarily high dimensions.
- FLANN⁴ (Fast Library for Approximate Nearest Neighbors): a library for performing fast approximate nearest neighbor searches in high dimensional spaces. It is written in C++ and runs on GPU [213].
- FAISS⁵ (Facebook AI Similarity Search): a library for efficient similarity search and clustering of dense vectors. It contains algorithms that search in sets of vectors of any size. It is written in C++ and runs on GPU [143].
- hnswlib⁶ (Hierarchical Navigable Small World graphs library): a library written in C++ that runs on CPU, for the approximate K-nearest neighbor search it uses navigable small world graphs with controllable hierarchy [183].
- GGNN⁷ (Graph-based GPU Nearest Neighbor search): its search structure is based on nearest neighbor graphs and information propagation on graphs. the code is designed to take advantage of GPU architectures to accelerate the hierarchical building of the index structure and for performing the query [115].

These libraries have two main operations: the construction of the tree, and the search for neighbours. The first operation is the creation of the tree structure from which the search for neighbours is done. We benchmark these codes based on the usage

³The code is public and available here: <http://www.cs.umd.edu/~mount/ANN/>

⁴The code is public and available here: <https://github.com/flann-lib/flann>

⁵The code is public and available here: <https://github.com/facebookresearch/faiss>

⁶The code is public and available here: <https://github.com/nmslib/hnswlib>

⁷The code is public and available here: <https://github.com/chingyaoc/ggnn.pytorch>

that they would have in ISTEEDDAS, therefore we use a three-dimensional space and we test a number of points that could resemble the number of stars in star clusters $N = [2^{11}, 2^{13}, 2^{14}, 2^{15}, 2^{16}, 2^{17}]$. For each code, and for each number of stars, I save both the time needed to build the tree structure and the searches (or queries) of the first 64 neighbours on N_q stars. For the benchmarks, N_q is chosen to be an integer fraction of N : $[1, N/128, N/32, N/8, N/2, N]$. The benchmarks in Fig.(2.3,2.4) were done on a laptop with the specifics in Table 2.1.

CPU	:	Intel(R) Core(TM) i7-10750H 2.60GHz
RAM	:	16GB DDR4
GPU	:	NVIDIA GeForce GTX 1650 Ti
GRAM	:	4GB GDDR6

Table 2.1: Laptop specifics.

Fig.2.3 shows the scalability of each library with respect to the increasing number of points and the increasing number of queries, moreover, it is also shown the time comparison for the creation of the tree. Instead, in Fig.2.4, the same data are rearranged to show the time comparison for the neighbours searches among the 5 libraries. From the point of view of building the tree, the two best options are ANN and FLANN, ANN performs much better with smaller N , and FLANN scales better with increasing N . In contrast, from the point of view of the searches, hnsplib perform better than anyone else with $N_q = 1$ for every N , however increasing N and N_q , the two best options for ISTEEDDAS are, again, ANN and FLANN. Probably, the reason behind these results is that the other libraries are optimized for high-dimensional spaces, while we just need a three-dimensional tree. For ISTEEDDAS, on a single GPU, the best possible combination would be to use ANN with a small number of stars and FLANN with a large number of stars, with the separation around 2^{14} - 2^{15} stars. However, because ANN does not scale on multiple nodes and can use only one CPU (see Section 5.1), while FLANN can scale on multiple GPUs, it will be crucial to take advantage of FLANN inside ISTEEDDAS in order to achieve good scaling over tens or hundreds of GPUs on the next-generation supercomputers. Since ANN was already implemented inside the code and the difference between ANN and FLANN is not significantly high on a single GPU, we stick with it, leaving the implementation of FLANN in ISTEEDDAS for future work. The library ANN is implemented in ISTEEDDAS, and it was modified to run the search for neighbours in parallel with OpenMP. This optimization speeds up the ANN library on a single node, however it still cannot scale with multiple nodes.

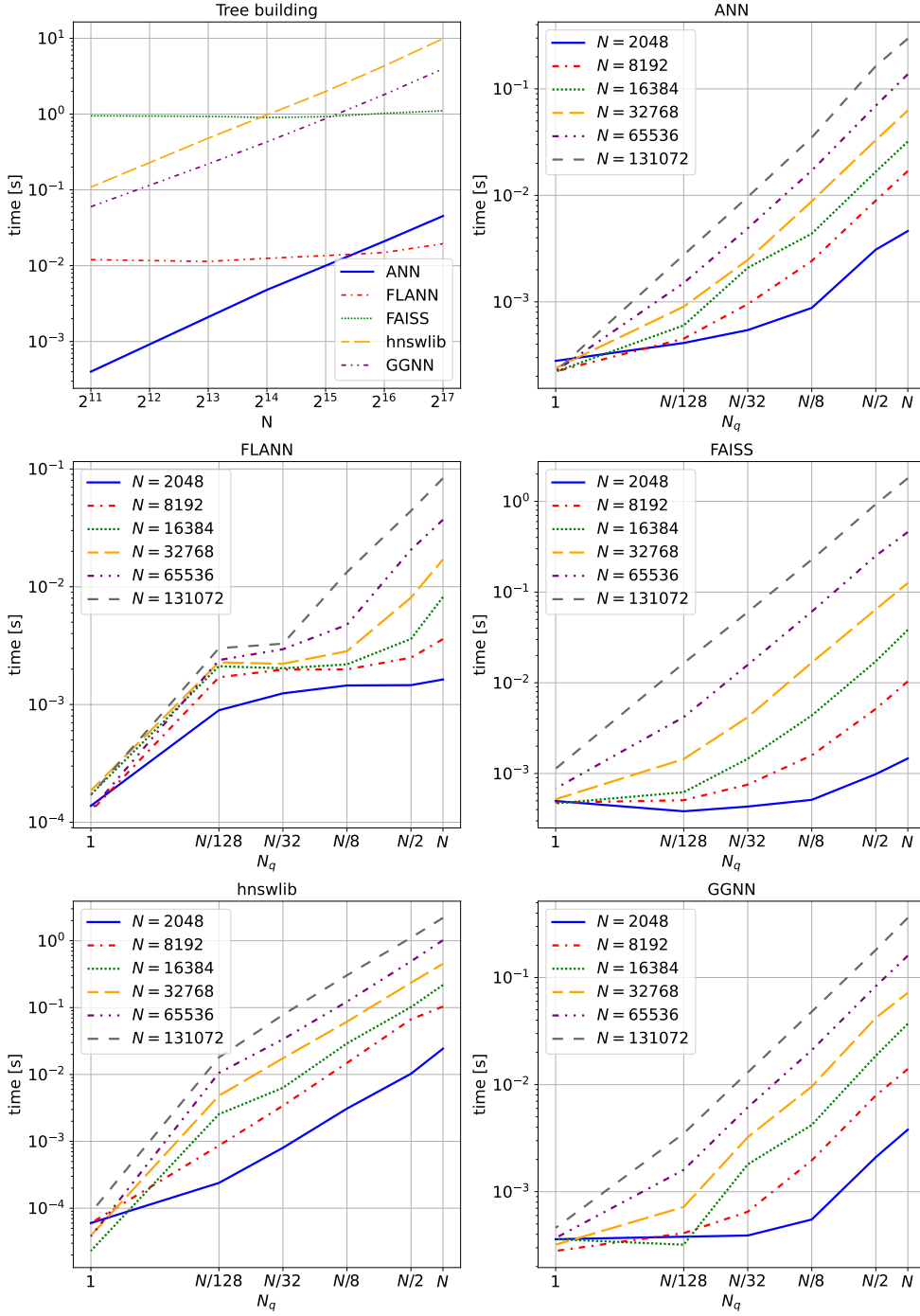


Figure 2.3: Benchmarks of the 5 tested libraries. In the top-left panel it is shown the time taken by each library to build the 3D tree structure in function of the total number of stars. In the other 5 panels it is shown, for each library, the time taken to perform a search (or query) of the first 64 neighbours on N_q points. N_q is a fraction of the total number of stars N : $[1, N/128, N/32, N/8, N/2, N]$. N is chosen as a power of 2: $[2^{11}, 2^{13}, 2^{14}, 2^{15}, 2^{16}, 2^{17}]$.

2.4 Optimizations and parallelization

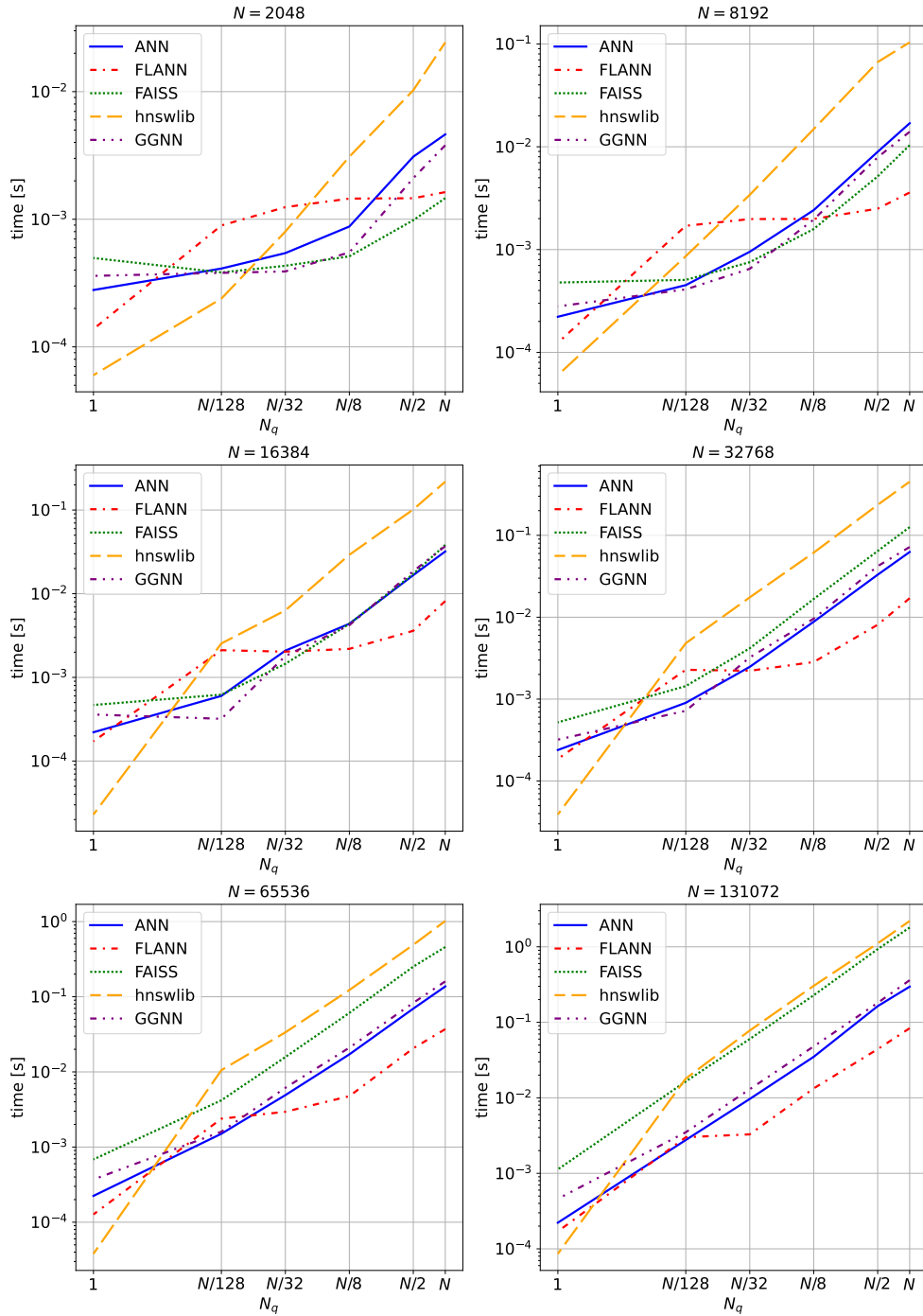


Figure 2.4: Benchmarks of the 5 tested libraries. In each panel it is shown, for a certain total number of stars N , the time taken by each library to perform a search (or query) of the first 64 neighbours on N_q points (stars). N_q is a fraction of the total number of stars N : $[1, N/128, N/32, N/8, N/2, N]$. N is chosen as a power of 2: $[2^{11}, 2^{13}, 2^{14}, 2^{15}, 2^{16}, 2^{17}]$.

Chapter 3

The few body code TSUNAMI

While the 6th order Hermite integrator is a powerful main integrator in ISTEEDDAS, it might not be suitable for the long-term integration of stable, very tight systems (e.g. binaries, triples). To integrate a tight binary, the Hermite integrator would significantly reduce the time step time, making the numerical integration of the whole system stall, and accumulating numerical error very fast. Thus, implementing a fast, high-accuracy algorithm to take care of tight systems in ISTEEDDAS is crucial, especially if our aim is to investigate the evolution of merging compact-object binaries and their GW emission. Therefore, we have coupled ISTEEDDAS with TSUNAMI, a code for the high-accuracy numerical integration of binaries and hierarchical systems [288, 289, 291]. TSUNAMI is based on the following techniques: regularization of the equations of motion, chain coordinates to reduce round-off errors, and Bulirsch–Stoer extrapolation. The first technique (regularization) takes care of the singularity of the gravitational potential (when the distance between the two bodies is near zero). The second technique (chain coordinates) helps reduce the round-off errors in hierarchical systems, which arise when moving to center-of-mass coordinates, without introducing numerically expensive techniques of compensated summation. The third method (Bulirsch–Stoer extrapolation) increases the accuracy of the integration and makes it adaptable over a wide dynamical range. Furthermore, TSUNAMI includes additional features such as perturbative forces, general relativity corrections through post-Newtonian terms up to 3.5 order, tidal interactions, and a collision-detection algorithm. In this chapter, I will go into further detail on these techniques.

3.1 The algorithmic regularization chain

TSUNAMI implements the algorithmic regularization chain (ARChain) integrator for high accuracy computation of particle motion in small N-body system [204, 206–208]. The method addresses very high accuracy and comparatively little computational effort by combining: a time-coordinate transformation (regularized time), the 2nd-order symplectic Leapfrog integrator, the Bulirsch-Stoer algorithm, and the use of chained coordinates.

3.1.1 The time regularization

The N-body system Hamiltonian is defined as:

$$H = K + U = \frac{1}{2} \sum_i^N m_i |\mathbf{v}_i|^2 - \sum_{i < j}^N \frac{m_i m_j}{|\mathbf{r}_{ij}|}, \quad (3.1)$$

where K and U are the kinetic and potential energy. This Hamiltonian contains a singularity for $|\mathbf{r}_{ij}| \rightarrow 0$ that makes the N-body integration less precise, especially when at least two bodies are very near to each other. The Algorithmic Regularization removes the singularity in the Hamiltonian performing a time transformation on the coordinates:

$$ds = dt (\alpha U + \beta \Omega + \gamma), \quad (3.2)$$

where ds and dt are the regularized and physical time steps, (α, β, γ) are three parameters that determine which kind of transformation is performed:

Logarithmic Hamiltonian	$(\alpha, \beta, \gamma) = (1, 0, 0),$
Transformed Leapfrog	$(\alpha, \beta, \gamma) = (0, 1, 0),$
Normal Leapfrog	$(\alpha, \beta, \gamma) = (0, 0, 1).$

Ω is an analytic function that mimics the evolution of the potential energy, however, since for my purposes I am going to use only the Logarithmic Hamiltonian and the normal Leapfrog, I will not go into the details of Ω . The Logarithmic Hamiltonian transformation removes the singularity making the integration more precise, in particular, in avoiding error accumulation while integrating those systems with very near bodies inside.

3.1.2 Chain coordinates

In the simulation of a star cluster using an N-body approach, the proximity between two bodies undergoing a close encounter (approximately AU scale) is represented as a difference in large numerical values (around pc scale), considering the possible distance of the bodies from the system's origin. Consequently, round-off errors can become a significant source of numerical error. To mitigate this issue, TSUNAMI employs chain coordinates instead of Cartesian coordinates.

The chain method involves constructing a sequence of inter-particle vectors, ensuring that all particles are encompassed within the chain. Special attention is given to incorporating small distances into the chain. Initially, distances are sorted to identify the shortest, which becomes the initial link in the chain. The process continues by identifying the particle closest to either end of the existing chain and adding it to the chain, repeating until all particles are included. Following each integration step, the code assesses whether any non-chained vector is shorter than the smallest chained vectors in contact with its ends or if any triangle formed by consecutive chain vectors has a non-chained side shorter than the others, triggering the formation of a new chain [208]. Fig.3.1 illustrates the decision-making process for constructing the chain.

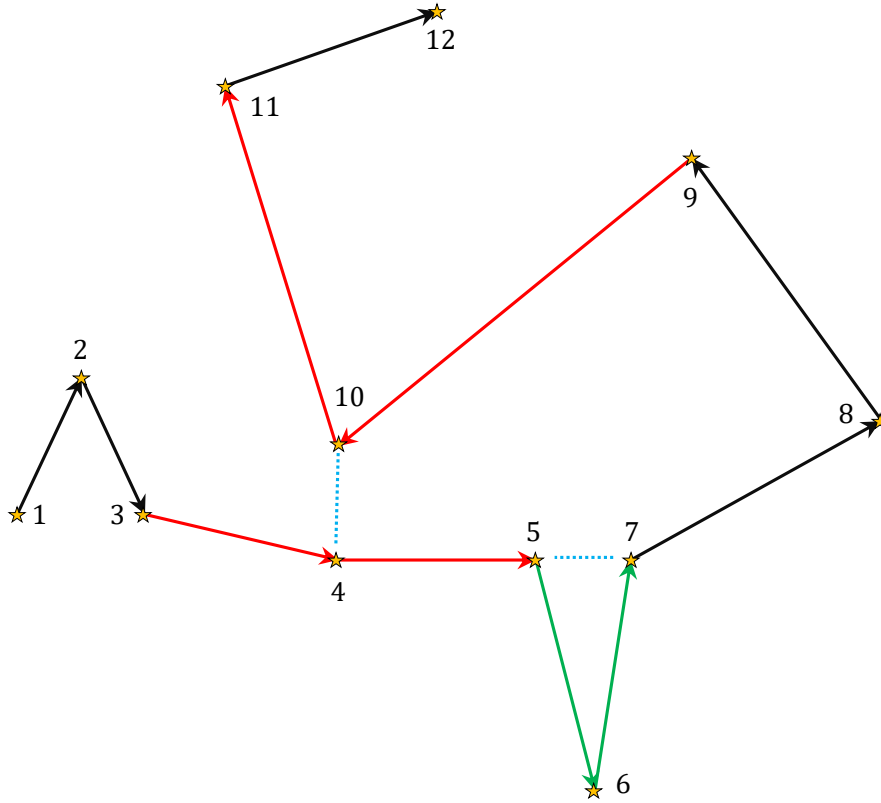


Figure 3.1: Visualization of the chain and criteria for switching conditions. Numbered yellow stars represent the bodies in the example system, and arrows depict the constructed chain. Distances like $|\mathbf{r}_{5,7}|$ (blue dotted line) are compared with the shorter of $|\mathbf{r}_{5,6}|$ and $|\mathbf{r}_{6,7}|$ (green arrows). Inter-particle distances such as $|\mathbf{r}_{4,10}|$ (blue dotted line) are compared with the smallest distances in contact with the considered distance: $|\mathbf{r}_{3,4}|$, $|\mathbf{r}_{4,5}|$, $|\mathbf{r}_{9,10}|$, $|\mathbf{r}_{10,11}|$ (red arrows). [204]

The use of chain coordinates simplifies distance computations, thereby facilitating the calculation of accelerations and potential energy. Distances between closely positioned stars in the chain (e.g., (1, 2), (2, 3), (3, 4)) are readily available, while distances between arbitrary stars can be efficiently computed by summing the necessary chain vectors (e.g., $\mathbf{r}_{3,6} = \mathbf{r}_{3,4} + \mathbf{r}_{4,5} + \mathbf{r}_{5,6}$).

3.1.3 The modified midpoint method

The modified midpoint method advances a vector of dependent variables $y(x)$ from a point x to a point $x + dt$ through a series of n sub-steps, each with a size defined as:

$$h = dt/n. \quad (3.3)$$

In theory, one could employ the modified midpoint method independently as an integrator for ordinary differential equations (ODEs). However, its primary significance is

realized within the more robust Bulirsch-Stoer technique, discussed in the subsequent paragraph.

The modified midpoint method demands a total of $n + 1$ evaluations of the right-hand side. The method's formulas are presented by [239]:

$$\begin{aligned} z_0 &\equiv y(x), \\ z_1 &= z_0 + hf(x, z_0), \\ z_{m+1} &= z_{m-1} + 2hf(x + mh, z_m) \quad \text{for } m = 1, 2, \dots, n-1, \\ y(x + dt) &\approx y_n \equiv \frac{1}{2} [z_n + z_{n-1} + hf(x + dt, z_n)] \end{aligned} \quad (3.4)$$

Here, the z 's represent intermediate approximations advancing in steps of h , while y_n stands as the ultimate approximation to $y(x + dt)$. The method essentially resembles a ‘‘centered difference’’ or ‘‘midpoint’’ method, with modifications at the initial and final points, hence the term ‘‘modified’’.

While the modified midpoint method is a second-order technique, it offers the advantage of requiring only one derivative evaluation per step h , asymptotically for large n . This is in contrast to, for instance, the second-order Runge-Kutta method, which necessitates two evaluations. The method's utility within the Bulirsch-Stoer technique stems from the error in the presented equations, expressed as a power series in h (the step size) containing only even powers of h [239]:

$$y_n - y(x + dt) = \sum_{i=1}^{\infty} \alpha_i h^{2i}. \quad (3.5)$$

While dt remains constant, h varies with changing n . The significance of this even power series lies in its capacity to eliminate higher-order error terms by combining steps, resulting in a gain of two orders at a time.

For instance, assuming n is even, and denoting $y_{n/2}$ as the result of applying $h = dt/n$ and using the modified midpoint algorithm (Eqs. 3.4) with half as many steps ($n \rightarrow n/2$), the estimate [239]:

$$y(x + dt) \approx \frac{4y_n - y_{n/2}}{3}, \quad (3.6)$$

proves to be fourth-order accurate, equivalent to fourth-order Runge-Kutta, yet demanding only approximately 1.5 derivative evaluations per step h instead of the 4 required by Runge-Kutta.

3.1.4 The Bulirsch-Stoer algorithm

The numerical integration employed here follows the symplectic Drift-Kick-Drift (DKD) Leapfrog method, characterized by the following sequence:

$$\begin{array}{ll} \text{Drift} & \mathbf{r}_{t+dt/2} = \mathbf{v}_t \frac{dt}{2} + \mathbf{r}_t, \\ \text{Kick} & \mathbf{v}_{t+dt} = \mathbf{a}_{t+dt/2} dt + \mathbf{v}_t, \\ \text{Drift} & \mathbf{r}_{t+dt} = \mathbf{v}_t \frac{dt}{2} + \mathbf{r}_t, \end{array}$$

where t denotes the initial time, dt the time-step, and $t + dt$ the final time. In this scheme, \mathbf{r} , \mathbf{v} , and \mathbf{a} represent positions, velocities, and accelerations, respectively, with subscripts indicating the time at which these vectors are computed. While the Leapfrog method is a second-order technique, its accuracy may be limited for highly constrained systems. Consequently, the Bulirsch-Stoer algorithm is incorporated to generate higher-order outcomes by extrapolating from a series of lower-order results via an extrapolation table [239, 306].

In greater detail, the Bulirsch–Stoer algorithm combines Richardson extrapolation, the use of rational function extrapolation, and the modified midpoint method. This amalgamation results in accurate numerical solutions for ordinary differential equations (ODEs) with relatively minimal computational effort. The approach involves treating the final solution of a numerical calculation as an analytic function of an adjustable parameter, the integration step dt . By performing the calculation with various dt values, the analytic function is probed, fitted, and evaluated at $dt = 0$. The fitting function can be a rational function or a polynomial of variable degree; in this study, a polynomial function is utilized.

The original Bulirsch and Stoer sequence, proposed as

$$n = 2, 4, 6, 8, 12, 16, 24, 32, 48, 64, 96, \dots, [n_j = 2n_{j-2}], \dots \quad (3.7)$$

is adapted in TSUNAMI to a sequence of even multiples of 2:

$$n = 2, 4, 6, 8, 10, 12, 14, 16, 18, \dots, [n_j = 2j], \dots \quad (3.8)$$

proving to be more efficient than the original sequence [67, 68].

For each sub-step count, Leapfrog integration occurs from t to $t + dt$ with enhanced accuracy, and the final results are used to extrapolate the solution ideally over an infinite number of infinitesimal sub-steps. The sequence’s upper limit is not predetermined; after each n is tested, an extrapolation is attempted, providing extrapolated values and error estimates. If the errors are satisfactory, the algorithm proceeds to the next step, initiating with $n = 2$. The maximum number of sub-steps in TSUNAMI is set to 18.

A visual representation of the Richardson extrapolation within the Bulirsch-Stoer method is depicted in Fig. 3.2. Here, different numbers of sub-steps are employed for multiple integration runs, demonstrating the extrapolation process for quantities such as the positions and velocities of stars.

Lastly, the modified midpoint method advances a vector of dependent variables $\mathbf{y}(t)$ from time t to $t + dt$ through a sequence of n Leapfrog sub-steps, each of size $h = dt/n$.

3.2 Coupling ISTEDDAS and TSUNAMI

TSUNAMI is completely re-implemented inside ISTEDDAS as a module of it and it runs completely on the CPU. The crucial part of the coupling is the “decision making”, that is the totality of the effective criteria to decide whether a group of stars must be regularized with TSUNAMI, or it is better to leave it within ISTEDDAS. This is

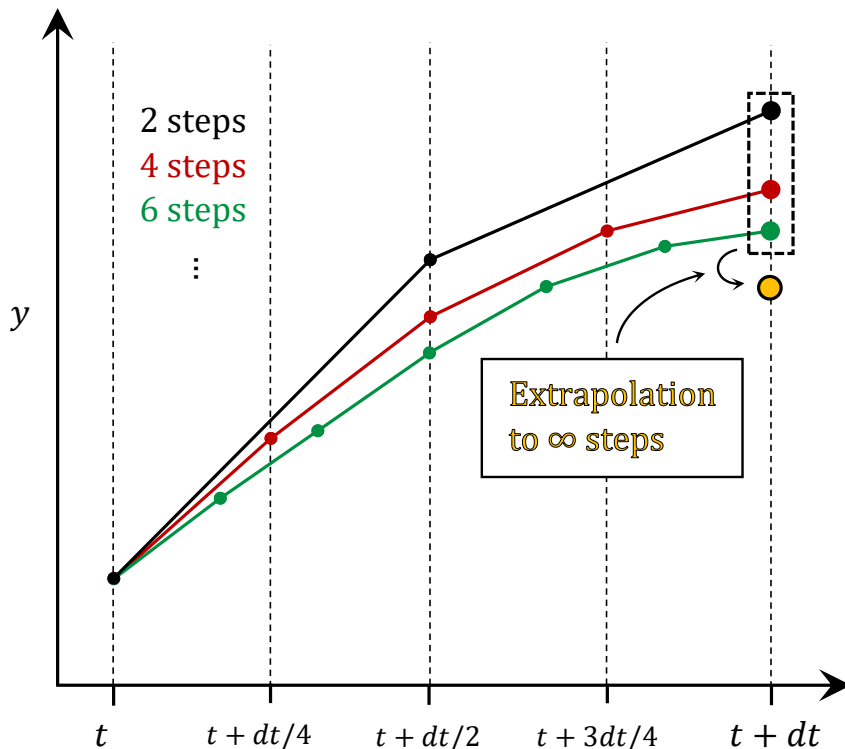


Figure 3.2: Illustration of the Richardson extrapolation within the Bulirsch-Stoer method. The horizontal axis represents time with its step and sub-steps, while the vertical axis, y , symbolizes a generic integrated and extrapolated quantity. In this context, the quantities correspond to the positions and velocities of stars. The integration is repeated with varying sub-step counts, represented by the three example broken lines (black, red, green).

important because TSUNAMI runs entirely on CPU code while ISTEEDAS is designed to run entirely on GPU. Thus, switching-on regularization would imply significant CPU-GPU data transfer, which might become a bottleneck if the decision-making is not carefully implemented.

3.2.1 Decision Making

In ISTEEDAS the decision making is similar to that described in [3, 149], but with some crucial differences. Finding the binary systems in an N -body system is a slow procedure with time complexity $O(N^2)$, but using the already built k -d tree from the Ahmad-Cohen scheme (see Section 2.3) we have it for free since we already know the nearest neighbours of every star in the system. There are two possible systems for which the code decides to integrate a group of stars using TSUNAMI: binary systems or close encounters. Before entering into details, let us define the important length scale

to check the proximity of two stars: the close encounter radius, defined as:

$$R_{cl} = 2 \frac{\bar{m}}{\sigma^2} \eta_r, \quad (3.9)$$

where \bar{m} and σ^2 are the average mass and the velocity dispersion, and η_r is a free parameter used to conveniently adjust R_{cl} . We do not consider the whole N-body system to compute these quantities, but only the nearest $n_{n,max}$ stars (see eq. 2.29), in this way, we are computing the local R_{cl} for each star. In addition, To understand whether two stars are a bound (soft or hard binary) or unbound (close encounter) system we use the total energy, that is:

$$E_{tot} = U + K = -\frac{m_i m_j}{|\mathbf{r}_{ij}|} + \frac{1}{2} m_i |\mathbf{v}_i - \mathbf{v}_{com}|^2 + \frac{1}{2} m_j |\mathbf{v}_j - \mathbf{v}_{com}|^2, \quad (3.10)$$

where U and K are the gravitational potentials and kinetic energy of the two stars, $m_{i,j}$ and $v_{i,j}$ are the masses and the velocities, $v_{com} = (m_i v_i + m_j v_j) / (m_i + m_j)$ is the velocity of the two stars' center of mass, and $|\mathbf{r}_{ij}|$ is the distance between the two stars. The sign of the total energy carries an important physical meaning, a negative E_{tot} is associated with a bound gravitational system, and a positive E_{tot} is associated with an unbound gravitational system. therefore, comparing E_{tot} with the average kinetic energy of the N-body system ($\bar{K} > 0$) we understand the type of bound between the two considered stars:

$$\begin{aligned} E_{tot}/\bar{K} \leq -1 & \quad \text{bound system (hard binary)}, \\ -1 < E_{tot}/\bar{K} < 0 & \quad \text{bound system (soft binary)}, \\ 0 \leq E_{tot}/\bar{K} & \quad \text{unbound system (close encounter)}, \end{aligned}$$

Putting everything together, we have a binary system if two stars are separated by a distance lesser than R_{cl} and they are a hard binary from the energy point of view, while we have a close encounter if two stars are separated by a distance lesser than R_{cl} , they are an unbound system and they are pointing to each other (the dot product between their relative position and velocity is negative). I can finally summarize the conditions as:

$$\begin{aligned} \text{Binary system:} & \quad |\mathbf{r}_{ij}| < R_{cl} \quad \& \quad E_b/\bar{K} \leq 1, \\ \text{Close encounter:} & \quad |\mathbf{r}_{ij}| < R_{cl} \quad \& \quad E_b/\bar{K} \geq 0 \quad \& \quad \mathbf{r}_{ij} \cdot \mathbf{v}_{ij} < 0, \end{aligned}$$

where the vectors \mathbf{r}_{ij} and \mathbf{v}_{ij} are the relative position and velocity of the two stars, and the symbol $\&$ is the logic ‘‘and’’.

Once the code has found two stars for TSUNAMI it also checks if the next nearest star wants to be part of the system. For close encounters, the code simply checks the distance between the extra star and the center of mass of the two stars already in TSUNAMI:

$$|\mathbf{r}_{ij}| < \frac{2}{3} R_{cl}.$$

In this case, we would have a three-body close encounter, however, to add other stars the check is done considering the center of mass of the most bound couple of stars in

the system (called inner binary, the one with minimum E_b). For a binary system, we have the exact same check as above, however, there are other two conditions, based on orbital parameters, for stars to enter TSUNAMI and form a multiple-body system. First of all, the orbital eccentricity between the entering body and the harder binary, and the semi-major axis of the inner binary in the TSUNAMI system are defined as:

$$e = \frac{1}{\mu} \left| \left(|\mathbf{v}_{bk}| - \frac{\mu}{|\mathbf{r}_{bk}|} \right) \mathbf{r}_{bk} - (\mathbf{r}_{bk} \cdot \mathbf{v}_{bk}) \mathbf{v}_{bk} \right|, \quad (3.11)$$

$$a = \frac{m_b}{2} \left(\frac{|\mathbf{v}_{ij}|^2}{2} - \frac{m_b}{|\mathbf{r}_{ij}|} \right)^{-1}, \quad (3.12)$$

where $m_b = m_i + m_j$, $\mu = m_b + m_k$, the quantities labeled with bj are relative to the center of mass of the inner binary (b) and the entering stars (k), and the ones labeled with ij are relative to the stars in the inner binary. The other two exclusive conditions to let a star enter the TSUNAMI integration are relative to the orbit configurations:

$$\begin{aligned} e > 1 (\text{open orbit case}) & \quad \& \quad |\mathbf{r}_{ij}| < R_{cl} \sqrt{0.5 N \mu}, \\ e \leq 1 (\text{close orbit case}) & \quad \& \quad \gamma \geq \gamma_{crit}, \end{aligned}$$

where N is total number of stars in the N-body system, the symbol $\&$ is the logic “and”, and γ is the perturbation parameter defined as:

$$\gamma = \frac{2\bar{m}}{m_b} \left(\frac{a}{|\mathbf{r}_{ij}|} \right)^3, \quad (3.13)$$

$\gamma_{crit} = 2^{-6} = 0.015625$ is a fixed parameter, \bar{m} is the average mass of the N-body system and m_b is the mass of the binary system.

At the end of this selection, we could have one or multiple systems of stars that need to be integrated with the ARChain algorithm, those systems will be called regularized systems in the rest of this thesis. Inside TSUNAMI the stars will be shifted in the center of mass reference frame, while in ISTEEDAS the center of mass of the regularized system takes the place of one of those stars and it is evolved with the Hermite integrator, the other stars become “ghost” particles with $m = 0$.

It is crucial to identify, and carefully take care of, another set of stars, that is the perturbers. They will have two roles: they will enter the TSUNAMI integration as differential external accelerations during the Leapfrog and will be checked to see if new stars need to be part of the regularized system. The perturbers are selected among the nearest bodies for each regularized system using the perturbation parameter defined above (eq. 3.13):

$$\gamma > \gamma_{pert},$$

where $\gamma_{pert} = 10^{-6}$ is a fixed parameter.

The final part of the decision-making is the termination conditions, that is the checks that establish whether a star will continue to be integrated using the ARChain or will go back to the Hermite integrator. For binary systems there is a single condition to break the regularization:

$$|\mathbf{r}_{ij}| > 2 R_{cl}.$$

In contrast, for multiple stars systems, a particle can exit the regularization if the following 3 conditions are satisfied:

$$![e < 1 \quad \& \quad |\mathbf{r}_{bj}| < 10 R_{cl}] , \quad (3.14)$$

$$\mathbf{r}_{bj} \cdot \mathbf{v}_{bj} > 0 , \quad (3.15)$$

$$\gamma < \gamma_{crit} , \quad (3.16)$$

where the symbol $\&$ is the logic “and”, and the symbol $!$ is the logic negation. The first condition is important for the hierarchical system in which a third body has a very eccentric and elongated orbit, we want to avoid the body entering and exiting the regularization at each orbit (see Fig.5.7). The second condition is to ensure that the body is moving away from the harder binary, while the third condition is, again, a threshold on the perturbation parameter. After the termination, the exiting stars will regain their mass in ISTEDDAS and, if the regularized system survives, the center of mass coordinate is updated accordingly.

3.2.2 Time synchronization with the block time-step method

The block time-steps method (see Section 2.2) is a powerful addition to ISTEDDAS, as it significantly increase the performance of the code without losing accuracy. The centers of mass of the regularized systems are always considered without neighbours in ISTEDDAS ($r_{neigh} = 0$), therefore they have always single time-step (Δ_{far}). When the center of mass does a step in ISTEDDAS, the regularized system relative to the center of mass is integrated simultaneously in TSUNAMI on the same time-step. However, the TSUNAMI works with the regularized time coordinate, which is not quantized as the time step of the centre of mass and is related to physical time through the integral Equation 3.2. Thus, synchronizing the integration time of the regularized system and that of the associated centre of mass results in potential time-synchronization errors. To fix this issue, I implemented the following strategy: the ARChain integrator stops right after the physical time step that overpasses the centre of mass step, and the initial quantities of this last step are used to re-initialize the integrator that will run again for the remaining amount of time using a normal Leapfrog $((\alpha, \beta, \gamma) = (0, 0, 1))$. In this way, the last piece of time before the synchronization with ISTEDDAS is done without regularization (the algorithm can not change the time-step), and the ARChain ends the integration exactly at the desired time. However, using this method results, sometimes, in a slightly wrong computation of the orbits in the final step, especially when the regularized system is very tight or very eccentric, and this, after a long integration, accumulates a lot of errors on the energy of the system. Therefore, I implement another strategy to solve the synchronization problem without losing precision: as before, the ARChain integrator stops right after the step that overpasses the desired time, and the initial quantities of this last step are used to re-initialize the integrator that will run again for the remaining amount of time but forcing the time-step to be roughly an order on magnitude smaller than the one computed by the integrator. If the desired final time is surpassed without reaching the desired precision, the previous step is retrieved and the timestep is decreased again. I keep adjusting these final time-steps

to reach the convergence at the ISTEEDDAS time-step within a certain small threshold. This strategy does not take more time with respect to the other described strategy and completely solves the synchronization problem without losing the accuracy of the ARChain integrator.

3.2.3 Parallelization

TSUNAMI runs on CPU and, in order to speed it up, I parallelize it using OpenMP, however, it is important to stress that also the ANN library is running in parallel using OpenMP. Thus, I use the OpenMP tasks: the entire ISTEEDDAS loop is run by the master thread of OpenMP on each node, then, when the simulation needs a tree-search, or to integrate a system in TSUNAMI, a task is open by the master thread, that spawns the needed amount of threads to parallelize the operation. Using an OpenMP task is a good strategy since the master thread can go on in the simulation while the spawned threads keep working in parallel. Thus, even if both the two operations are needed, the two different tasks will spawn different threads to run them in parallel with each other. While the ANN library must do its search before the new computation of forces, and so it needs a barrier before the forces-evaluation kernel on GPU, TSUNAMI is free to run independently from ISTEEDDAS. Because of this, the TSUNAMI threads do not need any barrier and can run asynchronously with the GPU for multiple ISTEEDDAS steps until their next synchronization with the ISTEEDDAS time-step, which can happen, borderline, after a single step of ISTEEDDAS. Each thread of TSUNAMI will run one regularized systems, or multiple if they are too many to evolve. Since each system will have its own time-step in ISTEEDDAS, the entire OpenMP task will synchronize with ISTEEDDAS when the regularized system with the faster time-step will be synchronized with the ISTEEDDAS time-step.

Chapter 4

The population-synthesis code SEVN

In an N-body code, the evolution of single and binary stars can be implemented following different approaches. A possible strategy is to use a stellar evolution code (e.g., PARSEC [45, 54, 55, 62, 217, 276]) to evolve stars every time that is needed, but this is a very slow approach because stellar evolution codes are very sophisticated and need to integrate the equations for the internal structure of stars, at each step. Another strategy is to use fitting formulas for all the stellar parameters. This approach is very fast but the generation of such formulas is very complicated and time-consuming since, each time a stellar prescription has to be updated, all the formulas must be re-derived from scratch. Therefore, it would be hard to keep up with the state-of-the-art stellar evolution prescriptions. In contrast, a look-up table-based population-synthesis code uses pre-evolved stellar evolution tracks that are provided in the form of look-up tables, for a grid of masses and metallicities, which are read and interpolated on the fly. This strategy has two crucial advantages: (i) it is computationally very fast, and (ii) users can easily switch to a different set of look-up tables, thus investigating the impact of different stellar evolution prescriptions is possible without changing any lines in the code. ISTEEDAS is designed to be interfaced with the SEVN population-synthesis code. In this chapter, I will give an overview of the strategies adopted in our code to implement single and binary stellar evolutionary processes. Moreover, I will describe SEVN following [136].

4.1 SEVN description

SEVN (short for “Stellar EVolution for N-body”) stands as a rapid binary population synthesis code, employing interpolated pre-calculated stellar tracks sets for stellar evolution computations [136, 192, 268–270]. The evolution is characterized by analytical and semi-analytical prescriptions, enhancing the code’s versatility and generality. One key advantage lies in the ease with which stellar evolution models in SEVN can be modified or upgraded by simply loading a new set of look-up tables at runtime. This flexibility extends to the ability to select stellar tables dynamically without necessitating alterations to the code’s internal structure or recompilation. While the present iteration of SEVN shares fundamental concepts with its predecessors (as seen

in [268, 270]), the code has undergone comprehensive refactoring, featuring enhancements in various aspects such as time step and modularity. Additionally, it has been enriched with new functionalities and options, incorporating the latest PARSEC stellar evolution tracks [45, 54, 55, 62, 217, 276]. Developed entirely in C++ without external dependencies, SEVN adheres to the object-oriented programming paradigm and harnesses CPU parallelization through OpenMP. Figure 4.1 illustrates a schematic overview of the essential SEVN components and their interrelations. The subsequent subsections delve into a comprehensive exploration of SEVN’s main features and options. For accessibility, SEVN is publicly accessible at the provided [link](#).

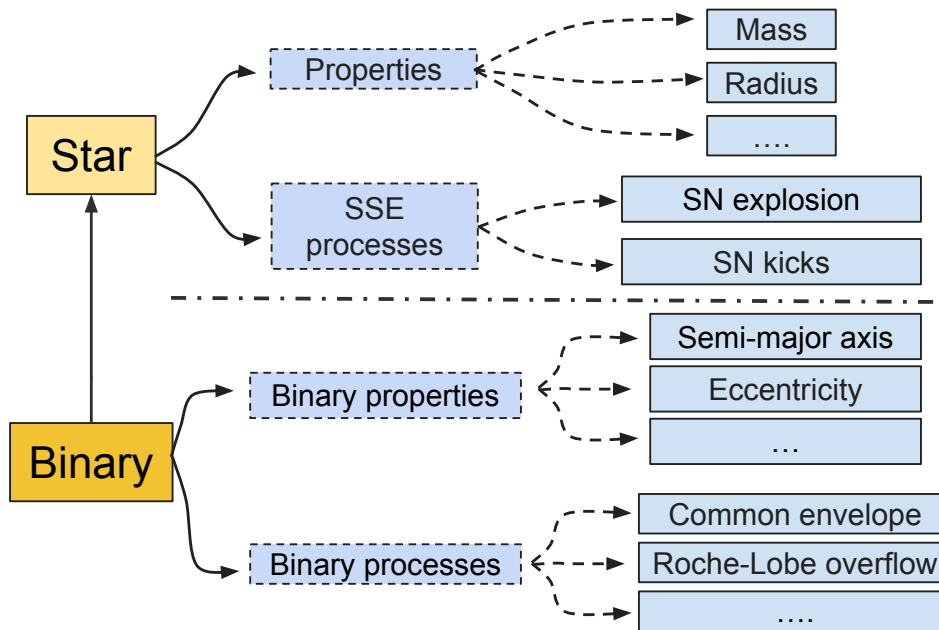



Figure 4.1: In SEVN, single stars, binary systems, properties, and processes are represented with C++ classes. Single stars are characterized by their properties (mass, radius, ...) and single stellar evolution processes (supernova explosion type and natal kicks). Binary stars are characterized by their properties (semi-major axis, eccentricity, ...), binary-evolution processes (mass transfer by winds, Roche-lobe overflow, CE, tides, ...), and by the two stars component of the binary system. (Image credit: [136] )

4.1.1 Single stars evolution

In the following subsections, I am going to describe the main ingredients used in SEVN to integrate stellar evolution from the ZAMS to the formation of the compact remnant.

Stellar evolution tables

The stellar-evolution tables within SEVN encapsulate the progression of properties for a defined set of stellar tracks characterized by their initial mass M_{ZAMS} and metallicity Z . To function optimally, SEVN necessitates two distinct table sets as input: one tailored for stars initiating their lifecycle from the hydrogen main sequence (MS, referred to as H stars), and the other tailored for stars depleted of hydrogen (referred to as pure-He stars). It is assumed within SEVN that the stellar models inherently incorporate wind mass loss.

SEVN tables				
Table	Units	Type	Interpolation	
Time	Myr	M	R	
Phase*	Myr	M	R	
Mass	M_{\odot}	M	LIN	
Luminosity	L_{\odot}	M	LOG	
Radius	R_{\odot}	M	LOG	
He-core mass	M_{\odot}	M	LIN	
CO-core mass	M_{\odot}	M	LIN	
He-core radius	R_{\odot}	O	LIN	
CO-core radius	R_{\odot}	O	LIN	
Stellar inertia	$M_{\odot}R_{\odot}^2$	O	LOG	
Envelope binding energy	$M_{\odot}^2R_{\odot}^{-1}G^{-1}$	O	LOG	
Surface abundances (H,He,C,N,O)	mass fraction	O	LIN	
Convective envelope				
Mass	normalized to star mass	O	LIN	
Depth	normalized to star radius	O	LIN	
Turnover time	yr	O	LIN	

Table 4.1: Summary of the stellar evolution tables used in SEVN. The first column reports the property stored in the table, the second column its units and the third column specifies if a table is mandatory (M) or optional (O). SEVN includes analytic recipes to replace the optional tables if they are not available. The fourth column indicates the type of weights used by SEVN during the property interpolation: rational (R), linear (LIN), log (LOG). * The phase table reports the starting time of each SEVN phase (Table 4.2). The envelope binding energy is normalized over the gravitational constant G (assumed in solar units and years). Table credit: [136].

Table 4.1 provides an overview of the tables incorporated in SEVN. Each stellar evolution model encompasses (at least) seven tables categorized by metallicity, and these tables for each metallicity are stored in distinct directories. Each table corresponds to a specific stellar property, with seven obligatory tables representing key stellar attributes: time, total stellar mass, He-core mass, CO-core mass, stellar radius, bolometric luminosity, and stellar phase. Every row in these tables represents a star

characterized by a given M_{ZAMS} and Z , and each column stores the property value at the time corresponding to the identical row and column in the time table. The initial column of each row in the mass table designates the M_{ZAMS} of the star. The stellar phase table denotes the initiation time for various stellar phases, while SEVN implicitly considers the conclusion of the evolution (i.e., stellar lifetime) to be equivalent to the last reported value in the time tables. Optionally, additional properties like He and CO core radii, envelope binding energy, and convective envelope properties (mass, extension, eddy turnover timescale) can be included. In the absence of these optional tables, SEVN computes these properties using alternative analytical approximations. Although non-mandatory, these tables offer crucial information not commonly found in most stellar-evolution tracks, significantly contributing to the accurate modeling of various evolutionary processes. For instance, convective envelope properties aid in identifying evolutionary phases, estimating mass transfer stability, and playing a pivotal role in determining the efficiency of stellar tides. The modular design of SEVN facilitates the seamless integration of new tables to monitor the evolution of additional stellar properties. Importantly, SEVN refrains from assuming a specific definition for the mass and radius of He and CO cores, deferring to the adopted stellar evolution models or user choices in generating SEVN tables for these estimations.

TRACKCRUNCHER

The most important requirement for the tables lies in their ability to encompass all critical aspects of the stellar tracks from which they originate. Simultaneously, these tables must remain as compact as possible, typically within a few megabytes each, to facilitate swift interpolation and mitigate memory costs. To meet these criteria, TRACKCRUNCHER code was developed and employed to efficiently generate tables for SEVN. This code identifies the pertinent properties to be stored in SEVN tables from a given set of stellar tracks while estimating the initiation times of SEVN phases. Furthermore, TRACKCRUNCHER strategically determines which time steps from the original tracks can be omitted in the final tables to minimize table size. Specifically, only those time steps ensuring errors below 2% in a linear interpolation for modeling stellar property evolution are retained in the final tables. This undersampling of tracks substantially reduces table size from the order of gigabytes to around tens of megabytes. For instance, the complete set of tables for H stars (pure-He stars) utilized in this study occupies approximately ~ 30 MB (~ 10 MB), compared to the original tracks consuming around ~ 5 GB (~ 6 GB) of disk space. This process significantly diminishes both the storage requirements and runtime memory footprint of SEVN while concurrently expediting individual stellar evolution computations. TRACKCRUNCHER is openly accessible at the provided [link](#). It is optimized at processing outputs from PARSEC[45], FRANEC [166], and the mist stellar tracks [56], with adaptability for extension to other stellar evolution codes. Additionally, TRACKCRUNCHER serves as a tool for compressing and reducing the memory size of stellar tracks.

Stellar phases

The enhancement of stellar evolution property interpolation is notable when employing the percentage of a star’s lifespan rather than the absolute time value, as discussed in [270]. To further refine interpolation, the percentage of life is assessed within three primary stellar macro-phases: the H phase, the He phase, and the CO phase. In the current iteration of SEVN, the definition of macro-phases has been refined to encompass seven physically motivated phases. The initial phase, spanning from time 0 to the ignition of hydrogen burning in the core, is designated as the pre-main sequence (PMS, phase id = 0). Core-hydrogen burning characterizes the main sequence (MS, phase id = 1) until the He core initiates growth, leading the star into the terminal-age MS (TAMS, phase id = 2). Subsequent phases include shell H burning (SHB, phase id = 3) when hydrogen in the core is depleted, core He burning (CHeB, phase id = 4) at the ignition of core helium burning, terminal-age core He burning (TCHeB, phase id = 5) with a CO core present, and shell He burning (SHeB, phase id = 6), beginning when the core’s helium is exhausted. The remnant phase (id = 7) initiates when the evolution time exceeds the star’s lifetime, signifying its transition into a compact remnant. Throughout its evolution, a star may lose its hydrogen envelope due to effective stellar winds or binary interactions. If the He-core mass exceeds 97.9% of the total stellar mass, SEVN categorizes the star as a Wolf-Rayet (WR) star, transitioning to a new interpolating track on the pure-He tables. Pure-He stars in SEVN correspond to naked-He stars in other population synthesis codes derived from BSE [131]. During binary evolution, an evolved pure-He star may shed its He envelope, becoming a naked-CO star in SEVN, considered as a compact remnant-like object. The correspondence between SEVN stellar phases and BSE stellar types [130] is summarized in Table 4.2.

Interpolation

The code utilizes interpolation to estimate the properties of each star at a given time. Upon initialization, SEVN assigns four interpolating tracks from the hydrogen or pure-He look-up tables to a star. These tracks encompass two different metallicities (Z_1, Z_2) and four distinct ZAMS masses ($M_{\text{ZAMS},1}, M_{\text{ZAMS},2}, M_{\text{ZAMS},3}, M_{\text{ZAMS},4}$, two per metallicity). The selection criteria are defined as $M_{\text{ZAMS},1/3} \leq M_{\text{ZAMS}} < M_{\text{ZAMS},1}$ and $Z_1 \leq Z < Z_2$, where M_{ZAMS} and Z denote the ZAMS mass and the metallicity of the target star. In cases where M_{ZAMS} and/or Z match the maximum values in the tables, $M_{\text{ZAMS},1/3} \leq M_{\text{ZAMS}} < M_{\text{ZAMS},1}$ and $Z_1 \leq Z < Z_2$ are employed. The estimation of a given interpolated property W (e.g., stellar mass) is determined by the formula:

$$W = \frac{Z_2 - Z}{Z_2 - Z_1} W_{Z,1} + \frac{Z - Z_1}{Z_2 - Z_1} W_{Z,2}, \quad (4.1)$$

where

$$\begin{aligned} W_{Z,1} &= \beta_1 W_{\text{ZAMS},1} + \beta_2 W_{\text{ZAMS},2}, \\ W_{Z,2} &= \beta_3 W_{\text{ZAMS},3} + \beta_4 W_{\text{ZAMS},4}, \end{aligned} \quad (4.2)$$

and $W_{\text{ZAMS},i}$ represents the property W values in the interpolating tracks with $M_{\text{ZAMS},i}$, while β denotes interpolation weights. SEVN incorporates three interpolation weights:

Phase	Phase ID	Remnant phase	Remnant ID	BSE stellar-type equivalent
PMS	0	–	0	not available
MS	1	–	0	1 if $f_{conv} < 0.8$, else 0
TAMS	2	–	0	2 if $f_{conv} < 0.33$, else 3
SHB	3	–	0	
CHeB	4	–	0	7 if WR, else 4
THeB	5	–	0	7 if WR, else: 4 if $f_{conv} < 0.33$, else 5
SHeB	6	–	0	8 if WR, else: 4 if $f_{conv} < 0.33$, else 5
Remnant	7	HeWD	1	10
		COWD	2	11
		ONeWD	3	12
		ECNS	4	13
		CCNS	5	13
		BH	6	14
		No compact remnant	–1	15

Table 4.2: SEVN stellar evolutionary phases (Column 0), identifiers (Column 1), and remnant types (Column 2). Column 3 shows the correspondence to BSE [130, 131] stellar types: 0, low-mass main sequence (MS); 1, main sequence (MS); 2, Hertzsprung-gap (HG); 3, first giant branch (GB); 4, core-helium burning (CHeB); 5, early asymptotic giant branch (EAGB); 7, naked-helium MS (HeMS); 8, naked-helium HG (HeHG). The BSE stellar types 6 (thermally pulsating AGB) and 9 (naked-helium giant branch) do not have a correspondent SEVN phase. ECNS and CCNS are NSs produced by electron capture and core-collapse supernovae, respectively. f_{conv} is the mass fraction of the convective envelope over the total envelope mass (total mass in case of MS stars), WR indicates Wolf-Rayet (WR) stars, i.e., stars which have a He core mass larger than 97.9% of the total mass. Table credit: [136].

linear, logarithmic, and rational (see [136] for extra details). Linear weights are utilized for most properties, while logarithmic weights are applied to properties stored and interpolated in logarithmic scales, such as radius and luminosity. The rational weights [270] notably enhance interpolation, particularly in estimating the starting times of stellar phases and the overall star lifetime.

Upon initialization, SEVN employs Eqs. 4.1 and 4.2 to set the starting times of stellar phases, denoted as $t_{start,p}$, with $W_{ZAMS,i}$ representing the phase times from the phase table. The stellar lifetime is similarly interpolated, assuming the last element in the SEVN time table establishes the stellar lifetime. For other properties, W needs to be estimated at a given time t . The corresponding $W_{ZAMS,i}$ in the tables is not determined at the same absolute time t but at the same percentage of life in the phase of the interpolated star:

$$\Theta_p = \frac{t - t_{start,p}}{t_{start,p_{next}} - t_{start,p}}, \quad (4.3)$$

where $t_{start,p}$ is the starting time of the current phase p , and $t_{start,p_{next}}$ denotes the starting time of the next phase p_{next} . Consequently, SEVN evaluates $W_{ZAMS,i}$ at time:

$$t_i = t_{start,p,i} + \Theta_p \Delta_{p,i}, \quad (4.4)$$

where $t_{start,p,i}$ and $\Delta_{p,i}$ represent the starting time and time duration of the current phase for the interpolating track. In practice, SEVN uses Eq. 4.3 to compute times for each of the fourth interpolating tracks. It then estimates $W_{ZAMS,i}$ in Eq. 4.2 by linearly interpolating the values stored in the tables. The division into phases ensures that all interpolating stars share the same internal structure, such as the presence or absence of a core.

Spin evolution

The modeling of stellar rotation in SEVN involves three key properties. The primary variable tracked is the spin angular momentum, denoted as J_{spin} . The angular velocity, Ω_{spin} , is derived from J_{spin} as $\Omega_{spin} = J_{spin} I^{-1}$, where I represents the inertia. The spin parameter, ω_{spin} , is then estimated as the ratio of Ω_{spin} to the critical angular velocity, Ω_{crit} , given by $\Omega_{crit} = \sqrt{GM(1.5R)^{-3}}$, where G is the gravitational constant, and M and R are the stellar mass and radius. The code calculates stellar inertia using the formula proposed by [131]:

$$I = 0.1 (M - M_c) R^2 + 0.21 M_c R_c^2. \quad (4.5)$$

Here, M_c denotes the core mass, and R_c represents the core radius. The initial rotation of the star is determined by the input value of ω_{spin} . Throughout the evolution, a portion of the stellar angular momentum is removed through stellar winds and magnetic braking [242]. Stellar winds are modeled as [131]:

$$\dot{J}_{spin,wind} = \frac{2}{3} \dot{M}_{wind} R^2, \quad (4.6)$$

where \dot{M}_{wind} denotes the wind mass loss rate, and magnetic braking is expressed as:

$$\dot{J}_{spin,mb} = -5.83 \times 10^{-16} \frac{M_{env}}{M} (\Omega_{spin} R^3) M_\odot R_\odot^2 \text{yr}^{-2}. \quad (4.7)$$

Here, M_{env} represents the envelope mass of the star, and magnetic braking is inactive if the star lacks a core. In each time-step, the spin angular momentum is reduced according to Eqs. 4.6 and 4.7. The constraint is imposed that J_{spin} cannot become negative. Following the adjustment of angular momentum, SEVN updates angular velocity and spin. If the spin surpasses unity (indicating over-critical rotation), the angular momentum is reset to the value for which $\Omega_{spin} = \Omega_{crit}$. Notably, this work does not consider the amplification of mass loss in stars approaching critical rotation, and mass accretion on critically rotating stars is not halted. The stellar tracks employed in this study are computed for non-rotating stars. While this may seem inconsistent, it is a necessary approach to account for spin-dependent binary evolution processes, such as stellar tides. Given the adaptability of SEVN, future investigations can seamlessly incorporate rotating stellar tracks (e.g., [217]) to explore the impact of stellar rotation on stellar and binary evolution, as well as compact object formation (e.g., [192, 195]).

4.1.2 Compact remnant formation

A compact remnant emerges when the evolutionary time surpasses the stellar lifespan. Based on the final mass of the CO core ($M_{CO,f}$), SEVN can initiate the formation of a white dwarf (WD), if $M_{CO,f} < 1.38M_{\odot}$, an electron capture supernova (ECSN) leading to a neutron star (NS) for $1.38M_{\odot} \leq M_{CO,f} < M_{Ch}$, where $M_{Ch} = 1.44M_{\odot}$ denotes the Chandrasekhar mass, or a core-collapse supernova (CCSN) resulting in a NS or a black hole (BH) for $M_{CO,f} \geq M_{Ch}$. In the case of WD formation, the final mass and subtype are determined as follows. If the ZAMS mass (M_{ZAMS}) of the current interpolating track is below the helium flash threshold mass (approximately $2M_{\odot}$ [130]), the WD is a helium WD (HeWD) with a mass equal to the final helium mass of the progenitor star, $M_{He,f}$. Otherwise, if $M_{He,f} < 1.6M_{\odot}$, the compact remnant is a carbon-oxygen WD (COWD), otherwise, it is an oxygen-neon WD (ONeWD) [130]. The radius and luminosity of the WD are determined as per [130, 287]:

$$L_{WD} = \frac{635MZ^{0.4}}{[A(t+0.1)]^{1.4}}, \quad (4.8)$$

$$R_{WD} = \max \left(R_{NS}, 0.0115 \sqrt{\left(\frac{M_{Ch}}{M_{WD}}\right)^{2/3} - \left(\frac{M_{WD}}{M_{Ch}}\right)^{2/3}} \right). \quad (4.9)$$

Here, t represents the age since formation, A is the effective baryon number for the WD composition (for HeWD $A = 4$, for COWD $A = 15$, and for ONeWD $A = 17$), and in SEVN, the radius of the NS is set to $R_{NS} = 11$ km. In the case of an ECSN occurrence (e.g., [146, 297]), the star leaves behind a NS (ECNS, see Table 4.2). The mass of the NS depends on the chosen supernova model.

Core-collapse supernova

SEVN employs two models for core-collapse supernovae, distinguished as the delayed and rapid models [96]. The primary difference lies in the revival time of the shock: < 250 ms for the rapid model and > 500 ms for the delayed model. If the final carbon-oxygen core mass $M_{CO,f} \geq 11M_{\odot}$ (in both models) or $6M_{\odot} \leq M_{CO,f} < 7M_{\odot}$ (in the rapid model only), the star undergoes direct collapse to form a black hole (BH). In such instances, the mass of the compact remnant equals the pre-supernova mass of the progenitor, M_f , with adjustments for neutrino mass loss. In other scenarios, where the core-collapse supernova explosion is successful, a certain amount of fallback occurs. Consequently, the final remnant mass depends on $M_{CO,f}$ (which determines the fallback fraction) and M_f [96]. Ultimately, the compact remnant is classified as a neutron star (NS, CCNS, Table 4.2) if the final mass is below $3M_{\odot}$ and as a BH otherwise.

In the absence of a reliable astrophysical model for NS masses, SEVN adopts a default toy model: it samples the masses of all NSs (resulting from ECSNe or CCSNe) from a Gaussian distribution centered at $1.33M_{\odot}$ with a standard deviation of $0.09M_{\odot}$. This choice is based on a fit to the masses of Galactic binary neutron stars (BNSs) [147, 224, 225]. However, with this toy model, NSs with a mass greater than $1.6M_{\odot}$ are

rare, a crucial feature for accurately reproducing the primary masses of both GW170817 [11] and GW190425 [10]. The minimum NS mass is fixed at $1.1M_{\odot}$.

The default NS radius is set to $M_{NS} = 11$ km [49], while the bolometric NS luminosity follows the prescription from [130]:

$$L_{NS} = \frac{0.02M^{2/3}}{[\max(t, 0.1)]^2}. \quad (4.10)$$

The BH radius is determined by the Schwarzschild radius, $R_{BH} = R_S = 2GM_{BH}/c^2$, where c is the speed of light. The BH luminosity is set to an arbitrarily small value ($10^{-10}L_{\odot}$ [130]).

Pair instability and pulsational pair instability

Massive stars ($M_{He,f} \gtrsim 32M_{\odot}$, nearing the conclusion of carbon burning) actively generate electron-positron pairs within their core. The inception of pair creation diminishes central pressure, inducing a hydrodynamical instability that leads to core contraction and the explosive ignition of oxygen, or even silicon. This process initiates a sequence of pulses intensifying mass loss, known as pulsational pair-instability (PPI) [313, 315, 317]. Following these pulses, the star returns to hydrostatic equilibrium, progressing in its evolution until the eventual collapse of the iron core [313, 314]. At higher core masses ($64 \lesssim M_{He,f} \lesssim 135$, concluding carbon burning), a robust single pulse dismantles the entire star, leaving no compact remnant—a phenomenon termed a pair-instability supernova (PISN) [28, 41, 120, 220]. In cores with very high masses ($M_{He,f} \gtrsim 135M_{\odot}$), pair instability induces the direct collapse of the star. SEVN incorporates two new models for PPIs and PISNe: M20 and F19. M20 is a reimplementation of the model introduced in the earlier version of SEVN [192], based on a fit by [268] to black hole masses derived from 1D hydrodynamical simulations [313]. PPI occurs if the pre-supernova He-core mass, $M_{He,f}$, lies within $32M_{\odot}$ and $64M_{\odot}$, while PISN is triggered for $64 \leq M_{He,f}/M_{\odot} \leq 135$. Beyond $M_{He,f} = 135M_{\odot}$, the star directly collapses to form a black hole, resulting in an intermediate-mass black hole. PISNe leave no compact remnant, and the final mass of the compact remnant after PPI (M_{PPI}) is derived by adjusting the black hole mass predicted by the chosen core-collapse supernova model (M_{CCSN}):

$$M_{PPI} = \begin{cases} \alpha_P M_{CCSN} & \text{if } \alpha_P M_{CCSN} \geq 4.5M_{\odot} \\ 0 & \text{if } \alpha_P M_{CCSN} < 4.5M_{\odot} \end{cases}. \quad (4.11)$$

The correction factor α_P relies on $M_{He,f}$ and the pre-supernova mass ratio between the mass of the He core and the total stellar mass [192]. α_P can assume values from 1 to 0 (with 0 indicating a PISN). If $\alpha_P M_{CCSN} < 4.5M_{\odot}$, a PISN is triggered, resulting in a zero-mass compact remnant. The threshold of $4.5M_{\odot}$ is based on the least massive black hole formed in the simulations by [313]. Model F19, based on MESA simulations of pure-He stars [86], associates the pre-supernova mass of the CO core, $M_{CO,f}$, as a reliable indicator for the activation of PISNe and PPIs. In this model, PPI occurs

if $38 \leq M_{CO,f}/M_{\odot} \leq 60$, while the PISN regime begins at $M_{CO,f} > 60M_{\odot}$. The He-mass threshold for pair-instability leading to the direct collapse of a very massive star is approximately $M_{He} \approx 130 - 135M_{\odot}$ for their fiducial value of the $^{12}C(\alpha, \gamma)^{16}O$ reaction rate [86, 313]. Therefore, SEVN adopts a threshold $M_{He,f} = 135M_{\odot}$ for the transition between PISN and direct collapse in both F19 and M20 models. In both models, a PISN explosion leaves no compact remnant. The compact remnant mass in the PPI regime for model F19 is estimated as

$$M_{PPI} = \min(M_f, M_{F19}) , \quad (4.12)$$

where M_f is the pre-supernova mass of the exploding star, and M_{F19} is the mass of the black hole according to [86]:

$$M_{BH} = \begin{cases} 4 + M_{CO,f} & M_{CO,f} < 38M_{\odot} \\ a_1 M_{CO,f}^2 + a_2 M_{CO,f} + a_3 \log_{10}(Z) + a_4 & 38M_{\odot} \leq M_{CO,f} \leq 60M_{\odot} , \\ 0 & 60M_{\odot} < M_{CO,f} \end{cases} \quad (4.13)$$

where $a_1 = -0.096$, $a_2 = 8.564$, $a_3 = -2.07$, $a_4 = -152.97$. Since only pure-He stars were simulated, SEVN implicitly assumes that the first pulse completely removes any remaining hydrogen layer in the star. This assumption is reasonable, as the binding energy of the envelope in the late evolutionary stages ($\lesssim 10^{48} - 10^{49}$ erg [136]) is lower than the energy liberated during a pulse ($\gtrsim 10^{49}$ erg [313]). In all PPI/PISN models used in SEVN, if the correction for pair-instability results in a zero-mass compact remnant, the remnant is classified as ‘‘No compact remnant’’ (Table 4.2).

Neutrino mass loss

Irrespective of the supernova mechanism, in order to correctly estimate the final mass of the compact remnants is essential to incorporate neutrino mass loss. In SEVN, the following correction is implemented [161, 324]:

$$M_{rem} = \max \left[\frac{\sqrt{1 + 0.3M_{rem,bar}} - 1}{0.15}, (M_{rem,bar} - 0.5M_{\odot}) \right] , \quad (4.14)$$

where M_{rem} and $M_{rem,bar}$ represent the gravitational and baryonic mass of the compact remnant, respectively. It’s important to note that this correction is not applied to the default model for neutron star (NS) masses in SEVN. The default NS mass model involves drawing masses from a Gaussian distribution, which is already fitted to Galactic binary neutron star (BNS) masses [224]. As a result, there is no need for an additional correction to account for neutrino loss.

Supernova kicks

Following a supernova event, whether electron capture supernova (ECSN) or core-collapse supernova (CCSN), the compact remnant experiences a natal kick. SEVN

incorporates three formalisms for the natal kick. In the first model (K σ 265), the kick magnitude V_{kick} is drawn from a Maxwellian curve with a one-dimensional root-mean-square (rms) value of σ_{kick} , and the kick direction is drawn from an isotropic distribution. The kick is assumed in an arbitrary Cartesian frame of reference where the compact remnant is at rest. The default 1D rms, $\sigma_{\text{kick}} = 265 \text{ km s}^{-1}$, is based on the proper motions of young Galactic pulsars [127]. In the second model, the impact of reducing the kick dispersion is studied by setting $\sigma_{\text{kick}} = 150 \text{ km s}^{-1}$. In the third model (KGM20), the kick magnitude is estimated as

$$V_{\text{kick}} = f_{H05} \frac{\langle M_{\text{ej}} \rangle}{M_{\text{rem}}} \frac{M_{\text{ej}}}{\langle M_{\text{ej}} \rangle}, \quad (4.15)$$

where f_{H05} is a random number drawn from a Maxwellian distribution with $\sigma_{\text{kick}} = 265 \text{ km s}^{-1}$; $\langle M_{\text{NS}} \rangle$ and $\langle M_{\text{ej}} \rangle$ are the average NS mass and ejecta mass from single stellar evolution, respectively, while M_{rem} and M_{ej} are the compact object mass and the ejecta mass [109]. The calibration of $\langle M_{\text{ej}} \rangle$ values is conducted using single stellar SEVN simulations at $Z = 0.02$ and assuming a Kroupa initial mass function. In this model, ECSNe and stripped (pure-He pre-supernova stars)/ultra-stripped (naked CO pre-supernova stars) supernovae naturally yield smaller kicks compared to non-stripped CCSNe due to the lower amount of ejected mass [279, 280]. BHs originating from a direct collapse receive zero natal kicks from this mechanism.

In a binary system, natal kicks induce changes in orbital properties, the relative orbital velocity, and the center of mass of the binary (see [131]). Following the kick, the orbital properties of the binary are updated, considering the new relative orbital velocity and the new total mass in the binary. If the semi-major axis is smaller than 0 and/or the eccentricity is larger than 1, the binary does not survive the kick. The center-of-mass velocity and the orbital properties of the binary system change even without natal kicks (i.e., after WD formation or direct collapse) due to the mass lost by the system at the formation of the compact remnant (the so-called Blaauw kick [39]).

4.1.3 Binary stars evolution

SEVN includes the following binary evolution processes: wind mass transfer, Roche-lobe overflow (RLO), common envelope (CE), stellar tides, circularisation at the RLO onset, collision at periastron, orbit decay by GW emission, and stellar mergers.

Wind mass transfer

In the context of SEVN, the assumption is made that the stellar tracks already account for wind mass loss, thus ensuring a self-consistent treatment of wind mass loss in single stellar evolution. Within SEVN, consideration is given to the potential accretion of mass and angular momentum by the stellar companion (accretor) from the mass lost by the donor star. Following the formalism established in [131], the orbit-averaged accretion rate is determined using the Bondi accretion mechanism [42]

and the fast wind approximation (wind velocity exceeding orbital velocity). In this scenario, the mass accretion rate \dot{M}_a is expressed as

$$\dot{M}_a = -\frac{\alpha_{wind}}{\sqrt{1-e^2}} \left(\frac{GM_a}{V_{wind}^2} \right)^2 \frac{\dot{M}_d}{2a^2 (1+V_f^2)^3 / 2}, \quad (4.16)$$

where \dot{M}_d represents the wind mass loss rate of the donor star, a denotes the binary system's semi-major axis, and V_{wind} and V_f respectively stand for the wind velocity and the ratio between the characteristic orbital velocity and the wind velocity, defined as

$$V_{wind}^2 = 2\beta_{wind} \frac{GM_d}{R_{eff}}, \quad (4.17)$$

$$V_f^2 = G \frac{G(M_d + M_a)}{aV_{wind}^2}. \quad (4.18)$$

Here, R_{eff} signifies the stellar effective radius, defined as the minimum between the star's radius and its Roche lobe (RL) radius. The mass parameters, M_d and M_a , refer to the donor and accretor masses, respectively. The default dimensionless wind parameters are set as $\alpha_{wind} = 1.5$ (appropriate for Bondi-Hoyle accretion [131]) and $\beta_{wind} = 0.125$ (derived from observations of cool super-giant stars [131, 157]).

In eccentric orbits, Eq. 4.16 may predict an accreted mass exceeding the actual wind mass loss from the donor. To address this, the upper limit for wind mass accretion is capped at $0.8|\dot{M}_{d,wind}|$. For accretors identified as compact objects (BH, NS, or WD), the mass accretion rate is constrained by the Eddington limit:

$$\dot{M}_{Edd} = 2.08 \times 10^{-3} M_{\odot} \text{yr}^{-1} \eta_{Edd} (1+X)^{-1} \frac{R_a}{R_{\odot}}, \quad (4.19)$$

where R_a represents the radius of the accretor (in this case, the compact object), $X = 0.760 - 3.0Z$ denotes the hydrogen mass fraction of the accreted material, and η_{Edd} is a free parameter used to enforce or reduce the Eddington limit [46].

Within the code, pure-He and naked-CO stars do not undergo mass accretion, given the expectation that the winds of these stars eject a thin envelope on a very short timescale. The accreted mass contributes additional angular momentum to the accretor, leading to an increase in its spin, as quantified by

$$\dot{J}_{accreted} = \frac{2}{3} R_{eff}^2 \dot{M}_a \Omega_{spin,d}, \quad (4.20)$$

where $\Omega_{spin,d}$ denotes the angular velocity of the donor star. This expression is derived under the assumption that winds remove a thin shell of matter from the donor star, as discussed in the spin evolution section for single-star evolution.

Mass exchange through stellar winds induces changes in the orbital angular momentum, thereby affecting the orbital parameters [131]:

$$\frac{\dot{a}}{a} = -\frac{\dot{M}_d}{M_a + M_d} - \left(\frac{2-e^2}{M_a} + \frac{1+e^2}{M_a + M_d} \right) \frac{\dot{M}_a}{1-e^2}, \quad (4.21)$$

$$\frac{\dot{e}}{e} = -\dot{M}_a \left(\frac{1}{M_a + M_d} + \frac{1}{2M_a} \right). \quad (4.22)$$

While wind mass loss tends to widen the orbit, the accretion of mass onto the companion star mitigates this effect, returning some of the lost angular momentum back to the system. Additionally, wind mass accretion works to reduce eccentricity, promoting the circularization of the orbit. Nevertheless, the eccentricity variations induced by wind mass accretion are considered negligible when compared to those driven by stellar tides, even during phases of intense wind mass loss [131].

Roche-lobe overflow

Under the assumptions of circular and synchronous orbits, an approximate expression for the Roche lobe (RL) radius can be written [77]:

$$R_L = a \frac{0.49q^{2/3}}{0.6q^{2/3} + \ln(1 + q^{2/3})}, \quad (4.23)$$

where q represents the mass ratio between the star and its companion. In the framework of SEVN, the initiation of Roche lobe overflow (RLO) occurs whenever the radius of either star equals or exceeds R_L . The RLO persists until this condition is no longer met or if mass transfer results in a merger or a common envelope (CE). This condition is assessed at each time step within SEVN. The BSE stellar types (refer to Table 4.2) are employed in SEVN to implement Roche lobe overflow, assess mass transfer stability, and handle common envelope events.

Stability criterion

Roche lobe overflow (RLO) induces alterations in the mass ratio, masses, and semi-major axis of the binary system. Consequently, the Roche lobe (RL) undergoes either contraction or expansion (as per Equation 21). If the RL contracts more rapidly than the donor's radius, or if the RL expands less swiftly than the donor's radius due to the adiabatic response of the star to mass loss, the mass transfer becomes dynamically unstable. This instability can lead to either a stellar merger or the formation of a common envelope (CE) configuration. The stability of mass transfer is often assessed by comparing the adiabatic or thermal response of the donor to mass loss (ζ) with the response to RL variation (ζ_L):

$$\zeta = \frac{d \log R}{d \log M}, \quad (4.24)$$

$$\zeta_L = \frac{d \log R_L}{d \log M}. \quad (4.25)$$

Stars with radiative envelopes typically contract in response to mass loss, while those with deep convective envelopes tend to maintain the same radius or experience a slight expansion [101–104, 148, 281]. In practical terms, population synthesis codes commonly employ a simplified framework where mass transfer stability is determined by comparing the mass ratio $q = M_d/M_a$ (with M_d and M_a being the donor and accretor masses, respectively) to a critical value q_c . If the mass ratio exceeds q_c , the mass transfer is considered dynamically unstable. For stars with radiative envelopes (e.g., Main

Sequence stars, stars in the Hertzsprung-gap phase, and pure-He stars), the critical mass ratio is often assumed to be relatively large (e.g., > 2), while it is smaller for stars with deep convective envelopes.

BSE type of the donor	SEVN q_c option		
	QCBSE	QCRS	QCBB
0 (low mass MS)	0.695	0.695	0.695
1 (MS)	3.0	stable	stable
2 (HG)	4.0	stable	stable
3/5 (GB/EAGB)	Eq.4.26	Eq.4.26	Eq.4.26
4 (CHeB)	3.0	3.0	3.0
7 (HeMS)	3.0	3.0	stable
8 (HeHG)	0.784	0.784	stable
> 9 (WD)	0.628	0.628	0.628

Table 4.3: Critical mass ratios as a function of the donor BSE stellar type for different SEVN options. See Table 4.2 for further details on BSE types and their correspondence to SEVN phases. The word stable indicates that the mass transfer is always stable. Table credit: [136].

In SEVN, three stability options are available, where the critical mass ratio is contingent on the donor’s stellar type: QCBSE, QCRS, and QCBB (refer to Table 4.2). The corresponding q_c values are outlined in Table 4.3. The QCBSE option mirrors the stability criterion employed in BSE [131], MOBSE [106, 107, 109, 270]. Specifically, for giant stars with deep convective envelopes (BSE phases 3 and 5),

$$q_c = 0.362 + \frac{1}{3} \left(1 - \frac{M_{He,d}}{M_d} \right)^{-1}, \quad (4.26)$$

where $M_{He,d}$ denotes the core helium mass of the donor star. This equation, based on condensed polytrope models [310], is widely adopted in population synthesis codes (e.g., BSE, MOBSE). The QCRS option employs the same q_c as [131], with the assumption that mass transfer is always stable for donor stars with radiative envelopes, i.e., stars in the Main Sequence (MS) or Hertzsprung-gap (HG) phase (BSE phases 1 and 2). The QCBB option assumes stable mass transfer not only for MS and HG donor stars (BSE phases 1 and 2) but also for donor pure-He stars (BSE phases 7, 8).

In addition to the mentioned mass transfer stability criterion, SEVN accounts for special cases. If the Roche lobe (RL) is smaller than the core radius of the donor star (He core in hydrogen stars and CO core for pure-He stars), mass transfer is invariably considered unstable, irrespective of the chosen stability criterion. In instances of unstable mass transfer in WD binaries, where both the donor and accretor are helium-rich WDs (BSE type 10), and the mass transfer is unstable, the accretor undergoes an SNIa explosion, resulting in a mass-less remnant. For all other cases of unstable mass transfer in WD binaries, the donor is fully engulfed, leaving a mass-less compact remnant, and no mass is accreted onto the companion. If both stars have a radius $R \geq R_L$,

the evolution leads to either a Common Envelope (CE) (when at least one of the two stars exhibits clear core-envelope separation, corresponding to BSE phases 3, 4, 5, 8) or a stellar merger (for all other BSE phases). If the object filling the RL is a Black Hole (BH) or a Neutron Star (NS), the companion must also be a BH or NS. In this scenario, the system undergoes a compact binary coalescence.

Stable Mass transfer

In the latest iteration of SEVN, modifications have been introduced to the formulation governing stable mass transfer. Noteworthy distinctions are elucidated below. The donor's mass loss rate (\dot{M}_d) hinges on its Roche lobe (RL) overflow [131]:

$$\dot{M}_d = -F(M_d) \left(\ln \frac{R_d}{R_L} \right)^3 M_{\odot} \text{yr}^{-1}, \quad (4.27)$$

with the normalization factor:

$$F(M_d) = 3 \times 10^{-6} (\min [M_d, M_{\max, SMT}])^2 \times \begin{cases} \max [M_{\text{env}, d} / M_d, 0.01] & (A) \\ 10^3 M_d (\max [R_d, 10^{-4}])^{-1} & (B) \\ 1 & (C) \end{cases}, \quad (4.28)$$

where (A), (B), and (C) correspond to HG phase donors, WD donors, and all other cases, respectively. Quantities are in solar units, and $M_{\max, SMT} = 5M_{\odot}$. For giant-like stars, the mass transfer is restricted to the thermal rate, as per [131], whereas for other stellar types (MS stars and WR stars without a CO core), the limit is determined by the dynamical rate [131]. The mass accretion rate (\dot{M}_a) is parameterized as:

$$\dot{M}_a = \begin{cases} \min (\dot{M}_{Edd}, -f_{MT} \dot{M}_d) & \text{if the accretor is a compact object} \\ -f_{MT} \dot{M}_d & \text{otherwise} \end{cases}, \quad (4.29)$$

where \dot{M}_{Edd} is the Eddington rate, and $f_{MT} \in [0, 1]$, with $f_{MT} = 0.5$. When an accretor is a compact object (WD, NS, or BH), the Eddington limit is enforced. Moreover, pure-He and naked-CO stars undergo no mass accretion during RL overflow. If the accretor is a WD and the accreted material is hydrogen-dominated (i.e., the donor star is not a WR star), a nova explosion is triggered, reducing the actual accreted mass by a factor of $\epsilon_{\text{nova}} = 0.001$. Furthermore, for stars in BSE phases 1, 2, and 4, Eq. 4.29 is substituted with:

$$\dot{M}_a = -\min \left(1.0, 10 \frac{\tau_M}{\tau_{KH, a}} \right) \dot{M}_d, \quad \text{where } \tau_M = \frac{M_a}{|\dot{M}_d|}, \quad (4.30)$$

and $\tau_{KH, a}$ is the thermal timescale of the accretor. For BSE stellar types 3 and 5, this model assumes that the accretor can absorb any transferred material ($f_{MT} = 1$ in Eq. 4.29). Additionally, in a pure-He-pure-He binary, the stars are allowed to accrete mass during RL overflow following the prescription in Eq. 4.30.

Orbital variations

In the context of non-conservative mass transfer ($f_{MT} \neq 1$), a portion of angular momentum is expelled from the system, and this angular momentum loss is expressed as:

$$\Delta J_{orb,lost} = -|\Delta M_{loss}| \gamma_{RLO} a^2 \sqrt{1 - e^2} \frac{2\pi}{P}, \quad (4.31)$$

where P denotes the orbital period, and ΔM_{loss} represents the actual mass lost from the system in a given evolutionary step, defined as the disparity between the mass shed by the donor and that assimilated by the companion. Assuming an isotropic loss of unaccreted mass from the donor, $\gamma_{RLO} = M_d^2 / (M_a + M_d)^2$. In addition to the mass loss from the system, conservation of the total binary angular momentum (comprising stellar spins and orbital angular momentum) is assumed during Roche lobe overflow (RLO). Consequently, the spin angular momentum lost by the donor is incorporated into the orbital angular momentum:

$$\Delta J_{orb,d} = -\Delta J_{spin,d} = -\Delta M_d R_L^2 \Omega_{spin,d}, \quad (4.32)$$

where ΔM_d represents the mass lost by the donor in an evolutionary step, and $\Omega_{spin,d}$ is the angular velocity of the donor. Conversely, mass accreted onto the companion diminishes orbital angular momentum and augments the accretor's spin:

$$\Delta J_{orb,a} = -\Delta J_{spin,a} = -\Delta M_a \sqrt{GM_a R_{acc}}. \quad (4.33)$$

The accretion radius, R_{acc} , is computed following the methodology outlined in [170, 295]. The minimum radial distance of the mass stream to the secondary is estimated as per [170]:

$$R_{min} = 0.0425 (q^{-1} + q^{-2})^{0.25} a. \quad (4.34)$$

If $R_{min} > R_a$ (where R_a is the radius of the accretor), it is assumed that the mass is accreted from the inner edge of an accretion disc, and $R_{acc} = R_a$. Otherwise, in the absence of an accretion disc, the material from the donor directly impacts the accretor in a stream. In this case, the angular momentum of the transferred material is estimated using the radius at which the disc would have formed if allowed, i.e., $R_{acc} = 1.7 R_{min}$ [295]. Finally, the variation in the semi-major axis resulting from RLO is approximated as:

$$\Delta a = \frac{(J_{orb} + \Delta J_{orb,lost} + \Delta J_{orb,d} + \Delta J_{orb,a})^2 (M_a + M_d)}{G (1 - e^2) M_d^2 M_a^2} - a, \quad (4.35)$$

where the masses are considered after the mass exchange in the current time-step.

Unstable mass transfer

The outcome of an unstable mass transfer is contingent upon the stellar type of the donor. In instances of unstable mass transfer, stars resembling giants (BSE types 3, 4, 5, 8) progress through a common envelope (CE) phase, while stars lacking a

distinct envelope/core demarcation (BSE types 0, 1, 7) directly merge with their companion. Stars in the Hertzsprung-gap (HG) phase (BSE type 2) present a distinctive case wherein the differentiation between the helium core and hydrogen envelope is not fully established [72, 141]. The resolution of whether unstable mass transfer with an HG donor leads to a CE evolution (as postulated in the optimistic scenario of [72, 300]) or culminates in a direct merger (as suggested in the pessimistic scenario of [72, 107]) remains uncertain.

Quasi-Homogeneous evolution

In the Quasi-Homogeneous Evolution (QHE) scenario, a star attains a substantial spin rate through the accretion of material during a stable Roche Lobe Overflow (RLO) mass transfer. Consequently, the star undergoes full mixing during the Main Sequence (MS), leading to the complete conversion of hydrogen into helium [48, 229]. The implementation of the QHE in SEVN adheres to the methodology outlined in [79, 80]. Upon activating the QHE option, SEVN initiates the QHE evolution for Main Sequence (MS) stars with metallicity $Z \leq 0.004$. These stars must accrete a minimum of 5% of their initial mass through stable RLO mass transfer and attain a post-accretion mass of at least $10M_{\odot}$. Once a star satisfies the QHE criteria, the evolution of its radius is halted. Subsequently, at the conclusion of the MS phase, the star transitions into a pure helium star, and the evolutionary phase directly advances to phase 4 (core helium burning, see Table 4.2).

Common Envelope (CE) evolution

The Common Envelope (CE) phase constitutes a distinctive evolutionary stage in a binary system, wherein the binary becomes enveloped within the expanded envelope of one or both of its components. The loss of co-rotation between the binary orbit and the envelope induces drag forces that lead to orbit shrinkage, while the CE gains energy and expands [139]. The CE evolution expounded in this section relies on the energy formalism [131, 135, 167, 296, 309]. This formalism hinges on a comparison between the energy required to unbind the stellar envelope(s) and the orbital energy before and after the CE event. The assessment of these energy terms is contingent on two parameters: λ_{CE} and α_{CE} . The first parameter, λ_{CE} , serves as a structural parameter defining the binding energy of the stellar envelope. Consequently, the binding energy of the CE is expressed as:

$$E_{bind,i} = -G \left(\frac{M_1 M_{env1}}{\lambda_{CE1} R_1} + \frac{M_2 M_{env2}}{\lambda_{CE2} R_2} \right), \quad (4.36)$$

Here, M_1 (M_2) denotes the mass of the primary (secondary) star, M_{env1} (M_{env2}) represents the mass of the envelope of the primary (secondary) star, and R_1 (R_2) corresponds to the radius of the primary (secondary) star. In cases where the accretor is a compact object or a star lacking an envelope, M_{env2} is set to 0. If both stars possess an envelope, both lose it upon the ejection of the CE. SEVN employs the same formalism for λ_{CE} as utilized in BSE [57]. According to this formalism, λ_{CE} is contingent on the mass of the

star, its evolutionary phase, the mass of the convective envelope, and its radius. For pure-He stars, a constant value of $\lambda_{CE} = 0.5$ is assumed.

The parameter α_{CE} signifies the fraction of orbital energy transformed into kinetic energy of the envelope during CE evolution. The variation in orbital energy during CE is expressed as:

$$\Delta E_{orb} = \frac{1}{2}GM_{c,1}M_{c,2} \left(\frac{1}{a_f} - \frac{1}{a_i} \right), \quad (4.37)$$

Here, $M_{c,1}$ and $M_{c,2}$ denote the masses of the cores of the two stars, and a_f (a_i) corresponds to the semi-major axis after (before) the CE phase. Following the same formalism as in BSE, $E_{bind} = 0$, and $M_c = M$ for Main Sequence (MS) stars, pure-He stars without a CO core, naked-CO stars, and compact remnants. The post-CE separation is determined by enforcing $E_{bind,i} = \alpha_{CE}\Delta E_{orb}$. If neither star fills its Roche Lobe in the post-CE configuration, the CE is assumed to be ejected. Otherwise, the two stars undergo coalescence. α_{CE} can assume values within the range of 0.5 to 5. Values of $\alpha_{CE} > 1$ deviate from the original definition of this parameter, accounting for the fact that the orbital energy variation is not the sole source of energy contributing to unbinding the envelope (e.g., [255]).

Tides

Tidal interactions between two stars in a binary system play a crucial role in synchronizing stellar and orbital rotations, leading to orbit circularization (e.g., [132, 144, 200]). SEVN incorporates tidal effects on the orbit and stellar rotation using weak friction analytical models proposed by [132]. This model is built upon the spin-orbit coupling resulting from the misalignment of tidal bulges in a star and the perturbing potential generated by its companion. The secular average equations implemented in SEVN are given by:

$$\dot{a} = -6k_{tides}q(q+1) \left(\frac{R_{eff}}{a} \right)^8 \frac{a}{(1-e^2)^{7.5}} \left(f_1 - (1-e^2)^{2/3} f_1 \frac{\Omega_{spin}}{\Omega_{orb}} \right), \quad (4.38)$$

$$\dot{e} = -27k_{tides}q(q+1) \left(\frac{R_{eff}}{a} \right)^8 \frac{e}{(1-e^2)^{6.5}} \left(f_3 - \frac{11}{18}(1-e^2)^{2/3} f_4 \frac{\Omega_{spin}}{\Omega_{orb}} \right), \quad (4.39)$$

$$\dot{J} = 3k_{tides}q^2MR^2 \left(\frac{R_{eff}}{a} \right)^6 \left(\frac{R_{eff}}{R} \right)^2 \frac{\Omega_{orb}}{(1-e^2)^6} \left(f_2 - (1-e^2)^{2/3} f_5 \frac{\Omega_{spin}}{\Omega_{orb}} \right), \quad (4.40)$$

Here, q represents the mass ratio between the perturbing star and the star affected by tides, Ω_{spin} is the stellar angular velocity, R is the stellar radius, and $R_{eff} = \min[R_L, R]$ is the effective radius. The effective radius ensures that, during stable Roche Lobe (RL) mass transfer, the star's actual radius remains close to its RL. In all other cases, the effective radius coincides with the stellar radius. These equations are derived under the assumption that $R < a$ [132]. The re-scaling factor $R_{eff}^2R^{-2}$ accounts for the stellar inertia ($J_{spin} = \Omega_{spin}I$ and $I \propto R^2$). Polynomial functions f_1 , f_2 , f_3 , f_4 , and f_5 of e^2 are utilized [132].

The term k_{tides} is the inverse of the tidal evolution timescale, estimated for radiative envelopes [131, 319, 320]:

$$k_{tides} = 3.156 \times 10^{-5} \left(\frac{M}{M_{\odot}} \right)^{3.34} \left(\frac{R}{R_{\odot}} \right) \left(\frac{a}{R_{\odot}} \right)^{-2.5} \text{ yr}^{-1}, \quad (4.41)$$

and for convective envelopes [131, 243, 320]:

$$k_{tides} = \frac{2}{21} \left(\frac{\tau_{conv}}{\text{yr}} \right)^{-1} \frac{M_{conv}}{M} \min \left[1, \left(\frac{\pi}{(\Omega_{orb} - \Omega_{spin}) \tau_{conv}} \right)^2 \right] \text{ yr}^{-1}, \quad (4.42)$$

where M_{conv} is the mass of the convective envelope, and τ_{conv} is the eddy turnover timescale. The amount of variation in a , e , and J_{spin} is estimated by multiplying Eqs. 4.38, 4.39, 4.40 by the current time-step and combining the effects of the two stars in the system. SEVN assumes that compact remnants (WDs, BHs, NSs) and naked-CO stars are not influenced by tides and act merely as a source of perturbation for the companion star.

A specific stellar rotation, Ω_{eq} ($= \Omega_{orb}$ when $e = 0$), exists for which Eq. 4.40 is 0, indicating that no further angular momentum exchange can occur between the star and the orbit. If necessary, the effective time-step for tidal processes is reduced to ensure that both stars do not undergo excessive spin-down (or up) past Ω_{eq} [131]. Tidal effects are particularly pronounced when there is a substantial mismatch between Ω_{spin} and Ω_{eq} , in tight systems ($R \approx a$), and for stars with large convective envelopes (Eq. 4.42 yields larger k_{tides} compared to Eq. 4.41).

Circularization during RLO and collision at periastron

Despite the strong tendency of tides to reduce orbital eccentricity prior to the initiation of Roche Lobe Overflow (RLO), there are instances where RLO commences with a notable residual eccentricity ($e \approx 0.2 - 0.5$). Given that the RLO formalism assumes circular orbits, SEVN, by default, provides an option to fully circularize the orbit at the onset of RLO. Various options for handling orbit circularization are available in SEVN. One approach is to circularize the orbit at periastron, resulting in $a_{new} = a_{old}(1 - e_{old})$ and $e_{new} = 0$, where a_{old} and e_{old} denote the semi-major axis and eccentricity before circularization [300]. Another option is to circularize the system not only at the onset of RLO but also whenever either of the two stars fills its Roche Lobe at periastron, i.e., when $R \geq R_{L,per}$, with $R_{L,per}$ estimated using Eq.4.23 by replacing the semi-major axis a with the periastron radius $a(1 - e)$. In this case, the orbit is circularized at periastron, initiating an RLO episode.

Other available options in SEVN assume that circularization conserves either the orbital angular momentum, i.e., $a_{new} = a_{old}(1 - e_{old}^2)$, or the semi-major axis, i.e., $a_{new} = a_{old}$. In the latter case, the orbital angular momentum increases after circularization. Alternatively, circularization can be disabled, preserving any residual eccentricity during RLO (this assumption is the default in BSE). Throughout RLO, stellar tides and other processes remain active, implying that the binary can still undergo circularization during an ongoing RLO. During binary evolution, SEVN assesses

whether the two stars are in contact at periastron, specifically if $R_1 + R_2 \leq a(1 - e)$. If this condition is met, SEVN triggers a collision. By default, this check is disabled during an ongoing RLO. The outcome of the collision mirrors the results of unstable mass transfer during RLO. If at least one of the two stars exhibits a clear core-envelope separation (BSE types > 3 , see Table 4.2), the collision triggers a Common Envelope (CE) event; otherwise, a direct stellar merger occurs.

Gravitational waves

SEVN incorporates the impact of gravitational wave (GW) emission on orbital elements using the same formalism as BSE[131]:

$$\dot{a} = -\frac{64G^3M_1M_2(M_1 + M_2)}{5c^5a^3(1 - e^2)^{7/2}} \left(1 + \frac{73}{24}e^2 + \frac{37}{96}e^4\right), \quad (4.43)$$

$$\dot{e} = -\frac{304G^3M_1M_2(M_1 + M_2)}{15c^5a^4(1 - e^2)^{5/2}} \left(1 + \frac{121}{304}e^2\right) e. \quad (4.44)$$

These equations, as outlined in [228], capture the effects of gravitational wave-induced orbital decay and circularization. In contrast to BSE—where these equations are activated only when the semi-major axis is < 10 AU—in SEVN, they become active whenever the gravitational wave merger timescale, t_{merge} , is shorter than the Hubble time.

Stellar mergers

In the event of a merger between two stars in SEVN, their carbon-oxygen (CO) cores, helium (He) cores, and total masses are combined. The resultant merger product inherits both the phase and the percentage of the lifespan from the most evolved progenitor star involved. The determination of the most evolved star relies on the highest SEVN phase ID (Table 4.2) or, in cases where merging stars share the same phase, the one with the largest life percentage. Notably, SEVN does not necessitate a collision table for the merger between two stars. The interpolation algorithm independently determines the new post-merger track without the need to assign a specific stellar type to the merger product.

Conversely, SEVN employs a collision table (Table 4.4) exclusively to describe the outcomes of mergers involving compact objects. When a star merges with a compact object (black hole (BH), neutron star (NS), or white dwarf (WD)), the star undergoes destruction, and no mass is transferred to the compact object. Mergers involving white dwarfs have the potential to trigger a Supernova Ia (SNIa) explosion, resulting in the absence of a compact object (Table 4.4). Post-merger oxygen-neon (ONe) white dwarfs exceeding the Chandrasekhar mass limit ($1.44M_\odot$) evolve into neutron stars (NSs). Similarly, post-merger neutron stars exceeding the Tolman-Oppenheimer-Volkoff mass limit (defaulted to $3.0M_\odot$) become black holes (BHs). Except for cases leading to an SNIa, the outcome of a merger involving two compact objects yields a compact object with a mass equivalent to the total mass of the pre-merger system. The mass lost

through gravitational wave (GW) emission, typically around $\sim 5\%$ of the total system mass, is not currently accounted for (e.g., [142]). A formalism to address this omission is slated for inclusion in future versions of SEVN.

Compact object	Companion	Merger outcome
BH/NS/WD	H-star/pure-He star	BH/NS/WD (no mass accretion)
BH	BH/NS/WD	BH
NS	NS/WD	if $M_f < 3M_\odot$: NS, else: BH
HeWD	HeWD	SNIa
COWD	COWD/HeWD	if $M_f < 1.44M_\odot$: COWD, else: SNIa
ONeWD	WD	if $M_f < 1.44M_\odot$: ONeWD, else: NS

Table 4.4: This Table describes the outcome of a merger between a compact object and its companion, as implemented in SEVN. An SNIa leaves no compact remnant. Here Tolman-Oppenheimer-Volkoff mass limit for NSs and Chandrasekhar mass limit for WDs are assumed. Table credit: [136].

4.1.4 The evolution algorithm

Adaptive time-step

SEVN uses a prediction-correction method to adapt the time-step accounting for the large physical range of timescales (from a few minutes to several Gyr) typical of stellar and binary evolution. To decide the time-step, it looks at a sub-set of stellar and binary properties (total mass, radius, mass of the He and CO core, semi-major axis, eccentricity, and amount of mass loss during an RLO): if any of them changes too much during a time-step, the time-step is reduced and repeat the calculation. In practice, the code chooses a maximum relative variation δ_{max} (0.05 by default) and impose that

$$\max_{P \in \text{properties}} |\delta P| \leq \delta_{max}, \quad (4.45)$$

where $|\delta P|$ is the absolute value of the relative property variation. SEVN predicts the next time-step dt_{next} as

$$dt_{next} = \min_{P \in \text{properties}} \left(\delta_{max} \frac{dt_{last}}{|\delta P_{last}|} \right), \quad (4.46)$$

where dt_{last} is the last time-step and δP_{last} is the relative variation of property P during the last time-step, hence $|\delta P_{last}|/dt_{last}$ represents the absolute value of the δP_{last} time derivative. After the evolution step, if the condition in Eq.4.45 is not satisfied, a new (smaller) time step is predicted using Eq.4.46 and the updated values of δP_{last} and dt_{last} . Then, the evolution of all the properties is repeated with the new predicted time-step until condition 4.45 is satisfied or until the previous and the new proposed time steps differ by less than 20%. SEVN uses a special treatment when a star approaches a change of phase (including the transformation to a compact remnant). In this case,

the prediction-correction method is modified to guarantee that the stellar properties are evaluated just after and before the change of phase. In practice, if the predicted time-step is large enough to cross the time boundary of the current phase, SEVN reduces it so that the next evolution step brings the star/binary 10^{-10} Myr before the phase change. Then, the following time-step is set to bring the star/binary 10^{-10} Myr beyond the next phase. This allows the code to accurately models stellar evolution across a phase change. In particular, it is necessary to properly set the stellar properties before a supernova explosion or WD formation. On top of the adaptive method, SEVN includes a number of predefined time-step upper limits: the evolution time cannot exceed the simulation ending time or the next output time; the stellar evolution cannot skip more than two points on the tabulated tracks; a minimum number of evaluations (= 10 by default) for each stellar phase has to be guaranteed. The time-step distribution in a typical binary evolution model spans 9 – 10 orders of magnitude, from a few hours to several Myr.

Temporal evolution

Fig.4.2 summarises the SEVN temporal evolution scheme. During each time-step, SEVN evolves the two stars independently, then it evaluates and accumulates the property variations, ΔP , caused by each binary-evolution process. The binary prescriptions use as input the orbital and stellar properties at the beginning of the evolution step, $P(t_0)$. After the integration of the binary-evolution processes, SEVN updates each stellar and binary property (Fig.4.2). In particular, each binary property (e.g., semi-major axis, eccentricity) is updated as $P(t) = P(t_0) + \Delta P$. Each stellar evolution property (e.g., mass of each star) is calculated as $P(t) = P_s(t) + \Delta P$, where $P_s(t)$ is the value of the property at the end of the time-step as predicted by stellar evolution only. For example, if the property $P(t)$ is the mass of an accretor star during RLO, $P_s(t)$ is the mass predicted at the end of the time-step by stellar evolution (accounting for mass loss by winds), while ΔP is the mass accreted by RLO and by wind-mass transfer during the time-step. If necessary, the single and binary evolution step is repeated until the adaptive time-step conditions are satisfied. SEVN evolves the compact remnants passively maintaining their properties constant. SEVN treats naked-CO stars similar to compact remnants: they evolve passively until they terminate their life and turn into compact remnants. SEVN assumes that the transition from a star to a compact remnant happens at the beginning of the time-step. In this case, SEVN assigns a mass and a natal kick to the new-born compact object, based on the adopted supernova model. Then, it estimates the next time-step for the updated system. Similarly, SEVN does not use the general adaptive time-step criterion when one of the following processes takes place: RLO circularisation, merger, or CE. In such cases, SEVN uses an arbitrarily small time-step ($dt_{\text{tiny}} = 10^{-15}$ Myr) and calculates only the aforementioned process during such time-step. Then, it estimates the new time-step. At the very end of each evolutionary step, SEVN checks if a SNIa must take place. A SNIa is triggered if any of the following conditions is satisfied: *i*) a HeWD with mass larger than $0.7M_{\odot}$ has accreted He-rich mass from a WR star, or *ii*) a COWD has accreted at least $0.15M_{\odot}$ from a WR star. Furthermore, SEVN checks if any ONeWD (NS) has reached a mass

larger than $1.44M_{\odot}$ ($3M_{\odot}$) during the time-step. If this happens, the ONeWD (NS) becomes a NS (BH). Finally, SEVN checks if the stars in the binary need to jump to a new interpolating track.

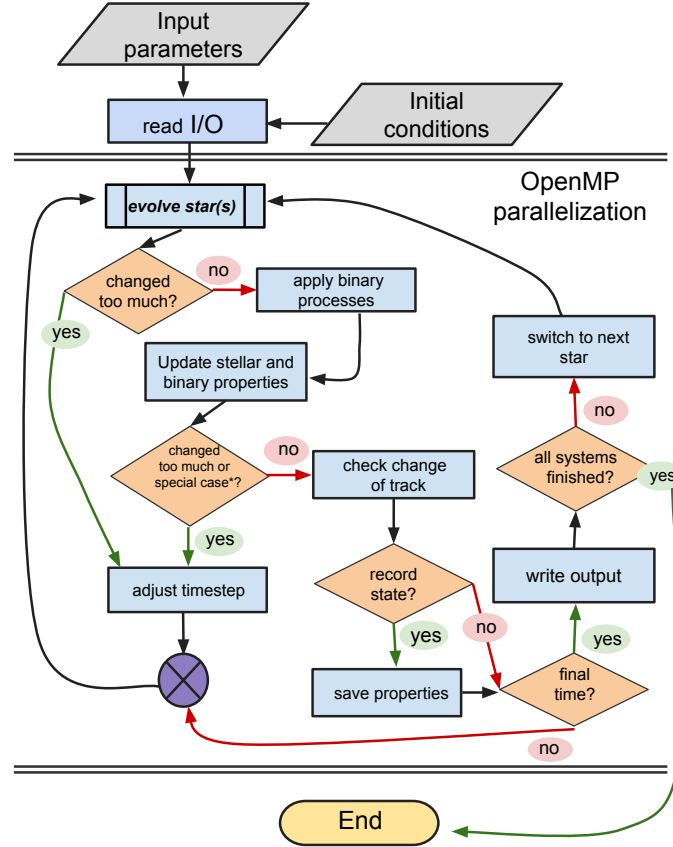



Figure 4.2: Schematic representation of the SEVN evolution algorithm. The “changed too much” checks refer to the variation of the stellar and/or binary properties. In the case of single-stellar evolution or in the case of an ionized binary, SEVN skips the sections “apply binary processes” and “update stellar and binary properties”. The “special case” check refers to all the cases in which SEVN repeats the evolution to follow a particular binary evolution process, i.e. CE, merger, and circularization at the onset of the RLO. (Image credit: [136] )

Change of interpolating tracks

During binary evolution, a star can change its mass significantly due to mass loss/accretion, or after a stellar merger. In these cases, SEVN needs to find a new track, which better matches the current stellar properties. For stars without a core (MS H-stars or core He burning pure-He stars), SEVN moves onto a new evolutionary track every time the net cumulative mass variations due to binary processes (RLO, wind mass accretion) is larger than 1% of the current star mass. When a decoupled (He or CO) core is present, its properties drive the evolution of the star [130]. For

this reason, we do not allow stars with a He or CO core (H-star with phase > 2 and pure-He stars with phase > 4) to change track unless the core mass has changed. After a stellar merger, SEVN always moves the merger product to a new stellar track. When an H-rich star fulfils the WR star condition (He-core mass larger than 97.9% of the total mass), the star jumps to a new pure-He track. When a star moves to a new track, SEVN searches the track that best matches the mass (or the mass of the core) of the current star at the same evolutionary stage (SEVN phase and percentage of life) and metallicity. We define the ZAMS mass of such a track as $M_{\text{ZAMS},new}$. In general, SEVN searches the new track in the H (pure-He) tables for H-rich (pure-He) stars. The only exceptions occur when a H-rich star is turned into a pure-He star (in this case, SEVN jumps to pure-He tables), and when a pure-He star is transformed back to a H-rich star after a merger (SEVN jumps from a pure-He table to a H-rich table). SEVN adopts two different strategies to find the best $M_{\text{ZAMS},new}$ for stars with or without a core. For stars without a core-envelope separation, SEVN finds the best $M_{\text{ZAMS},new}$. Hereafter, we define M as the current mass of the star, M_p as the mass of the star with ZAMS mass M_{ZAMS} , estimated at the same phase and percentage of life of the star that is changing track. $M_{\text{ZAMS},old}$ is the ZAMS mass of the current interpolating track. Assuming a local linear relation between M_{ZAMS} and M_p , $M_{\text{ZAMS},old}$ can be estimated using the equation

$$M = \frac{M_{p,2} - M_{p,1}}{M_{\text{ZAMS},2} - M_{\text{ZAMS},1}} (M_{\text{ZAMS},new} - M_{\text{ZAMS},1}) + M_{p,1}. \quad (4.47)$$

As a first guess, we set $M_{\text{ZAMS},1} = M_{\text{ZAMS},old}$ and $M_{\text{ZAMS},2} = M_{\text{ZAMS},old} + 1.2\delta M$, where δM is the cumulative amount of mass loss/accreted due to the binary processes. $M_{\text{ZAMS},new}$ is accepted as the ZAMS mass of the new interpolating track if

$$\frac{|M_{p,new} - M|}{M} < 0.005, \quad (4.48)$$

otherwise Eq.4.47 is iterated replacing $M_{\text{ZAMS},1}$ or $M_{\text{ZAMS},2}$ with the last estimated $M_{\text{ZAMS},new}$. The iteration stops when the condition in Eq.4.48 is fulfilled, or after 10 steps, or if $M_{\text{ZAMS},new}$ is outside the range of the ZAMS mass covered by the stellar tables. If the convergence is not reached, the best $M_{\text{ZAMS},new}$ will be the one that gives the minimum value of $|M_{p,new}|/M$ (it could also be the original $M_{\text{ZAMS},old}$). SEVN applies this method also when H-rich stars without a CO-core turn into pure-He stars (phase ≤ 4). If the phase is < 4 , SEVN sets the evolutionary stage of the new track at the beginning of the core-He burning (phase 4). For stars with a core, SEVN looks for the best $M_{\text{ZAMS},new}$ matching the mass of the innermost core M_c (He-core for stellar phases 2, 3, 4, and CO-core for phases 5, 6, see Table 4.2). For this purpose, SEVN makes use of the bisection method in the ZAMS mass range $[\max(M_c, M_{\text{ZAMS},min}), M_{\text{ZAMS},max}]$, where $M_{\text{ZAMS},min}$ and $M_{\text{ZAMS},max}$ represent the boundaries of the ZAMS mass range covered by the stellar tables (see Table 4.2). SEVN iterates the bisection method until Eq.4.48 is valid considering the core masses. If the convergence is not reached within 10 steps, SEVN halts the iteration and the best $M_{\text{ZAMS},new}$ is the one that gives the best match to the core mass. Sometimes (e.g. after a merger) the CO core is so massive that no matches can be found. In those cases, SEVN applies the same method trying

to match the mass of the He core. If the He-core mass is not matched, SEVN applies the linear iterative method to match the total mass of the star. SEVN uses this method also when a pure-He star turns back to an H-rich star after accreting an hydrogen envelope or when a H-rich star with a CO core turns into a pure-He star. Finally, the star jumps to the new interpolating track with ZAMS mass $M_{\text{ZAMS},\text{new}}$. SEVN updates the four interpolating tracks and synchronises all the stellar properties with the values of the new interpolating track. The only exceptions are the mass properties (mass, He-core mass, CO-core mass). If the track-finding methods do not converge (Eq. 4.48 is not valid), the change of track might introduce discontinuities in these properties. To avoid this problem, Spera et al. (2019) added a formalism that guarantees a continuous temporal evolution. In practice, SEVN evolves the stellar mass and mass of the cores using

$$M_{t_1} = M_{t_0}(1 + \delta m), \text{ where } \delta m = \frac{m_{t_1} - m_{t_0}}{m_{t_0}}, \quad (4.49)$$

where M_{t_1} and M_{t_0} are the masses of the star (or of the core) estimated at time t_1 and t_0 , while m_{t_1} and m_{t_0} are the masses obtained from the interpolating tracks at time t_1 and t_0 . Fig. 4.3 summarises the algorithm SEVN uses to check and handle a change of track.

4.2 Coupling ISTEEDDAS and SEVN

SEVN can work as a stand-alone code (for fast population synthesis studies in the field) or can be linked to an N-body code, without having performance penalties. Our dynamical evolution code ISTEEDDAS is coupled with the new population-synthesis code SEVN.

There are only three quantities that have to be communicated between the two codes, for each star: mass, radius, and the stellar evolution time-step. The radius is important to check whether two stars collide/merge or they are only passing close to each other. The new masses are needed by ISTEEDDAS to correctly compute the new accelerations. The evolution time-step is needed to synchronize the evolution of the stars with the block time-steps method in ISTEEDDAS.

An aspect that is worth mentioning is that SEVN lacks the evolutionary tables for low-mass stars (mass $\lesssim 2M_{\odot}$). Such low-mass tracks will be included in an upcoming version of the SEVN code (Spera, M., private communication). Therefore, for now, in ISTEEDDAS we select and evolve only the stars with a mass larger than a certain threshold (default at $3M_{\odot}$, for safety). The other stars will be considered as non-evolving point-mass stars. This is an acceptable approximation considering that the ISTEEDDAS code is still under development and for preliminary tests, we do not evolve star clusters for more than a few hundred of Myrs.

4.2.1 Single star evolution

The selected single stars are evolved by SEVN, which will adjust the evolutionary time-step according to its own algorithms, for multiple time steps until the mass has

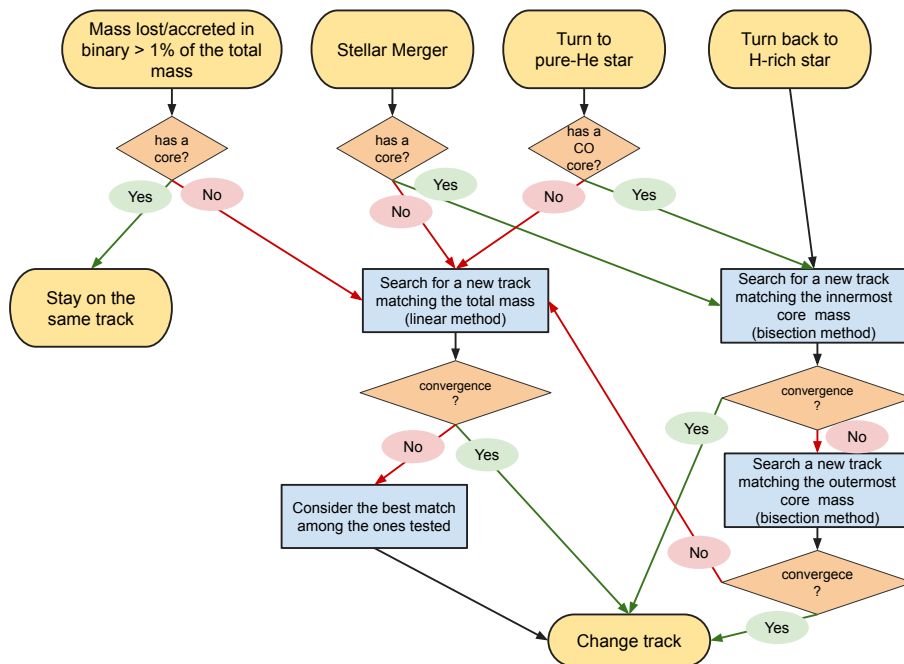



Figure 4.3: Schematic representation of the algorithm SEVN uses during a change of stellar track. The elements in the upper row indicate all the cases for which the code searches for a new stellar track: a significant mass loss/mass accretion due to binary interactions, a stellar merger, an H-rich star that loses its envelope turning into a pure-He star, and a pure-He star that accretes a new H envelope turning back into a H-rich star. In stars with both an He and CO cores, the latter is the innermost core. In stars with only an He core the innermost and outermost cores coincide. (Image credit: [136] )

changed beyond a certain percentage threshold (by default we choose 2%). For each time step, the mass of the stars in ISTEEDAS is evolved through a linear interpolation between the initial and the final mass of the stars. This is done during the predictor step. To perform such interpolation on GPU we communicate two quantities: the angular coefficient (a_m) and the intercept (b_m) of the line ($m(t) = a_m t + b_m$), that is:

$$a_m = \dot{m} = \frac{dm}{dt} = \frac{m(t_1) - m(t_0)}{t_1 - t_0},$$

$$b_m = m(t_0) - a_m t_0,$$

where for t_0 and t_1 we consider the initial and final time of the total step performed by SEVN. In Fig.4.4 I show the evolution of an example star born with $\sim 61M_\odot$ and $Z = 0.002Z_\odot$ on the ZAMS. The comparison between SEVN and the SEVN module in ISTEEDAS are perfectly superposed, since they correctly use the same algorithms to evolve stars, while the interpolation made on GPU slightly differs from them, as expected. I also plotted the evolution of the core masses, the radius, and the luminosity, to show a complete picture of the star's evolution.

4.2 Coupling ISTEEDDAS and SEVN

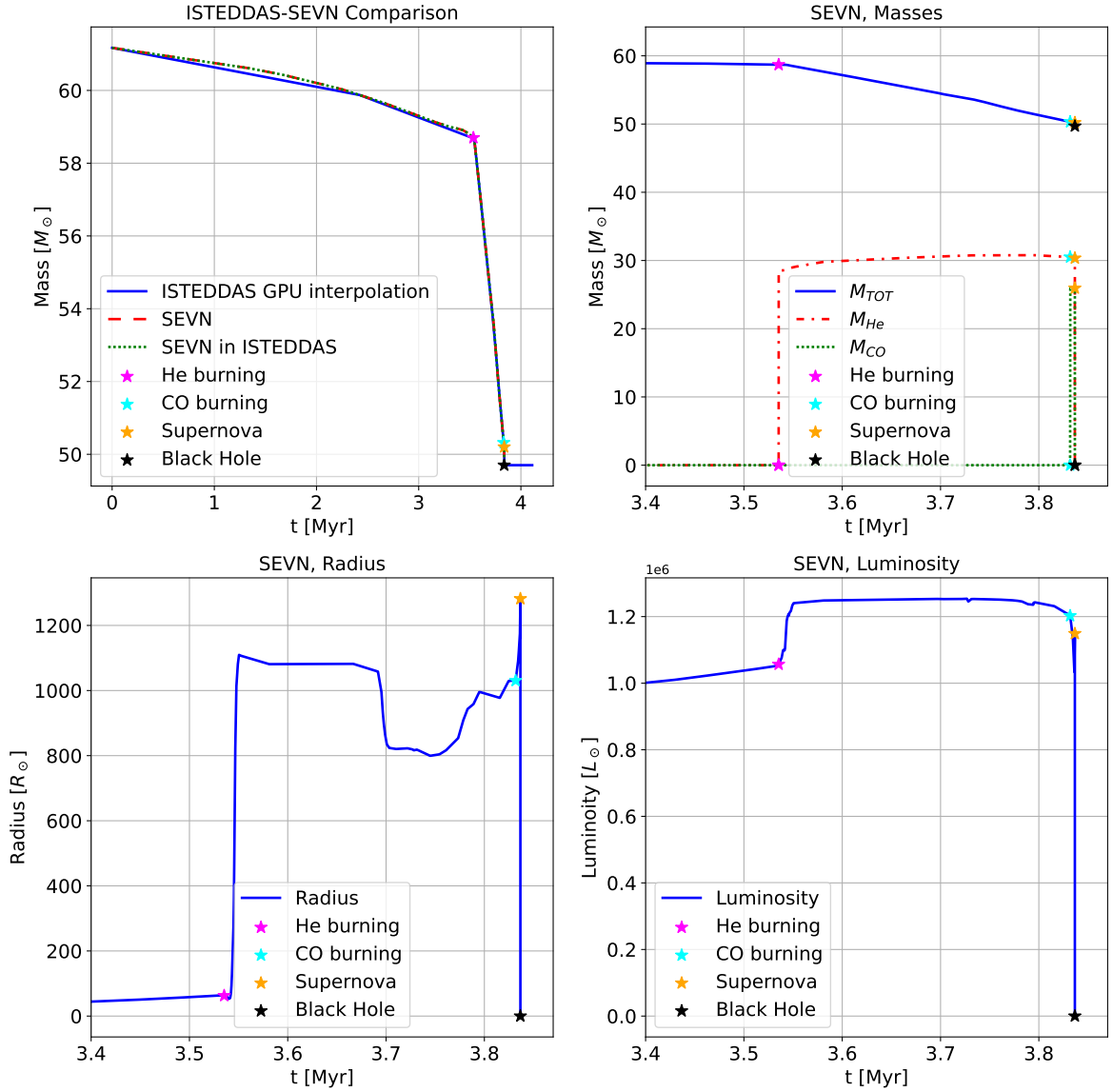


Figure 4.4: The plots in this figure are referred to the evolution of a star born with $\sim 61M_{\odot}$ and $Z = 0.002Z_{\odot}$. In the top-left panel, I show the comparison between the mass evolution over time simulated in SEVN (red), in the SEVN module in ISTEEDDAS (green), and its GPU interpolation in the ISTEEDDAS integrator (blue). In the top-right panel, I show the total mass evolution (blue), and the mass evolution of the Helium core (red) and the Carbon-Oxygen core (green). In the bottom-left and bottom-right panels, I show the evolution of the radius and the luminosity of the star respectively. In the last three plots, I zoomed on the last moment of the life of the star. In all the plots, the four colored stars represent the important moments in the star's evolution: the starting of the Helium burning phase (fuchsia), the starting of the Carbon-Oxygen burning phase (cyan), the supernova (orange), and the formation of the black hole (black).

Using SEVN, the mass of stars is no longer a constant, it changes because of the various mechanisms involved in the stellar evolution, therefore we modified the equations for the derivatives of the acceleration used in ISTEEDAS (Eqs.2.5,2.6,2.34) to consider the variation of the star's masses. In this way, all the stars can feel the mass changes of other stars in the cluster by adjusting their dynamical time-step in ISTEEDAS, see Eq.2.9. Moreover, it is crucial to modify the derivatives of the acceleration to stabilize the dynamical integrator, in fact, without this correction, the high derivatives tend to accumulate errors until the simulation becomes unstable. The new acceleration of a single star (see Eq.2.4) is:

$$\mathbf{a}_i = \sum_{j \neq i}^N \frac{m_j}{|\mathbf{r}_{ij}|^3} \mathbf{r}_{ij} = \sum_{j \neq i}^N m_j \mathcal{Q}_{ij}, \quad (4.50)$$

where \mathcal{Q}_{ij} contains all the terms but the mass, and we have assumed the gravitational constant $G = 1$. In this way, the derivatives become:

$$\begin{aligned} \dot{\mathbf{a}}_i &= \sum_{j \neq i}^N m_j \dot{\mathcal{Q}}_{ij} & \longrightarrow & \dot{\mathbf{a}}_i = \sum_{j \neq i}^N m_j \dot{\mathcal{Q}}_{ij} + \dot{m}_j \mathcal{Q}_{ij}, \\ \ddot{\mathbf{a}}_i &= \sum_{j \neq i}^N m_j \ddot{\mathcal{Q}}_{ij} & \longrightarrow & \ddot{\mathbf{a}}_i = \sum_{j \neq i}^N m_j \ddot{\mathcal{Q}}_{ij} + 2\dot{m}_j \dot{\mathcal{Q}}_{ij}, \\ \dddot{\mathbf{a}}_i &= \sum_{j \neq i}^N m_j \dddot{\mathcal{Q}}_{ij} & \longrightarrow & \dddot{\mathbf{a}}_i = \sum_{j \neq i}^N m_j \dddot{\mathcal{Q}}_{ij} + 3\ddot{m}_j \ddot{\mathcal{Q}}_{ij}, \end{aligned}$$

where \dot{m} corresponds to the angular coefficient a_m , and all the successive derivatives of the mass are zero since we interpolate it linearly. The extra terms on the right are not computationally expensive since we already compute them: in $\dot{\mathbf{a}}_i$ we need $\dot{m}_j \mathcal{Q}_{ij}$, but \mathcal{Q}_{ij} it has already been computed for \mathbf{a}_i , in $\ddot{\mathbf{a}}_i$ we need $2\dot{m}_j \dot{\mathcal{Q}}_{ij}$, but $\dot{\mathcal{Q}}_{ij}$ it has already been computed for $\dot{\mathbf{a}}_i$, and in $\dddot{\mathbf{a}}_i$ we need $3\ddot{m}_j \ddot{\mathcal{Q}}_{ij}$, but $\ddot{\mathcal{Q}}_{ij}$ it has already been computed for $\ddot{\mathbf{a}}_i$.

These adjustments aim to anticipate mass changes among stars in the cluster, yet they don't entirely resolve the issue. When a star, labeled ISTEEDAS, progresses to evolve within SEVN ($t_{ist} \geq t_{sevn,i}$), inactive stars at that point won't immediately sense the \dot{m} change until they become active. Consequently, their time-steps will be updated too late. To tackle this, synchronizing the entire cluster each time a single star desires to evolve in SEVN was considered. However, this approach would impose a substantial computational burden and negate the advantages of the block time-step method. Hence, we opted to synchronize only the neighboring stars, identified through the Ahmad-Cohen scheme, of the evolving star.

To achieve this, we verify in advance whether star i intends to evolve with SEVN based on the condition:

$$t_{ist} + \Delta t_c \geq t_{sevn,i}, \quad (4.51)$$

where Δt_c represents the time-step relative to the star's neighbors. If this condition holds true, we proceed to evolve the star in SEVN and, in the subsequent step, designate

all its neighbors as active particles artificially. This adjustment allows them to adapt their time-steps according to the newly computed accelerations and derivatives based on the updated \dot{m} . Importantly, this artificial activation doesn't disrupt the synchronization of the block time-step method. As the star is placed within the same active block as the evolving star, the method remains reliable even if the actual time-step executed by the star doesn't align as a power of 2. In instances where a star is among the neighbors of multiple evolving stars, its block in the subsequent step will be set to the largest (or smallest time-step) among the blocks of the involved evolving stars.

Additionally, there's another issue concerning the time-step that must be addressed. In cases where the SEVN evolution involves one or multiple exceedingly small steps, the dynamical time-step of a star might be large enough to bypass these steps, resulting in the loss of information regarding the changing \dot{m} . Consequently, if the dynamical steps of a star meet this condition, we constrain it to not skip over more than a single SEVN step. Subsequently, the neighboring stars follow its time-step using the previously outlined algorithm.

At the end of star evolution, massive stars can have different fates: become a neutron star or a black hole after a supernova explosion, or they disintegrate because of the PISN mechanism. In the first case, we stop the evolution of the mass, assigning the final mass of the remnant, and we add to the corrected velocity of the body the kick velocity due to the supernova explosion. In the second case, the star is simply removed from the N-body system. Since the kick velocity can be much higher than the escape velocity of the simulated star cluster, those stars who receive a strong kick will become "super-fast stars". Since these stars have not reached such high speeds gradually because of accelerations, but instead, their speeds were instantaneously increased because of the supernova kick, their neighbours will not be able to adapt their time steps accordingly. Therefore, after a supernova kick, we checked the velocity of the newborn remnant, if it is higher than the escape velocity of the cluster (See section 1.5.7) we force its neighbours to have an equal or smaller time-step with respect to the considered star. This is achieved in the exact same way as was already explained for the synchronization of the SEVN steps and the ISTEDDAS steps.

4.2.2 Binary star evolution

As for the single star evolution, binary stars are also evolved in SEVN only if both stars have greater masses than the chosen threshold. If, instead, only one of the two stars has a greater mass with respect to the threshold, that star will evolve as a single star in SEVN.

When ISTEDDAS detects a binary that is tight enough to be integrated with TSUNAMI (see the explanation on the decision making in Subsec.3.2.1), if both the stars have masses greater with respect to the threshold and the system is gravitationally bound, a binary is created in SEVN. It has already been explained that the time steps in SEVN are adaptive, and that we do not evolve stars one step at a time: the stars keep evolving until their mass has changed beyond a certain percentage threshold. Thus, because of the nature of the time steps, creating a binary in SEVN is not an easy task. First of

all, it is necessary to synchronize the two stars, to do so, for each evolving star, we create two of them to track both the actual and the last state of the stars. In this way, when a binary is created, we can bring back the two involved stars to their last state, and evolve them again until the exact moment of the binary creation. In particular, we evolve the stars until they overpass that moment for one step, then we restore their state and redo the very last step with the needed time step (using a specific function of SEVN to impose a time step). Therefore, at the creation of the binary, the two stars have the same age in SEVN, ISTEEDDAS, and TSUNAMI, as it is supposed to be.

The selected binaries are evolved by SEVN for multiple time steps until either one of the two masses, the eccentricity, or the semi-major axis of the system has changed beyond a certain percentage threshold (by default we choose 2%). Then, the inner dynamics of the binary is evolved with TSUNAMI while the dynamics of its center of mass is evolved, along with the rest of the star cluster, by ISTEEDDAS. Because of the binary evolution, the masses of the two stars change over time, so ISTEEDDAS interpolates the total mass of the system in the same way as it was for the single stellar evolution. However, we can not use the same approach with TSUNAMI due to the way its algorithm works: it uses the relative error of the energy of the system to adjust its internal time step, however, by interpolating the masses, we cannot preserve the conservation of energy and the algorithm will not be able to compute the regularized time steps. In the worst-case scenario, the Bulirsch-Stoer algorithm will not be able to converge, blocking the whole simulation. In order to avoid this problem, we wait for the binary system to be synchronized in SEVN and TSUNAMI, then we communicate the changed masses from SEVN to TSUNAMI. The time synchronization between SEVN binary evolution and TSUNAMI dynamical evolution is achieved in the way of the synchronization of two single stars before the creation of the binary. Thus, for each binary, we have two copies of it to track both the actual and the last state of the binary stars. When the binary feels that, on the next step, the dynamical evolution will overpass its evolution time, the binary is reset to its last state and re-evolved to the exact time when TSUNAMI will arrive with its own time step. We also implement another check in TSUNAMI: whether the eccentricity or the semi-major axis of the system has changed beyond a certain percentage threshold (on default we choose 10%), TSUNAMI will ask for a time synchronization with SEVN in advance with respect to the time set by SEVN; this also happens if TSUNAMI decides to terminate the binary. Somebody could notice that using this method we evolve every binary star two times, however, this will never become a computational bottleneck since SEVN is orders of magnitudes faster than the dynamical integrators of ISTEEDDAS and TSUNAMI.

When, in the next step, the binary is perfectly synchronized in SEVN and TSUNAMI, it will be possible to coherently communicate between the two codes. SEVN has to communicate to TSUNAMI the new masses of the two stars, and the new orbital parameters, that are the semi-major axis and the eccentricity (the evolution of binaries can change these parameters because of the exchange of mass in the system), and simultaneously, TSUNAMI has to communicate to SEVN its own new orbital parameters. The fact that the orbital parameters are influenced simultaneously by the dynamics and the binary stellar evolution, complicates this otherwise trivial communication. What would

physically happen in reality is that the orbital parameters would continuously vary because of both the contributions happening simultaneously, however, in our case, we will approximate this behavior by combining the two contributions every time that a synchronization happens. This is the very reason why we use those thresholds to stop the codes and synchronize them, to combine the orbital parameters in the smoothest way possible. The orbital parameter combination is:

$$\begin{aligned} a_1 &= a_0 + da_{\text{SEVN}} + da_{\text{TSUNAMI}}, \\ e_1 &= e_0 + de_{\text{SEVN}} + de_{\text{TSUNAMI}}, \end{aligned}$$

where a_1 and e_1 are the new combined semi-major axis and eccentricity respectively, a_0 and e_0 are the previous ones, which is the same for both the codes because of the previous synchronization, and finally da and de are the contributions from SEVN and TSUNAMI for the actual step and are computed as the difference between the values at the end of the step minus the values at the end :

$$\begin{aligned} da_{\text{SEVN}} &= a_{1,\text{SEVN}} - a_{0,\text{SEVN}}, \\ de_{\text{SEVN}} &= e_{1,\text{SEVN}} - e_{0,\text{SEVN}}, \\ da_{\text{TSUNAMI}} &= a_{1,\text{TSUNAMI}} - a_{0,\text{TSUNAMI}}, \\ de_{\text{TSUNAMI}} &= a_{1,\text{TSUNAMI}} - a_{0,\text{TSUNAMI}}. \end{aligned}$$

At this point TSUNAMI has the new orbital parameters and communicates them to SEVN that updates the old ones. However, since TSUNAMI use Cartesian coordinates to integrate systems, we have to translate these new orbital parameters into new positions and velocities for the two bodies. The starting point is for TSUNAMI to compute da_{TSUNAMI} and de_{TSUNAMI} , to do it we switch from Cartesian coordinates, that are positions and velocities (x, y, z, v_x, v_y, v_z) , to Keplerian coordinates, that are 6 orbital parameters: eccentricity (e), semi-major axis (a), inclination (i), longitude of the ascending node (Ω), argument of periapsis (ω) and true anomaly (ν), see appendix B for a detailed description. Then, using the new eccentricity and semi-major axis but maintaining fixed the old i , Ω , ω and ν , we pass again to Cartesian coordinates finding the relative positions of the two stars. Since SEVN does not give any information about the phase of the two bodies in their orbits, we do not have any way of retrieving those four angles, thus keeping the old ones from TSUNAMI is the only way to return to Cartesian coordinates.

Moreover, during this operation, we fix the position of the center of mass of the binary, that is like hypothesizing that the binary system loses mass isotopically, and we recompute positions and velocities of the two bodies with respect to the center of mass. To do so we use the following equations:

$$\mathbf{r}_{COM} = \frac{\mathbf{r}_1 m_1 + \mathbf{r}_2 m_2}{m_1 + m_2}, \quad (4.52)$$

$$\mathbf{v}_{COM} = \frac{\mathbf{v}_1 m_1 + \mathbf{v}_2 m_2}{m_1 + m_2}, \quad (4.53)$$

$$\mathbf{r}_{12} = \mathbf{r}_2 - \mathbf{r}_1, \quad (4.54)$$

$$\mathbf{v}_{12} = \mathbf{v}_2 - \mathbf{v}_1, \quad (4.55)$$

to obtain the final result:

$$\mathbf{r}_1 = \mathbf{r}_{COM} - \mathbf{r}_{12} \frac{m_2}{m_1 + m_2}, \quad (4.56)$$

$$\mathbf{r}_2 = \mathbf{r}_{COM} + \mathbf{r}_{12} \frac{m_1}{m_1 + m_2}, \quad (4.57)$$

$$\mathbf{v}_1 = \mathbf{v}_{COM} - \mathbf{v}_{12} \frac{m_2}{m_1 + m_2}, \quad (4.58)$$

$$\mathbf{v}_2 = \mathbf{v}_{COM} + \mathbf{v}_{12} \frac{m_1}{m_1 + m_2}. \quad (4.59)$$

Finally, if the regularized system has more than 2 bodies, TSUNAMI shifts the total center of mass of the system to zero to be consistent.

4.2.3 Energy conserving scheme

ISTEDDAS implements the Hermite 6th order integrator, which is an energy-conserving scheme, therefore we expect the total energy of the simulation to be conserved over time, except for the accumulation of numerical errors. On default, the total energy of the star cluster energy is computed considering point-mass stars with constant masses:

$$E = K + U = \frac{1}{2} \sum_{i=0}^N \left(m_i |\mathbf{v}_i|^2 - \sum_{j \neq i}^N \frac{m_i m_j}{|\mathbf{r}_{ij}|} \right), \quad (4.60)$$

here the potential energy U is divided by 2 because we are computing twice all the couples (i, j) of stars, and we have assumed the gravitational constant $G = 1$. It is crucial for an N-body code to conserve the total energy because the check on the relative error of the energy:

$$\frac{\Delta E}{E(t_0)} = \frac{E(t) - E(t_0)}{E(t_0)} = 0, \quad (4.61)$$

is a powerful tool to check whether the simulation has any numerical or algorithmic errors.

The addition of stellar evolution with SEVN breaks the conservation of energy because of the multiple stellar evolution processes simulated that continuously decrease the mass of the evolving stars. Because of the mass losses, it is impossible to conserve the total energy of the system computing it as above. Therefore, to be able to conserve the energy, we re-inject the energy of the lost mass using \dot{m} . Theoretically, if the mass is constant the time derivative of the total energy would be always zero, in this case, with a varying mass, we would have instead:

$$\dot{E} = \frac{1}{2} \sum_{i=0}^N \left(\dot{m}_i |\mathbf{v}_i|^2 - \sum_{j \neq i}^N \frac{\dot{m}_i m_j + m_i \dot{m}_j}{|\mathbf{r}_{ij}|} \right), \quad (4.62)$$

or, more simply:

$$\dot{E} = \sum_{i=0}^N \left(\frac{1}{2} \dot{m}_i |\mathbf{v}_i|^2 - \sum_{j \neq i}^N \frac{\dot{m}_i m_j}{|\mathbf{r}_{ij}|} \right). \quad (4.63)$$

All the derivatives which do not involve \dot{m} cancel each other out because, as mentioned before, if the mass is constant $\dot{E} = 0$. Thus, for each i star of the system, we integrate in time the lost energy:

$$E_{lost,i} = \int_0^t \dot{E}_i dt. \quad (4.64)$$

To numerically compute it, at each distant step and for each star, we accumulate $\dot{E}_i \Delta t_f$. At this point, we have retrieved the conservation of the energy as:

$$\frac{\Delta E}{E(t_0)} = \frac{E(t) - E(t_0) - E_{lost}}{E(t_0)} = 0, \quad (4.65)$$

where E_{lost} is the summation of $E_{lost,i}$ on all the evolving stars of the system.

Chapter 5

Numerical tests

In this chapter, I am going to show the preliminary results from the code. In particular, I will show the benchmark of the N-body code ISTEDDAS,

5.1 ISTEDDAS tests

The benchmarks in this section are done on the new CINECA supercomputer Leonardo¹, that today is the fourth most powerful supercomputer in the world accordingly to the TOP500 list². In Table 5.1 there are the specifics of the GPU nodes of Leonardo.

CPU	: Intel(R) Xeon(R) Platinum 8358 2.60GHz (32 cores, 1 thread per core)
RAM	: 512 (8 × 64) GB DDR4 3200 MHz
GPU	: 4 NVIDIA Ampere 100
GRAM	: 256 (4 × 64) GB HBM2
Network	: NVIDIA Mellanox HDR DragonFly++ 200Gb/s

Table 5.1: Leonardo’s nodes specifics. See [293] for further details about Leonardo’s architecture.

I will use a maximum of 2 nodes with 4 parallel GPUs each for the scaling tests, therefore 8 GPUs at maximum. In particular I will run scaling tests on 1, 2, 4 and 8 GPUs for star clusters with 2048 (2^{11}), 4096 (2^{12}), 8192 (2^{13}), 16384 (2^{14}), 32768 (2^{15}), 65536 (2^{16}), 131072 (2^{17}), and 262144 (2^{18}) stars (as shown in Table 5.2). The star clusters are generated using the MCLUSTER³ code [158]. All these clusters have a King density profile with $W_0 = 5$ (dimensionless parameter which specifies the model concentration), a half-mass radius of 2 pc, a velocity dispersion of $\sigma = 1.3127$ km/s, they are at the virial equilibrium, and their initial mass function follows the Kroupa

¹Check the link <https://wiki.u-gov.it/confluence/display/SCAIUS/UG3.4%3A+Leonardo+UserGuide> for extra details about Leonardo.

²TOP500 June 2023 link: <https://www.top500.org/lists/top500/2023/06/>

³The code is public and available here: <https://github.com/ahwkuepper/mcluster>.

IMF within the range of star’s masses $0.1M_{\odot} < M_* < 150M_{\odot}$. Moreover, these clusters do not have binary stars, tidal field, mass segregation, or fractality. All the simulations reach a total time of 10 in code units, check Table 5.2 to see how many Myr this corresponds for each simulation.

N_{stars}	M_{tot} [M_{\odot}]	ρ [M_{\odot}/pc^3]	t_{relax} [Myr]	T_{tot} [Myr]	$\tau_{\%}$
2048 (2^{11})	1322.4	57.37	109.71	4.11	3.75%
4096 (2^{12})	2597.9	77.53	82.65	2.93	3.54%
8192 (2^{13})	5165.0	154.13	41.82	2.08	4.97%
16384 (2^{14})	10398.5	310.31	20.63	1.46	7.07%
32768 (2^{15})	20429.9	609.66	10.69	1.04	9.73%
65536 (2^{16})	41664.7	1243.34	5.14	0.73	14.20%
131072 (2^{17})	83983.8	2506.21	2.53	0.52	20.55%
262144 (2^{18})	169716.0	5064.59	1.24	0.36	29.04%

Table 5.2: List of simulations made for the scaling tests of ISTEDDAS. It contains: the total number of stars, the total mass (in M_{\odot}), the two-body relaxation timescale computed with Eq.1.8 (in Myr), the total simulated time (in Myr), and the total simulated time as a percentage of the relaxation time: $\tau_{\%} = T_{tot}/t_{relax} \cdot 100$.

First of all, in Fig.5.1 I show the relative error on the total energy of the cluster (see Eq.4.61): note how well the energy conservation is maintained by the Hermite 6th order integrator for all the simulations made for the scaling tests. From the plot, one could think that the bigger the number of stars, the faster the error grows. In reality, the rate at which the error grows depends on how many t_{relax} were simulated. So, the total simulated time as a percentage of the relaxation time ($\tau_{\%} = T_{tot}/t_{relax} \cdot 100$, see Table 5.2) tells us that higher the number of particles higher $\tau_{\%}$, and so faster the error grows (for the specifically chosen settings of these simulations). In theory, in a set of simulations with settings chosen ad hoc to have $\tau_{\%}$ equal in all the simulations, we would see a similar error plot for all the cases. However, the error is always maintained quite low (maximum $\sim 10^{-5}$), and it is consistent among the simulations with different numbers of GPUs, proving the correctness of the multi-GPU implementation.

In Fig.5.2 and Fig.5.3 I show the results of the scaling tests on a single node. In particular, in Fig.5.2 I show the larger contributions to the total running time of the simulations: the ANN tree contribution (see the subsection 2.4.3), the MPI contribution, the computation of the forces due to far stars ($\mathbf{a}_{far,new}$ in Section 2.3), and the contribution from the searching algorithm that determines which stars need to be integrated for each step. Since the ANN tree contribution is the larger one, I also show its two main internal contributions: The tree construction, and the search for neighbours, which is the most computationally expensive operation in the code. Instead, in Fig.5.3 I show less important contributions together with the total running time for reference: the computation of the forces due to far stars, close stars, and the contribution from the old neighbours (respectively $\mathbf{a}_{far,new}$, $\mathbf{a}_{close,new}$, and $\mathbf{a}_{close,old}$ in Section 2.3), the contributions from the predictor and the corrector, the contribution from updating the time-steps of all the stars at each step, and the contribution from

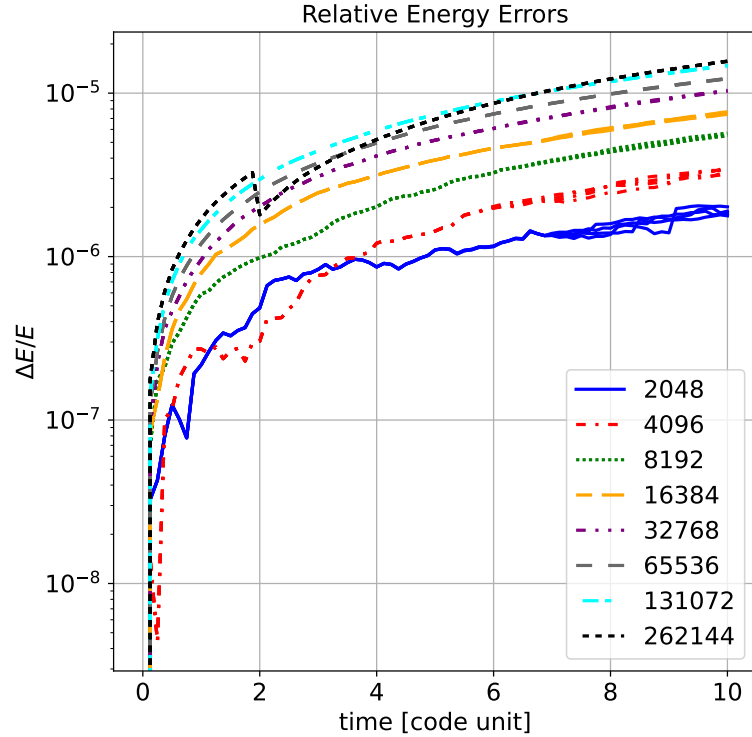


Figure 5.1: Relative error on the total energy of the system (see Eq.4.61) versus the time in code units for each scaling test simulation. For each simulation multiple lines are shown, one for each number of GPUs used (1,2,4, and 8), they have the same style and color since they superpose almost perfectly, as expected.

the memory transfers between CPUs and GPUs. In Fig.5.4 I show the scaling of the far forces kernel alone. In order to highlight how it performs, I plot the running time with a single GPU with the running time for other cases. The computation of the forces was the bottleneck in N-body codes for decades, therefore we optimize it as much as possible, obtaining a remarkable result. The cases with few stars do not scale well, as expected, since a single GPU can already handle that number of stars, and dividing the work just introduces extra operations: memory transfers, reductions, and gatherings. However, from 32768, stars the scaling on a single node becomes perfect, while on multiple nodes at least 65536 stars are needed to improve the performance. In Fig.5.5 I show the results of the scaling tests on two nodes: simulation characteristics are the same as in Fig.5.2, except for the fact I show just the two cases with more stars (131072 and 262144). From the plots, it is clear that the MPI implementation slows down ISTEDDAS too much, making it even worse than running the code on a single node.

The reason behind this behavior is that the far forces kernel is the only part of the code that can scale with an increasing number of GPUs. ISTEDDAS was designed in this way because that was the main bottleneck for N-body codes. Clearly from all the scaling tests that I have shown, the actual bottleneck of the code is the ANN tree and the MPI implementation, and both of these bottlenecks can be solved. For the

tree, as I extensively discussed in Section 2.4.3, the solution would be to switch to another library, in particular, we could use FLANN, which already runs on GPU and can scale on multiple GPUs. Another possible solution would be to think about a new algorithm to further reduce the number of tree constructions within each macro step, but this is beyond the scope of this thesis. For MPI, the solution would be to exploit the new technology in the new GPU supercomputers. For example, each node of the CINECA's supercomputer Leonardo is provided with a new NVIDIA Mellanox HDR Dragonfly++ network card that enables direct communication between GPUs from different nodes, and provides some preliminary calculations when needed, in order to speed up communications even more (for example if a reduction operation is called in the code). Moreover, the communication between GPUs on the same nodes can avoid passing through the CPU because of the InfiniBand connections between GPUs. Nowadays, almost all the most powerful supercomputers in the world are provided with GPUs and use a similar technology to speed up communications among accelerators. Among them, Frontier⁴ and LUMI⁵ (that use AMD GPUs) or Leonardo⁶, Summit⁷, and Sierra⁸ (that use NVIDIA GPUs). Clearly, this technology represents the future of GPU computation. In order to use such technology one could use the CUDA-Aware MPI (for NVIDIA hardware), which is an implementation of MPI that can exploit the new connections between GPUs, or one could use NCCL, an NVIDIA library for communication that underneath uses CUDA-Aware MPI. These optimizations will be done in future works related to the development of ISTEDDAS.

⁴First position in the TOP500, website: <https://www.olcf.ornl.gov/frontier/>

⁵Third position in the TOP500, website: <https://www.lumi-supercomputer.eu/>

⁶Fourth position in the TOP500, website: <https://leonardo-supercomputer.cineca.eu/it/home-it/>

⁷Fifth position in the TOP500, website: <https://www.olcf.ornl.gov/olcf-resources/compute-systems/summit/>

⁸Sixth position in the TOP500, website: <https://hpc.llnl.gov/hardware/compute-platforms/sierra>

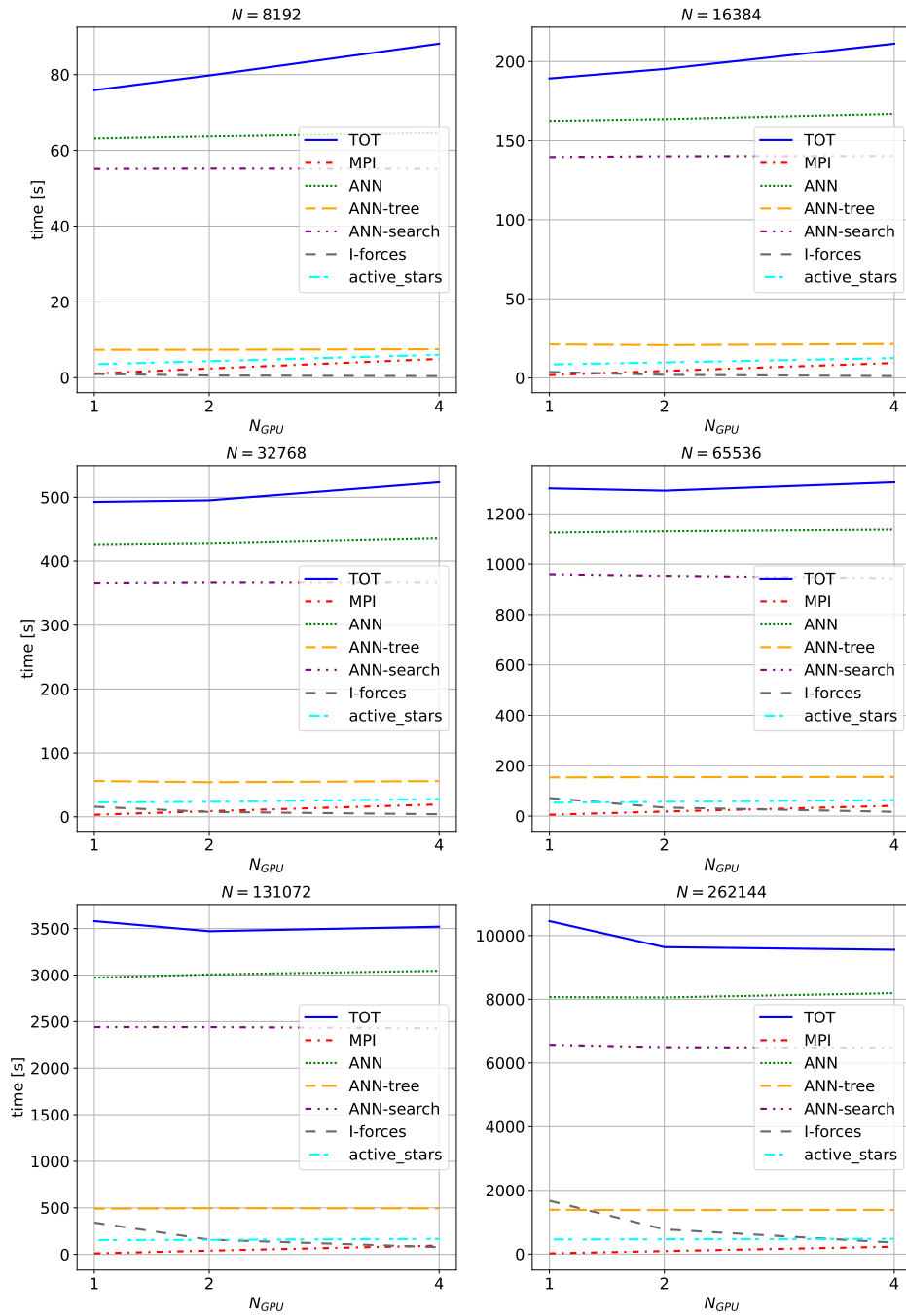


Figure 5.2: Scaling tests of ISTEDDAS. In each panel, it is shown, for a certain total number of stars N , the measured times versus the number of used GPUs (N_{GPU}). The six most important timings are shown together with the total time (“TOT” in blue): the MPI contribution (“MPI” in red), the ANN tree contribution (“ANN” in green), the tree construction and tree search contributions to ANN (“ANN-tree” in yellow, and “ANN-search” in purple), the contribution of the far forces computation (“I-forces” in grey), and the search for new active stars contribution (“active_stars” in cyan).

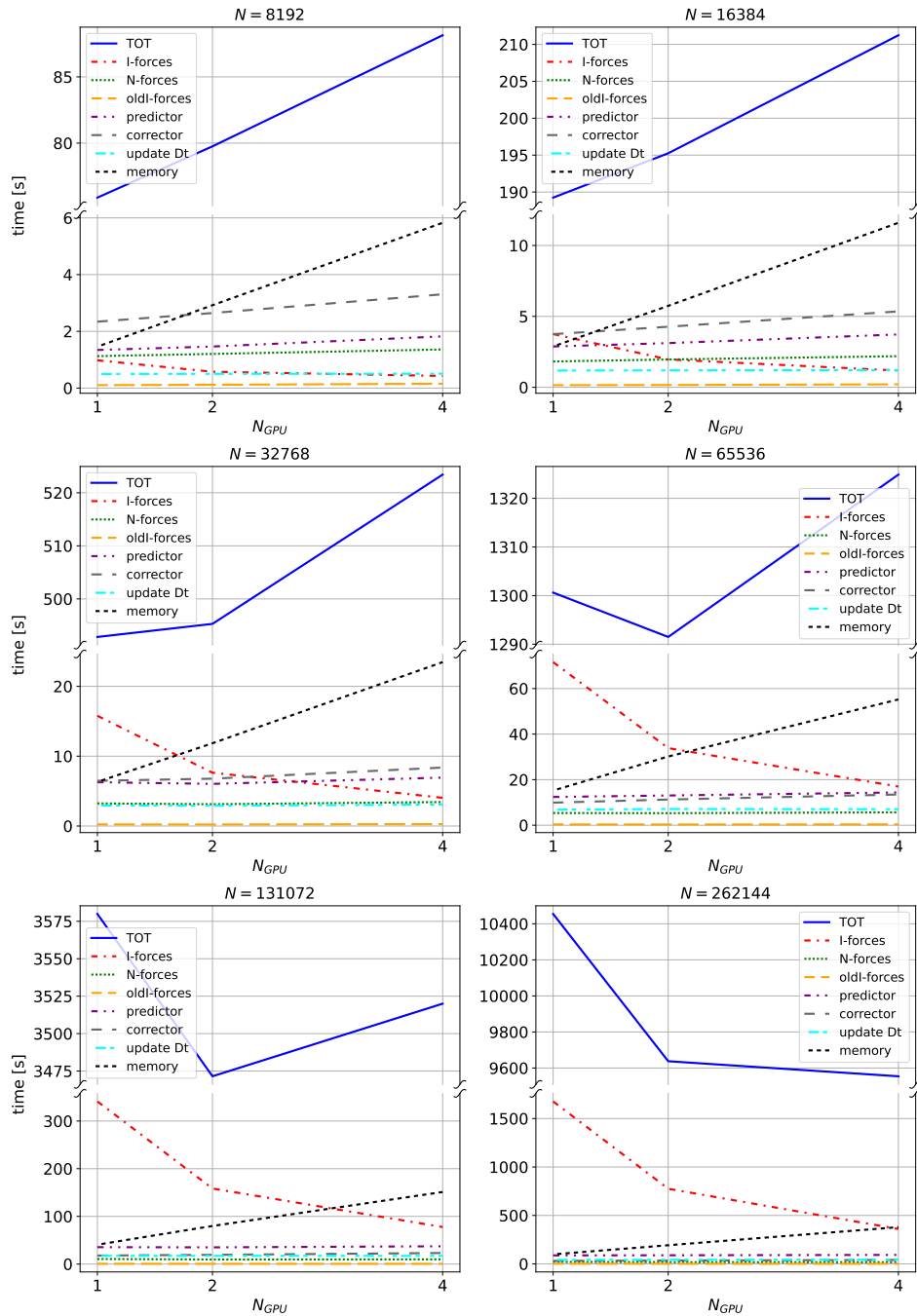


Figure 5.3: Scaling tests of ISTEEDDAS. In each panel, it is shown, for a certain total number of stars N , the measured times versus the number of used GPUs (N_{GPU}). The seven important but less costly timings are shown together with the total time (“TOT” in blue): the contribution of the far, near, and previous near forces computations (“I-forces” in red, “N-forces” in green, and “oldI-forces” in yellow), the predictor contribution (“predictor” in purple), the corrector contribution (“corrector” in grey), the contribution for updating the time-steps (“update_Dt” in cyan), and the memory transfer between CPUs and GPUs contribution (“memory” in black).

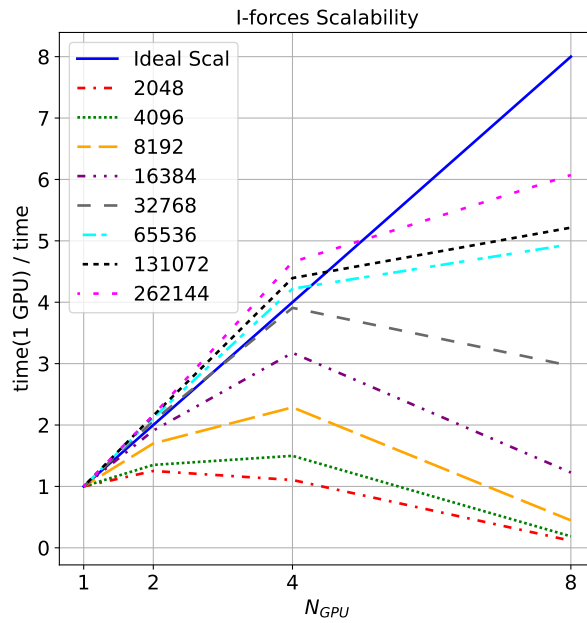


Figure 5.4: Scaling tests of ISTEDDAS. The plot shows the ratio between the measured times for a single GPU and the total number of used GPUs (t_{1GPU}/t_{NGPU}) versus the number of used GPUs (N_{GPU}). The blue line shows the ideal scaling, the other lines show the scaling of the far forces computation kernel for each simulation.

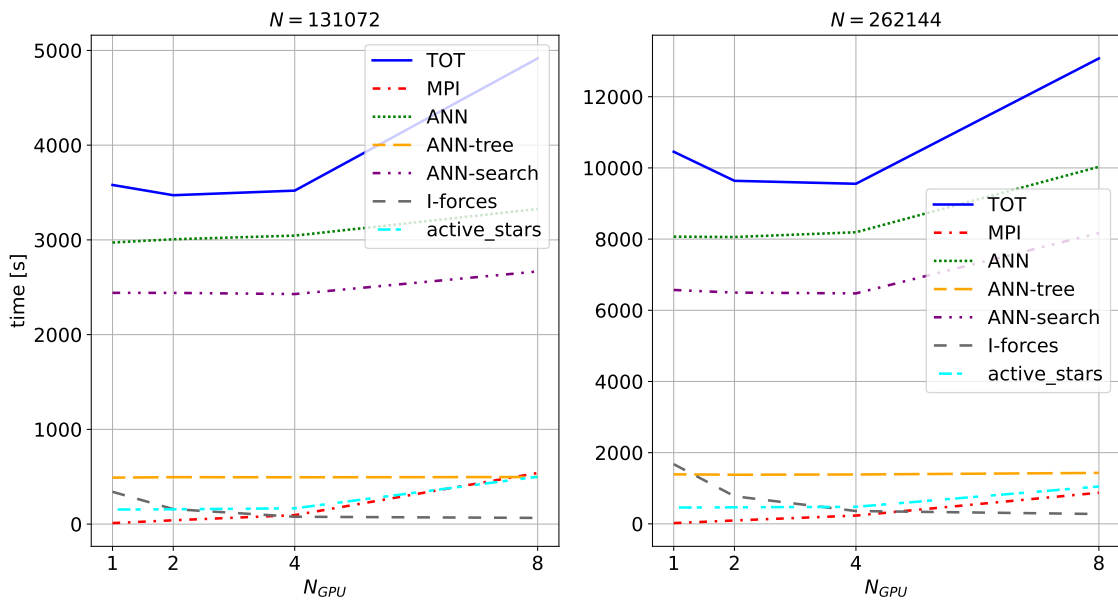


Figure 5.5: Scaling tests of ISTEDDAS. Same plot type of Fig.5.2. In this case with the “8 GPUS” entry on the x-axis and just for the two more expensive simulations (N equal to 2^{17} and 2^{18}).

5.2 TSUNAMI tests

The following tests are made on a laptop, its specifications are in Table 2.1. For Fig.5.6 two simulations were done, both of them on the same star cluster with 2048 stars and one tight binary system. The two simulations run for the same amount of time on my laptop (5 minutes). The one with ISTEEDAS alone was able to evolve the star cluster for just ~ 1400 years. During the simulation, the error keeps increasing almost linearly (red and red dashed lines), this is due to the vicinity of the two stars in the binary: the Hermite 6th order integrator is a powerful tool but is not symplectic and cannot integrate correctly such a tight binary system. Moreover, the block time-step method (see Section 2.2) assigns the smallest possible time-step to the system because of the enormous acceleration and its derivatives involved (see Eq.2.9). As a consequence, the simulation takes so many steps to progress that the numerical error accumulation becomes an important contribution to the total energy error of the simulation. Thus, ISTEEDAS alone gets “stuck” accumulating numerical errors in simulation with tight binaries, in this case even a tiny star cluster, as the one in this example, could become challenging to simulate. Instead, the simulation with TSUNAMI was able to evolve the star cluster for ~ 40000 years keeping the relative error on the energy of the star cluster stable under 10^{-7} (blue dashed line), since the binary was correctly integrated with the ARC integrator with a minimal error accumulation (green dotted line). This plot demonstrates the importance of using two distinct integrators for direct N-body simulation of star clusters: one to take care of long-range interactions and one to take care of tight systems such as binary stars, hierarchical systems, and close encounters.

In Fig.5.7 and Fig.5.8 two examples of hierarchical systems are shown, an unstable one and a stable one respectively. Both of them have three levels of zoom, in order to show both the motion of the overall system and the specific motion of the tight binaries. In both the plot the real movement of stars in the combination ISTEEDAS+TSUNAMI came out: TSUNAMI integrates the internal motion of the system (binary stars or hierarchical system), while ISTEEDAS integrates the motion of its center of mass in the cluster. Therefore, when plotting the orbits, a “twitchy” movement came out, where the orbits do not evolve smoothly together with the center of mass, they evolve for the amount of time of the next ISTEEDAS step but fixed in the previous center of mass coordinates. Moreover, in Fig.5.7, one can also see how the decision-making (in particulate the condition in Eq.3.14) keeps this system in TSUNAMI even when the third body and the inner binary are very far at their apoastron. This is necessary until the three bodies are in a bound configuration with a very tight periastron in order to avoid the system going in and out from TSUNAMI at each orbit.

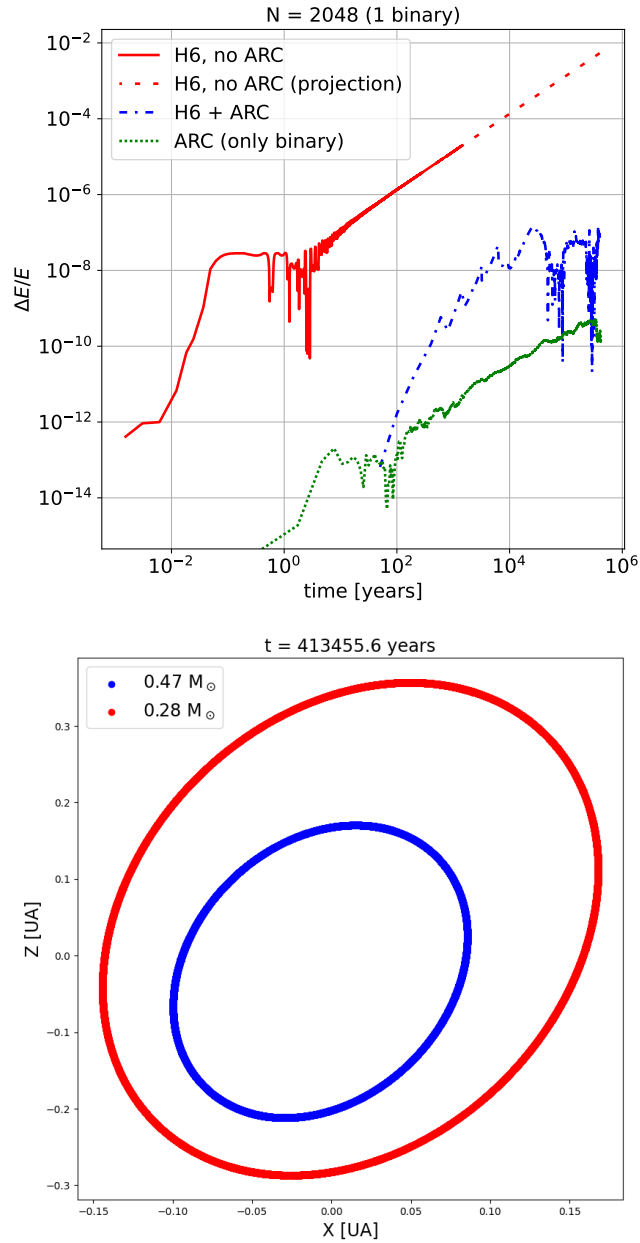


Figure 5.6: Simulation of a star cluster with 2048 stars and a single binary made with ISTEEDAS alone using just the Hermite 6^{th} order integrator, and then made with ISTEEDAS+TSUNAMI, using the ARC integrator for the binary. The top panel shows the relative error of the energy of the star cluster versus the time in years. In red is shown the error for the simulation with ISTEEDAS alone, and the red dashed line shows the projection of the error. In blue is shown the error for the simulation where the binary is integrated by TSUNAMI, and in green is shown the error of the ARC integrator (TSUNAMI) on the binary alone. The bottom panel shows, in the x - z plane (in astronomical units), the evolution of the orbit of the binary. The coordinates are re-centered in the center of mass of the binary in order to show its stability in 413455 years of evolution.

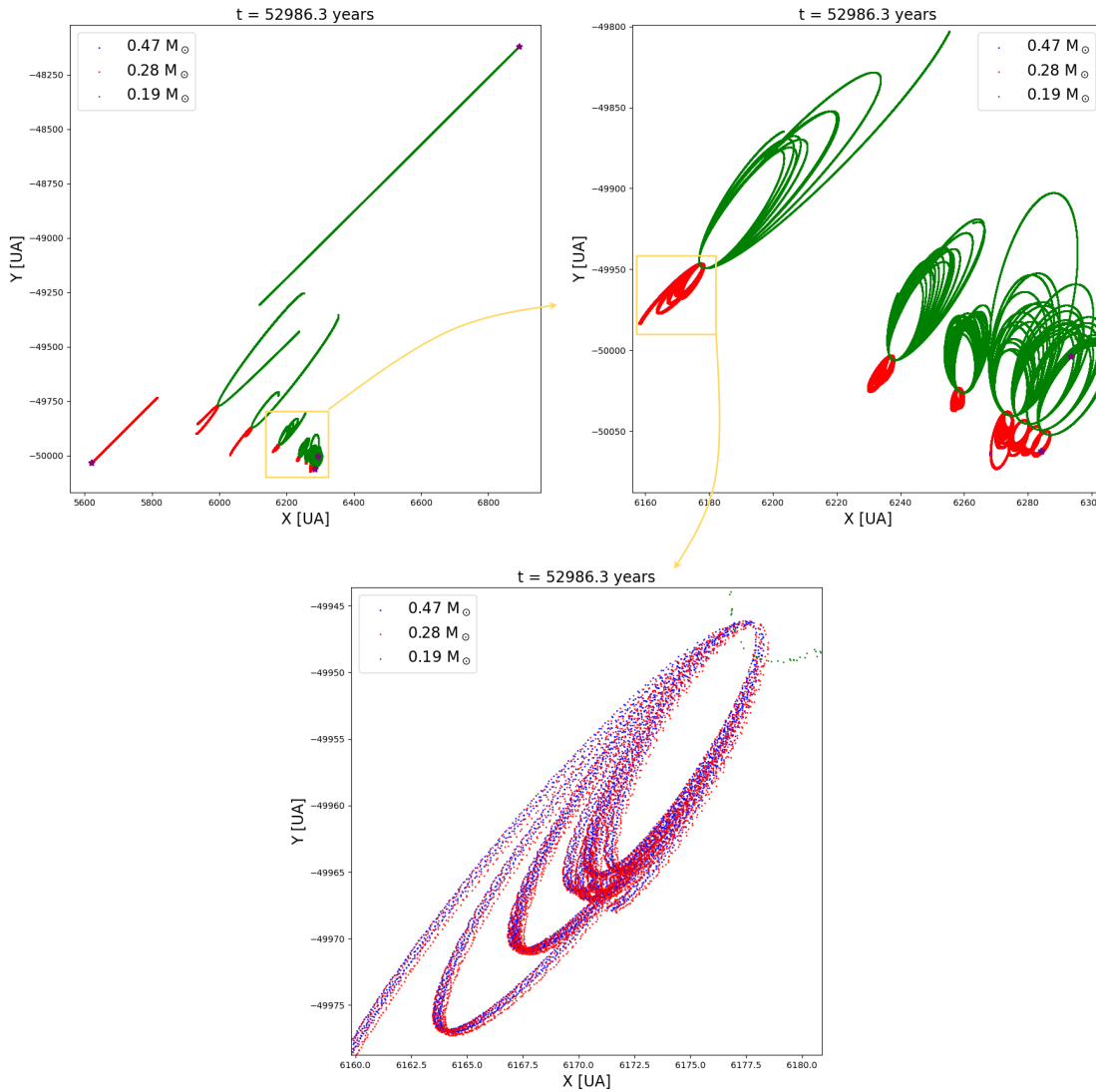


Figure 5.7: Example of the evolution of a hierarchical system in an unstable configuration. The following plots are in the x - y plane (in astronomical units) where the position (0,0) is the center of mass of the star clusters. The inner binary is formed by two stars with masses $0.47M_{\odot}$ (blue) and $0.28M_{\odot}$ (red), and the third body has a mass of $0.19M_{\odot}$ (green). The top-left panel shows the entire evolution of the system for 52986 years, from its beginning to its disruption. The top-right panel is a zoom of the yellow square in the first panel, it shows the orbits in the initial part of the evolution. The bottom panel is a zoom of the yellow square in the second panel, it shows the orbit of the inner binary, which is so tight is not visible in the other two plots.

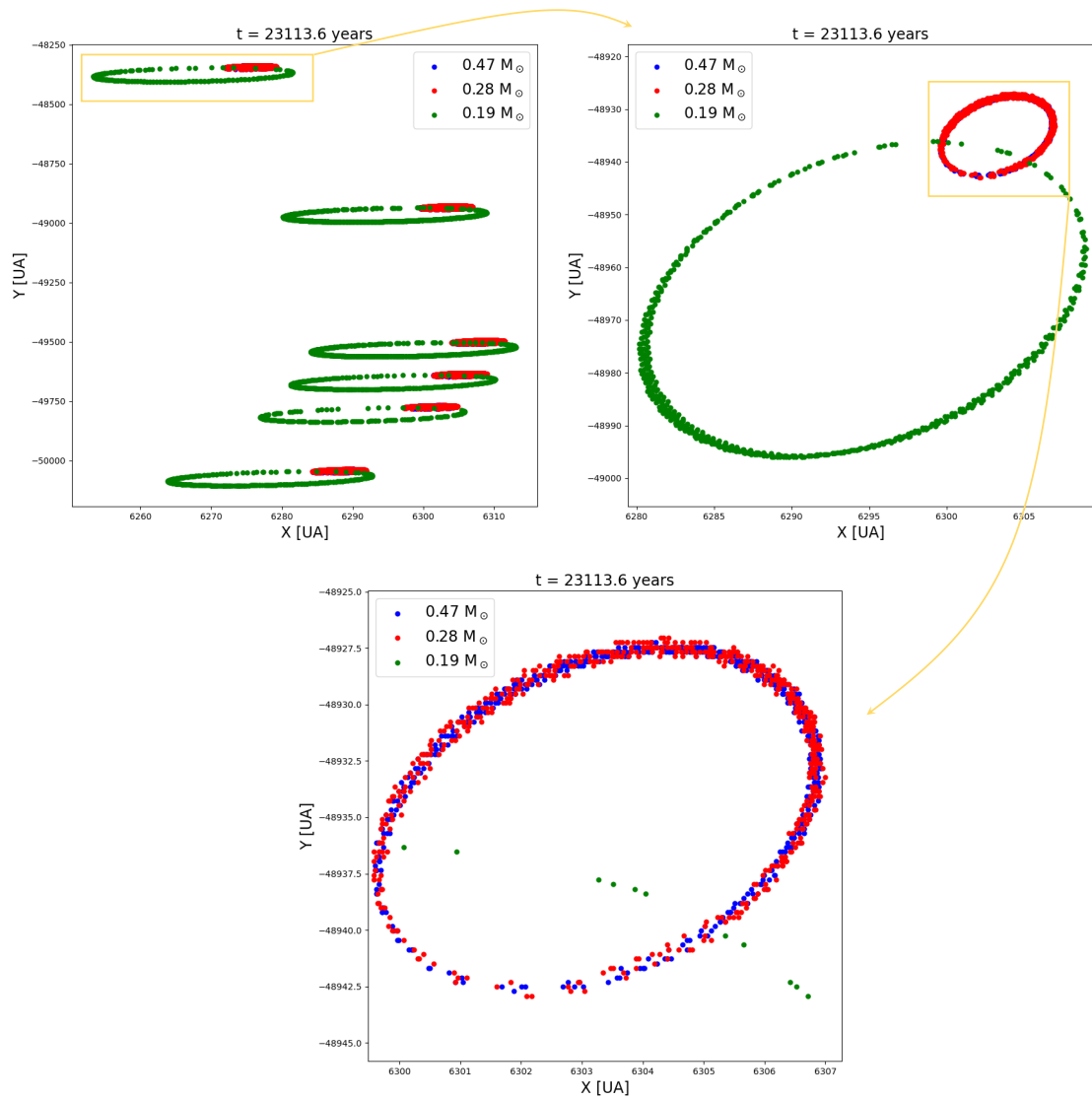


Figure 5.8: Example of the evolution of a hierarchical system in a stable configuration. The following plots are in the x - y plane (in astronomical units) where the position (0,0) is the center of mass of the star clusters. The inner binary is formed by two stars with masses $0.47M_{\odot}$ (blue) and $0.28M_{\odot}$ (red), and the third body has a mass of $0.19M_{\odot}$ (green). The top-left panel shows the entire evolution of the system for 23113 years. The top-right panel is a zoom of the yellow square in the first panel, and the bottom panel is a zoom of the yellow square in the second panel, it shows the orbit of the inner binary, which is so tight is not visible in the other two plots.

Conclusions

In this thesis work, I presented the strategies in place to develop ISTEDDAS, a new direct N-body code written in C++ and CUDA, that is designed to run natively on GPUs (proven to be much more proficient than CPUs in handling highly parallelizable problems) and that uses a combination of a high-order integrator (Hermite 6th order) with block time-step and the Ahmad-Cohen neighbours scheme to significantly speed up high-accuracy N-body simulations.

Direct N-body simulations of star clusters still struggle to resolve small-scale binary interactions while simulating large systems simultaneously. Achieving high resolution in areas where binary interactions occur is computationally demanding and often limits the size of the simulated cluster or the number of particles that can be realistically tracked. Some codes avoid a direct N-body approach to solve this computational problem (e.g. using tree-based codes) and, although the statistical properties of star clusters are reproduced correctly, they do not compute precisely the trajectories of stars, overall losing precision. On top of this, most N-body codes are coupled with outdated population-synthesis codes to evolve stars. These population-synthesis codes are difficult to update with the recent prescriptions for single and binary stellar evolution.

ISTEDDAS is expected to overcome the shortcomings of current state-of-the-art N-body codes.

ISTEDDAS can accurately integrate very tight binaries, strong gravitational interactions, and hierarchical few-body systems thanks to the coupling with the state-of-the-art code TSUNAMI, which implements the Algorithmic Regularization Chain combined with the Bulirsch-Stoer method. This allows us to resolve all the spans of spatial and temporal scales of star clusters and to investigate the formation and evolution of compact-object binaries (i.e., the progenitors of the gravitational-wave events observed by the LIGO-Virgo-KAGRA collaboration) with high accuracy.

ISTEDDAS has also been coupled with the population synthesis code SEVN, a new, up-to-date population-synthesis code based on look-up tables, that takes care of the evolution of both single and binary stars. Because of the use of look-up tables, updating SEVN does not require much effort and this makes it the perfect tool in order to keep the simulations always updated with the new stellar evolution prescriptions.

At the moment, a preliminary version of ISTEDDAS coupled with TSUNAMI and SEVN is already functional, and some results have been presented in this thesis. The interface ISTEDDAS – TSUNAMI supports the dynamical evolution of tight systems and binaries and the interface ISTEDDAS – SEVN supports the evolution of single stars. Binary stellar evolution, which represents the final coupling of all three codes, is currently

under testing.

From the point of view of the performance, ISTEEDDAS demonstrates to be very effective in computing the forces within the star cluster. In fact, while the raw complete computation of force scales as N^2 , the kernel that computes forces in ISTEEDDAS scales roughly linearly on multiple GPUs (see Fig.5.4). However, the overall performance of the code is still sub-optimal since all the extra operations made to optimize the forces computation are still to be fully optimized, especially the ANN-tree part. Optimization strategies are possible and they are currently under discussion.

TSUNAMI already demonstrates its efficiency in handling tight systems with respect to the ISTEEDDAS integrator (see Fig.5.6). In this thesis, we presented some preliminary results. However, the interface is still under intensive testing: there are still some peculiar cases in which the decision-making algorithm is sub-optimal.

SEVN was the last addition and its interface and it seems to have almost no impact on the performance of the code since both ISTEEDDAS and TSUNAMI are significantly more computationally demanding.

Regarding the future of the code, the plan is to continue developing and optimizing the interfaces, also implementing the one between TSUNAMI and SEVN. We plan to further optimize the code by implementing a new GPU library for the approximate nearest-neighbors search algorithm to overcome the current bottleneck of the N-body integrator, and by implementing the GPU version of TSUNAMI to speed up the parallel integration of many regularized systems, in order to optimize the code for star clusters with a high fraction of binary systems. We also plan to implement the possibility of adding an external potential to the force calculation in order to simulate the interaction of dense stellar systems with an external tidal field (e.g., host galaxy).

The combination ISTEEDDAS – TSUNAMI – SEVN, once 100% operational, will be able to help investigate a plethora of different problems related, in general, to star clusters and galaxies, not only gravitational waves from compact binary coalescences. The code will be able to accurately simulate all the trajectories in the system, comprehensive of binary systems and tight hierarchical systems, and to handle the stellar evolution of single and binary stars with up-to-date stellar prescriptions.

In essence, the code’s ability to efficiently simulate dense stellar systems while considering both stellar evolution and dynamics in a comprehensive manner is pivotal. ISTEEDDAS fills a critical gap, offering a more coherent and precise approach to understanding the multifaceted interactions within star clusters, their relation to compact object binaries and gravitational waves, their galactic context, and their impact on the evolution of galaxies as a whole.

Appendix A

GWs analytical derivation

Let us start with the Riemann curvature tensor in GR:

$$R_{\nu\rho\sigma}^{\mu} = \partial_{\rho}\Gamma_{\nu\sigma}^{\mu} - \partial_{\sigma}\Gamma_{\nu\rho}^{\mu} + \Gamma_{\lambda\rho}^{\mu}\Gamma_{\nu\sigma}^{\lambda} - \Gamma_{\lambda\sigma}^{\mu}\Gamma_{\nu\rho}^{\lambda}, \quad (\text{A.1})$$

where ∂_{ρ} is the compact form of the partial derivative:

$$\partial_{\rho} = \frac{\partial}{\partial x^{\rho}}, \quad (\text{A.2})$$

$\Gamma_{\nu\rho}^{\mu}$ are the Christoffel symbol:

$$\Gamma_{\nu\rho}^{\mu} = \frac{1}{2}g^{\mu\kappa}(\partial_{\nu}g_{\rho\kappa} + \partial_{\rho}g_{\nu\kappa} - \partial_{\kappa}g_{\nu\rho}), \quad (\text{A.3})$$

$g_{\mu\nu}$ is the general metric tensor:

$$g_{\mu\nu} = \eta_{\alpha\beta}\partial_{\mu}\xi^{\alpha}\partial_{\nu}\xi^{\beta}, \quad (\text{A.4})$$

ξ_{α} is the locally inertial coordinate system, and $\eta_{\mu\nu}$ is the metric tensor that governs the local inertial system, that is the Minkowskian, or flat, metric tensor:

$$\begin{vmatrix} -1 & 0 & 0 & 0 \\ 0 & +1 & 0 & 0 \\ 0 & 0 & +1 & 0 \\ 0 & 0 & 0 & +1 \end{vmatrix}. \quad (\text{A.5})$$

. The Riemann can be contracted to obtain the Ricci tensor:

$$R_{\mu\nu} = R_{\mu\lambda\nu}^{\lambda}, \quad (\text{A.6})$$

and the scalar curvature:

$$R = R_{\mu}^{\mu}. \quad (\text{A.7})$$

Using the above quantities one can write the Einstein field equations as:

$$R_{\mu\nu} - \frac{1}{2}g_{\mu\nu}R = 8\pi T_{\mu\nu}, \quad (\text{A.8})$$

where $T_{\mu\nu}$ is the momentum-energy tensor and describes the density and flux of energy and momentum in any space-time, and we assume $G = 1$ and $c = 1$. Let us now consider the weak field limit of GR, that is the linearized theory that arises when the field equations, are worked out under a first order expansion of a nearly-Minkowskian metric. This approach will also lead to the prediction of gravitational radiation, though in this limit we are neglecting the self-gravity by radiation itself. Let us then define:

$$g_{\mu\nu} = \eta_{\mu\nu} + h_{\mu\nu}, \quad |h_{\mu\nu}| \ll 1, \quad (\text{A.9})$$

where $h_{\mu\nu}$ is the perturbation. The Minkowski metric tensor, rather than the general metric tensor, will be used to raise or lower indices as a background metric to avoid the rise of second-order terms. Since any derivatives of the Minkowskian metric tensor yield 0, the Christoffel symbols become:

$$\Gamma_{\mu\nu\rho} = \frac{1}{2} (\partial_\nu h_{\rho\mu} + \partial_\nu h_{\rho\mu} - \partial_\mu h_{\nu\rho}), \quad (\text{A.10})$$

leading to the linearized Riemann tensor:

$$R_{\mu\nu\rho\sigma} = \partial_\rho \Gamma_{\mu\nu\sigma} - \partial_\sigma \Gamma_{\mu\nu\rho} = \frac{1}{2} (\partial_\rho \partial_\nu h_{\mu\sigma} \partial_\sigma \partial_\mu h_{\nu\rho} - \partial_\sigma \partial_\nu h_{\mu\rho} - \partial_\rho \partial_\mu h_{\nu\sigma}). \quad (\text{A.11})$$

with contractions

$$R_{\mu\nu} = R_{\mu\lambda\nu}^\lambda = \frac{1}{2} (\partial_\mu \partial_\lambda h_{\nu}^\lambda + \partial_\nu \partial_\lambda h_{\mu}^\lambda - \partial_\mu \partial_\nu h - \square h_{\mu\nu}), \quad (\text{A.12})$$

and

$$R = R_\nu^\mu = \partial^\mu \partial^\nu h_{\mu\nu} - \square h, \quad (\text{A.13})$$

where $h = h^\mu_\mu$, and $\square = \partial^\mu \partial_\mu$. Let us now impose the condition for harmonic coordinates:

$$\Gamma^\lambda = \eta^{\mu\nu} \Gamma_{\mu\nu}^\lambda = 0 \quad \longrightarrow \quad \partial_\mu h_\nu^\mu = \frac{1}{2} \partial_\nu h. \quad (\text{A.14})$$

Then, the Einstein tensor simplifies greatly, leading to the linearized field equations:

$$R_{\mu\nu} - \frac{1}{2} g_{\mu\nu} R = -\frac{1}{2} \left(\square h_{\mu\nu} - \frac{1}{2} \eta_{\mu\nu} \square h \right) = 16\pi T_{\mu\nu}. \quad (\text{A.15})$$

Finally, it is convenient to introduce the trace reversed field tensor

$$\bar{h}_{\mu\nu} = \frac{1}{2} \eta_{\mu\nu} h, \quad (\text{A.16})$$

for which $\bar{h} = -h$ and $\partial_\mu \bar{h}_\nu^\mu = 0$, and the linearized field equations are simply

$$\square \bar{h}_{\mu\nu} = -16\pi T_{\mu\nu}. \quad (\text{A.17})$$

The crucial consequence of the weak field equation is the prediction of gravitational radiation. In vacuum we have

$$\square \bar{h}_{\mu\nu} = \partial^\lambda \partial_\lambda \bar{h}_{\mu\nu} = (-\partial_t^2 + \nabla^2) \bar{h}_{\mu\nu} = 0, \quad (\text{A.18})$$

which is a set of 10 hyperbolic equations for gravitational waves propagating at the speed of light ($c = 1$). The simplest solution to look for is that for plane waves:

$$\bar{h}_{\mu\nu} = A_{\mu\nu} e^{ik_\lambda x^\lambda}, \quad (\text{A.19})$$

with $A_{\mu\nu}$ the amplitude tensor and $k_\mu = (\omega, \mathbf{k})$ the wave 4-vector. Using the Lorentz gauge one could demonstrate that $A_{\mu\nu}$ is a transverse-traceless (TT) tensor, that is:

$$A_{\mu\nu} u^\nu = 0, \quad A^\mu{}_\mu = 0, \quad (\text{A.20})$$

for a given time-like unit vector u^ν . The traceless condition leads to the simplification that $\bar{h}_{\mu\nu} = h_{\mu\nu}$. If we now choose a Lorentz frame where $u_\mu = (1, 0, 0, 0)$ and spatial propagation along z alone, then $k_\mu = (\omega, 0, 0, k_z = \omega)$ and the plane wave is described by

$$h_{\mu\nu}^{TT} = A_{\mu\nu} e^{i(k_z z - \omega t)}. \quad (\text{A.21})$$

The only non-vanishing components are

$$A_{xx} = -A_{yy} = A^+, \quad A_{xy} = A_{yx} = A^\times, \quad (\text{A.22})$$

corresponding to two independent polarizations in the $x - y$ plane, both transverse to the propagation direction z . One can compute the accelerations on some particles that feel the passage of gravitational waves using \ddot{h}_{ij}^{TT} (i, j are the spatial indices), and verify that the effects of the two different polarization are the ones shows in Fig.A.1. Let us see how we could get a measurement of the effect of a passing gravitational

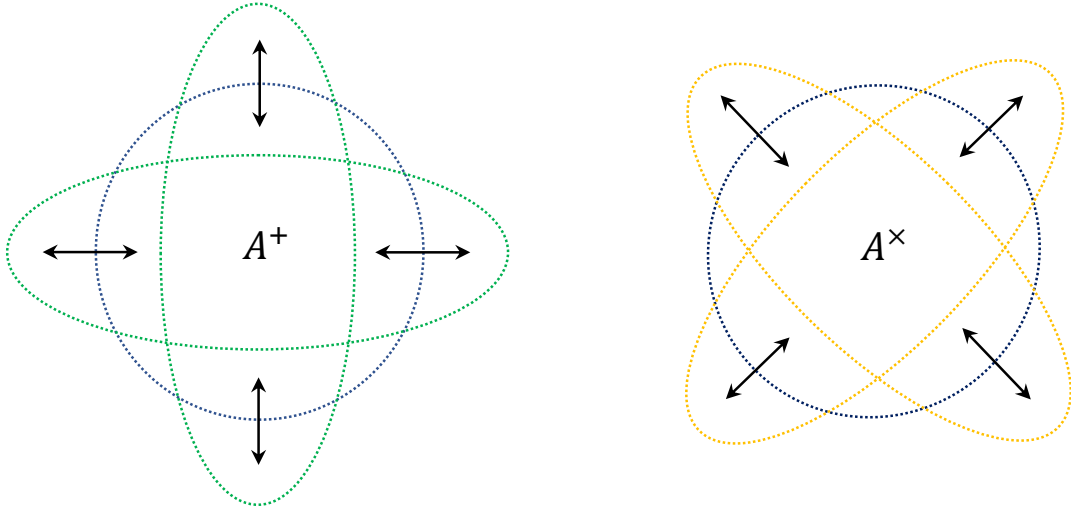


Figure A.1: The cartoon shows the effects of A^+ (green) and A^\times (yellow) polarized GWs on a ring of free falling particles (blue).

wave, considering two nearby particles, initially at rest, located one at the origin and one displaced by L along the x axis. Both will remain attached at the respective

initial positions, but the proper distance (calculated at the same time) between the two particles will be

$$\delta L = \int |g_{\mu\nu} dx^\mu dx^\nu|^{1/2} \simeq |g_{xx}(x=0)|^{1/2} L \simeq \left(1 + \frac{1}{2} h_{xx}^{TT}(x=0)\right) L. \quad (\text{A.23})$$

Now the proper distance δL does depend on time, precisely through the $h_{xx}^{TT}(x=0) = A^+ e^{-i\omega t}$. The above expression tells us an important thing concerning GW detection: the displacement is proportional to the initial separation L of any masses used in the detector (this is why ground-based detectors like VIRGO and LIGO are several km long, or millions of km in space for future experiments as LISA, see Subsec.1.6). With further mathematical calculations, it is possible to demonstrate that \bar{h}_{ij} can be written as a quadrupole emission term, both the monopole and the dipole terms disappear in standard GR. Thus, we do expect gravitational waves signal from events like the merging of two massive and dense objects, such as black holes or neutron stars, in fact, the strain in Eq.1.1 can be retrieved from the integral in Eq.A.23 for such binary systems.

Appendix B

Keplerian coordinates

The Keplerian coordinates are formed by 6 orbital elements, which are the parameters required to uniquely identify a specific orbit (see Fig.B.1): eccentricity (e), semi-major axis (a), inclination (i), longitude of the ascending node (Ω), argument of periapsis (ω) and true anomaly (ν). When viewed from an inertial frame, two orbiting bodies (a binary system) trace out distinct trajectories. Each of these trajectories has its focus on the common center of mass. When viewed from a non-inertial frame centered on one of the bodies, only the trajectory of the opposite body is apparent; Keplerian elements describe these non-inertial trajectories. An orbit has two sets of Keplerian elements depending on which body is used as the point of reference, in this work we use the primary body (the more massive object) as the reference point.

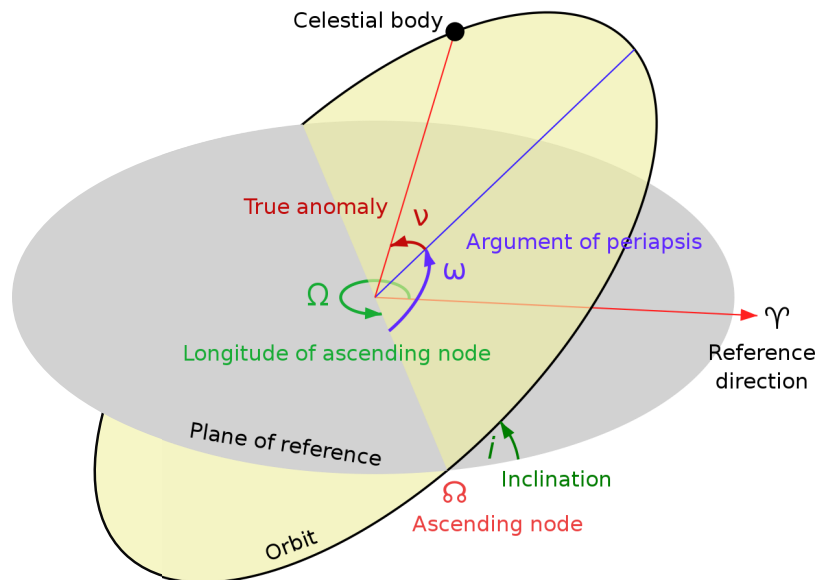


Figure B.1: In this diagram, the orbital plane (yellow) intersects a reference plane (gray) in the line of nodes and connects the ascending node with the descending node. The four angles used as orbital parameters are shown in the figure. The celestial body is the secondary body of the binary, while the primary is in the center.

The 6 orbital elements correspond, in Cartesian coordinates, to the 3 components of position and velocity of the second body, that, in this reference frame, are equivalent to the relative positions and velocities between the two bodies. Before going into the details of the transformation it is useful to define some quantities:

$$M = m_1 + m_2, \quad (\text{B.1})$$

$$E = \frac{|\mathbf{v}|^2}{2} - \frac{M}{|\mathbf{r}|}, \quad (\text{B.2})$$

$$\mathbf{L} = \mathbf{r} \times \mathbf{v}, \quad (\text{B.3})$$

$$\mathbf{n} = \{n_x = -L_y; n_y = L_x; 0\}, \quad (\text{B.4})$$

where m_1 and m_2 are the masses of the two bodies, E is the internal energy of the system, \mathbf{r} and \mathbf{v} are the position and velocity vectors, \mathbf{L} is the specific angular momentum, \mathbf{n} is the line of the nodes (the vector pointing along the ascending node, see Fig.B.1), and we assume the gravitational constant $G = 1$. The transformation between Cartesian and Keplerian coordinates is:

$$e = \frac{1}{M} \left| \left(|\mathbf{v}|^2 - \frac{M}{|\mathbf{r}|} \right) \mathbf{r} - (\mathbf{r} \cdot \mathbf{v}) \mathbf{v} \right|, \quad (\text{B.5})$$

$$a = -\frac{M}{2E}, \quad (\text{B.6})$$

$$i = \arccos \left(\frac{L_z}{|\mathbf{L}|} \right), \quad (\text{B.7})$$

$$\Omega = \arccos \left(\frac{n_x}{|\mathbf{n}|} \right), \quad (\text{B.8})$$

$$\omega = \begin{cases} \text{planar orbit } (i = 0) & \arccos(e_x/|e|) - \Omega \\ \text{non-planar orbit } (i \neq 0) & \arccos(r_x/|\mathbf{r}|) - \arccos(e_x/|e|) \end{cases}, \quad (\text{B.9})$$

$$\nu = \begin{cases} \text{planar orbit } (i = 0) & \arccos(e \cdot \mathbf{n}/|e||\mathbf{n}|) \\ \text{non-planar orbit } (i \neq 0) & \arccos(\mathbf{r} \cdot \mathbf{n}/|\mathbf{r}||\mathbf{n}|) - \omega \end{cases}. \quad (\text{B.10})$$

Before going into the details of the inverse transformation it is useful to define the modules for positions and velocities:

$$r_0 = a \frac{1 - e^2}{1 + e \cos \nu}, \quad (\text{B.11})$$

$$v_0 = \sqrt{\frac{M}{a(1 - e^2)}}. \quad (\text{B.12})$$

Finally, the transformation between Keplerian and Cartesian coordinates is:

$$r_x = r_0[\cos \Omega (\cos \omega \cos \nu - \sin \omega \sin \nu) + \sin \Omega \cos i (\sin \omega \cos \nu + \cos \omega \sin \nu)], \quad (\text{B.13})$$

$$r_y = r_0[\sin \Omega (\cos \omega \cos \nu - \sin \omega \sin \nu) + \cos \Omega \cos i (\sin \omega \cos \nu + \cos \omega \sin \nu)], \quad (\text{B.14})$$

$$r_z = r_0[\sin i (\sin \omega \cos \nu + \cos \omega \sin \nu)], \quad (\text{B.15})$$

$$v_x = v_0[(e + \cos \nu) (-\cos i \cos \omega \sin \Omega - \cos \Omega \sin \omega) + \sin \nu (\cos \omega \cos \Omega - \cos i \sin \omega \sin \Omega)], \quad (\text{B.16})$$

$$v_y = v_0[(e + \cos \nu) (\cos i \cos \omega \cos \Omega - \sin \Omega \sin \omega) + \sin \nu (\cos \omega \sin \Omega + \cos i \sin \omega \cos \Omega)], \quad (\text{B.17})$$

$$v_z = v_0[(e + \cos \nu) \cos \omega \sin i - \sin \nu \sin i \sin \omega]. \quad (\text{B.18})$$

Bibliography

- [1] S. J. Aarseth. From NBODY1 to NBODY6: The Growth of an Industry. *Publications of the Astronomical Society of the Pacific*, 111(765):1333–1346, Nov. 1999. doi:10.1086/316455.
- [2] S. J. Aarseth. Star Cluster Simulations: the State of the Art. In J. Henrard and S. Ferraz-Mello, editors, *Impact of Modern Dynamics in Astronomy*, page 127, Jan. 1999. URL: <https://ui.adsabs.harvard.edu/abs/1999imda.coll.127A>.
- [3] S. J. Aarseth. *Gravitational N-Body Simulations: Tools and Algorithms*. Cambridge Monographs on Mathematical Physics. Cambridge University Press, 2003. doi:10.1017/CB09780511535246.
- [4] S. J. Aarseth. Regularization tools for binary interactions. In J. Makino and P. Hut, editors, *Astrophysical Supercomputing using Particle Simulations*, volume 208, page 295, jan 2003. arXiv:astro-ph/0110148.
- [5] S. J. Aarseth. Regularization tools for binary interactions. In J. Makino and P. Hut, editors, *Astrophysical Supercomputing using Particle Simulations*, volume 208, page 295, jan 2003. arXiv:astro-ph/0110148.
- [6] B. P. Abbott, R. Abbott, T. D. Abbott, M. R. Abernathy, F. Acernese, K. Ackley, C. Adams, T. Adams, P. Addesso, R. Adhikari, et al. Observation of gravitational waves from a binary black hole merger. *Phys. Rev. Lett.*, 116:061102, Feb 2016. URL: <https://link.aps.org/doi/10.1103/PhysRevLett.116.061102>, doi:10.1103/PhysRevLett.116.061102.
- [7] B. P. Abbott, R. Abbott, T. D. Abbott, M. R. Abernathy, F. Acernese, K. Ackley, C. Adams, T. Adams, P. Addesso, R. X. Adhikari, et al. Astrophysica implications of the binary black hole merger GW150914. *The Astrophysical Journal*, 818(2):L22, feb 2016. doi:10.3847/2041-8205/818/2/L22.
- [8] B. P. Abbott, R. Abbott, T. D. Abbott, M. R. Abernathy, F. Acernese, K. Ackley, C. Adams, T. Adams, P. Addesso, R. X. Adhikari, et al. GW151226: Observation of Gravitational Waves from a 22-Solar-Mass Binary Black Hole Coalescence. *Phys. Rev. Lett.*, 116(24):241103, June 2016. arXiv:1606.04855, doi:10.1103/PhysRevLett.116.241103.

-
- [9] B. P. Abbott, R. Abbott, T. D. Abbott, S. Abraham, F. Acernese, K. Ackley, C. Adams, R. X. Adhikari, V. B. Adya, Affeldt, et al. GWTC-1: A Gravitational-Wave Transient Catalog of Compact Binary Mergers Observed by LIGO and Virgo during the First and Second Observing Runs. *Physical Review X*, 9(3):031040, July 2019. [arXiv:1811.12907](https://arxiv.org/abs/1811.12907), [doi:10.1103/PhysRevX.9.031040](https://doi.org/10.1103/PhysRevX.9.031040).
- [10] B. P. Abbott, R. Abbott, T. D. Abbott, S. Abraham, F. Acernese, K. Ackley, C. Adams, R. X. Adhikari, V. B. Adya, et al. GW190425: Observation of a Compact Binary Coalescence with Total Mass $\sim 3.4 M_{\odot}$. *ApJ*, 892(1):L3, Mar. 2020. [arXiv:2001.01761](https://arxiv.org/abs/2001.01761), [doi:10.3847/2041-8213/ab75f5](https://doi.org/10.3847/2041-8213/ab75f5).
- [11] B. P. Abbott, R. Abbott, T. D. Abbott, F. Acernese, K. Ackley, C. Adams, T. Adams, P. Addesso, R. X. Adhikari, et al. Gw170817: Observation of gravitational waves from a binary neutron star inspiral. *Phys. Rev. Lett.*, 119:161101, Oct 2017. URL: <https://link.aps.org/doi/10.1103/PhysRevLett.119.161101>, [doi:10.1103/PhysRevLett.119.161101](https://doi.org/10.1103/PhysRevLett.119.161101).
- [12] R. Abbott, T. D. Abbott, S. Abraham, F. Acernese, K. Ackley, A. Adams, C. Adams, R. X. Adhikari, V. B. Adya, et al. Population Properties of Compact Objects from the Second LIGO-Virgo Gravitational-Wave Transient Catalog. *ApJ*, 913(1):L7, May 2021. [arXiv:2010.14533](https://arxiv.org/abs/2010.14533), [doi:10.3847/2041-8213/abe949](https://doi.org/10.3847/2041-8213/abe949).
- [13] R. Abbott, T. D. Abbott, S. Abraham, F. Acernese, K. Ackley, C. Adams, R. X. Adhikari, V. B. Adya, C. Affeldt, et al. GW190412: Observation of a binary-black-hole coalescence with asymmetric masses. *Phys. Rev. D*, 102(4):043015, Aug. 2020. [arXiv:2004.08342](https://arxiv.org/abs/2004.08342), [doi:10.1103/PhysRevD.102.043015](https://doi.org/10.1103/PhysRevD.102.043015).
- [14] R. Abbott, T. D. Abbott, S. Abraham, F. Acernese, K. Ackley, C. Adams, R. X. Adhikari, V. B. Adya, C. Affeldt, et al. Gw190521: A binary black hole merger with a total mass of $150 M_{\odot}$. *Phys. Rev. Lett.*, 125:101102, Sep 2020. URL: <https://link.aps.org/doi/10.1103/PhysRevLett.125.101102>, [doi:10.1103/PhysRevLett.125.101102](https://doi.org/10.1103/PhysRevLett.125.101102).
- [15] R. Abbott, T. D. Abbott, S. Abraham, F. Acernese, K. Ackley, C. Adams, R. X. Adhikari, V. B. Adya, C. Affeldt, et al. GW190814: Gravitational Waves from the Coalescence of a 23 Solar Mass Black Hole with a 2.6 Solar Mass Compact Object. *ApJ*, 896(2):L44, June 2020. [arXiv:2006.12611](https://arxiv.org/abs/2006.12611), [doi:10.3847/2041-8213/ab960f](https://doi.org/10.3847/2041-8213/ab960f).
- [16] R. Abbott, T. D. Abbott, S. Abraham, F. Acernese, K. Ackley, C. Adams, R. X. Adhikari, V. B. Adya, C. Affeldt, et al. Properties and Astrophysical Implications of the $150 M_{\odot}$ Binary Black Hole Merger GW190521. *ApJ*, 900(1):L13, Sept. 2020. [arXiv:2009.01190](https://arxiv.org/abs/2009.01190), [doi:10.3847/2041-8213/aba493](https://doi.org/10.3847/2041-8213/aba493).
- [17] A. Ahmad and L. Cohen. A numerical integration scheme for the n-body gravitational problem. *Journal of Computational Physics*, 12(3):389–
-

- 402, 1973. URL: <https://www.sciencedirect.com/science/article/pii/S0021999173901605>, doi:[https://doi.org/10.1016/0021-9991\(73\)90160-5](https://doi.org/10.1016/0021-9991(73)90160-5).
- [18] F. Antonini and M. Gieles. Population synthesis of black hole binary mergers from star clusters. *Monthly Notices of the Royal Astronomical Society*, 492(2):2936–2954, 01 2020. [arXiv:https://academic.oup.com/mnras/article-pdf/492/2/2936/31889363/stz3584.pdf](https://academic.oup.com/mnras/article-pdf/492/2/2936/31889363/stz3584.pdf), doi:[10.1093/mnras/stz3584](https://doi.org/10.1093/mnras/stz3584).
- [19] F. Antonini, M. Gieles, and A. Gualandris. Black hole growth through hierarchical black hole mergers in dense star clusters: implications for gravitational wave detections. *MNRAS*, 486(4):5008–5021, July 2019. [arXiv:1811.03640](https://arxiv.org/abs/1811.03640), doi:[10.1093/mnras/stz1149](https://doi.org/10.1093/mnras/stz1149).
- [20] F. Antonini and H. B. Perets. Secular Evolution of Compact Binaries near Massive Black Holes: Gravitational Wave Sources and Other Exotica. *ApJ*, 757(1):27, Sept. 2012. [arXiv:1203.2938](https://arxiv.org/abs/1203.2938), doi:[10.1088/0004-637X/757/1/27](https://doi.org/10.1088/0004-637X/757/1/27).
- [21] F. Antonini and F. A. Rasio. Merging Black Hole Binaries in Galactic Nuclei: Implications for Advanced-LIGO Detections. *ApJ*, 831(2):187, nov 2016. [arXiv:1606.04889](https://arxiv.org/abs/1606.04889), doi:[10.3847/0004-637X/831/2/187](https://doi.org/10.3847/0004-637X/831/2/187).
- [22] M. Arca Sedda, A. Askar, and M. Giersz. MOCCA-Survey Database - I. Unravelling black hole subsystems in globular clusters. *MNRAS*, 479(4):4652–4664, Oct. 2018. [arXiv:1801.00795](https://arxiv.org/abs/1801.00795), doi:[10.1093/mnras/sty1859](https://doi.org/10.1093/mnras/sty1859).
- [23] M. Arca Sedda, M. Mapelli, M. Benacquista, and M. Spera. Population synthesis of black hole mergers with B-POP: the impact of dynamics, natal spins, and intermediate-mass black holes on the population of gravitational wave sources. *arXiv e-prints*, page arXiv:2109.12119, sep 2021. [arXiv:2109.12119](https://arxiv.org/abs/2109.12119).
- [24] M. Arca-Sedda, F. P. Rizzuto, T. Naab, J. Ostriker, M. Giersz, and R. Spurzem. Breaching the Limit: Formation of GW190521-like and IMBH Mergers in Young Massive Clusters. *ApJ*, 920(2):128, Oct. 2021. [arXiv:2105.07003](https://arxiv.org/abs/2105.07003), doi:[10.3847/1538-4357/ac1419](https://doi.org/10.3847/1538-4357/ac1419).
- [25] A. Askar, M. Szkudlarek, D. Gondek-Rosińska, M. Giersz, and T. Bulik. MOCCA-SURVEY Database - I. Coalescing binary black holes originating from globular clusters. *MNRAS*, 464(1):L36–L40, Jan. 2017. [arXiv:1608.02520](https://arxiv.org/abs/1608.02520), doi:[10.1093/mnrasl/slw177](https://doi.org/10.1093/mnrasl/slw177).
- [26] M. Bailes, B. K. Berger, P. R. Brady, M. Branchesi, K. Danzmann, M. Evans, K. Holley-Bockelmann, B. R. Iyer, T. Kajita, S. Katsanevas, et al. Gravitational-wave physics and astronomy in the 2020s and 2030s. *Nature Reviews Physics*, 3(5):344–366, Apr. 2021. doi:[10.1038/s42254-021-00303-8](https://doi.org/10.1038/s42254-021-00303-8).
- [27] S. Banerjee. Stellar-mass black holes in young massive and open stellar clusters and their role in gravitational-wave generation. *Monthly Notices of the Royal Astronomical Society*, 467(1):524–539, 01 2017. [arXiv:https://academic.oup](https://arxiv.org/abs/https://academic.oup).

-
- [com/mnras/article-pdf/467/1/524/10493546/stw3392.pdf](https://www.mnras.com/mnras/article-pdf/467/1/524/10493546/stw3392.pdf), doi:10.1093/mnras/stw3392.
- [28] Z. Barkat, G. Rakavy, and N. Sack. Dynamics of supernova explosion resulting from pair formation. *Phys. Rev. Lett.*, 18:379–381, Mar 1967. URL: <https://link.aps.org/doi/10.1103/PhysRevLett.18.379>, doi:10.1103/PhysRevLett.18.379.
- [29] J. W. Barrett, S. M. Gaebel, C. J. Neijssel, A. Vigna-Gómez, S. Stevenson, C. P. L. Berry, W. M. Farr, and I. Mandel. Accuracy of inference on the physics of binary evolution from gravitational-wave observations. *MNRAS*, 477(4):4685–4695, July 2018. [arXiv:1711.06287](https://arxiv.org/abs/1711.06287), doi:10.1093/mnras/sty908.
- [30] I. Bartos, B. Kocsis, Z. Haiman, and S. Márka. Rapid and Bright Stellar-mass Binary Black Hole Mergers in Active Galactic Nuclei. *ApJ*, 835(2):165, Feb. 2017. [arXiv:1602.03831](https://arxiv.org/abs/1602.03831), doi:10.3847/1538-4357/835/2/165.
- [31] J. Bédorf, E. Gaburov, and S. Portegies Zwart. Bonsai: A GPU Tree-Code. In R. Capuzzo-Dolcetta, M. Limongi, and A. Tornambè, editors, *Advances in Computational Astrophysics: Methods, Tools, and Outcome*, volume 453 of *Astronomical Society of the Pacific Conference Series*, page 325, July 2012. [arXiv:1204.2280](https://arxiv.org/abs/1204.2280), doi:10.48550/arXiv.1204.2280.
- [32] J. Bédorf, E. Gaburov, and S. Portegies Zwart. Sapporo2: a versatile direct N-body library. *Computational Astrophysics and Cosmology*, 2:8, Oct. 2015. [arXiv:1510.04068](https://arxiv.org/abs/1510.04068), doi:10.1186/s40668-015-0012-z.
- [33] K. Belczynski, V. Kalogera, and T. Bulik. A Comprehensive Study of Binary Compact Objects as Gravitational Wave Sources: Evolutionary Channels, Rates, and Physical Properties. *ApJ*, 572(1):407–431, jun 2002. [arXiv:astro-ph/0111452](https://arxiv.org/abs/astro-ph/0111452), doi:10.1086/340304.
- [34] K. Belczynski, V. Kalogera, F. A. Rasio, R. E. Taam, A. Zezas, T. Bulik, T. J. Maccarone, and N. Ivanova. Compact Object Modeling with the Star-Track Population Synthesis Code. *ApJS*, 174(1):223–260, jan 2008. [arXiv:astro-ph/0511811](https://arxiv.org/abs/astro-ph/0511811), doi:10.1086/521026.
- [35] M. J. Benacquista and J. M. B. Downing. Relativistic Binaries in Globular Clusters. *Living Reviews in Relativity*, 16(1):4, Mar. 2013. [arXiv:1110.4423](https://arxiv.org/abs/1110.4423), doi:10.12942/lrr-2013-4.
- [36] P. Berczik, R. Spurzem, L. Wang, S. Zhong, and S. Huang. Up to 700k GPU cores, Kepler, and the Exascale future for simulations of star clusters around black holes. In *Third International Conference "High Performance Computing*, pages 52–59, Oct. 2013. [arXiv:1312.1789](https://arxiv.org/abs/1312.1789).
- [37] H. A. Bethe and G. E. Brown. Evolution of binary compact objects that merge. *The Astrophysical Journal*, 506(2):780–789, oct 1998. doi:10.1086/306265.
-

- [38] J. Binney and S. Tremaine. *Galactic dynamics*. Princeton University Press, 1987. URL: <https://ui.adsabs.harvard.edu/abs/1987gady.book.....B>.
- [39] A. Blaauw. On the origin of the O- and B-type stars with high velocities (the “run-away” stars), and some related problems. *Bull. Astron. Inst. Netherlands*, 15:265, May 1961. URL: <https://ui.adsabs.harvard.edu/abs/1961BAN...15..265B>.
- [40] T. Böker, S. Laine, R. P. van der Marel, M. Sarzi, H.-W. Rix, L. C. Ho, and J. C. Shields. A Hubble Space Telescope Census of Nuclear Star Clusters in Late-Type Spiral Galaxies. I. Observations and Image Analysis. *AJ*, 123(3):1389–1410, Mar. 2002. [arXiv:astro-ph/0112086](https://arxiv.org/abs/astro-ph/0112086), [doi:10.1086/339025](https://doi.org/10.1086/339025).
- [41] J. R. Bond, W. D. Arnett, and B. J. Carr. The evolution and fate of Very Massive Objects. *ApJ*, 280:825–847, May 1984. [doi:10.1086/162057](https://doi.org/10.1086/162057).
- [42] H. Bondi and F. Hoyle. On the Mechanism of Accretion by Stars. *Monthly Notices of the Royal Astronomical Society*, 104(5):273–282, 10 1944. [arXiv:https://academic.oup.com/mnras/article-pdf/104/5/273/8072203/mnras104-0273.pdf](https://academic.oup.com/mnras/article-pdf/104/5/273/8072203/mnras104-0273.pdf), [doi:10.1093/mnras/104.5.273](https://doi.org/10.1093/mnras/104.5.273).
- [43] Y. Bouffanais, M. Mapelli, F. Santoliquido, N. Giacobbo, G. Iorio, and G. Costa. Constraining accretion efficiency in massive binary stars with LIGO -Virgo black holes. *MNRAS*, 505(3):3873–3882, aug 2021. [arXiv:2010.11220](https://arxiv.org/abs/2010.11220), [doi:10.1093/mnras/stab1589](https://doi.org/10.1093/mnras/stab1589).
- [44] P. G. Breen and D. C. Heggie. Dynamical evolution of black hole subsystems in idealized star clusters. *MNRAS*, 432(4):2779–2797, July 2013. [arXiv:1304.3401](https://arxiv.org/abs/1304.3401), [doi:10.1093/mnras/stt628](https://doi.org/10.1093/mnras/stt628).
- [45] A. Bressan, P. Marigo, L. Girardi, B. Salasnich, C. Dal Cero, S. Rubele, and A. Nanni. PARSEC: stellar tracks and isochrones with the PAdova and TRieste Stellar Evolution Code. *MNRAS*, 427(1):127–145, nov 2012. [arXiv:1208.4498](https://arxiv.org/abs/1208.4498), [doi:10.1111/j.1365-2966.2012.21948.x](https://doi.org/10.1111/j.1365-2966.2012.21948.x).
- [46] M. M. Briel, H. F. Stevance, and J. J. Eldridge. Understanding the high-mass binary black hole population from stable mass transfer and super-Eddington accretion in bpass. *Monthly Notices of the Royal Astronomical Society*, 520(4):5724–5745, 02 2023. [arXiv:https://academic.oup.com/mnras/article-pdf/520/4/5724/49355087/stad399.pdf](https://arxiv.org/abs/https://academic.oup.com/mnras/article-pdf/520/4/5724/49355087/stad399.pdf), [doi:10.1093/mnras/stad399](https://doi.org/10.1093/mnras/stad399).
- [47] M. Campanelli, C. Lousto, Y. Zlochower, and D. Merritt. Large Merger Recoils and Spin Flips from Generic Black Hole Binaries. *ApJ*, 659(1):L5–L8, Apr. 2007. [arXiv:gr-qc/0701164](https://arxiv.org/abs/gr-qc/0701164), [doi:10.1086/516712](https://doi.org/10.1086/516712).
- [48] M. Cantiello, S. C. Yoon, N. Langer, and M. Livio. Binary star progenitors of long gamma-ray bursts. *A&A*, 465(2):L29–L33, Apr. 2007. [arXiv:astro-ph/0702540](https://arxiv.org/abs/astro-ph/0702540), [doi:10.1051/0004-6361:20077115](https://doi.org/10.1051/0004-6361:20077115).

-
- [49] C. D. Capano, I. Tews, S. M. Brown, B. Margalit, S. De, S. Kumar, D. A. Brown, B. Krishnan, and S. Reddy. Stringent constraints on neutron-star radii from multimessenger observations and nuclear theory. *Nature Astronomy*, 4:625–632, Mar. 2020. [arXiv:1908.10352](#), [doi:10.1038/s41550-020-1014-6](#).
- [50] R. Capuzzo-Dolcetta and M. Spera. A performance comparison of different graphics processing units running direct N-body simulations. *Computer Physics Communications*, 184(11):2528–2539, nov 2013. [arXiv:1304.1966](#), [doi:10.1016/j.cpc.2013.07.005](#).
- [51] R. Capuzzo-Dolcetta, M. Spera, and D. Punzo. A fully parallel, high precision, N-body code running on hybrid computing platforms. *Journal of Computational Physics*, 236:580–593, Mar. 2013. [arXiv:1207.2367](#), [doi:10.1016/j.jcp.2012.11.013](#).
- [52] S. Chandrasekhar. *Principles of stellar dynamics*. Publisher: Dover Publications, New York, 1942. URL: <https://ui.adsabs.harvard.edu/abs/1942psd.book.....C>.
- [53] S. Chandrasekhar. Dynamical Friction. I. General Considerations: the Coefficient of Dynamical Friction. *ApJ*, 97:255, Mar. 1943. [doi:10.1086/144517](#).
- [54] Y. Chen, A. Bressan, L. Girardi, P. Marigo, X. Kong, and A. Lanza. PARSEC evolutionary tracks of massive stars up to $350 M_{\odot}$ at metallicities $0.0001 \leq Z \leq 0.04$. *MNRAS*, 452(1):1068–1080, Sept. 2015. [arXiv:1506.01681](#), [doi:10.1093/mnras/stv1281](#).
- [55] Y. Chen, L. Girardi, A. Bressan, P. Marigo, M. Barbieri, and X. Kong. Improving PARSEC models for very low mass stars. *MNRAS*, 444(3):2525–2543, Nov. 2014. [arXiv:1409.0322](#), [doi:10.1093/mnras/stu1605](#).
- [56] J. Choi, A. Dotter, C. Conroy, M. Cantiello, B. Paxton, and B. D. Johnson. Mesa Isochrones and Stellar Tracks (MIST). I. Solar-scaled Models. *ApJ*, 823(2):102, June 2016. [arXiv:1604.08592](#), [doi:10.3847/0004-637X/823/2/102](#).
- [57] J. S. W. Claeys, O. R. Pols, R. G. Izzard, J. Vink, and F. W. M. Verbunt. Theoretical uncertainties of the Type Ia supernova rate. *A&A*, 563:A83, Mar. 2014. [arXiv:1401.2895](#), [doi:10.1051/0004-6361/201322714](#).
- [58] J. P. A. Clark and D. M. Eardley. Evolution of close neutron star binaries. *ApJ*, 215:311–322, jul 1977. [doi:10.1086/155360](#).
- [59] J. P. A. Clark, E. P. J. van den Heuvel, and W. Sutantyo. Formation of neutron star binaries and their importance for gravitational radiation. *A&A*, 72:120–128, feb 1979. URL: <https://ui.adsabs.harvard.edu/abs/1979A&A....72..120C>.
- [60] S. A. Colgate. Stellar Coalescence and the Multiple Supernova Interpretation of Quasi-Stellar Sources. *ApJ*, 150:163, Oct. 1967. [doi:10.1086/149319](#).
-

- [61] M. Colpi, M. Mapelli, and A. Possenti. Probing the Presence of a Single or Binary Black Hole in the Globular Cluster NGC 6752 with Pulsar Dynamics. *ApJ*, 599(2):1260–1271, Dec. 2003. [arXiv:astro-ph/0309017](#), [doi:10.1086/379543](#).
- [62] G. Costa, A. Bressan, M. Mapelli, P. Marigo, G. Iorio, and M. Spera. Formation of GW190521 from stellar evolution: the impact of the hydrogen-rich envelope, dredge-up, and $^{12}\text{C}(\alpha, \gamma)^{16}\text{O}$ rate on the pair-instability black hole mass gap. *MNRAS*, 501(3):4514–4533, Mar. 2021. [arXiv:2010.02242](#), [doi:10.1093/mnras/staa3916](#).
- [63] Z. Cui and X.-D. Li. A Study of Magnetized White Dwarf + Helium Star Binary Evolution to Type Ia Supernovae. *Research in Astronomy and Astrophysics*, 22(2):025001, Feb. 2022. [arXiv:2111.04496](#), [doi:10.1088/1674-4527/ac3744](#).
- [64] S. De, M. MacLeod, R. W. Everson, A. Antoni, I. Mandel, and E. Ramirez-Ruiz. Common Envelope Wind Tunnel: The Effects of Binary Mass Ratio and Implications for the Accretion-driven Growth of LIGO Binary Black Holes. *ApJ*, 897(2):130, July 2020. [arXiv:1910.13333](#), [doi:10.3847/1538-4357/ab9ac6](#).
- [65] S. E. de Mink, M. Cantiello, N. Langer, S. C. Yoon, I. Brott, E. Glebbeek, M. Verkoulen, and O. R. Pols. Rotational mixing in close binaries. In L. Deng and K. L. Chan, editors, *The Art of Modeling Stars in the 21st Century*, volume 252, pages 365–370, oct 2008. [arXiv:0805.2544](#), [doi:10.1017/S1743921308023223](#).
- [66] S. E. de Mink and I. Mandel. The chemically homogeneous evolutionary channel for binary black hole mergers: rates and properties of gravitational-wave events detectable by advanced LIGO. *MNRAS*, 460(4):3545–3553, aug 2016. [arXiv:1603.02291](#), [doi:10.1093/mnras/stw1219](#).
- [67] P. Deuffhard. Recent progress in extrapolation methods for ordinary differential equations. *SIAM Review*, 27(4):505–535, 1985. URL: <http://www.jstor.org/stable/2031057>.
- [68] P. Deuffhard, E. Hairer, and J. Zugck. One-step and extrapolation methods for differential-algebraic systems. *Numerische Mathematik*, 51:501–516, 1987. URL: <http://eudml.org/doc/133209>.
- [69] U. N. Di Carlo, N. Giacobbo, M. Mapelli, M. Pasquato, M. Spera, L. Wang, and F. Haardt. Merging black holes in young star clusters. *MNRAS*, 487(2):2947–2960, Aug. 2019. [arXiv:1901.00863](#), [doi:10.1093/mnras/stz1453](#).
- [70] U. N. Di Carlo, M. Mapelli, Y. Bouffanais, N. Giacobbo, F. Santoliquido, A. Bressan, M. Spera, and F. Haardt. Binary black holes in the pair instability mass gap. *MNRAS*, 497(1):1043–1049, Sept. 2020. [arXiv:1911.01434](#), [doi:10.1093/mnras/staa1997](#).
- [71] U. N. Di Carlo, M. Mapelli, N. Giacobbo, M. Spera, Y. Bouffanais, S. Rastello, F. Santoliquido, M. Pasquato, A. Ballone, A. A. Trani, et al. Binary black holes

- in young star clusters: the impact of metallicity. *MNRAS*, 498(1):495–506, oct 2020. [arXiv:2004.09525](#), [doi:10.1093/mnras/staa2286](#).
- [72] M. Dominik, K. Belczynski, C. Fryer, D. E. Holz, E. Berti, T. Bulik, I. Mandel, and R. O’Shaughnessy. Double Compact Objects. I. The Significance of the Common Envelope on Merger Rates. *ApJ*, 759(1):52, nov 2012. [arXiv:1202.4901](#), [doi:10.1088/0004-637X/759/1/52](#).
- [73] J. M. B. Downing, M. J. Benacquista, M. Giersz, and R. Spurzem. Compact binaries in star clusters – I. Black hole binaries inside globular clusters. *Monthly Notices of the Royal Astronomical Society*, 407(3):1946–1962, 09 2010. [arXiv:https://academic.oup.com/mnras/article-pdf/407/3/1946/18445086/mnras0407-1946.pdf](#), [doi:10.1111/j.1365-2966.2010.17040.x](#).
- [74] J. M. B. Downing, M. J. Benacquista, M. Giersz, and R. Spurzem. Compact binaries in star clusters - II. Escapers and detection rates. *MNRAS*, 416(1):133–147, Sept. 2011. [arXiv:1008.5060](#), [doi:10.1111/j.1365-2966.2011.19023.x](#).
- [75] G. Duchêne and A. Kraus. Stellar Multiplicity. *ARA&A*, 51(1):269–310, Aug. 2013. [arXiv:1303.3028](#), [doi:10.1146/annurev-astro-081710-102602](#).
- [76] P. Eggleton. *Evolutionary Processes in Binary and Multiple Stars*. Cambridge University Press, 2006. URL: <https://www.cambridge.org/core/books/evolutionary-processes-in-binary-and-multiple-stars/4CE2D87C5DE2FB2EA9008A1614BB9899>.
- [77] P. P. Eggleton. Aproximations to the radii of Roche lobes. *ApJ*, 268:368–369, may 1983. [doi:10.1086/160960](#).
- [78] A. Einstein. Über Gravitationswellen. *Sitzungsberichte der Königlich Preußischen Akademie der Wissenschaften (Berlin)*, pages 154–167, jan 1918. URL: <https://ui.adsabs.harvard.edu/abs/1918SPAW.....154E>.
- [79] J. J. Eldridge, N. Langer, and C. A. Tout. Runaway stars as progenitors of supernovae and gamma-ray bursts. *Monthly Notices of the Royal Astronomical Society*, 414(4):3501–3520, 07 2011. [arXiv:https://academic.oup.com/mnras/article-pdf/414/4/3501/18713752/mnras0414-3501.pdf](#), [doi:10.1111/j.1365-2966.2011.18650.x](#).
- [80] J. J. Eldridge and E. R. Stanway. The effect of stellar evolution uncertainties on the rest-frame ultraviolet stellar lines of C^{iv} and Heⁱⁱ in high-redshift Lyman-break galaxies. *Monthly Notices of the Royal Astronomical Society*, 419(1):479–489, 12 2011. [arXiv:https://academic.oup.com/mnras/article-pdf/419/1/479/18703561/mnras0419-0479.pdf](#), [doi:10.1111/j.1365-2966.2011.19713.x](#).
- [81] J. J. Eldridge and E. R. Stanway. bpass predictions for binary black hole mergers. *Monthly Notices of the Royal Astronomical Society*, 462(3):3302–3313, 07

2016. [arXiv:https://academic.oup.com/mnras/article-pdf/462/3/3302/8008420/stw1772.pdf](https://academic.oup.com/mnras/article-pdf/462/3/3302/8008420/stw1772.pdf), [doi:10.1093/mnras/stw1772](https://doi.org/10.1093/mnras/stw1772).
- [82] J. J. Eldridge, E. R. Stanway, and P. N. Tang. A consistent estimate for gravitational wave and electromagnetic transient rates. *Monthly Notices of the Royal Astronomical Society*, 482(1):870–880, 10 2018. [arXiv:https://academic.oup.com/mnras/article-pdf/482/1/870/26182720/sty2714.pdf](https://academic.oup.com/mnras/article-pdf/482/1/870/26182720/sty2714.pdf), [doi:10.1093/mnras/sty2714](https://doi.org/10.1093/mnras/sty2714).
- [83] J. J. Eldridge, E. R. Stanway, L. Xiao, L. A. S. McClelland, G. Taylor, M. Ng, S. M. L. Greis, and J. C. Bray. Binary Population and Spectral Synthesis Version 2.1: Construction, Observational Verification, and New Results. PASA, 34:e058, nov 2017. [arXiv:1710.02154](https://arxiv.org/abs/1710.02154), [doi:10.1017/pasa.2017.51](https://doi.org/10.1017/pasa.2017.51).
- [84] R. Elson, P. Hut, and S. Inagaki. Dynamical evolution of globular clusters. *ARA&A*, 25:565–601, Jan. 1987. [doi:10.1146/annurev.aa.25.090187.003025](https://doi.org/10.1146/annurev.aa.25.090187.003025).
- [85] P. Esposito, G. L. Israel, D. Milisavljevic, M. Mapelli, L. Zampieri, L. Sidoli, G. Fabbiano, and G. A. Rodríguez Castillo. Periodic signals from the Circinus region: two new cataclysmic variables and the ultraluminous X-ray source candidate GC X-1. *MNRAS*, 452(2):1112–1127, sep 2015. [arXiv:1506.05808](https://arxiv.org/abs/1506.05808), [doi:10.1093/mnras/stv1379](https://doi.org/10.1093/mnras/stv1379).
- [86] R. Farmer, M. Renzo, S. E. de Mink, P. Marchant, and S. Justham. Mind the gap: The location of the lower edge of the pair-instability supernova black hole mass gap. *The Astrophysical Journal*, 887(1):53, dec 2019. URL: <https://dx.doi.org/10.3847/1538-4357/ab518b>, [doi:10.3847/1538-4357/ab518b](https://doi.org/10.3847/1538-4357/ab518b).
- [87] B. Farr, D. E. Holz, and W. M. Farr. Using Spin to Understand the Formation of LIGO and Virgo’s Black Holes. *ApJ*, 854(1):L9, Feb. 2018. [arXiv:1709.07896](https://arxiv.org/abs/1709.07896), [doi:10.3847/2041-8213/aaaa64](https://doi.org/10.3847/2041-8213/aaaa64).
- [88] W. M. Farr, S. Stevenson, M. C. Miller, I. Mandel, B. Farr, and A. Vecchio. Distinguishing spin-aligned and isotropic black hole populations with gravitational waves. *Nature*, 548(7667):426–429, Aug. 2017. [arXiv:1706.01385](https://arxiv.org/abs/1706.01385), [doi:10.1038/nature23453](https://doi.org/10.1038/nature23453).
- [89] R. Fernández, E. Quataert, K. Kashiyama, and E. R. Coughlin. Mass ejection in failed supernovae: variation with stellar progenitor. *MNRAS*, 476(2):2366–2383, May 2018. [arXiv:1710.01735](https://arxiv.org/abs/1710.01735), [doi:10.1093/mnras/sty306](https://doi.org/10.1093/mnras/sty306).
- [90] L. Ferrarese, P. Côté, A. Jordán, E. W. Peng, J. P. Blakeslee, S. Piatek, S. Mei, D. Merritt, M. Milosavljević, J. L. Tonry, and M. J. West. The ACS Virgo Cluster Survey. VI. Isophotal Analysis and the Structure of Early-Type Galaxies. *ApJS*, 164(2):334–434, June 2006. [arXiv:astro-ph/0602297](https://arxiv.org/abs/astro-ph/0602297), [doi:10.1086/501350](https://doi.org/10.1086/501350).

-
- [91] W. Fong and E. Berger. The Locations of Short Gamma-Ray Bursts as Evidence for Compact Object Binary Progenitors. *ApJ*, 776(1):18, Oct. 2013. [arXiv:1307.0819](#), [doi:10.1088/0004-637X/776/1/18](#).
- [92] G. Fragione and B. Kocsis. Black hole mergers from an evolving population of globular clusters. *Phys. Rev. Lett.*, 121:161103, Oct 2018. URL: <https://link.aps.org/doi/10.1103/PhysRevLett.121.161103>, [doi:10.1103/PhysRevLett.121.161103](#).
- [93] G. Fragione, N. W. C. Leigh, and R. Perna. Black hole and neutron star mergers in galactic nuclei: the role of triples. *MNRAS*, 488(2):2825–2835, Sept. 2019. [arXiv:1903.09160](#), [doi:10.1093/mnras/stz1803](#).
- [94] G. Fragione, A. Loeb, and F. A. Rasio. On the Origin of GW190521-like Events from Repeated Black Hole Mergers in Star Clusters. *ApJ*, 902(1):L26, Oct. 2020. [arXiv:2009.05065](#), [doi:10.3847/2041-8213/abbc0a](#).
- [95] M. Freitag, M. A. Gürkan, and F. A. Rasio. Runaway collisions in young star clusters - II. Numerical results. *MNRAS*, 368(1):141–161, May 2006. [arXiv:astro-ph/0503130](#), [doi:10.1111/j.1365-2966.2006.10096.x](#).
- [96] C. L. Fryer, K. Belczynski, G. Wiktorowicz, M. Dominik, V. Kalogera, and D. E. Holz. Compact remnant mass function: Dependence on the explosion mechanism and metallicity. *The Astrophysical Journal*, 749(1):91, mar 2012. URL: <https://dx.doi.org/10.1088/0004-637X/749/1/91>, [doi:10.1088/0004-637X/749/1/91](#).
- [97] M. S. Fujii, A. Tanikawa, and J. Makino. The detection rates of merging binary black holes originating from star clusters and their mass function. *PASJ*, 69(6):94, Dec. 2017. [arXiv:1709.02058](#), [doi:10.1093/pasj/psx108](#).
- [98] E. Gaburov, J. Bédorf, and S. P. Zwart. Gravitational tree-code on graphics processing units: implementation in cuda. *Procedia Computer Science*, 1(1):1119–1127, 2010. ICCS 2010. URL: <https://www.sciencedirect.com/science/article/pii/S1877050910001250>, [doi:https://doi.org/10.1016/j.procs.2010.04.124](#).
- [99] E. Gaburov, J. C. Lombardi, and S. Portegies Zwart. Mixing in massive stellar mergers. *MNRAS*, 383(1):L5–L9, Jan. 2008. [arXiv:0707.3021](#), [doi:10.1111/j.1745-3933.2007.00399.x](#).
- [100] V. Gayathri, J. Healy, J. Lange, B. O’Brien, M. Szczepanczyk, I. Bartos, M. Campanelli, S. Klimentko, C. Lousto, and R. O’Shaughnessy. Eccentricity Estimate for Black Hole Mergers with Numerical Relativity Simulations. *arXiv e-prints*, page arXiv:2009.05461, Sept. 2020. [arXiv:2009.05461](#), [doi:10.48550/arXiv.2009.05461](#).
-

- [101] H. Ge, M. S. Hjellming, R. F. Webbink, X. Chen, and Z. Han. Adiabatic mass loss in binary stars. i. computational method. *The Astrophysical Journal*, 717(2):724, jun 2010. URL: <https://dx.doi.org/10.1088/0004-637X/717/2/724>, doi: [10.1088/0004-637X/717/2/724](https://doi.org/10.1088/0004-637X/717/2/724).
- [102] H. Ge, R. F. Webbink, X. Chen, and Z. Han. Adiabatic mass loss in binary stars. ii. from zero-age main sequence to the base of the giant branch. *The Astrophysical Journal*, 812(1):40, oct 2015. URL: <https://dx.doi.org/10.1088/0004-637X/812/1/40>, doi: [10.1088/0004-637X/812/1/40](https://doi.org/10.1088/0004-637X/812/1/40).
- [103] H. Ge, R. F. Webbink, X. Chen, and Z. Han. Adiabatic Mass Loss in Binary Stars. III. From the Base of the Red Giant Branch to the Tip of the Asymptotic Giant Branch. *ApJ*, 899(2):132, Aug. 2020. [arXiv:2007.09848](https://arxiv.org/abs/2007.09848), doi: [10.3847/1538-4357/aba7b7](https://doi.org/10.3847/1538-4357/aba7b7).
- [104] H. Ge, R. F. Webbink, and Z. Han. The thermal equilibrium mass-loss model and its applications in binary evolution. *The Astrophysical Journal Supplement Series*, 249(1):9, jul 2020. URL: <https://dx.doi.org/10.3847/1538-4365/ab98f6>, doi: [10.3847/1538-4365/ab98f6](https://doi.org/10.3847/1538-4365/ab98f6).
- [105] D. Gerosa and E. Berti. Are merging black holes born from stellar collapse or previous mergers? *Phys. Rev. D*, 95(12):124046, June 2017. [arXiv:1703.06223](https://arxiv.org/abs/1703.06223), doi: [10.1103/PhysRevD.95.124046](https://doi.org/10.1103/PhysRevD.95.124046).
- [106] N. Giacobbo and M. Mapelli. The impact of electron-capture supernovae on merging double neutron stars. *Monthly Notices of the Royal Astronomical Society*, 482(2):2234–2243, 10 2018. [arXiv:https://academic.oup.com/mnras/article-pdf/482/2/2234/26489944/sty2848.pdf](https://academic.oup.com/mnras/article-pdf/482/2/2234/26489944/sty2848.pdf), doi: [10.1093/mnras/sty2848](https://doi.org/10.1093/mnras/sty2848).
- [107] N. Giacobbo and M. Mapelli. The progenitors of compact-object binaries: impact of metallicity, common envelope and natal kicks. *MNRAS*, 480(2):2011–2030, oct 2018. [arXiv:1806.00001](https://arxiv.org/abs/1806.00001), doi: [10.1093/mnras/sty1999](https://doi.org/10.1093/mnras/sty1999).
- [108] N. Giacobbo and M. Mapelli. Revising natal kick prescriptions in population synthesis simulations. *The Astrophysical Journal*, 891(2):141, mar 2020. URL: <https://dx.doi.org/10.3847/1538-4357/ab7335>, doi: [10.3847/1538-4357/ab7335](https://doi.org/10.3847/1538-4357/ab7335).
- [109] N. Giacobbo and M. Mapelli. Revising natal kick prescriptions in population synthesis simulations. *The Astrophysical Journal*, 891(2):141, mar 2020. URL: <https://dx.doi.org/10.3847/1538-4357/ab7335>, doi: [10.3847/1538-4357/ab7335](https://doi.org/10.3847/1538-4357/ab7335).
- [110] N. Giacobbo, M. Mapelli, and M. Spera. Merging black hole binaries: the effects of progenitor’s metallicity, mass-loss rate and Eddington factor. *MNRAS*, 474(3):2959–2974, Mar. 2018. [arXiv:1711.03556](https://arxiv.org/abs/1711.03556), doi: [10.1093/mnras/stx2933](https://doi.org/10.1093/mnras/stx2933).

-
- [111] M. Giersz, N. Leigh, A. Hypki, N. Lützgendorf, and A. Askar. MOCCA code for star cluster simulations - IV. A new scenario for intermediate mass black hole formation in globular clusters. *MNRAS*, 454(3):3150–3165, Dec. 2015. [arXiv:1506.05234](#), [doi:10.1093/mnras/stv2162](#).
- [112] J. A. González, U. Sperhake, B. Brügmann, M. Hannam, and S. Husa. Maximum Kick from Nonspinning Black-Hole Binary Inspiral. *Phys. Rev. Lett.*, 98(9):091101, Mar. 2007. [arXiv:gr-qc/0610154](#), [doi:10.1103/PhysRevLett.98.091101](#).
- [113] A. W. Graham and L. R. Spitler. Quantifying the coexistence of massive black holes and dense nuclear star clusters. *MNRAS*, 397(4):2148–2162, Aug. 2009. [arXiv:0907.5250](#), [doi:10.1111/j.1365-2966.2009.15118.x](#).
- [114] R. Gratton, A. Bragaglia, E. Carretta, V. D’Orazi, S. Lucatello, and A. Sollima. What is a globular cluster? An observational perspective. *A&A Rev.*, 27(1):8, Nov. 2019. [arXiv:1911.02835](#), [doi:10.1007/s00159-019-0119-3](#).
- [115] F. Groh, L. Ruppert, P. Wieschollek, and H. P. A. Lensch. GGNN: Graph-based GPU Nearest Neighbor Search. *arXiv e-prints*, page arXiv:1912.01059, Dec. 2019. [arXiv:1912.01059](#), [doi:10.48550/arXiv.1912.01059](#).
- [116] P. Gupta, H. Suzuki, H. Okawa, and K.-i. Maeda. Gravitational waves from hierarchical triple systems with Kozai-Lidov oscillation. *Phys. Rev. D*, 101(10):104053, May 2020. [arXiv:1911.11318](#), [doi:10.1103/PhysRevD.101.104053](#).
- [117] M. A. Gürkan, J. M. Fregeau, and F. A. Rasio. Massive Black Hole Binaries from Collisional Runaways. *ApJ*, 640(1):L39–L42, Mar. 2006. [arXiv:astro-ph/0512642](#), [doi:10.1086/503295](#).
- [118] Z. Han, P. Podsiadlowski, and P. P. Eggleton. A possible criterion for envelope ejection in asymptotic giant branch or first giant branch stars. *MNRAS*, 270:121–130, Sept. 1994. [doi:10.1093/mnras/270.1.121](#).
- [119] W. E. Harris, G. L. H. Harris, and M. Alessi. A Catalog of Globular Cluster Systems: What Determines the Size of a Galaxy’s Globular Cluster Population? *ApJ*, 772(2):82, Aug. 2013. [arXiv:1306.2247](#), [doi:10.1088/0004-637X/772/2/82](#).
- [120] A. Heger, C. L. Fryer, S. E. Woosley, N. Langer, and D. H. Hartmann. How massive single stars end their life. *The Astrophysical Journal*, 591(1):288, jul 2003. URL: <https://dx.doi.org/10.1086/375341>, [doi:10.1086/375341](#).
- [121] D. C. Heggie. Binary Evolution in Stellar Dynamics. *Monthly Notices of the Royal Astronomical Society*, 173(3):729–787, 12 1975. [arXiv:https://academic.oup.com/mnras/article-pdf/173/3/729/2929251/mnras173-0729.pdf](#), [doi:10.1093/mnras/173.3.729](#).
-

- [122] J. G. Hills. Encounters between binary and single stars and their effect on the dynamical evolution of stellar systems. *AJ*, 80:809–825, Oct. 1975. doi:[10.1086/111815](https://doi.org/10.1086/111815).
- [123] J. G. Hills. The effect of low-velocity, low-mass intruders (collisionless gas) on the dynamical evolution of a binary system. *AJ*, 88:1269–1283, Aug. 1983. doi:[10.1086/113418](https://doi.org/10.1086/113418).
- [124] J. G. Hills and L. W. Fullerton. Computer simulations of close encounters between single stars and hard binaries. *AJ*, 85:1281–1291, sep 1980. doi:[10.1086/112798](https://doi.org/10.1086/112798).
- [125] D. Hils, P. L. Bender, and R. F. Webbink. Gravitational Radiation from the Galaxy. *ApJ*, 360:75, sep 1990. doi:[10.1086/169098](https://doi.org/10.1086/169098).
- [126] B.-M. Hoang, S. Naoz, B. Kocsis, W. M. Farr, and J. McIver. Detecting Supermassive Black Hole-induced Binary Eccentricity Oscillations with LISA. *ApJ*, 875(2):L31, Apr. 2019. arXiv:[1903.00134](https://arxiv.org/abs/1903.00134), doi:[10.3847/2041-8213/ab14f7](https://doi.org/10.3847/2041-8213/ab14f7).
- [127] G. Hobbs, D. R. Lorimer, A. G. Lyne, and M. Kramer. A statistical study of 233 pulsar proper motions. *MNRAS*, 360(3):974–992, July 2005. arXiv:[astro-ph/0504584](https://arxiv.org/abs/astro-ph/0504584), doi:[10.1111/j.1365-2966.2005.09087.x](https://doi.org/10.1111/j.1365-2966.2005.09087.x).
- [128] K. Holley-Bockelmann, K. Gültekin, D. Shoemaker, and N. Yunes. Gravitational Wave Recoil and the Retention of Intermediate-Mass Black Holes. *ApJ*, 686(2):829–837, Oct. 2008. arXiv:[0707.1334](https://arxiv.org/abs/0707.1334), doi:[10.1086/591218](https://doi.org/10.1086/591218).
- [129] R. A. Hulse and J. H. Taylor. Discovery of a pulsar in a binary system. *ApJ*, 195:L51–L53, jan 1975. doi:[10.1086/181708](https://doi.org/10.1086/181708).
- [130] J. R. Hurley, O. R. Pols, and C. A. Tout. Comprehensive analytic formulae for stellar evolution as a function of mass and metallicity. *MNRAS*, 315(3):543–569, July 2000. arXiv:[astro-ph/0001295](https://arxiv.org/abs/astro-ph/0001295), doi:[10.1046/j.1365-8711.2000.03426.x](https://doi.org/10.1046/j.1365-8711.2000.03426.x).
- [131] J. R. Hurley, C. A. Tout, and O. R. Pols. Evolution of binary stars and the effect of tides on binary populations. *MNRAS*, 329(4):897–928, feb 2002. arXiv:[astro-ph/0201220](https://arxiv.org/abs/astro-ph/0201220), doi:[10.1046/j.1365-8711.2002.05038.x](https://doi.org/10.1046/j.1365-8711.2002.05038.x).
- [132] P. Hut. Tidal evolution in close binary systems. *A&A*, 99:126–140, jun 1981. URL: <https://ui.adsabs.harvard.edu/abs/1981A&A....99..126H>.
- [133] P. Hut, S. McMillan, J. Goodman, M. Mateo, E. S. Phinney, C. Pryor, H. B. Richer, F. Verbunt, and M. Weinberg. Binaries in Globular Clusters. *PASP*, 104:981, nov 1992. doi:[10.1086/133085](https://doi.org/10.1086/133085).
- [134] A. Hypki and M. Giersz. *molca* code for star cluster simulations – I. Blue stragglers, first results. *Monthly Notices of the Royal Astronomical Society*, 429(2):1221–1243, 12 2012. arXiv:<https://academic.oup.com/mnras/advance-article-abstract/doi/10.1093/mnras/stt001/1111111>.

-
- [com/mnras/article-pdf/429/2/1221/18456484/sts415.pdf](https://www.mnras.com/mnras/article-pdf/429/2/1221/18456484/sts415.pdf), doi:10.1093/mnras/sts415.
- [135] I. Iben and M. Livio. Common envelopes in binary star evolution. *Publications of the Astronomical Society of the Pacific*, 105(694):1373, dec 1993. URL: <https://dx.doi.org/10.1086/133321>, doi:10.1086/133321.
- [136] G. Iorio, G. Costa, M. Mapelli, M. Spera, G. J. Escobar, C. Sgalletta, A. A. Trani, E. Korb, F. Santoliquido, M. Dall’Amico, N. Gaspari, and A. Bressan. Compact object mergers: exploring uncertainties from stellar and binary evolution with SEVN. *arXiv e-prints*, page arXiv:2211.11774, Nov. 2022. arXiv:2211.11774, doi:10.48550/arXiv.2211.11774.
- [137] T. Ito and K. Ohtsuka. The Lidov-Kozai Oscillation and Hugo von Zeipel. *Monographs on Environment, Earth and Planets*, 7(1):1–113, nov 2019. arXiv:1911.03984, doi:10.5047/meep.2019.00701.0001.
- [138] N. Ivanova and S. Chaichenets. Common Envelope: Enthalpy Consideration. *ApJ*, 731(2):L36, Apr. 2011. arXiv:1103.2790, doi:10.1088/2041-8205/731/2/L36.
- [139] N. Ivanova, S. Justham, X. Chen, O. De Marco, C. L. Fryer, E. Gaburov, H. Ge, E. Glebbeek, Z. Han, X. D. Li, G. Lu, T. Marsh, P. Podsiadlowski, A. Potter, N. Soker, R. Taam, T. M. Tauris, E. P. J. van den Heuvel, and R. F. Webbink. Common envelope evolution: where we stand and how we can move forward. *A&A Rev.*, 21:59, Feb. 2013. arXiv:1209.4302, doi:10.1007/s00159-013-0059-2.
- [140] N. Ivanova, P. Podsiadlowski, and H. Spruit. Hydrodynamical simulations of the stream-core interaction in the slow merger of massive stars. *MNRAS*, 334(4):819–832, Aug. 2002. arXiv:astro-ph/0109524, doi:10.1046/j.1365-8711.2002.05543.x.
- [141] N. Ivanova and R. E. Taam. Thermal Timescale Mass Transfer and the Evolution of White Dwarf Binaries. *ApJ*, 601(2):1058–1066, Feb. 2004. arXiv:astro-ph/0310126, doi:10.1086/380561.
- [142] X. Jiménez-Forteza, D. Keitel, S. Husa, M. Hannam, S. Khan, and M. Pürrer. Hierarchical data-driven approach to fitting numerical relativity data for nonprecessing binary black holes with an application to final spin and radiated energy. *Phys. Rev. D*, 95:064024, Mar 2017. URL: <https://link.aps.org/doi/10.1103/PhysRevD.95.064024>, doi:10.1103/PhysRevD.95.064024.
- [143] J. Johnson, M. Douze, and H. Jégou. Billion-scale similarity search with GPUs. *arXiv e-prints*, page arXiv:1702.08734, Feb. 2017. arXiv:1702.08734, doi:10.48550/arXiv.1702.08734.
-

- [144] A. B. Justesen and S. Albrecht. Temperature and Distance Dependence of Tidal Circularization in Close Binaries: A Catalog of Eclipsing Binaries in the Southern Hemisphere Observed by the TESS Satellite. *ApJ*, 912(2):123, May 2021. [arXiv:2103.09216](#), [doi:10.3847/1538-4357/abefcd](#).
- [145] T. O. Kimpson, M. Spera, M. Mapelli, and B. M. Ziosi. Hierarchical black hole triples in young star clusters: impact of Kozai–Lidov resonance on mergers. *Monthly Notices of the Royal Astronomical Society*, 463(3):2443–2452, 08 2016. [arXiv:https://academic.oup.com/mnras/article-pdf/463/3/2443/18236687/stw2085.pdf](#), [doi:10.1093/mnras/stw2085](#).
- [146] F. S. Kitaura, H. T. Janka, and W. Hillebrandt. Explosions of O-Ne-Mg cores, the Crab supernova, and subluminous type II-P supernovae. *A&A*, 450(1):345–350, Apr. 2006. [arXiv:astro-ph/0512065](#), [doi:10.1051/0004-6361:20054703](#).
- [147] B. Kiziltan, A. Kottas, M. De Yoreo, and S. E. Thorsett. The Neutron Star Mass Distribution. *arXiv e-prints*, page arXiv:1309.6635, Sept. 2013. [arXiv:1309.6635](#), [doi:10.48550/arXiv.1309.6635](#).
- [148] J. Klencki, G. Nelemans, A. G. Istrate, and M. Chruslinska. It has to be cool: Supergiant progenitors of binary black hole mergers from common-envelope evolution. *A&A*, 645:A54, Jan. 2021. [arXiv:2006.11286](#), [doi:10.1051/0004-6361/202038707](#).
- [149] S. Konstantinidis and K. D. Kokkotas. MYRIAD: a new N-body code for simulations of star clusters. *A&A*, 522:A70, Nov. 2010. [arXiv:1006.3326](#), [doi:10.1051/0004-6361/200913890](#).
- [150] Y. Kozai. Secular perturbations of asteroids with high inclination and eccentricity. *AJ*, 67:591–598, Nov. 1962. [doi:10.1086/108790](#).
- [151] K. Kremer, C. L. Rodriguez, P. Amaro-Seoane, K. Breivik, S. Chatterjee, M. L. Katz, S. L. Larson, F. A. Rasio, J. Samsing, C. S. Ye, and M. Zevin. Post-Newtonian dynamics in dense star clusters: Binary black holes in the LISA band. *Phys. Rev. D*, 99(6):063003, Mar. 2019. [arXiv:1811.11812](#), [doi:10.1103/PhysRevD.99.063003](#).
- [152] K. Kremer, M. Spera, D. Becker, S. Chatterjee, U. N. Di Carlo, G. Fragione, C. L. Rodriguez, C. S. Ye, and F. A. Rasio. Populating the Upper Black Hole Mass Gap through Stellar Collisions in Young Star Clusters. *ApJ*, 903(1):45, Nov. 2020. [arXiv:2006.10771](#), [doi:10.3847/1538-4357/abb945](#).
- [153] M. U. Kruckow, T. M. Tauris, N. Langer, M. Kramer, and R. G. Izzard. Progenitors of gravitational wave mergers: binary evolution with the stellar grid-based code COMBINE. *MNRAS*, 481(2):1908–1949, Dec. 2018. [arXiv:1801.05433](#), [doi:10.1093/mnras/sty2190](#).

-
- [154] M. U. Kruckow, T. M. Tauris, N. Langer, D. Szécsi, P. Marchant, and P. Podsiadlowski. Common-envelope ejection in massive binary stars. Implications for the progenitors of GW150914 and GW151226. *A&A*, 596:A58, Nov. 2016. [arXiv:1610.04417](#), [doi:10.1051/0004-6361/201629420](#).
- [155] J. Kumamoto, M. S. Fujii, and A. Tanikawa. Gravitational-wave emission from binary black holes formed in open clusters. *Monthly Notices of the Royal Astronomical Society*, 486(3):3942–3950, 04 2019. [arXiv:https://academic.oup.com/mnras/article-pdf/486/3/3942/28554983/stz1068.pdf](#), [doi:10.1093/mnras/stz1068](#).
- [156] J. Kumamoto, M. S. Fujii, and A. Tanikawa. Merger rate density of binary black holes formed in open clusters. *MNRAS*, 495(4):4268–4278, July 2020. [arXiv:2001.10690](#), [doi:10.1093/mnras/staa1440](#).
- [157] A. Kučinskas. Circumstellar Shells of the Mass-Losing Asymptotic Giant Branch Stars: Limits for the Dust-Driven Winds. *Ap&SS*, 262(2):127–143, Mar. 1998. URL: <https://ui.adsabs.harvard.edu/abs/1998Ap&SS.262..127K>.
- [158] A. H. W. Küpper, T. Maschberger, P. Kroupa, and H. Baumgardt. Mass segregation and fractal substructure in young massive clusters – I. The McLuster code and method calibration. *Monthly Notices of the Royal Astronomical Society*, 417(3):2300–2317, 10 2011. [arXiv:https://academic.oup.com/mnras/article-pdf/417/3/2300/3826875/mnras0417-2300.pdf](#), [doi:10.1111/j.1365-2966.2011.19412.x](#).
- [159] C. J. Lada and E. A. Lada. Embedded Clusters in Molecular Clouds. *ARA&A*, 41:57–115, Jan. 2003. [arXiv:astro-ph/0301540](#), [doi:10.1146/annurev.astro.41.011802.094844](#).
- [160] J. M. Lattimer and D. N. Schramm. Black-Hole-Neutron-Star Collisions. *ApJ*, 192:L145, sep 1974. [doi:10.1086/181612](#).
- [161] J. M. Lattimer and A. Yahil. Analysis of the Neutrino Events from Supernova 1987A. *ApJ*, 340:426, May 1989. [doi:10.1086/167404](#).
- [162] J. A. P. Law-Smith, R. W. Everson, E. Ramirez-Ruiz, S. E. de Mink, L. A. C. van Son, Y. Götzberg, S. Zellmann, A. Vigna-Gómez, M. Renzo, S. Wu, S. L. Schröder, R. J. Foley, and T. Hutchinson-Smith. Successful Common Envelope Ejection and Binary Neutron Star Formation in 3D Hydrodynamics. *arXiv e-prints*, page arXiv:2011.06630, Nov. 2020. [arXiv:2011.06630](#), [doi:10.48550/arXiv.2011.06630](#).
- [163] H. M. Lee. Evolution of galactic nuclei with $10-M_{\odot}$ black holes. *MNRAS*, 272(3):605–617, Feb. 1995. [arXiv:astro-ph/9409073](#), [doi:10.1093/mnras/272.3.605](#).
-

- [164] M. L. Lidov. The evolution of orbits of artificial satellites of planets under the action of gravitational perturbations of external bodies. *Planet. Space Sci.*, 9(10):719–759, Oct. 1962. doi:[10.1016/0032-0633\(62\)90129-0](https://doi.org/10.1016/0032-0633(62)90129-0).
- [165] A. P. Lightman and S. L. Shapiro. The dynamical evolution of globular clusters. *Rev. Mod. Phys.*, 50:437–481, Apr 1978. URL: <https://link.aps.org/doi/10.1103/RevModPhys.50.437>, doi:[10.1103/RevModPhys.50.437](https://doi.org/10.1103/RevModPhys.50.437).
- [166] M. Limongi and A. Chieffi. Presupernova Evolution and Explosive Nucleosynthesis of Rotating Massive Stars in the Metallicity Range $-3 \leq [\text{Fe}/\text{H}] \leq 0$. *ApJS*, 237(1):13, July 2018. arXiv:[1805.09640](https://arxiv.org/abs/1805.09640), doi:[10.3847/1538-4365/aac24](https://doi.org/10.3847/1538-4365/aac24).
- [167] M. Livio and N. Soker. The Common Envelope Phase in the Evolution of Binary Stars. *ApJ*, 329:764, June 1988. doi:[10.1086/166419](https://doi.org/10.1086/166419).
- [168] C. O. Lousto and Y. Zlochower. Modeling gravitational recoil from precessing highly spinning unequal-mass black-hole binaries. *Phys. Rev. D*, 79(6):064018, Mar. 2009. arXiv:[0805.0159](https://arxiv.org/abs/0805.0159), doi:[10.1103/PhysRevD.79.064018](https://doi.org/10.1103/PhysRevD.79.064018).
- [169] A. J. Loveridge, M. V. van der Sluys, and V. Kalogera. Analytical Expressions for the Envelope Binding Energy of Giants as a Function of Basic Stellar Parameters. *ApJ*, 743(1):49, Dec. 2011. arXiv:[1009.5400](https://arxiv.org/abs/1009.5400), doi:[10.1088/0004-637X/743/1/49](https://doi.org/10.1088/0004-637X/743/1/49).
- [170] S. H. Lubow and F. H. Shu. Gas dynamics of semidetached binaries. *ApJ*, 198:383–405, June 1975. doi:[10.1086/153614](https://doi.org/10.1086/153614).
- [171] M. MacLeod, A. Antoni, A. Murguia-Berthier, P. Macias, and E. Ramirez-Ruiz. Common Envelope Wind Tunnel: Coefficients of Drag and Accretion in a Simplified Context for Studying Flows around Objects Embedded within Stellar Envelopes. *ApJ*, 838(1):56, Mar. 2017. arXiv:[1704.02372](https://arxiv.org/abs/1704.02372), doi:[10.3847/1538-4357/aa6117](https://doi.org/10.3847/1538-4357/aa6117).
- [172] M. MacLeod and A. Loeb. Pre-common-envelope Mass Loss from Coalescing Binary Systems. *ApJ*, 895(1):29, May 2020. arXiv:[2003.01123](https://arxiv.org/abs/2003.01123), doi:[10.3847/1538-4357/ab89b6](https://doi.org/10.3847/1538-4357/ab89b6).
- [173] M. MacLeod and A. Loeb. Runaway Coalescence of Pre-common-envelope Stellar Binaries. *ApJ*, 893(2):106, Apr. 2020. arXiv:[1912.05545](https://arxiv.org/abs/1912.05545), doi:[10.3847/1538-4357/ab822e](https://doi.org/10.3847/1538-4357/ab822e).
- [174] M. MacLeod, P. Macias, E. Ramirez-Ruiz, J. Grindlay, A. Batta, and G. Montes. Lessons from the Onset of a Common Envelope Episode: the Remarkable M31 2015 Luminous Red Nova Outburst. *ApJ*, 835(2):282, Feb. 2017. arXiv:[1605.01493](https://arxiv.org/abs/1605.01493), doi:[10.3847/1538-4357/835/2/282](https://doi.org/10.3847/1538-4357/835/2/282).
- [175] M. MacLeod, E. C. Ostriker, and J. M. Stone. Runaway Coalescence at the Onset of Common Envelope Episodes. *ApJ*, 863(1):5, Aug. 2018. arXiv:[1803.03261](https://arxiv.org/abs/1803.03261), doi:[10.3847/1538-4357/aacf08](https://doi.org/10.3847/1538-4357/aacf08).

- [176] M. MacLeod and E. Ramirez-Ruiz. Asymmetric Accretion Flows within a Common Envelope. *ApJ*, 803(1):41, Apr. 2015. [arXiv:1410.3823](#), [doi:10.1088/0004-637X/803/1/41](#).
- [177] M. MacLeod and E. Ramirez-Ruiz. On the Accretion-fed Growth of Neutron Stars during Common Envelope. *ApJ*, 798(1):L19, Jan. 2015. [arXiv:1410.5421](#), [doi:10.1088/2041-8205/798/1/L19](#).
- [178] J. Makino and S. J. Aarseth. On a Hermite Integrator with Ahmad-Cohen Scheme for Gravitational Many-Body Problems. *Publications of the Astronomical Society of Japan*, 44:141–151, Apr. 1992. URL: <https://ui.adsabs.harvard.edu/abs/1992PASJ...44..141M>.
- [179] J. Makino, T. Fukushige, M. Koga, and K. Namura. GRAPE-6: Massively-Parallel Special-Purpose Computer for Astrophysical Particle Simulations. *PASJ*, 55:1163–1187, Dec. 2003. URL: <https://ui.adsabs.harvard.edu/abs/2003PASJ...55.1163M>, [arXiv:astro-ph/0310702](#), [doi:10.1093/pasj/55.6.1163](#).
- [180] J. Makino and P. Hut. Performance Analysis of Direct N-Body Calculations. *ApJS*, 68:833, Dec. 1988. [doi:10.1086/191306](#).
- [181] J. Makino, E. Kokubo, and M. Taiji. HARP: A Special-Purpose Computer for N-Body Problem. *PASJ*, 45:349–360, June 1993. URL: <https://ui.adsabs.harvard.edu/abs/1993PASJ...45..349M>.
- [182] J. Makino and M. Taiji. *Scientific Simulations with Special-Purpose Computers—the GRAPE Systems*. Wiley, 1998. URL: <https://ui.adsabs.harvard.edu/abs/1998sssc.book.....M>.
- [183] Y. A. Malkov and D. A. Yashunin. Efficient and robust approximate nearest neighbor search using Hierarchical Navigable Small World graphs. *arXiv e-prints*, page arXiv:1603.09320, Mar. 2016. [arXiv:1603.09320](#), [doi:10.48550/arXiv.1603.09320](#).
- [184] I. Mandel and S. E. de Mink. Merging binary black holes formed through chemically homogeneous evolution in short-period stellar binaries. *MNRAS*, 458(3):2634–2647, may 2016. [arXiv:1601.00007](#), [doi:10.1093/mnras/stw379](#).
- [185] M. Mapelli. Massive black hole binaries from runaway collisions: the impact of metallicity. *MNRAS*, 459(4):3432–3446, jul 2016. [arXiv:1604.03559](#), [doi:10.1093/mnras/stw869](#).
- [186] M. Mapelli. Formation Channels of Single and Binary Stellar-Mass Black Holes. In *Handbook of Gravitational Wave Astronomy*, page 16. Springer Singapore, 2021. [doi:10.1007/978-981-15-4702-7_16-1](#).

- [187] M. Mapelli, M. Colpi, A. Possenti, and S. Sigurdsson. The fingerprint of binary intermediate-mass black holes in globular clusters: suprathermal stars and angular momentum alignment. *MNRAS*, 364(4):1315–1326, Dec. 2005. [arXiv:astro-ph/0506405](#), [doi:10.1111/j.1365-2966.2005.09653.x](#).
- [188] M. Mapelli, M. Dall’Amico, Y. Bouffanais, N. Giacobbo, M. Arca Sedda, M. C. Artale, A. Ballone, U. N. Di Carlo, G. Iorio, F. Santoliquido, and S. Torniamenti. Hierarchical black hole mergers in young, globular and nuclear star clusters: the effect of metallicity, spin and cluster properties. *MNRAS*, 505(1):339–358, July 2021. [arXiv:2103.05016](#), [doi:10.1093/mnras/stab1334](#).
- [189] M. Mapelli, A. Ferrara, and N. Rea. Constraints on Galactic intermediate mass black holes. *MNRAS*, 368(3):1340–1350, May 2006. [arXiv:astro-ph/0602388](#), [doi:10.1111/j.1365-2966.2006.10201.x](#).
- [190] M. Mapelli, N. Giacobbo, E. Ripamonti, and M. Spera. The cosmic merger rate of stellar black hole binaries from the Illustris simulation. *Monthly Notices of the Royal Astronomical Society*, 472(2):2422–2435, 08 2017. [arXiv:https://academic.oup.com/mnras/article-pdf/472/2/2422/19943102/stx2123.pdf](#), [doi:10.1093/mnras/stx2123](#).
- [191] M. Mapelli, B. Moore, L. Giordano, L. Mayer, M. Colpi, E. Ripamonti, and S. Callegari. Intermediate-mass black holes and ultraluminous X-ray sources in the Cartwheel ring galaxy. *Monthly Notices of the Royal Astronomical Society*, 383(1):230–246, 12 2007. [arXiv:https://academic.oup.com/mnras/article-pdf/383/1/230/3688541/mnras0383-0230.pdf](#), [doi:10.1111/j.1365-2966.2007.12534.x](#).
- [192] M. Mapelli, M. Spera, E. Montanari, M. Limongi, A. Chieffi, N. Giacobbo, A. Bressan, and Y. Bouffanais. Impact of the Rotation and Compactness of Progenitors on the Mass of Black Holes. *ApJ*, 888(2):76, Jan. 2020. [arXiv:1909.01371](#), [doi:10.3847/1538-4357/ab584d](#).
- [193] M. Mapelli, L. Zampieri, E. Ripamonti, and A. Bressan. Dynamics of stellar black holes in young star clusters with different metallicities – I. Implications for X-ray binaries. *Monthly Notices of the Royal Astronomical Society*, 429(3):2298–2314, 01 2013. [arXiv:https://academic.oup.com/mnras/article-pdf/429/3/2298/3244007/sts500.pdf](#), [doi:10.1093/mnras/sts500](#).
- [194] P. Marchant, N. Langer, P. Podsiadlowski, T. M. Tauris, and T. J. Moriya. A new route towards merging massive black holes. *A&A*, 588:A50, apr 2016. [arXiv:1601.03718](#), [doi:10.1051/0004-6361/201628133](#).
- [195] P. Marchant and T. J. Moriya. The impact of stellar rotation on the black hole mass-gap from pair-instability supernovae. *A&A*, 640:L18, Aug. 2020. [arXiv:2007.06220](#), [doi:10.1051/0004-6361/202038902](#).

-
- [196] C. Maureira-Fredes and P. Amaro-Seoane. GraviDy, a GPU modular, parallel direct-summation N-body integrator: dynamics with softening. *Monthly Notices of the Royal Astronomical Society*, 473(3):3113–3127, 09 2017. [arXiv:https://academic.oup.com/mnras/article-pdf/473/3/3113/21736460/stx2468.pdf](https://academic.oup.com/mnras/article-pdf/473/3/3113/21736460/stx2468.pdf), [doi:10.1093/mnras/stx2468](https://doi.org/10.1093/mnras/stx2468).
- [197] C. Maureira-Fredes and P. Amaro-Seoane. GraviDy, a GPU modular, parallel direct-summation N-body integrator: dynamics with softening. *Monthly Notices of the Royal Astronomical Society*, 473(3):3113–3127, 09 2017. [arXiv:https://academic.oup.com/mnras/article-pdf/473/3/3113/21736460/stx2468.pdf](https://academic.oup.com/mnras/article-pdf/473/3/3113/21736460/stx2468.pdf), [doi:10.1093/mnras/stx2468](https://doi.org/10.1093/mnras/stx2468).
- [198] B. McKernan, K. E. S. Ford, J. Bellovary, N. W. C. Leigh, Z. Haiman, B. Kocsis, W. Lyra, M. M. Mac Low, B. Metzger, M. O’Dowd, S. Endlich, and D. J. Rosen. Constraining Stellar-mass Black Hole Mergers in AGN Disks Detectable with LIGO. *ApJ*, 866(1):66, Oct. 2018. [arXiv:1702.07818](https://arxiv.org/abs/1702.07818), [doi:10.3847/1538-4357/aadae5](https://doi.org/10.3847/1538-4357/aadae5).
- [199] S. McMillan, P. Hut, and J. Makino. Star Cluster Evolution with Primordial Binaries. II. Detailed Analysis. *ApJ*, 372:111, may 1991. [doi:10.1086/169958](https://doi.org/10.1086/169958).
- [200] S. Meibom and R. D. Mathieu. A robust measure of tidal circularization in coeval binary populations: The solar-type spectroscopic binary population in the open cluster m35*. *The Astrophysical Journal*, 620(2):970, feb 2005. URL: <https://dx.doi.org/10.1086/427082>, [doi:10.1086/427082](https://doi.org/10.1086/427082).
- [201] M. Mencagli, N. Nazarova, and M. Spera. ISTEDDAS: a new direct n-body code to study merging compact-object binaries. *Journal of Physics: Conference Series*, 2207(1):012051, mar 2022. [doi:10.1088/1742-6596/2207/1/012051](https://doi.org/10.1088/1742-6596/2207/1/012051).
- [202] N. Mennekens and D. Vanbeveren. Massive double compact object mergers: gravitational wave sources and r-process element production sites. *A&A*, 564:A134, Apr. 2014. [arXiv:1307.0959](https://arxiv.org/abs/1307.0959), [doi:10.1051/0004-6361/201322198](https://doi.org/10.1051/0004-6361/201322198).
- [203] Y. Miki and M. Umemura. GOTHIC: Gravitational oct-tree code accelerated by hierarchical time step controlling. *New A*, 52:65–81, Apr. 2017. [arXiv:1610.07279](https://arxiv.org/abs/1610.07279), [doi:10.1016/j.newast.2016.10.007](https://doi.org/10.1016/j.newast.2016.10.007).
- [204] S. Mikkola and S. J. Aarseth. An Implementation of N-Body Chain Regularization. *Celestial Mechanics and Dynamical Astronomy*, 57(3):439–459, Nov. 1993. [doi:10.1007/BF00695714](https://doi.org/10.1007/BF00695714).
- [205] S. Mikkola and S. J. Aarseth. An efficient integration method for binaries in n-body simulations. *New Astronomy*, 3(5):309–320, 1998. URL: <https://www.sciencedirect.com/science/article/pii/S1384107698000189>, [doi:https://doi.org/10.1016/S1384-1076\(98\)00018-9](https://doi.org/10.1016/S1384-1076(98)00018-9).
-

- [206] S. Mikkola and D. Merritt. Algorithmic regularization with velocity-dependent forces. *Monthly Notices of the Royal Astronomical Society*, 372(1):219–223, 09 2006. [arXiv:https://academic.oup.com/mnras/article-pdf/372/1/219/5780989/mnras0372-0219.pdf](https://academic.oup.com/mnras/article-pdf/372/1/219/5780989/mnras0372-0219.pdf), doi:10.1111/j.1365-2966.2006.10854.x.
- [207] S. Mikkola and D. Merritt. Implementing few-body algorithmic regularization with post-newtonian terms. *The Astronomical Journal*, 135(6):2398–2405, may 2008. doi:10.1088/0004-6256/135/6/2398.
- [208] S. Mikkola and K. Tanikawa. Algorithmic regularization of the few-body problem. *Monthly Notices of the Royal Astronomical Society*, 310(3):745–749, 12 1999. [arXiv:https://academic.oup.com/mnras/article-pdf/310/3/745/3134407/310-3-745.pdf](https://academic.oup.com/mnras/article-pdf/310/3/745/3134407/310-3-745.pdf), doi:10.1046/j.1365-8711.1999.02982.x.
- [209] M. C. Miller and D. P. Hamilton. Four-Body Effects in Globular Cluster Black Hole Coalescence. *ApJ*, 576(2):894–898, sep 2002. [arXiv:astro-ph/0202298](https://arxiv.org/abs/astro-ph/0202298), doi:10.1086/341788.
- [210] M. C. Miller and N. Yunes. The new frontier of gravitational waves. *Nature*, 568(7753):469–476, Apr. 2019. doi:10.1038/s41586-019-1129-z.
- [211] M. Moe and R. Di Stefano. Mind Your Ps and Qs: The Interrelation between Period (P) and Mass-ratio (Q) Distributions of Binary Stars. *ApJS*, 230(2):15, June 2017. [arXiv:1606.05347](https://arxiv.org/abs/1606.05347), doi:10.3847/1538-4365/aa6fb6.
- [212] M. Morscher, B. Pattabiraman, C. Rodriguez, F. A. Rasio, and S. Umbreit. The Dynamical Evolution of Stellar Black Holes in Globular Clusters. *ApJ*, 800(1):9, Feb. 2015. [arXiv:1409.0866](https://arxiv.org/abs/1409.0866), doi:10.1088/0004-637X/800/1/9.
- [213] M. Muja and D. G. Lowe. Fast approximate nearest neighbors with automatic algorithm configuration. In *International Conference on Computer Vision Theory and Applications*, 2009. URL: http://www.image.ntua.gr/iva/files/MujaLowe_ICCVTA2009%20-%20Fast%20Approximate%20Nearest%20Neighbors%20with%20Automatic%20Algorithm%20Configuration.pdf.
- [214] S. Naoz. The Eccentric Kozai-Lidov Effect and Its Applications. *ARA&A*, 54:441–489, Sept. 2016. [arXiv:1601.07175](https://arxiv.org/abs/1601.07175), doi:10.1146/annurev-astro-081915-023315.
- [215] R. Narayan, T. Piran, and A. Shemi. Neutron Star and Black Hole Binaries in the Galaxy. *ApJ*, 379:L17, sep 1991. doi:10.1086/186143.
- [216] N. Neumayer, A. Seth, and T. Böker. Nuclear star clusters. *A&A Rev.*, 28(1):4, July 2020. [arXiv:2001.03626](https://arxiv.org/abs/2001.03626), doi:10.1007/s00159-020-00125-0.
- [217] C. T. Nguyen, G. Costa, L. Girardi, G. Volpato, A. Bressan, Y. Chen, P. Marigo, X. Fu, and P. Goudfrooij. PARSEC V2.0: Stellar tracks and isochrones of low- and intermediate-mass stars with rotation. *A&A*, 665:A126, Sept. 2022. [arXiv:2207.08642](https://arxiv.org/abs/2207.08642), doi:10.1051/0004-6361/202244166.

-
- [218] K. Nitadori, M. Iwasawa, and J. Makino. 6th and 8th Order Hermite Integrator Using Snap and Crackle. In E. Vesperini, M. Giersz, and A. Sills, editors, *Dynamical Evolution of Dense Stellar Systems*, volume 246, pages 473–474, May 2008. doi:[10.1017/S1743921308016207](https://doi.org/10.1017/S1743921308016207).
- [219] A. H. Nitz, C. D. Capano, S. Kumar, Y.-F. Wang, S. Kastha, M. Schäfer, R. Dhurkunde, and M. Cabero. 3-OGC: Catalog of gravitational waves from compact-binary mergers. *The Astrophysical Journal*, 922(1):76, nov 2021. doi:[10.3847/1538-4357/ac1c03](https://doi.org/10.3847/1538-4357/ac1c03).
- [220] W. W. Ober, M. F. El Eid, and K. J. Fricke. Evolution of Massive Pregalactic Stars - Part Two - Nucleosynthesis in Pair Creation Supernovae and Pregalactic Enrichment. *A&A*, 119:61, Mar. 1983. URL: <https://ui.adsabs.harvard.edu/abs/1983A&A...119...610>.
- [221] S. T. Ohlmann, F. K. Röpkke, R. Pakmor, and V. Springel. Hydrodynamic Moving-mesh Simulations of the Common Envelope Phase in Binary Stellar Systems. *ApJ*, 816(1):L9, Jan. 2016. arXiv:[1512.04529](https://arxiv.org/abs/1512.04529), doi:[10.3847/2041-8205/816/1/L9](https://doi.org/10.3847/2041-8205/816/1/L9).
- [222] R. M. O’Leary, F. A. Rasio, J. M. Fregeau, N. Ivanova, and R. O’Shaughnessy. Binary mergers and growth of black holes in dense star clusters. *The Astrophysical Journal*, 637(2):937–951, feb 2006. doi:[10.1086/498446](https://doi.org/10.1086/498446).
- [223] S. Olsen, T. Venumadhav, J. Mushkin, J. Roulet, B. Zackay, and M. Zaldarriaga. New binary black hole mergers in the LIGO–Virgo O3a data. *arXiv e-prints*, page arXiv:2201.02252, jan 2022. arXiv:[2201.02252](https://arxiv.org/abs/2201.02252).
- [224] F. Özel and P. Freire. Masses, radii, and the equation of state of neutron stars. *Annual Review of Astronomy and Astrophysics*, 54(1):401–440, 2016. arXiv:<https://doi.org/10.1146/annurev-astro-081915-023322>, doi:[10.1146/annurev-astro-081915-023322](https://doi.org/10.1146/annurev-astro-081915-023322).
- [225] F. Özel, D. Psaltis, R. Narayan, and J. E. McClintock. The Black Hole Mass Distribution in the Galaxy. *ApJ*, 725(2):1918–1927, Dec. 2010. arXiv:[1006.2834](https://arxiv.org/abs/1006.2834), doi:[10.1088/0004-637X/725/2/1918](https://doi.org/10.1088/0004-637X/725/2/1918).
- [226] B. Paczynski. Common Envelope Binaries. In P. Eggleton, S. Mitton, and J. Whelan, editors, *Structure and Evolution of Close Binary Systems*, volume 73, page 75, jan 1976. URL: <https://ui.adsabs.harvard.edu/abs/1976IAUS...73...75P>.
- [227] J.-C. Passy, O. De Marco, C. L. Fryer, F. Herwig, S. Diehl, J. S. Oishi, M.-M. Mac Low, G. L. Bryan, and G. Rockefeller. Simulating the Common Envelope Phase of a Red Giant Using Smoothed-particle Hydrodynamics and Uniform-grid Codes. *ApJ*, 744(1):52, Jan. 2012. arXiv:[1107.5072](https://arxiv.org/abs/1107.5072), doi:[10.1088/0004-637X/744/1/52](https://doi.org/10.1088/0004-637X/744/1/52).

- [228] P. C. Peters. Gravitational radiation and the motion of two point masses. *Phys. Rev.*, 136:B1224–B1232, Nov 1964. URL: <https://link.aps.org/doi/10.1103/PhysRev.136.B1224>, doi:10.1103/PhysRev.136.B1224.
- [229] J. Petrovic, N. Langer, and K. A. van der Hucht. Constraining the mass transfer in massive binaries through progenitor evolution models of Wolf-Rayet+O binaries. *A&A*, 435(3):1013–1030, June 2005. [arXiv:astro-ph/0504242](https://arxiv.org/abs/astro-ph/0504242), doi:10.1051/0004-6361:20042368.
- [230] E. S. Phinney. The Rate of Neutron Star Binary Mergers in the Universe: Minimal Predictions for Gravity Wave Detectors. *ApJ*, 380:L17, oct 1991. doi:10.1086/186163.
- [231] P. Podsiadlowski, S. Rappaport, and Z. Han. On the formation and evolution of black hole binaries. *MNRAS*, 341(2):385–404, may 2003. [arXiv:astro-ph/0207153](https://arxiv.org/abs/astro-ph/0207153), doi:10.1046/j.1365-8711.2003.06464.x.
- [232] S. F. Portegies Zwart, H. Baumgardt, P. Hut, J. Makino, and S. L. W. McMillan. Formation of massive black holes through runaway collisions in dense young star clusters. *Nature*, 428(6984):724–726, Apr. 2004. [arXiv:astro-ph/0402622](https://arxiv.org/abs/astro-ph/0402622), doi:10.1038/nature02448.
- [233] S. F. Portegies Zwart, J. Makino, S. L. W. McMillan, and P. Hut. Star cluster ecology. III. Runaway collisions in young compact star clusters. *A&A*, 348:117–126, Aug. 1999. [arXiv:astro-ph/9812006](https://arxiv.org/abs/astro-ph/9812006), doi:10.48550/arXiv.astro-ph/9812006.
- [234] S. F. Portegies Zwart and S. L. W. McMillan. The Runaway Growth of Intermediate-Mass Black Holes in Dense Star Clusters. *ApJ*, 576(2):899–907, Sept. 2002. [arXiv:astro-ph/0201055](https://arxiv.org/abs/astro-ph/0201055), doi:10.1086/341798.
- [235] S. F. Portegies Zwart, S. L. W. McMillan, and M. Gieles. Young Massive Star Clusters. *ARA&A*, 48:431–493, Sept. 2010. [arXiv:1002.1961](https://arxiv.org/abs/1002.1961), doi:10.1146/annurev-astro-081309-130834.
- [236] S. F. Portegies Zwart, S. L. W. McMillan, P. Hut, and J. Makino. Star cluster ecology — IV. Dissection of an open star cluster: photometry. *Monthly Notices of the Royal Astronomical Society*, 321(2):199–226, 02 2001. [arXiv:https://academic.oup.com/mnras/article-pdf/321/2/199/3023740/321-2-199.pdf](https://academic.oup.com/mnras/article-pdf/321/2/199/3023740/321-2-199.pdf), doi:10.1046/j.1365-8711.2001.03976.x.
- [237] S. F. Portegies Zwart and F. Verbunt. Population synthesis of high-mass binaries. *A&A*, 309:179–196, May 1996. URL: <https://ui.adsabs.harvard.edu/abs/1996A&A...309..179P>.
- [238] K. A. Postnov and L. R. Yungelson. The Evolution of Compact Binary Star Systems. *Living Reviews in Relativity*, 17(1):3, may 2014. [arXiv:1403.4754](https://arxiv.org/abs/1403.4754), doi:10.12942/lrr-2014-3.

- [239] W. Press, S. Teukolsky, W. Vetterling, and B. Flannery. *Numerical Recipes 3rd Edition: The Art of Scientific Computing*. Cambridge University Press, 2007. URL: <https://books.google.it/books?id=1aA0dzK3FegC>.
- [240] G. D. Quinlan. The dynamical evolution of massive black hole binaries I. Hardening in a fixed stellar background. *New A*, 1(1):35–56, July 1996. [arXiv:astro-ph/9601092](#), [doi:10.1016/S1384-1076\(96\)00003-6](#).
- [241] D. Raghavan, H. A. McAlister, T. J. Henry, D. W. Latham, G. W. Marcy, B. D. Mason, D. R. Gies, R. J. White, and T. A. ten Brummelaar. A Survey of Stellar Families: Multiplicity of Solar-type Stars. *ApJS*, 190(1):1–42, Sept. 2010. [arXiv:1007.0414](#), [doi:10.1088/0067-0049/190/1/1](#).
- [242] S. Rappaport, F. Verbunt, and P. C. Joss. A new technique for calculations of binary stellar evolution application to magnetic braking. *ApJ*, 275:713–731, Dec. 1983. [doi:10.1086/161569](#).
- [243] F. A. Rasio, C. A. Tout, S. H. Lubow, and M. Livio. Tidal Decay of Close Planetary Orbits. *ApJ*, 470:1187, Oct. 1996. [arXiv:astro-ph/9605059](#), [doi:10.1086/177941](#).
- [244] S. Rastello, M. Mapelli, U. N. Di Carlo, N. Giacobbo, F. Santoliquido, M. Spera, A. Ballone, and G. Iorio. Dynamics of black hole-neutron star binaries in young star clusters. *MNRAS*, 497(2):1563–1570, Sept. 2020. [arXiv:2003.02277](#), [doi:10.1093/mnras/staa2018](#).
- [245] M. Rees, R. Ruffini, and J. A. Wheeler. *Black holes, gravitational waves, and cosmology : an introduction to current research*. Gordon and Breach, 1974. URL: <https://ui.adsabs.harvard.edu/abs/1974bhgw.book.....R>.
- [246] M. Renzo, R. J. Farmer, S. Justham, S. E. de Mink, Y. Götberg, and P. Marchant. Sensitivity of the lower edge of the pair-instability black hole mass gap to the treatment of time-dependent convection. *MNRAS*, 493(3):4333–4341, Apr. 2020. [arXiv:2002.08200](#), [doi:10.1093/mnras/staa549](#).
- [247] P. M. Ricker and R. E. Taam. The Interaction of Stellar Objects within a Common Envelope. *ApJ*, 672(1):L41, Jan. 2008. [arXiv:0710.3631](#), [doi:10.1086/526343](#).
- [248] P. M. Ricker and R. E. Taam. An AMR Study of the Common-envelope Phase of Binary Evolution. *ApJ*, 746(1):74, Feb. 2012. [arXiv:1107.3889](#), [doi:10.1088/0004-637X/746/1/74](#).
- [249] F. P. Rizzuto, T. Naab, R. Spurzem, M. Giersz, J. P. Ostriker, N. C. Stone, L. Wang, P. Berczik, and M. Rampp. Intermediate mass black hole formation in compact young massive star clusters. *MNRAS*, 501(4):5257–5273, Mar. 2021. [arXiv:2008.09571](#), [doi:10.1093/mnras/staa3634](#).

- [250] C. L. Rodriguez, S. Chatterjee, and F. A. Rasio. Binary black hole mergers from globular clusters: Masses, merger rates, and the impact of stellar evolution. *Phys. Rev. D*, 93(8):084029, Apr. 2016. [arXiv:1602.02444](#), [doi:10.1103/PhysRevD.93.084029](#).
- [251] C. L. Rodriguez, M. Morscher, B. Pattabiraman, S. Chatterjee, C.-J. Haster, and F. A. Rasio. Binary black hole mergers from globular clusters: Implications for advanced ligo. *Phys. Rev. Lett.*, 115:051101, Jul 2015. URL: <https://link.aps.org/doi/10.1103/PhysRevLett.115.051101>, [doi:10.1103/PhysRevLett.115.051101](#).
- [252] C. L. Rodriguez, M. Morscher, L. Wang, S. Chatterjee, F. A. Rasio, and R. Spurzem. Million-body star cluster simulations: comparisons between Monte Carlo and direct N-body. *MNRAS*, 463(2):2109–2118, dec 2016. [arXiv:1601.04227](#), [doi:10.1093/mnras/stw2121](#).
- [253] C. L. Rodriguez, B. Pattabiraman, S. Chatterjee, A. Choudhary, W.-k. Liao, M. Morscher, and F. A. Rasio. A new hybrid technique for modeling dense star clusters. *Computational Astrophysics and Cosmology*, 5(1):5, Nov. 2018. [arXiv:1511.00695](#), [doi:10.1186/s40668-018-0027-3](#).
- [254] C. L. Rodriguez, M. Zevin, P. Amaro-Seoane, S. Chatterjee, K. Kremer, F. A. Rasio, and C. S. Ye. Black holes: The next generation—repeated mergers in dense star clusters and their gravitational-wave properties. *Phys. Rev. D*, 100(4):043027, Aug. 2019. [arXiv:1906.10260](#), [doi:10.1103/PhysRevD.100.043027](#).
- [255] F. K. Roepke and O. De Marco. Simulations of common-envelope evolution in binary stellar systems: physical models and numerical techniques. *arXiv e-prints*, page arXiv:2212.07308, Dec. 2022. [arXiv:2212.07308](#), [doi:10.48550/arXiv.2212.07308](#).
- [256] I. Romero-Shaw, P. D. Lasky, E. Thrane, and J. Calderón Bustillo. GW190521: Orbital Eccentricity and Signatures of Dynamical Formation in a Binary Black Hole Merger Signal. *ApJ*, 903(1):L5, Nov. 2020. [arXiv:2009.04771](#), [doi:10.3847/2041-8213/abbe26](#).
- [257] J. Samsing. Eccentric black hole mergers forming in globular clusters. *Phys. Rev. D*, 97(10):103014, May 2018. [arXiv:1711.07452](#), [doi:10.1103/PhysRevD.97.103014](#).
- [258] J. Samsing, M. MacLeod, and E. Ramirez-Ruiz. The Formation of Eccentric Compact Binary Inspirals and the Role of Gravitational Wave Emission in Binary-Single Stellar Encounters. *ApJ*, 784(1):71, Mar. 2014. [arXiv:1308.2964](#), [doi:10.1088/0004-637X/784/1/71](#).

-
- [259] J. Samsing, M. MacLeod, and E. Ramirez-Ruiz. Formation of Tidal Captures and Gravitational Wave Inspirals in Binary-single Interactions. *ApJ*, 846(1):36, Sept. 2017. [arXiv:1609.09114](#), [doi:10.3847/1538-4357/aa7e32](#).
- [260] J. Samsing and E. Ramirez-Ruiz. On the assembly rate of highly eccentric binary black hole mergers. *The Astrophysical Journal*, 840(2):L14, may 2017. [doi:10.3847/2041-8213/aa6f0b](#).
- [261] H. Sana, J.-B. L. Bouquin, S. Lacour, J.-P. Berger, G. Duvert, L. Gauchet, B. Norris, J. Olofsson, D. Pickel, G. Zins, O. Absil, A. de Koter, K. Kratter, O. Schnurr, and H. Zinnecker. Southern massive stars at high angular resolution: Observational campaign and companion detection. *The Astrophysical Journal Supplement Series*, 215(1):15, nov 2014. URL: <https://dx.doi.org/10.1088/0067-0049/215/1/15>, [doi:10.1088/0067-0049/215/1/15](#).
- [262] R. H. Sanders. The Effects of Stellar Collisions in Dense Stellar Systems. *ApJ*, 162:791, Dec. 1970. [doi:10.1086/150711](#).
- [263] I. I. Shevchenko. *The Lidov-Kozai Effect - Applications in Exoplanet Research and Dynamical Astronomy*, volume 441. Springer Cham, 2017. [doi:10.1007/978-3-319-43522-0](#).
- [264] S. Sigurdsson and L. Hernquist. Primordial black holes in globular clusters. *Nature*, 364(6436):423–425, jul 1993. [doi:10.1038/364423a0](#).
- [265] S. Sigurdsson and E. S. Phinney. Dynamics and Interactions of Binaries and Neutron Stars in Globular Clusters. *ApJS*, 99:609, Aug. 1995. [arXiv:astro-ph/9412078](#), [doi:10.1086/192199](#).
- [266] N. Soker. Energy and angular momentum deposition during common envelope evolution. *New A*, 9(5):399–408, June 2004. [arXiv:astro-ph/0311168](#), [doi:10.1016/j.newast.2004.01.004](#).
- [267] N. Soker. The jet feedback mechanism (JFM) in stars, galaxies and clusters. *New A Rev.*, 75:1–23, Dec. 2016. [arXiv:1605.02672](#), [doi:10.1016/j.newar.2016.08.002](#).
- [268] M. Spera and M. Mapelli. Very massive stars, pair-instability supernovae and intermediate-mass black holes with the sevn code. *MNRAS*, 470(4):4739–4749, oct 2017. [arXiv:1706.06109](#), [doi:10.1093/mnras/stx1576](#).
- [269] M. Spera, M. Mapelli, and A. Bressan. The mass spectrum of compact remnants from the PARSEC stellar evolution tracks. *MNRAS*, 451(4):4086–4103, aug 2015. [arXiv:1505.05201](#), [doi:10.1093/mnras/stv1161](#).
- [270] M. Spera, M. Mapelli, N. Giacobbo, A. A. Trani, A. Bressan, and G. Costa. Merging black hole binaries with the SEVN code. *MNRAS*, 485(1):889–907, may 2019. [arXiv:1809.04605](#), [doi:10.1093/mnras/stz359](#).
-

- [271] J. Spitzer, Lyman. Equipartition and the Formation of Compact Nuclei in Spherical Stellar Systems. *ApJ*, 158:L139, Dec. 1969. doi:[10.1086/180451](https://doi.org/10.1086/180451).
- [272] J. Spitzer, Lyman and M. H. Hart. Random Gravitational Encounters and the Evolution of Spherical Systems. I. Method. *ApJ*, 164:399, Mar. 1971. doi:[10.1086/150855](https://doi.org/10.1086/150855).
- [273] L. Spitzer. *Dynamical evolution of globular clusters*. Princeton University Press, 1987. URL: <https://ui.adsabs.harvard.edu/abs/1987degc.book.....S>.
- [274] S. Stevenson, A. Vigna-Gómez, I. Mandel, J. W. Barrett, C. J. Neijssel, D. Perkins, and S. E. de Mink. Formation of the first three gravitational-wave observations through isolated binary evolution. *Nature Communications*, 8:14906, apr 2017. arXiv:[1704.01352](https://arxiv.org/abs/1704.01352), doi:[10.1038/ncomms14906](https://doi.org/10.1038/ncomms14906).
- [275] N. C. Stone and B. D. Metzger. Rates of stellar tidal disruption as probes of the supermassive black hole mass function. *MNRAS*, 455(1):859–883, Jan. 2016. arXiv:[1410.7772](https://arxiv.org/abs/1410.7772), doi:[10.1093/mnras/stv2281](https://doi.org/10.1093/mnras/stv2281).
- [276] J. Tang, A. Bressan, P. Rosenfield, A. Slemer, P. Marigo, L. Girardi, and L. Bianchi. New PARSEC evolutionary tracks of massive stars at low metallicity: testing canonical stellar evolution in nearby star-forming dwarf galaxies. *Monthly Notices of the Royal Astronomical Society*, 445(4):4287–4305, 11 2014. arXiv:<https://academic.oup.com/mnras/article-pdf/445/4/4287/6097104/stu2029.pdf>, doi:[10.1093/mnras/stu2029](https://doi.org/10.1093/mnras/stu2029).
- [277] A. Tanikawa. Dynamical evolution of stellar mass black holes in dense stellar clusters: estimate for merger rate of binary black holes originating from globular clusters. *MNRAS*, 435(2):1358–1375, Oct. 2013. arXiv:[1307.6268](https://arxiv.org/abs/1307.6268), doi:[10.1093/mnras/stt1380](https://doi.org/10.1093/mnras/stt1380).
- [278] A. Tanikawa, H. Susa, T. Yoshida, A. A. Trani, and T. Kinugawa. Merger Rate Density of Population III Binary Black Holes Below, Above, and in the Pair-instability Mass Gap. *ApJ*, 910(1):30, mar 2021. arXiv:[2008.01890](https://arxiv.org/abs/2008.01890), doi:[10.3847/1538-4357/abe40d](https://doi.org/10.3847/1538-4357/abe40d).
- [279] T. M. Tauris, M. Kramer, P. C. C. Freire, N. Wex, H. T. Janka, N. Langer, P. Podsiadlowski, E. Bozzo, S. Chaty, M. U. Kruckow, E. P. J. van den Heuvel, J. Antoniadis, R. P. Breton, and D. J. Champion. Formation of Double Neutron Star Systems. *ApJ*, 846(2):170, Sept. 2017. arXiv:[1706.09438](https://arxiv.org/abs/1706.09438), doi:[10.3847/1538-4357/aa7e89](https://doi.org/10.3847/1538-4357/aa7e89).
- [280] T. M. Tauris, N. Langer, and P. Podsiadlowski. Ultra-stripped supernovae: progenitors and fate. *Monthly Notices of the Royal Astronomical Society*, 451(2):2123–2144, 06 2015. arXiv:<https://academic.oup.com/mnras/article-pdf/451/2/2123/5758766/stv990.pdf>, doi:[10.1093/mnras/stv990](https://doi.org/10.1093/mnras/stv990).

- [281] K. D. Temmink, O. R. Pols, S. Justham, A. G. Istrate, and S. Toonen. Coping with loss. Stability of mass transfer from post-main-sequence donor stars. *A&A*, 669:A45, Jan. 2023. [arXiv:2209.12707](#), [doi:10.1051/0004-6361/202244137](#).
- [282] The LIGO Scientific Collaboration, the Virgo Collaboration, the KAGRA Collaboration, R. Abbott, T. D. Abbott, F. Acernese, K. Ackley, C. Adams, N. Adhikari, R. Adhikari, et al. GWTC-3: Compact Binary Coalescences Observed by LIGO and Virgo During the Second Part of the Third Observing Run. *arXiv e-prints*, page arXiv:2111.03606, nov 2021. [arXiv:2111.03606](#).
- [283] The LIGO Scientific Collaboration, The Virgo Collaboration, and The KAGRA Scientific Collaboration. The population of merging compact binaries inferred using gravitational waves through GWTC-3. *arXiv e-prints*, page arXiv:2111.03634, nov 2021. [arXiv:2111.03634](#).
- [284] A. Tokovinin. Comparative statistics and origin of triple and quadruple stars. *MNRAS*, 389(2):925–938, Sept. 2008. [arXiv:0806.3263](#), [doi:10.1111/j.1365-2966.2008.13613.x](#).
- [285] A. Tokovinin. From Binaries to Multiples. II. Hierarchical Multiplicity of F and G Dwarfs. *AJ*, 147(4):87, Apr. 2014. [arXiv:1401.6827](#), [doi:10.1088/0004-6256/147/4/87](#).
- [286] S. Toonen, A. Hamers, and S. Portegies Zwart. The evolution of hierarchical triple star-systems. *Computational Astrophysics and Cosmology*, 3(1):6, Dec. 2016. [arXiv:1612.06172](#), [doi:10.1186/s40668-016-0019-0](#).
- [287] C. A. Tout, S. J. Aarseth, O. R. Pols, and P. P. Eggleton. Rapid binary star evolution for N-body simulations and population synthesis. *MNRAS*, 291(4):732–748, Nov. 1997. [doi:10.1093/mnras/291.4.732](#).
- [288] A. Trani, M. Spera, M. Mencagli, et al. The TSUNAMI code, 2024. In preparation.
- [289] A. A. Trani, M. S. Fujii, and M. Spera. The Keplerian Three-body Encounter. I. Insights on the Origin of the S-stars and the G-objects in the Galactic Center. *The Astrophysical Journal*, 875(1):42, Apr. 2019. [arXiv:1809.07339](#), [doi:10.3847/1538-4357/ab0e70](#).
- [290] A. A. Trani, S. Rastello, U. N. D. Carlo, F. Santoliquido, A. Tanikawa, and M. Mapelli. Compact object mergers in hierarchical triples from low-mass young star clusters. *MNRAS*, jan 2022. [arXiv:2111.06388](#), [doi:10.1093/mnras/stac122](#).
- [291] A. A. Trani, M. Spera, N. W. C. Leigh, and M. S. Fujii. The keplerian three-body encounter. II. comparisons with isolated encounters and impact on gravitational wave merger timescales. *The Astrophysical Journal*, 885(2):135, nov 2019. [doi:10.3847/1538-4357/ab480a](#).

- [292] A. A. Trani, A. Tanikawa, M. S. Fujii, N. W. C. Leigh, and J. Kumamoto. Spin misalignment of black hole binaries from young star clusters: implications for the origin of gravitational waves events. *Monthly Notices of the Royal Astronomical Society*, 504(1):910–919, 04 2021. [arXiv:https://academic.oup.com/mnras/article-pdf/504/1/910/37229676/stab967.pdf](https://academic.oup.com/mnras/article-pdf/504/1/910/37229676/stab967.pdf), [doi:10.1093/mnras/stab967](https://doi.org/10.1093/mnras/stab967).
- [293] M. Turisini, G. Amati, and M. Cestari. LEONARDO: A Pan-European Pre-Exascale Supercomputer for HPC and AI Applications. *arXiv e-prints*, page arXiv:2307.16885, July 2023. [arXiv:2307.16885](https://arxiv.org/abs/2307.16885), [doi:10.48550/arXiv.2307.16885](https://doi.org/10.48550/arXiv.2307.16885).
- [294] A. V. Tutukov and L. R. Yungelson. The merger rate of neutron star and black hole binaries. *MNRAS*, 260:675–678, feb 1993. [doi:10.1093/mnras/260.3.675](https://doi.org/10.1093/mnras/260.3.675).
- [295] R. K. Ulrich and H. L. Burger. The accreting component of mass-exchange binaries. *ApJ*, 206:509–514, June 1976. [doi:10.1086/154406](https://doi.org/10.1086/154406).
- [296] E. P. J. van den Heuvel. Late Stages of Close Binary Systems. In P. Eggleton, S. Mitton, and J. Whelan, editors, *Structure and Evolution of Close Binary Systems*, volume 73, page 35, jan 1976. URL: <https://ui.adsabs.harvard.edu/abs/1976IAUS...73...35V>.
- [297] E. P. J. van den Heuvel. Double Neutron Stars: Evidence For Two Different Neutron-Star Formation Mechanisms. In T. di Salvo, G. L. Israel, L. Piersant, L. Burderi, G. Matt, A. Tornambe, and M. T. Menna, editors, *The Multicolored Landscape of Compact Objects and Their Explosive Origins*, volume 924 of *American Institute of Physics Conference Series*, pages 598–606, Aug. 2007. [arXiv:0704.1215](https://arxiv.org/abs/0704.1215), [doi:10.1063/1.2774916](https://doi.org/10.1063/1.2774916).
- [298] E. P. J. van den Heuvel. High-Mass X-ray Binaries: progenitors of double compact objects. In L. M. Oskinova, E. Bozzo, T. Bulik, and D. R. Gies, editors, *High-mass X-ray Binaries: Illuminating the Passage from Massive Binaries to Merging Compact Objects*, volume 346, pages 1–13, Dec. 2019. [arXiv:1901.06939](https://arxiv.org/abs/1901.06939), [doi:10.1017/S1743921319001315](https://doi.org/10.1017/S1743921319001315).
- [299] M. Vick, M. MacLeod, D. Lai, and A. Loeb. The Impact of Tidal Dissipation on the Eccentric Onset of Common Envelope Phases. In *AAS/Division of Dynamical Astronomy Meeting*, volume 53 of *AAS/Division of Dynamical Astronomy Meeting*, page 200.03, June 2021. URL: <https://baas.aas.org/pub/2021n5i200p03>.
- [300] A. Vigna-Gómez, C. J. Neijssel, S. Stevenson, J. W. Barrett, K. Belczynski, S. Justham, S. E. de Mink, B. Müller, P. Podsiadlowski, M. Renzo, D. Szécsi, and I. Mandel. On the formation history of Galactic double neutron stars. *MNRAS*, 481(3):4009–4029, Dec. 2018. [arXiv:1805.07974](https://arxiv.org/abs/1805.07974), [doi:10.1093/mnras/sty2463](https://doi.org/10.1093/mnras/sty2463).

-
- [301] H. vonzeipel. Sur l'application des séries de M. Lindstedt à l'étude du mouvement des comètes périodiques. *Astronomische Nachrichten*, 183(22):345, Mar. 1910. doi:[10.1002/asna.19091832202](https://doi.org/10.1002/asna.19091832202).
- [302] J. E. Wall, M.-M. M. Low, S. L. W. McMillan, R. S. Klessen, S. P. Zwart, and A. Pellegrino. Modeling of the effects of stellar feedback during star cluster formation using a hybrid gas and n-body method. *The Astrophysical Journal*, 904(2):192, dec 2020. URL: <https://dx.doi.org/10.3847/1538-4357/abc011>, doi:[10.3847/1538-4357/abc011](https://doi.org/10.3847/1538-4357/abc011).
- [303] L. Wang, M. Iwasawa, K. Nitadori, and J. Makino. PETAR: a high-performance N-body code for modelling massive collisional stellar systems. *Monthly Notices of the Royal Astronomical Society*, 497(1):536–555, sep 2020. arXiv:[2006.16560](https://arxiv.org/abs/2006.16560), doi:[10.1093/mnras/staa1915](https://doi.org/10.1093/mnras/staa1915).
- [304] L. Wang, R. Spurzem, S. Aarseth, M. Giersz, A. Askar, P. Berczik, T. Naab, R. Schadow, and M. B. N. Kouwenhoven. The dragon simulations: globular cluster evolution with a million stars. *Monthly Notices of the Royal Astronomical Society*, 458(2):1450–1465, 03 2016. arXiv:<https://academic.oup.com/mnras/article-pdf/458/2/1450/18234441/stw274.pdf>, doi:[10.1093/mnras/stw274](https://doi.org/10.1093/mnras/stw274).
- [305] L. Wang, R. Spurzem, S. Aarseth, K. Nitadori, P. Berczik, M. B. N. Kouwenhoven, and T. Naab. nbody6++gpu: ready for the gravitational million-body problem. *Monthly Notices of the Royal Astronomical Society*, 450(4):4070–4080, 05 2015. arXiv:<https://academic.oup.com/mnras/article-pdf/450/4/4070/5782448/stv817.pdf>, doi:[10.1093/mnras/stv817](https://doi.org/10.1093/mnras/stv817).
- [306] Y.-H. Wang, N. W. C. Leigh, B. Liu, and R. Perna. SpaceHub: A high-performance gravity integration toolkit for few-body problems in astrophysics. *Monthly Notices of the Royal Astronomical Society*, 505(1):1053–1070, 04 2021. arXiv:<https://academic.oup.com/mnras/article-pdf/505/1/1053/38391786/stab1189.pdf>, doi:[10.1093/mnras/stab1189](https://doi.org/10.1093/mnras/stab1189).
- [307] J. L. Ward, J. M. D. Kruijssen, and H.-W. Rix. Not all stars form in clusters – Gaia-DR2 uncovers the origin of OB associations. *Monthly Notices of the Royal Astronomical Society*, 495(1):663–685, 04 2020. arXiv:<https://academic.oup.com/mnras/article-pdf/495/1/663/33240978/staa1056.pdf>, doi:[10.1093/mnras/staa1056](https://doi.org/10.1093/mnras/staa1056).
- [308] R. F. Webbink. Evolution of Helium White Dwarfs in Close Binaries. *Monthly Notices of the Royal Astronomical Society*, 171(3):555–568, 06 1975. arXiv:<https://academic.oup.com/mnras/article-pdf/171/3/555/2856499/mnras171-0555.pdf>, doi:[10.1093/mnras/171.3.555](https://doi.org/10.1093/mnras/171.3.555).
- [309] R. F. Webbink. Double white dwarfs as progenitors of R Coronae Borealis stars and type I supernovae. *ApJ*, 277:355–360, feb 1984. doi:[10.1086/161701](https://doi.org/10.1086/161701).
-

- [310] R. F. Webbink. The formation and evolution of symbiotic stars. In J. Mikolajewska, M. Friedjung, S. J. Kenyon, and R. Viotti, editors, *The Symbiotic Phenomenon*, pages 311–321, Dordrecht, 1988. Springer Netherlands. URL: https://link.springer.com/chapter/10.1007/978-94-009-2969-2_69.
- [311] C. Weidner and P. Kroupa. The maximum stellar mass, star-cluster formation and composite stellar populations. *MNRAS*, 365(4):1333–1347, Feb. 2006. [arXiv:astro-ph/0511331](https://arxiv.org/abs/astro-ph/0511331), [doi:10.1111/j.1365-2966.2005.09824.x](https://doi.org/10.1111/j.1365-2966.2005.09824.x).
- [312] C. Weidner, P. Kroupa, and I. A. D. Bonnell. The relation between the most-massive star and its parental star cluster mass. *Monthly Notices of the Royal Astronomical Society*, 401(1):275–293, 12 2009. [arXiv:https://academic.oup.com/mnras/article-pdf/401/1/275/18578058/mnras0401-0275.pdf](https://academic.oup.com/mnras/article-pdf/401/1/275/18578058/mnras0401-0275.pdf), [doi:10.1111/j.1365-2966.2009.15633.x](https://doi.org/10.1111/j.1365-2966.2009.15633.x).
- [313] S. E. Woosley. Pulsational pair-instability supernovae. *The Astrophysical Journal*, 836(2):244, feb 2017. URL: <https://dx.doi.org/10.3847/1538-4357/836/2/244>, [doi:10.3847/1538-4357/836/2/244](https://doi.org/10.3847/1538-4357/836/2/244).
- [314] S. E. Woosley. The Evolution of Massive Helium Stars, Including Mass Loss. *ApJ*, 878(1):49, June 2019. [arXiv:1901.00215](https://arxiv.org/abs/1901.00215), [doi:10.3847/1538-4357/ab1b41](https://doi.org/10.3847/1538-4357/ab1b41).
- [315] S. E. Woosley, S. Blinnikov, and A. Heger. Pulsational pair instability as an explanation for the most luminous supernovae. *Nature*, 450(7168):390–392, Nov. 2007. [arXiv:0710.3314](https://arxiv.org/abs/0710.3314), [doi:10.1038/nature06333](https://doi.org/10.1038/nature06333).
- [316] X.-J. Xu and X.-D. Li. On the Binding Energy Parameter λ of Common Envelope Evolution. *ApJ*, 716(1):114–121, June 2010. [arXiv:1004.4957](https://arxiv.org/abs/1004.4957), [doi:10.1088/0004-637X/716/1/114](https://doi.org/10.1088/0004-637X/716/1/114).
- [317] T. Yoshida, H. Umeda, K. Maeda, and T. Ishii. Mass ejection by pulsational pair instability in very massive stars and implications for luminous supernovae. *Monthly Notices of the Royal Astronomical Society*, 457(1):351–361, 01 2016. [arXiv:https://academic.oup.com/mnras/article-pdf/457/1/351/18168415/stv3002.pdf](https://arxiv.org/abs/https://academic.oup.com/mnras/article-pdf/457/1/351/18168415/stv3002.pdf), [doi:10.1093/mnras/stv3002](https://doi.org/10.1093/mnras/stv3002).
- [318] B. Zackay, T. Venumadhav, L. Dai, J. Roulet, and M. Zaldarriaga. Highly spinning and aligned binary black hole merger in the advanced ligo first observing run. *Phys. Rev. D*, 100:023007, Jul 2019. URL: <https://link.aps.org/doi/10.1103/PhysRevD.100.023007>, [doi:10.1103/PhysRevD.100.023007](https://doi.org/10.1103/PhysRevD.100.023007).
- [319] J. P. Zahn. The dynamical tide in close binaries. *A&A*, 41:329–344, July 1975. URL: <https://ui.adsabs.harvard.edu/abs/1975A&A....41..329Z>.
- [320] J. P. Zahn. Tidal friction in close binary systems. *A&A*, 57:383–394, May 1977. URL: <https://ui.adsabs.harvard.edu/abs/1977A&A....57..383Z>.

- [321] Y. B. Zel'dovich and M. A. Podurets. The Evolution of a System of Gravitationally Interacting Point Masses. *Soviet Ast.*, 9:742, apr 1966. URL: <https://ui.adsabs.harvard.edu/abs/1966SvA.....9..742Z>.
- [322] M. Zevin, S. S. Bavera, C. P. L. Berry, V. Kalogera, T. Fragos, P. Marchant, C. L. Rodriguez, F. Antonini, D. E. Holz, and C. Pankow. One Channel to Rule Them All? Constraining the Origins of Binary Black Holes Using Multiple Formation Pathways. *ApJ*, 910(2):152, apr 2021. [arXiv:2011.10057](https://arxiv.org/abs/2011.10057), [doi:10.3847/1538-4357/abe40e](https://doi.org/10.3847/1538-4357/abe40e).
- [323] M. Zevin, C. Pankow, C. L. Rodriguez, L. Sampson, E. Chase, V. Kalogera, and F. A. Rasio. Constraining Formation Models of Binary Black Holes with Gravitational-wave Observations. *ApJ*, 846(1):82, Sept. 2017. [arXiv:1704.07379](https://arxiv.org/abs/1704.07379), [doi:10.3847/1538-4357/aa8408](https://doi.org/10.3847/1538-4357/aa8408).
- [324] M. Zevin, M. Spera, C. P. L. Berry, and V. Kalogera. Exploring the lower mass gap and unequal mass regime in compact binary evolution. *The Astrophysical Journal Letters*, 899(1):L1, aug 2020. URL: <https://dx.doi.org/10.3847/2041-8213/aba74e>, [doi:10.3847/2041-8213/aba74e](https://doi.org/10.3847/2041-8213/aba74e).
- [325] B. M. Ziosi, M. Mapelli, M. Branchesi, and G. Tormen. Dynamics of stellar black holes in young star clusters with different metallicities - II. Black hole-black hole binaries. *MNRAS*, 441(4):3703–3717, jul 2014. [arXiv:1404.7147](https://arxiv.org/abs/1404.7147), [doi:10.1093/mnras/stu824](https://doi.org/10.1093/mnras/stu824).
- [326] S. F. P. Zwart and S. L. W. McMillan. Black hole mergers in the universe. *ApJ*, 528(1):L17–L20, jan 2000. [doi:10.1086/312422](https://doi.org/10.1086/312422).